Water splitting photoelectrocatalysis : the conception and construction of a photoelectrocatalytic water splitting cell

Samantha Hilliard

Université Pierre et Marie Curie (Paris VI)

Ecole doctorale 397

Le Laboratoire de chimie de la matière condensée de Paris / Matériaux Hybrides et Nanomatériaux

Photocatalyse de décomposition de l'eau :

Conception et construction d'une cellule photoelectrocatalyique pour la photodissociation de l'eau

Par Samantha Hilliard

Thèse de doctorat de Chimie des Matériaux

Dirigée par Professeur Christel Laberty-Robert et Docteur Vincent Artero

Présentée et soutenue publiquement le 23 février 2016

Devant un jury composé de :

Prof. Nicolas Alonso-Vante	Professeur (Université de Poitiers)	Rapporteur
Dr. Jean-François Hochepied	Directeur de Recherche (Mines Paris Tech, Paris)	Rapporteur
Prof. Roel Van de Krol	Directeur de Recherche (Helmholtz Zentrum Berlin)	Examinateur
Dr. Vincent Vivier	Directeur de Recherche (Lise, Paris VI)	Examinateur
Prof. Christel Laberty-Robert	Professeur (Université Pierre et Marie Curie, Paris)	Directrice de Thèse
Dr. Vincent Artero	Directeur de Recherche (CEA, Grenoble)	Co-Directeur de Thèse
Dr. Henri Strub	Conseiller Scientifique Chimie (Total Energies Nouvelles)	Encadrant

Water splitting photoelectrocatalysis:

The conception and construction of a photoelectrocatalytic water splitting cell

ACKNOWLEDGEMENTS

First and foremost I would like to thank my PhD directrice, Christel Laberty, who was a mentor and endless source of support, creativity, and guidance for me. Thank you for leaving me enough autonomy to grow and improve in my research while encouraging my efforts and supporting me throughout this venture. I could not have asked for a better directrice during this PhD experience.

I would like to thank the members of the jury: Roel Van de Krol, Nicolas Alonso-Vante, Vincent Vivier, Jean-François Hochepied, Henri Strub, Vincent Artero, and Christel Laberty, for your interest and accepting to examine my scientific efforts as well as validating my work and interest in the innovative field of material science and sustainability. I additionally want to thank the jury for enabling my defense be an enjoyable moment, and for the brilliant comments, suggestions, and discussions. I am proud to be able to say I have interacted with such brilliant minds and cherish the intellectual collaboration and passion in the shared ambition of progress. Thank you to Vincent Artero for accepting me into your laboratory and following my progress throughout the years as well as Bernard Sartor for his construction skills. And thank you to Henri Strub, Stéphane Kressman, Daniel Ferre-Curulla, Hadjar Benmansour, and Vincent Schachter for the guidance, support, and intellectual inspiration which enabled me to complete this project. I would also like to thank Guido Baldinozzi, David Montero, Dennis Freidrich, Abdi Fatwa, and all the other helpful intelligent individuals in the scientific world who dedicated to donate some of their knowledge and time to ameliorate this study.

I must thank my "binôme" Johanna Toupin. Completing a PhD thesis is generally known to be a very solitary undertaking. Fortunately, this was far from the case with Johanna, for the knowledge, support, and friendship between us was more than complementary. I treasure our many travels, experiences, and beers shared during these three years. I give this thesis partnership five stars. Top notch. Thanks Shauna.

Finally I must thank my family for their unconditional support and love, despite being 9000 km away. My best friends, Claire Ostroff, Lucas Winiarski, and Krista Enold for all the support, love, and pylons. Thank you to William Petit, for amicably integrating me into the world of savate boxe française and for his continued encouragement and maîtrise of the deuxième degré (on peut même dire "second" degré). Many thanks to the crazy characters in the alps and paris which invited me underground and enlightened me in several ways. And finally thank you to all my friends and "potes du labo" for the memorable experiences, love, and laughs.

TABLE OF CONTENTS

INTRODUCTION

The most abundant element in the universe, hydrogen, does not exist in the form of H_2 on Earth, but rather in molecular forms such as water and other organic compounds. Liberating hydrogen from these compounds by energetic methods is the root obstacle in the hydrogen energy economy [1]. Hydrogen's highly combustible characteristics enable it to be pursued as a promising energy vector, potentially in fuel cells for future automotive vehicles. Hydrogen possesses approximately 2.6 times the energy per unit mass as gasoline for fuel applications making it the richest chemical in energy per unit mass [2]. Though hydrogen is consumed in semiconductor processes, scientific and NASA applications, hydrogen is primarily utilized in oil refining and ammonia production for the petroleum and chemical industries, more precisely in the Haber process to synthesize ammonia from atmospheric nitrogen for the production of fertilizer [3]. As the population and technological advances on our planet increase, hunger and energy become commonplace issues which depend on fossil fuel originated chemical and energetic sources, many of which are nonrenewable. In the 1960s, the industrial production of hydrogen shifted towards a fossil-based feedstock, which is the main source for hydrogen production today [4]. Unfortunately the manufacture of hydrogen from fossil fuels is nonrenewable and furthermore leads to CO_2 as a byproduct, consequently contributing to greenhouse gas production. Fortuitously, hydrogen on Earth can be contrived by several techniques, some of which do not depend on fossil fuels. In order to evolve towards a sustainable environment, it is imperative to implement non-fossil based, renewable sources for use in chemical and energy industries. Therefore we must envision solutions in order to manufacture clean and renewable H_2 for future use as a chemical reagent as well as an efficient energy vector.

Amongst the current potential clean hydrogen production methods, the most developed solution is water electrolysis. Today, approximately 4% of industrial hydrogen is produced by water electrolysis and is the leading form of renewable hydrogen production [4-6]. There are three main types of water electrolysis technologies at present: alkaline electrolyzers (which have been used since the early 20^{th} century), proton exchange membrane electrolyzers (otherwise known as polymer electrolyte membrane electrolyzers which are recently commercially available), and solid oxide electrolyzers (which can work at higher temperatures). Although water electrolysis offers a convenient way to produce decarbonized hydrogen gas, the energy required by the process (excluding the chemical energy in CH_4) is roughly four times larger than the energy required for the production of hydrogen from natural gas processes [7]. If non-renewable power generation is used to create the electricity used for water electrolysis, it actually results in higher emissions compared to natural gas based production of hydrogen [8]. Electrolysis-based solutions are only beneficial for the environment if the electricity used for the electrolysis is produced from carbon-free fuels [9]. Therefore, combining this known water splitting technology with solar energy, a renewable source of electricity, has been adopted within the last few decades [10]. The coupling of photovoltaics with water electrolysis is an interesting concept which potentially manufactures "clean"

hydrogen from a renewable source. Employing the solar fuel concept, the direct current produced from the photovoltaic effect in semiconductors is able to power electrolyzers to split water and produce hydrogen as well as oxygen. Both of these technologies are mature and thus low risk in terms of financial investments, resulting in a plausible source of renewable hydrogen. A theoretical maximum of 29% photoconversion for a silicon photovoltaic coupled with an electrolyzer theoretical maximum of 83% suggests the highest solar to hydrogen conversion possible is 24% (not counting losses in transmission and conversion between the two technologies). Using current high performing photovoltaics coupled with electrolyzers has a potential solar to hydrogen (STH) efficiency of up to 18%; whereas, using average photovoltaic technologies this value is generally around 8% [11-20]. Much of the losses are due to connections in the system, DC-DC step regulators, and efficiencies of each technology arising from fundamental thermodynamic theoretical limitations [21]. The cost of hydrogen therefore will depend on several factors: the capital investments, land use, and especially the solar insolation based on the installation's location [13]. Several functioning systems have been experimentally tested concerning PV-electrolyzer coupled setups; nevertheless, there are several drawbacks concerning connections, infrastructure, scaling, safety, etc. [14-16, 22-24].

Water splitting by photoelectrocatalysis may circumvent several existing obstacles concerning PV-electrolysis coupling. This concept is similarly recognized as a photoelectrochemical cell (PEC). Photoelectrocatalysis combines and integrates the concepts of electrolysis and photovoltaic technologies for renewable hydrogen production. PEC cells use the photovoltaic effect of semiconductors to absorb photons in order to generate sufficient charge carriers to decompose water and produce hydrogen and oxygen gas. Specifically, this concept is based in utilization of the photovoltaic effect in semiconducting materials to create holes and electrons which then fuel electrochemical water splitting reaction at a cathode and/or anode [5, 25, 26]. The main difference between a photoelectrochemical and a photovoltaic device is that in the PEC case, a semiconductor-electrolyte junction is used as the active layer instead of the solid-state junctions in a photovoltaic structure [27, 28]. Advantages of direct conversion PEC over separate generation PV plus conventional electrolysis is the lower driving voltage, compact size, and the elimination of the electrical current collection network and concomitant current transmission losses [29].

The first chapter of this thesis discusses water splitting technologies, thermodynamic limitations, considerations, and state of the art cells and materials. These considerations aid in adopting the fundamental architecture and configuration for the conception and construction of a photoelectrocatalytic water splitting cell. Congruently, the cell will be configured in a tandem dual photosystem arrangement, consisting of thin film planar photoelectrodes. This photoelectrocatalytic water splitting cell aims to use a photoanode for oxygen production and a photocathode for hydrogen production as well as contain a

proton conducting membrane integrated to the device to form two compartments and facilitate gas separation of hydrogen and oxygen. It should additionally be assembled and fabricated utilizing the most efficient but simplified model while using facile processing of the anode – cathode coupled device system for practical application.

Chapter two discusses the initial research effectuated on materials as transparent thin films for the photoanode to produce oxygen in the water splitting half reaction. Essential restraints concerning natural resources are discussed, pursuing to avoid using non-noble, expensive, and rare metals as well as energetically demanding methods. Overall, research concerning materials aims to employ low cost and low temperature processes which can be scalable for industrial application and future application. Two different materials are discussed, fabricated, characterized, and optimized using low cost sol-gel dip coating processes. These materials are to be coupled with a photocathode for use in a water splitting cell for solar hydrogen production.

Finally the third chapter encompasses these photoanode materials which are then coupled with a complementary photocathode for use in a photoelectrocatalytic cell. This cell is conceptualized and constructed based on state of the art photoelectrochemical cell efforts as well as laboratory prerequisites regarding research and development in water splitting technologies. Results, ameliorations, and future perspectives are then discussed, concerning the results of a wire-connected tandem dual photosystem water splitting device and the thin film photoelectrode performance.

I. WATER SPLITTING TECHNOLOGIES: THERMODYNAMIC LIMITATIONS, CONSIDERATIONS, AND STATE OF THE ART

I.1. WATER ELECTROLYSIS

In response to the demand of hydrogen for use in the chemical and energy industries, water electrolysis has been a solution since the early 20th century. This technological concept uses electricity to split water molecules in order to form oxygen and hydrogen gases in a device called an electrolyzer. Decomposition of water occurs due to a direct current (DC) passed between two electrodes (cathode and anode) which are submerged in water separated by an ion-conducting (aqueous or solid) electrolyte. The total energy required for electrolytic hydrogen production at standard temperature and pressure (293 K and 1 atm) is shown below in equation (1).

$$\Delta G° = \Delta H° - T\Delta S° = (286.03 - 0.163 \cdot T)\ kJ/mol\ H_2 \quad (1)$$

The Gibb's free energy (ΔG°) corresponds to the minimum share of enthalpy (ΔH°) which has to be applied as work (electricity). The temperature and change in entropy (TΔS°) correspond to the maximum share of ΔH° which can be applied as thermal energy to the process. The overall electrolysis reaction (shown below) is a sum of two electrochemical reactions (also called the half reactions or the half-cell reactions), which occur at the electrodes. The stoichiometric net energetic reaction of electrolysis of water is described in equation (2):

$$H_2O_{(l)} + \frac{237.2\ kJ}{mol} + \frac{48.7\ kJ}{mol} \rightleftarrows H_{2(g)} + \frac{1}{2}O_{2(g)} \quad (2)$$

The necessary energy to split water to generate oxygen and hydrogen gases is approximately 286 kJ/mol. This is derived from the enthalpy change for the combustion energy of hydrogen, also known as the higher heating value (HHV); approximately, + 237 kJ of this energy derives directly from electrical energy, denoted as the Gibbs free energy, the rest (48 kJ/mol) is derived from heat. For this study, we consider the Gibbs free energy (ΔG) change for water splitting reaction: ΔG° = + 237.2 kJ/mol or 2.46 eV/molecule of H_2O [30]. (Since two electrons are involved in the reaction, this corresponds to 1.23 eV per electron). Controversially, because water splitting is an endothermic reaction, this suggests that heat is taken from surroundings and should be taken into account concerning the total energy input for hydrogen production from water splitting electrolysis, thus the HHV should be used for efficiency calculations (though the lower heating value (LHV) of 237 kJ/mol is more practical when comparing electrical input only). The voltage applied in electrolyzers requires energy greater than the free energy of formation of water corresponding to activation energy and ohmic losses in order to successfully split water molecules. For water electrolysis, system efficiency is calculated by dividing the heating value (LHV or HHV) by the real energy input in units of kWh/kg [31]. This leads to a maximum efficiency of about 83% based upon LHV

and the fundamental (33.3 kWh/kg) and 100% for HHV (39.4 kWh/kg) [32]. This study uses the LHV, as the electrical component to drive water is the focus. In Nernstian terms, the Gibbs free energy is rewritten below, which expresses the change in free energy for any extent of reaction:

$$\Delta G° = -nFE° \tag{3}$$

where n is the number of electrons transferred in the reaction, F is the Faraday constant (96,500 C/mol), and E° the change in potential ($E° = E°_{reduction} - E°_{oxidation}$). This can be rewritten in terms of electrochemical equations and charges involved in the complete reaction (4) and two half reactions: the oxygen evolution reaction (OER) and the hydrogen evolution reaction (HER), written below as it occurs in acidic conditions as (5) and (6) respectively:

$$2H_2O + 4h^+ + 4e^- \rightleftarrows 2H_2 + O_2 \tag{4}$$

$$2H_2O + 4h^+ \rightleftarrows O_2 + 4e^- + 4H^+ \qquad E^0_{H_2O/O_2} = 1.23\ V\ vs.NHE \tag{5}$$

$$4e^- + 4H^+ \rightleftarrows 2H_2 \qquad E^0_{H^+/H_2} = 0.00\ V\ vs.NHE \tag{6}$$

where E^0 is the energetic potential at standard temperature and pressure, STP, (25°C and 1bar) and the redox potentials for both the OER and HER are referenced to the normal hydrogen electrode (NHE). The NHE is a reference based on the hydrogen redox half-cell reaction completed with a platinum electrode in acidic solution (pH 0 ($[H^+]$ = 1.0 M) at 25 °C and 1 bar bubbled with hydrogen gas) which maintains the unity of the oxidized and reduced form. This suggests that E° is negative and the overall water splitting reaction is not spontaneous but rather demands energy to be completed. Since the decomposition of water is kinetically based and related to the concentration of protons in solution. Thus, at pH 7 ($[H^+]$ = 1.0×10^{-7} M) the pH of the solution shifts the potential energy needed to split water relative to the acidity of the solution. This shift in energy potentials due to concentration of acidic and basic species can influence the potentials required, relative to the NHE, for the desired water splitting reaction. For example, in conditions more alkaline than neutral, this Nernstian relation can be written for the reduction of protons in terms of hydroxide and proton concentration (equations (7) and (8)):

$$H_2O \rightleftarrows H^+ + OH^- \ with\ K_{eq} = \frac{[H^+][OH^-]}{[H_2O]} = 10^{-14} \tag{7}$$

$$E_{H^+/H_2} = E^0_{H^+/H_2} + \frac{RT}{nF} ln \frac{[H^+]^2}{p_{H_2}} \quad (8)$$

where R is the universal gas constant (8.314 $J \cdot K^{-1} \cdot mol^{-1}$), T temperature (K), *n* the number of moles of electrons transferred in the half-cell reaction, F the faradaic constant or the number of coulombs per mole of electrons (9.6485 x 10^4 $C \cdot mol^{-1}$), H^+ the concentration of protons (moles/liter), and p_{H2} the partial pressure of hydrogen. Similarly, in equation (9), the oxidation of water can be written as:

$$E_{H_2O/O_2} = E^0_{H_2O/O_2} + \frac{RT}{nF} ln\left(p_{O_2}[H^+]^4\right) \quad (9)$$

At STP these two equations become equations (10) and (11):

$$E_{H^+/H_2} = E^0_{H^+/H_2} - 0.059 \cdot pH \quad (10)$$

$$E_{H_2O/O_2} = E^0_{H_2O/O_2} - 0.059 \cdot pH \quad (11)$$

Therefore, in alkaline environments (pH 14) the water splitting reaction potentials shift and become equations (12) and (13) due to this Nernstian relation:

$$4H_2O + 4e^- \rightleftarrows 2H_2 + 4OH^- \qquad E^0_{H^+/H_2} = -0.82\ V\ vs.NHE \quad (12)$$

$$4OH^- + 4h^+ \rightleftarrows 2H_2O + O_2 \qquad E^0_{H_2O/O_2} = 0.40\ V\ vs.NHE \quad (13)$$

This relation can be described in a Pourbaix diagram, depicted below in Figure 1 [33]:

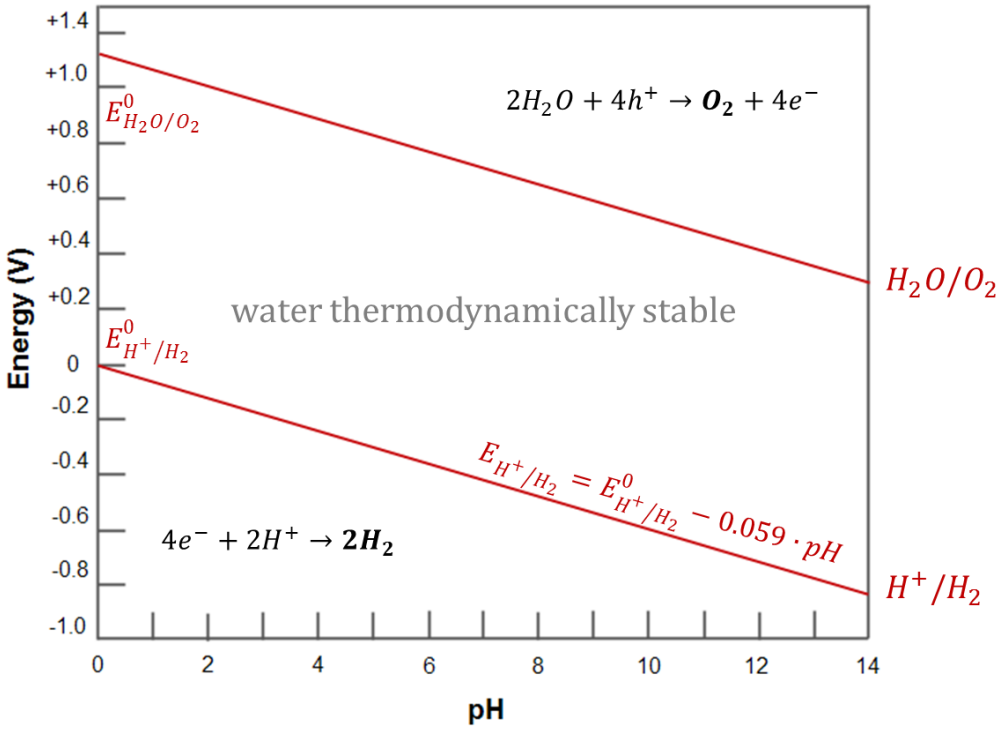

Figure 1: Thermodynamic water splitting oxidation and reduction potentials as a function of pH at STP

This Nernstian relation between potential differences at varying pH is referred to as the reversible hydrogen electrode (denoted RHE) in place of NHE throughout this study, which takes into account the pH of solution in relation to the reference potential applied in the reaction. By using a potential to drive the water splitting reaction, this indicates that it is kinetically controlled; therefore, the potential needed to drive the kinetics for water splitting oxidation and reduction require a greater applied potential to overcome several elements: the activation energy, ion mobility (diffusion and drift) and concentration, wire resistance, surface blockage (bubble formation), etc. Therefore, 1.23 V to split water is a modest approximation and in reality suggests that a larger potential is needed to drive this kinetically limited reaction. Many electrical sources exist to fuel water electrolysis; fortunately, the sun's vast energy may hold the potential to fuel this reaction.

I.2. The Photovoltaic Effect

Photovoltaics are semiconducting materials which exhibit the photovoltaic effect, otherwise defined as the ability of converting solar energy into direct current electricity. Photovoltaic efficiency depends on the ability of a material to absorb light and create charge carriers which can be extracted to produce an electrical current. This ability is directly related to the semiconductor's band gap, allowing absorption of

solar energy equal or greater to its respective band gap energy. Band gaps in semiconducting materials occur due to the electronic structures directly correlated to chemical bonding within the material. These bonds in photovoltaics are typically covalent and lead to hybrid overlap in the principle (p) orbitals, enabling the delocalization of charge carriers and thus the production of a DC current upon solar excitation to these vacant electronic states.

The proficiency of a solar cell is directly related to the semiconducting material characteristics (band gap), making it essentially a photon powered diode whose efficiency is the fraction of incident power converted to electricity. Illumination, or solar energy which fuels this conversion, majorly affects the performance of this technology. General solar irradiation power is benchmarked by the American Society for Testing and Materials (ASTM). This spectral power received on Earth is denoted AM1.5, which stands for Air Mass with 1.5 times the atmosphere thickness with a 37° tilted surface (global) or the direct normal spectral irradiance (direct) considering the solar zenith angle 48.19° which corresponds to the average of 48 states over the course of a year and therefore more or less an average irradiation applicable to the world's major population localities [34-36]. Irradiation for solar technology testing is considered to be 100 mW/cm², derived from integration of the AM1.5G spectra, presented in Figure 2:

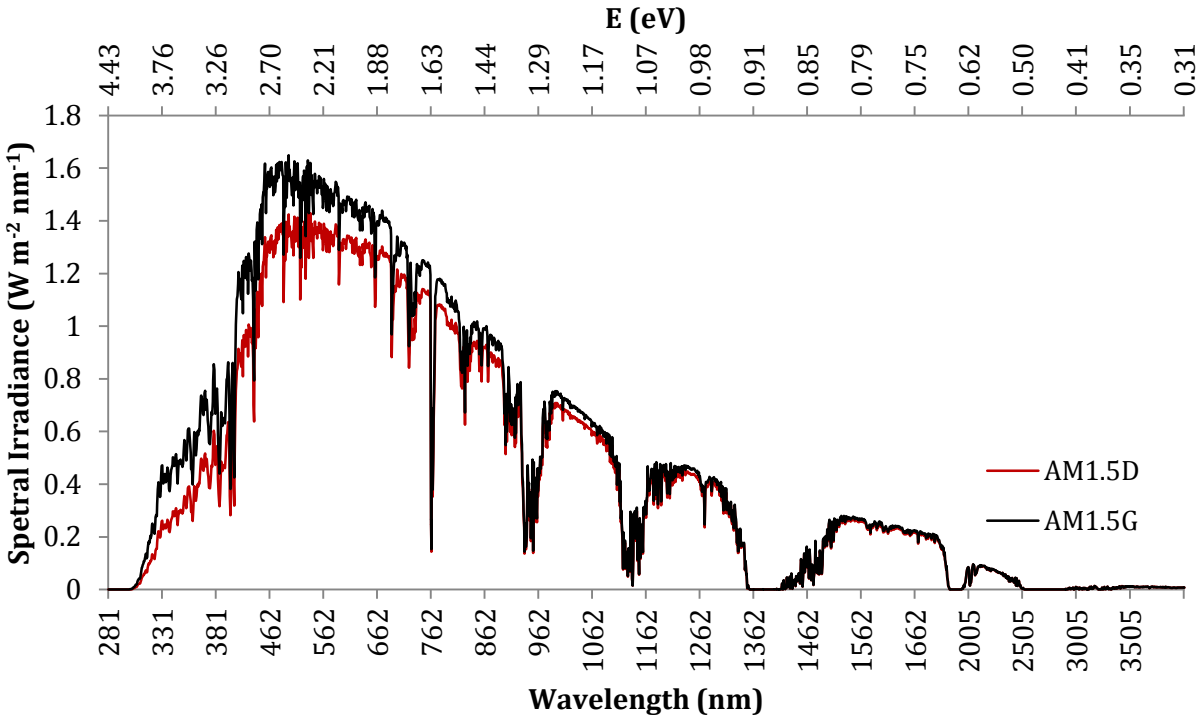

Figure 2: Solar spectrum (ASTM G173-03) reference solar spectra

Photovoltaics are consequently limited by fundamental thermodynamics associated with material characteristics and input power from solar irradiation [21]. Today several types of photovoltaics exist: silicon based (amorphous, crystalline, monocrystalline, polycrystalline, ribbon, etc.), thin film non silicon based PV – also known as II-VI photovoltaics (e.g. copper indium gallium (di)selenide, gallium arsenide, indium phosphide, and cadmium tellurium), organic photovoltaics, and dye-sensitized photovoltaics. Silicon, being abundant and relatively inexpensive, is the most commercialized even though it is not the most performant but can attain large quantum internal efficiencies. Current photovoltaic cell efficiencies employing silicon average around 17% solar to electricity efficiency. Though as of late, more complex and expensive photovoltaic architectures and materials exist. For instance, four-junction photovoltaic cells constructed of GaInP/GaAs and GaInAsP/GaInAs can reach up to 46% solar to electricity efficiency [37].

I.3. PHOTOVOLTAIC – ELECTROLYZER COUPLING

Integrating electrolyzers with photovoltaic modules necessitates DC-DC matching of the two technologies along with several additional obstacles typically involved with intermittent renewable energies. Typical alkaline electrolyzers have slow start up times and therefore when coupled with intermittent renewable sources of electricity, such as photovoltaics, drastically suffer in terms of efficiency. Polymer electrolyte membrane (PEM) electrolyzers have quicker start up times and thus are better coupled with PV technologies for clean hydrogen production, yet still suffer from intermittent photovoltaic consequences such as: lack of solar irradiation during night and cloud cover or poor weather resulting in power fluctuations which limit the overall system efficiency. Nevertheless it is proposed that any energetic losses in the system can potentially be made up by an increase in photovoltaic collector area, although requiring more land [12]. The potential high performing photovoltaic coupled with an electrolyzer has a potential STH efficiency of up to 18%; though coupling to an average photovoltaic module in moderately irradiated areas renders this value around 3-8% [11-15, 19]. Within the past few decades, much research has been completed to advance the coupling of these two technologies and to avoid losses typically implicated by PV-electrolyzer coupling. Eventually, this coupled technology may be replaced with a more direct solution to solar hydrogen production by means of photoelectrocatalysis.

I.4. PHOTOELECTROCATALYSIS

Photoelectrolysis (or photoelectrocatalysis) avoids transmission and conversion losses by directly placing the semiconductor in water to split water, creating a more compact and integrated design than PV-electrolyzer coupled systems [38]. The advantage of PEC direct conversion over separate PV generation in adjunction with conventional electrolysis is the elimination of the electrical current collection network and concomitant current transmission losses [29]. Photoelectrocatalysis of water has the potential to be competitive with electrolyzer-coupled photovoltaics, suggesting a theoretical solar to hydrogen (STH)

efficiency of 31 - 42% depending on the device configuration and materials [39-42]. In practical application including losses, this technology is projected to achieve upwards of 20% STH depending on the configuration and materials used [40, 41, 43, 44]. The STH calculation is based on the water splitting thermodynamic requirements of 1.23 V or of 237 kJ/mol H_2 referred to in equations (2) – (5). Depending on the type of semiconducting material(s) used, a theoretically current density of 15 – 25 mA/cm² (for a single photosystem; and half for a dual photosystem) is proposed for correct PEC functioning at solar intensities [30]. At these current densities, the voltage required for electrolysis is much lower than electrolyzers (i.e. 1.3 V for PECs in place of 1.8 or 2 V for typical electrolyzers); therefore, the corresponding electrolysis efficiency can potentially be higher [12, 30, 45].

The photovoltaic effect in semiconductors submerged in aqueous solutions to fuel the electrochemical water splitting half-cell reactions between a cathode and anode is a concept with many options, obstacles, goals, and benchmarks. Essentially, there are four main steps in order to split water in the production of hydrogen from solar energy. The initial step is the generation of a charge (electron or hole) at the photoelectrode surface from photon excitation – yielding electron-hole pairs. The second step is oxidation of a water molecule by holes at the photoanode surface to generate molecules of oxygen. Subsequently, protons are transported from the photoanode to the cathode by way of electrolyte where H^+ ions at the cathode surface will be reduced by electrons at the cathode yielding H_2 gas. Likewise, electrons created in the photoanode make their way to the cathode by means of a wire connection/circuit to additionally reduce protons found at the surface, completing the electrical circuit. Speculation suggests that the semiconductor liquid junction (SCLJ) may harness charge accumulation to create “wet electrons”, making charge transfer less energetically demanding [46, 47].

To date, the U.S. Department of Energy (DOE) has set a goal of 10% STH for PEC technologies, possessing a lifetime duration of 10,000 hours and a photocurrent density (noted j) of 8.1 mA/cm² [48]. Many institutions including NREL, MIT, the Helmholtz Zentrum, University of Hawaii, University of California Santa Barbara, MV Systems, GE Global Research, and Midwest Optoelectronics are amongst several research groups which play major roles in PEC research today in order to advance this technology for industrial application. Notwithstanding, there are many difficult obstacles to overcome considering this technology encounters electrochemical redox reactions, degradation/corrosion, surface chemistry, material science, optics, resistance, ohmic losses, etc. Materials which possess desired spectral qualities are not always stable or immune to corrosion in aqueous environments [49-52]. Therefore, photoelectrocatalysis water splitting is seen as a long term solution due to the fact that suitable materials should be: cost effective, possess desirable photon absorbing and semiconducting attributes, remain stable in aqueous solutions (resist corrosion), and exhibit STH yields efficient enough to become viable in the market

today [53-55]. Unfortunately, materials which fit these requirements have not yet been established. As a result, many efforts have been accomplished to find and optimize appropriate materials in appropriate combinations and configurations for the realization of this clean hydrogen technological concept. To further understand these needs and requirements, thermodynamic limitations due to solar insolation, material properties, and kinetics must be addressed.

I.4.1. THERMODYNAMIC LIMITATIONS

The photovoltaic effect in semiconductors is a large contributing factor in efficiency for photonic hydrogen production, which is grounded on power conversion efficiency of the ideal two band positioned photoconversion – a function of the band gap (E_g) and the incident spectrum. Intended for terrestrial implementation, the incident spectrum (the sun's electromagnetic spectrum which arrives on Earth) is relatively fixed; therefore, efficiency depends strongly on the band gap and its ability to absorb light [42]. For a pure material, the band gap is the energy range in a semiconductor where no electron states can exist. Thus to be conductive must absorb energy to excite charges across this energy gap to be collected for use. The actual photocurrent measured depends upon how efficiently the photogenerated carriers in the semiconductor are harvested at the contact or surface. Due to characteristics of photonic absorption in semiconductors, there is a definite threshold (the band gap energy) which can roughly be measured from the wavelength (λ) of the absorption edge: $E_g = hc/\lambda_g$ where h is Planck's constant and c is the speed of light. According to this threshold, there are four unavoidable energy losses in photonic conversion:

1. Solar photons with $\lambda \geq \lambda_g$ cannot be absorbed (they are lost to the conversion process).
2. Solar photons with $\lambda \leq \lambda_g$ can be absorbed, but the excess energy ($E - E_g$) is lost as heat – relaxed to the level of E_g. This energy is therefore not available to the conversion process and is generally lost as heat.
3. The energy of the excited state is thermodynamically an internal energy, therefore not ΔG, and a fraction (roughly 75%) of the excited state energy can be converted into work or stored as chemical energy. This explains why the open circuit (V_{oc}) extreme is known as the maximum potential difference or driving power of the reaction. A significant concentration of excited voltage/potential can never be as high as the band gap potential. (In a PEC these losses show up as a share of the overpotential).
4. When a photoconverter material is illuminated, the extra chemical potential of the excited states is dependent on the concentration. This optimum condition lies between the short circuit current (all excited states converted to products) and open circuit voltage (rate of production is zero). This point, in-between the two concentration states, exist at this condition and therefore there will always be some losses (1-2%) due to spontaneous emission (fluorescence) [56].

Like photovoltaics, the direct current created occurs because of diffusion of the charge carriers in the semiconductor. Referring to the notion of the photovoltaic effect in non-intrinsic semiconductors, electrons can be excited by photons and transfer electrons to the conduction band (E_C) from the valence band (E_V) which are then separated to conduct a direct current. These bands are closest to the Fermi level (E_F), which is halfway between the E_V and E_C at absolute zero. The Fermi level can be thought of as the energy at which the probability of finding an electron is ½, suggesting all electronic energy levels below E_F are occupied and those above are likely to be empty. According to Pauli's exclusion principle, electrons cannot exist in identical energy states; thus, at low temperatures they condense to fill lower energy states and result in compact population of charges. Above 0 K, the Fermi level related to these energetic levels can be shifted by impurities or defects in the materials resulting in additional energy states between the E_V and E_C. A majority concentration of negative mobile charges, electrons (e^-), is termed an n-type semiconductor; whereas, a majority of positive charges, holes (h^+), are called p-type semiconductors. Thus fixed positive charged materials are added to semiconductors to create mobile n-type behavior, and vice versa. This probability of distribution of particles can be applied by the charge neutrality principle and the Maxwell-Boltzmann function at thermal equilibrium for the concentration of donor atoms (N_D) in equation (14) and acceptor atoms (N_A) in equation (15) relative to the Fermi level:

$$N_D = N_C \, e^{\left[\frac{-(E_C - E_F)}{kT}\right]} \tag{14}$$

$$N_A = N_V e^{\left[\frac{-(E_F - E_V)}{kT}\right]} \tag{15}$$

where N_C is the density of state function of the conduction band and N_V in the valence band; relating to the effective mass of electrons and holes respectively. When an n and p-type semiconductor come into contact, the Fermi level alignment creates band bending between respective E_C and E_V energy levels and separated electrons and holes flow oppositely due to energetic diffusion. Hence, a diode generally is formed by placing these differing n and p-type semiconductors in contact to conduct a current in one direction due to energetic diffusion; similarly known as a p-n junction. This is the basis for the concept of a photodiode/photovoltaic cell and plays a very important role for choice of materials in this technological field. Using these distribution properties of energy states, impurities and defects are added to give rise to electron (N_D) and hole concentrations (N_A) for n and p-type semiconductors. Considering the E_C and E_V are fixed, the Fermi level will adjust according to the concentration of these acceptor and donor ratios

related to their characteristic energy levels. There are possibilities to engineer bandgaps, shift Fermi levels, and increase conductivity by doping, nanostructuration and using several p-n junctions (tandem configurations), increasing charge carrier mobility and separation for overall increase in efficiencies.

With the creation of photon induced free photogenerated carriers from the photovoltaic effect, there are two fundamental types of semiconductors to consider: direct and indirect. These classifications are named for the position of the energy levels which arise from symmetry in the material's crystal lattice otherwise known as Brillouin zones. Direct and indirect band gaps are defined by the crystal momentum k-vector in the Brillouin zone which represents allowed wave vectors. If the maximum energy state in the valence band and the lowest energy state in the conduction band are in the same k-vector, the semiconductor is direct and free photogenerated carriers can be created upon excitation by a photon (energy hν). When the lowest energy state of the conduction band and the maximum energy state of the valence band do not align directly, a change in momentum is needed in the k-vector. A phonon (collected vibration state of the crystal with energy hω) is needed in conjunction with a photon to make this energetic transition from the valence band to the conduction band. This change in crystal momentum is illustrated in direct semiconductor (displayed on the left in Figure 3) versus an indirect semiconductor (displayed on the right in Figure 3) below:

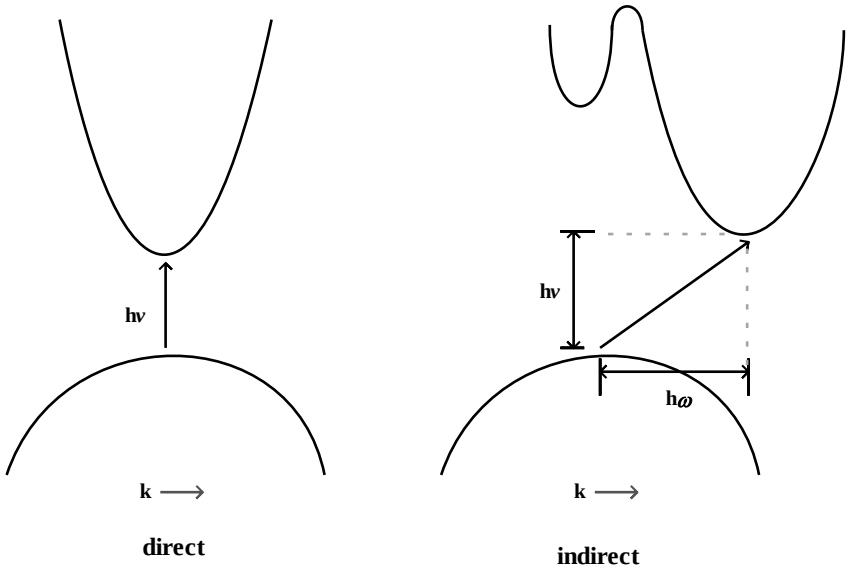

Figure 3: excitation in direct (left) and indirect (right) semiconductor energy vs. crystal momentum (*k*) diagram

To acquiesce to the change in crystal momentum k-vector energetic requirements, indirect band gap semiconductors are typically thicker than direct semiconductors, allowing for increased volume and increased chance of free photogenerated carriers from photon absorption.

The bandgap of materials can be determined by measurement of optical transitions by the absorption coefficient α, described below in equation (16):

$$\propto = \frac{A\left(h\upsilon - E_g\right)^m}{h\upsilon} \tag{16}$$

where A is a constant, hν the light energy from Planck's constant (h= and frequency (ν) determined by the speed of light (3×10^8 m s^{-1}) over the wavelength (λ in nm) by the Planck-Einstein relation. For direct semiconductors m = ½, whereas for indirect, m = 2. Extrapolation of $(\alpha h\nu)^{1/m}$ vs. hν yields a Tauc plot, indicating the band gap value from the x-axis intercept from the linear feature of the absorption edge.

According to the band gap position of semiconducting materials, it is possible to predict the open circuit voltage and highest current density in which determine the maximum power output possible when in contact with other energetic materials [57]. For example, when the photoabsorber comes into contact with water (or electrolyte) in the case of water splitting, the fermi level will align between the semiconductor and liquid which creates a space charge region, bending the E_C and E_V of the semiconductor. In response, a depletion layer or space charge is formed near the surface of the semiconductor which is counterbalanced by a compact assembly of opposite charges called the Helmholtz layer in the solution. When the semiconductor is under illumination, the solar potential applied (photovoltage or V_{ph}) upon the photoelectrode leads to band bending which creates disequilibrium between the electrolyte redox potential and the Fermi level, forming pseudo Fermi levels. The energy between the redox potential reaction and the semiconductor Fermi level is the open circuit voltage (V_{oc}) [58]. This is the amount of voltage the semiconductor can contribute towards the water splitting reaction. Typically the usable energy due to the open circuit voltage in semiconductors is only 50 – 70% that of the band gap. Larger band gap semiconductors may contribute larger V_{oc} but controversially they do not absorb a large number of photons from the solar spectrum [30]. Materials which contribute large V_{oc} may be energetically inappropriate and require overpotential (the difference between the applied potential and the open-circuit potential under illumination) to drive the desired reaction. This relation to the current density behavior is seen in equation (17):

$$V_{oc} = \frac{nkT}{q}\left(\frac{j}{j_0} - 1\right) \tag{17}$$

where k is the Boltzmann constant, T the absolute temperature, q the elemental charge, j the current density and j_0 the dark current density. As previously described, upon electrolyte contact, a charge space is formed in the material where band bending occurs. This is otherwise known as the depletion zone (W_D) where the semiconductor is depleted of majority carriers. This relation to the density of states is described in equation (18):

$$W_D = \sqrt{\frac{2\varepsilon_0\varepsilon}{eN}\phi - \frac{kT}{e}} \tag{18}$$

where ε_0 is the permittivity of free space, ε the dielectric constant of the semiconductor, e the charge of an electron, N the density of acceptor or donor states (N_D or N_A as previously specified), k the Boltzmann constant, T temperature, and ϕ_{SC} the voltage related to band bending due to the internal electric field produced. In the bulk of the material, it is often assumed that minority carriers are generated within a specific distance from the surface. Assuming these charges can reach the surface or the border of the depletion region, from which they are successfully extracted, giving rise to a photocurrent and/or chemical reactions at the surface of the semiconductor. However, free charge carriers (holes and electrons) traveling through the material may recombine within the semiconducting material before being extracted or used. This is called recombination, and constitutes a large source of loss for photovoltaic materials. The length the minority charge can travel before recombination is known as the diffusion length (L_D), and can be determined by equation (19); therefore, the thickness of thin films of photovoltaic materials attempt to acquiesce the distance minority carriers in the semiconductor can travel in the material before bulk recombination processes occur.

$$L_D = \sqrt{D\tau} \tag{19}$$

where τ refers to the carrier lifetime, and D is the diffusivity of free carriers which is related to mobility (μ) by the Nernst-Einstein equation D = ktμ/*e*. Longer diffusion lengths result in higher chances of minority carriers contributing to the overall conductivity and therefore larger current in photoelectrodes.

These prevailing mechanisms of band bending and charge collection of minority carriers by migration, due to electric field inside the space charge layer and by diffusion, are displayed below in Figure 4.

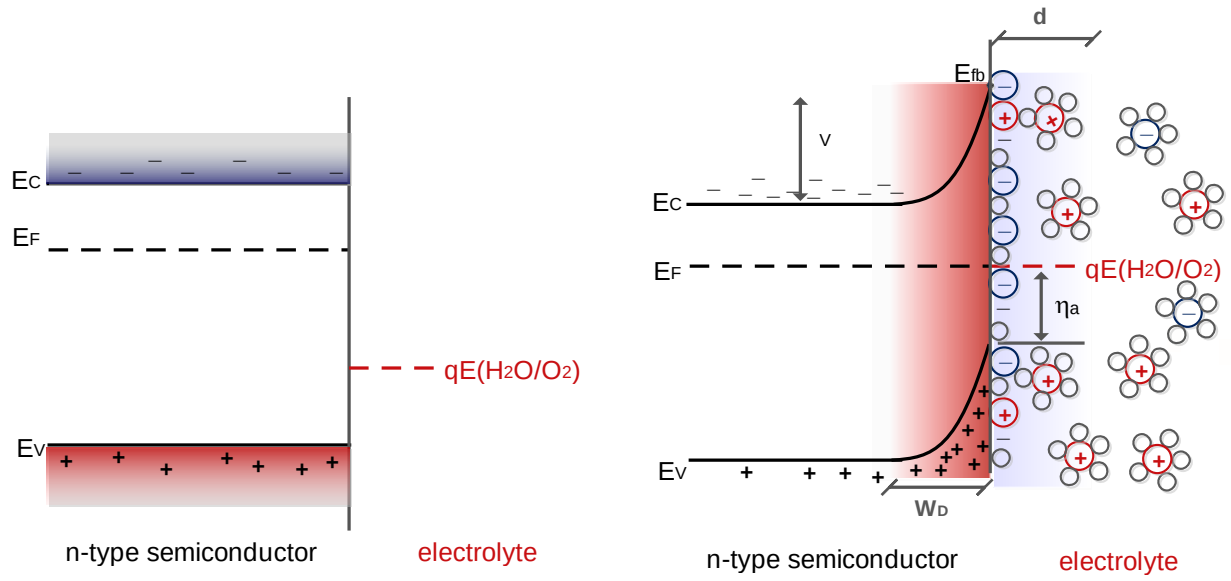

Figure 4: Depletion width (W_D), Helmholtz layer (d), and overpotential (η_a) arising from semiconductor band bending (left) before contact with electrolyte (right) after contact with electrolyte

Denoted as *d* in Figure 4, the Helmholtz layer is an angstrom thick sheet of charge which develops in response to the depletion width due to band bending upon contact with other materials and creates a capacitance. This capacitance of this layer can be measured in solution relative to the semiconductor in order to find the flat band position (E_{fb}) of the material, giving an indication of the position relative to a known potential (V). This concept is known as the Mott-Schottky relation (described below in equation (20)) which can determine the charge carrier concentration and band positions of a material.

$$\frac{1}{C^2} = \frac{2}{Ne\varepsilon}\left[\left(V - E_{fb}\right) - \frac{kT}{e}\right] \tag{20}$$

Considering these internal limitations of charge generation, separation, and mobility, the photocurrent density can be reapplied using Gärtner's model [59], shown below in equation (21):

$$j = j_0 + e\Phi\left(1 - \frac{exp(-\alpha W_D)}{1 + L_D}\right) \tag{21}$$

where j_0 is the saturation current density, q the charge of an electron, Φ the photon flux, L_D the diffusion length in the bulk of the semiconductor, α the absorption coefficient of the material, and W_D the depletion layer width (assuming monochromatic light and no recombination). A more refined model for the current due to minority carriers by Reichman takes into account doping concentrations, recombination in the semiconductor bulk (which plays a large role during flat band conditions). Nevertheless, the saturation current is negligible for metal oxides which possess band gaps larger than 1.8 eV and therefore the two models are comparable. These characteristics can all be measured and defined using electrochemical methods. Reference electrodes in a three-electrode setup measure the change in voltage between the working photoelectrode while current passes through the circuit to the counter (photo)electrode. In general, these (photo)electrochemical tests are repeatedly used, applying several known electrochemical methods to measure PEC characteristics in materials.

This semiconductor liquid junction (SCLJ) energetic interaction can be measured versus a reference electrode (e.g. NHE) and to the vacuum (E_{vacuum}). The water splitting reaction (specifically the proton reduction potential) is suggested to be around 4.5 eV from the vacuum (denoted simply as V in Figure 5) which displays an n-photoanode with cathodic bias ($-eV_A$) to achieve flat band configuration and with anodic bias (eV_A) to drive the OER [30]:

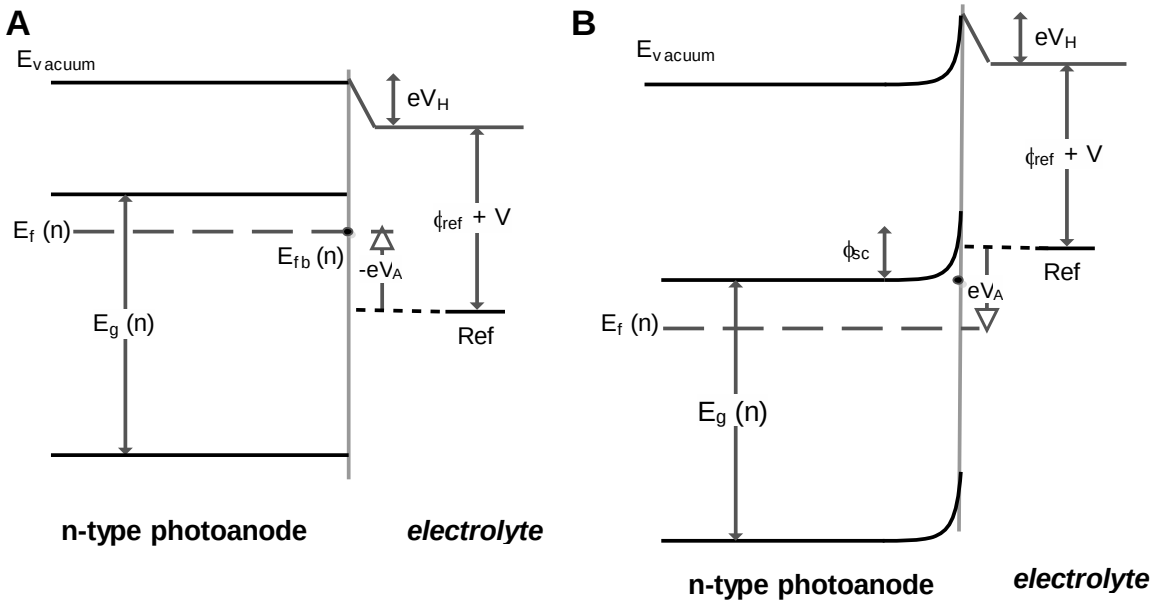

Figure 5: n-type photoanode liquid junction in relation to reference electrode with (A) applied cathodic bias and (B) anodic bias

Understanging these internal material energetic obstacles gives insight to why there are theoretical maximum efficiencies for both photovoltaics and PEC devices in terms of the photovoltaic effect and energetic losses at interfaces in these technologies. In theory, all solar photonic limiting efficiencies can be expressed as η_p in equation (22):

$$\eta_p = \frac{j \cdot \Delta\mu_{ex} \cdot \phi_{conv}}{P_{in}} \tag{22}$$

where $\Delta\mu_{ex}$ is the excess chemical potential generated by light absorption, Φ_{conv} is the quantum yield of the conversion process – essentially the fraction of excited states that contribute to a useful product, and J_g is the absorbed photon flux (denoted j_λ in photons $s^{-1}m^{-2}$) between λ-λ_g [26, 56]. The quantum yield is otherwise known as the external quantum efficiency or incident photon to current efficiency (denoted EQE or IPCE) of a photovoltaic or PEC device, described by the incident photon to current to electron conversion efficiency in equation (23).

$$IPCE = \frac{1239.8\ (V \cdot nm) \cdot |j(mA/cm^2)|}{P_{in}(mW/cm^2) \cdot \lambda\ (nm)} \tag{23}$$

where 1239.8 V·nm is simply the product of Planck's constant and the speed of light. P_{in} is the illumination power at a certain wavelength (λ), and j the photocurrent density. This is a measure of how many photons in the system give rise to electrons which form a current, i.e. the external quantum yield; however, it should be noted that this does not take into account optical (reflective) losses in the material (which would be the internal quantum efficiency). Slow surface kinetics, rapid charge trapping and short charge carrier diffusion lengths have all been suggested to increase recombination losses, thereby lowering the material's IPCE [60].

The photocurrent density (j) can be calculated using the spectral irradiance ($W \cdot m^{-2} \cdot nm^{-1}$) and a photon's energy at specific wavelengths ($h\nu$). This is the calculated maximum current that the material can deliver under short circuit conditions otherwise noted as I_{sc} (mA) or J_g (mA/cm^2). This value is directly related to the band gap energy and the integration over all shorter wavelengths/higher energies [61, 62]. This behavior can be expressed by equation (24) which integrates the number of photons per square meter second (j_λ) over all wavelengths equal or less than the band gap in the material with the corresponding IPCE. The related photon flux is shown below in Figure 6 (assuming 100% conversion efficiency):

$$j = \int_{\lambda_{min}}^{\lambda_g} j_\lambda(\lambda)\, \phi_{conv}(\lambda) d\lambda \tag{24}$$

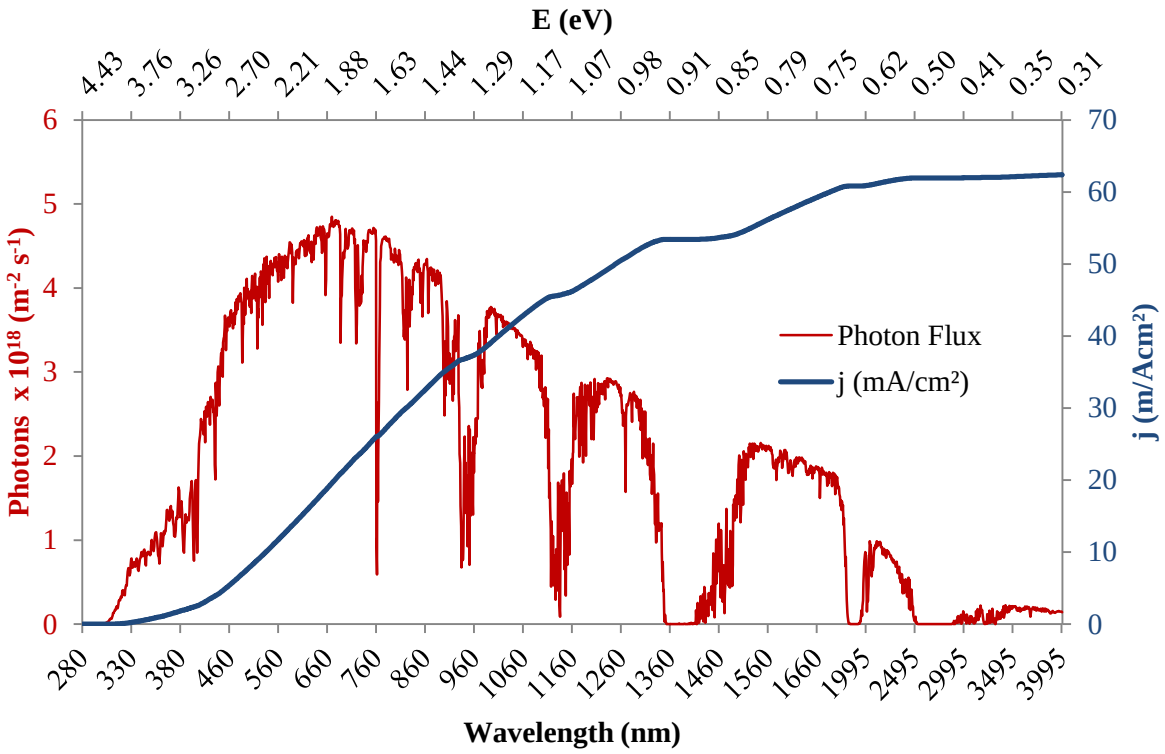

Figure 6: AM1.5G number of photons per square meter per second and the maximum photocurrent density as a function of band gap

A photocurrent arising from semiconductors correspondingly results from two main collection mechanisms: separation of carriers in the space charge field (a region of electric field extending into the semiconductor from the semiconductor/electrolyte interface) and diffusion of carriers toward the interface [30, 63, 64]. Integrating the photon flux from the solar minimum wavelength which has any significant energy output: ($\lambda_{min} \approx 300$ nm) on Earth under AM1.5G (displayed in Figure 6) to the band gap associated wavelength gives the maximum photocurrent obtainable. This assumes that one photon can create one free photogenerated carrier (i.e. 100% IPCE) and that there are no additional losses (i.e. recombination and optical losses). The application of these photoconversion fundamental limitations was completed by Shockley and Queisser in 1961 [21]. The Shockley-Queisser limitation for a single junction solar cell (illuminated with AM1.5 solar spectrum) with the band gap (E_g) of 1.4 eV for optimum photoconversion suggests 47% of the solar energy gets converted to heat (mainly due to phonons), 18% of the photons pass

through the solar cell, 2% of energy is lost from local recombination of newly created holes and electrons, thus only 33% of the sun's energy is theoretically converted to electricity [21, 42, 62, 64].

For PEC devices, the solar photons drive a chemical reaction (e.g. ΔG for water splitting). Thus solar photonic limiting efficiencies are not the only limitations in performance considerations. The chemical efficiency (η_c) in water splitting PEC devices can be defined by the following equation (25):

$$\eta_c = \frac{\Delta G_p^0 R_p}{P_{in} A} \tag{25}$$

where ΔG_p is the standard Gibbs energy in the product (p) formation, R_p is the rate (mol/s) of the generation of product *p* (in its standard state), P_{in} is the spectral irradiation (W/m²), and A the overall active area of the irradiated device (m²). This equation can also be rewritten according to Bolton et al. [39] as equation (26):

$$\eta_c = \eta_g \eta_{chem} \phi_{conv} \tag{26}$$

Equation (27) defines the efficiency of the material, η_g which is the fraction of incident solar irradiance ($\lambda \geq \lambda_g$) where λ_g is the threshold energy for the photoconversion process (the bandgap (E_g)):

$$\eta_g = \frac{j_g E_g}{P_{in}} \tag{27}$$

The chemical efficiency is defined by η_{chem} (equation (28)), which is the fraction of the excited state energy converted to stored chemical energy and is defined by:

$$\eta_{chem} = \frac{E - E_{loss}}{E_g} = \frac{\Delta G_p^0 / n}{E_g} \tag{28}$$

where *n* is the stoichiometric number associated to the number of photons required to drive the reaction. This assumes that the quantum yield is 100% (thus Φ_{conv} = 1). E_{loss} is the energy which is lost in conversion and can be approximated in equation (29) as:

$$E_{loss} = E_g - {}^{\Delta G_p^0}/_{n} \tag{29}$$

Note that this loss is **not** the energy lost when an excited state is created by a photon ($\lambda < \lambda_g$). Even for an ideal system, E_{loss} cannot go to zero because as noted above, the energy of the ensemble of excited states is thermodynamically *internal* energy and **not** Gibbs energy. Entropic considerations dictate that E_{loss} has a minimum value of 0.3 – 0.4 V, depending on the value of E [65]. In real systems, E_{loss} will be considerably higher (around 0.8 V) [56, 57, 65, 66]. Accordingly, with a fixed incident spectrum, η depends only on the band gap. If the band gap is very small, the working value of E would be too small. If it is very large, the photocurrent would be too small. Thus, when determining photovoltaic limiting efficiency, direct relation to J_g as well as E_g and the photons absorbed (λ_{min}-λ_g) are examined. All thermodynamic assumptions suggest standard testing conditions (STC) which specifies a temperature of 298 K (25 °C) and AM1.5 spectrum. Therefore, assuming AM1.5G incident sunlight (100 mW/cm²) spectral irradiance and no external applied bias, the efficiency can be simplified and directly related to the photocurrent (in mA/cm²) by $\eta_{STH} = 1.23 \times J_g$ [27, 30, 67].

Solar to hydrogen conversion efficiency, though highly weighted on the photovoltaic performance, is a result of the material efficiency, PV conversion efficiency, and the electrolysis efficiency combined. Neglecting losses/ heat, the minimum energy required to split water is 1.23 eV from the Gibbs free energy, and in compliance the device must be able to generate more than 1.23 V to account for these losses. The STH conversion efficiency in PEC cells, based on the previous assumptions, can be rewritten from equation (22) in equation (30) to describe the experimentally measured STH from photocurrent measurements:

$$\eta_{STH_1}(\%) = \left[\frac{j(mA/cm^2) \cdot (1.23V)}{P_{in}\ (mW/cm^2)}\right]_{AM1.5} \tag{30}$$

where j is photocurrent density generated in a PEC cell and the potential needed to split water 1.23 V the potential corresponding to the Gibbs free energy (ΔG = 237 kJ/mol) to split water, and P_{in} is the solar irradiance (mW/cm²) – *however,* this condition assumes 100% faradaic efficiency of H_2 and O_2 production with a corresponding 2:1 stoichiometric ratio, which is not always the case. Thus, alternatively, the STH can be expressed in terms of experimentally measured gas production (rewritten from equations (25) and (26)):

$$\eta_{STH_2}(\%) = \left[\frac{H_2(mmol/s) \cdot 237(kJ/mol)}{P_{in}(mW/cm^2)\ A\ (cm^2)}\right]_{AM1.5} \tag{31}$$

where the Gibbs free energy (237 kJ/mol), R_p the rate of hydrogen produced (mmol/s), P_{in} the solar irradiance, and A the active area of the cell which is illuminated and exposed to the electrolyte [56]. These equations hold true if the stoichiometric 2:1 ratio of H_2:O_2 is confirmed and if no sacrificial reagents are used [68]. If external bias is required to drive the reaction due to insufficient overpotential in the materials to drive the half reactions, the STH can be calculated by equation (32), but is otherwise known as the applied bias photon to current efficiency:

$$\eta_{ABPE}(\%) = \left[\frac{j(mA/cm^2) \cdot (1.23V - V_{bias})}{P_{in}\ (mW/cm^2)}\right]_{AM1.5} \tag{32}$$

To accurately take into account the photon to current and current to chemical efficiencies of the entire reaction, the STH efficiency should be calculated as shown below in equation (33) which encompasses both the photocurrent at water splitting potential as well as the faradaic efficiency (and addition of an external bias (V_{bias}) if applied):

$$\eta_{STH_3}(\%) = \left[\frac{j(mA/cm^2) \cdot (1.23V - V_{bias}) \cdot \eta_F}{P_{in}\ (mW/cm^2)}\right]_{AM1.5} \tag{33}$$

where η_F is the faradaic efficiency calculated by equation (34) using experimentally measured moles of gas divided by the theoretical number of moles of product gas:

$$\eta_F = \frac{n_{exp}}{(Q/F)/_n} \tag{34}$$

The denominator represents the moles of gas theoretically produced due to the charge measured in the photoelectrode. Thus, Q is the charge in coulombs corresponding to the photocurrent (mA/cm²) at time (s) due to the fact that C = A × s, divided by faraday's constant (96485.33 s·A/mol) divided by the number of charges needed to drive the reaction; 2 and 4 for hydrogen and oxygen respectively. Accordingly, n_{exp} is the gas measured experimentally, which gives the ultimate ratio of gas detected over the theoretical production, known as the faradaic efficiency.

Current PEC research report an overall STH of around 4 – 16% [5, 53, 69, 70]. Nevertheless, these calculations are not reliable, as many STH calculations based only upon the photocurrent density; thus, values are overestimated due to the exclusion of the faradic efficiency. Additionally, much of this research

lacks data on long term stability and generally includes expensive materials and processing. Considering differing laboratories measure efficiencies under different conditions and methods, it is often difficult to compare performances and efficiencies concerning water splitting materials and technology. Auspiciously, PEC technology performance suggests to increase to 20 – 30% in the future; yet to be a viable hydrogen generation source, as previously described, must last at least 10 years and have a STH of 10% [42, 70]. At this efficiency, in a location with average solar irradiation intensity of 250 W/m², the system should produce 0.7 g/s (7.8 L/s STP) per m² of collector [42]. Theoretically, the maximum solar to hydrogen efficiency for a single-photosystem device (utilizing one band gap) is 31% though multi-layer STH conversion efficiency for photoelectrolysis exceeds 41% (not taking into account electrochemical losses) [29, 42, 71]. This is determined based on detailed balance equation in the view that the limiting efficiency is based on photoconversion capability, much like the Shockley-Queisser publication pertaining to maximum theoretical photovoltaic efficiencies [21]. The photovoltaic characteristics previously discussed (arising from material characteristics such as band gap, band positions, doping, depletion width, conductivity, etc.) all contribute to the performance of a material for water splitting. The built in potential to drive the reaction depends on the potential between the electrolyte species and the Fermi levels of each respective electrode. Therefore, solar irradiation, material properties, and their ability to create, separate, and extract charges as well as undertake desired chemical reactions considerably limit the efficiency of water splitting devices.

I.4.2. PHOTOELECTROCATATLYIC DEVICES

Several different approaches to photoelectrocatalytic cell architecture and configuration have been proposed for clean hydrogen production. This technological idea is sophisticated to achieve, considering it requires many obstacles to overcome thermodynamic material and physical limitations, such as: mechanical engineering and dimensioning of electrolyzers, separation of oxygen and hydrogen gases for safety and efficient recovery, electrochemical processes and kinetics at the SCLJ, as well as general photovoltaic material stability, efficiency, and additional complications included during optimization regarding these aspects [72]. The final device must be air-tight for gas production and collection as well as optically optimized for the photovoltaic creation of charge carriers to fuel the water splitting reaction. This difference, between water electrolysis and photoelectrocatalysis is therefore significant, suggesting “photoelectrolysis” and “photoelectrochemical” efficiencies significantly depend on photo-absorption characteristics and thus exposure to illumination source must be optimized and incorporated into the architecture and configuration [73].

An initial approach to this technology encompasses colloidal suspensions of PV-active nanoparticles composed of the appropriate layered photovoltaic materials in order to achieve sufficient bandgap voltage

for water splitting electrolysis [74, 75]. However, gas separation is difficult colloidal suspensions and is potentially dangerous due to the mixing of combustible O_2 and H_2 gases in solution. Directly submerging photovoltaic films for use as planar photoactive electrodes proposes an easier engineering solution to gas separation and collection as the production of oxygen and hydrogen occur at different locations. These photovoltaic electrodes, otherwise known as photodiodes or photoelectrodes, can be positioned in arrays facing the sun and while immersed in a water reservoir so that oxygen gas is produced on the anode and hydrogen gas on the respective cathode, much like an electrolyzer. This allows an ionic separator (e.g. proton conductive membrane like Nafion®) to be placed between the two electrodes for gas separation and collection. (Note that the cathode may be simply a metal (e.g. platinum, titanium, ruthenium, etc.) or a photoactive cathode in more complex PEC cells) [26, 55, 76].

In order to realize a photoelectrocatalytic water splitting cell, several configurations, combinations, and architectures are considered to improve overall operation and efficiency. One compartment, two compartment, monolithic, or separated electrodes are all options as to architectural options for a PEC. Each architecture can be an assortment of material combinations (e.g. n-type photoanode, combined p-n photoanode/cathode, PV-PEC, etc.) which require different configuration of the materials for optimum efficiency [26]. Dependent on configuration, separated (or dual compartment) electrodes can be connected by external wires, or function in a wireless setup acting as the barrier and photoelectrode simultaneously. The electron pathway in wire connected electrodes (for dual compartment or monolithic devices) is considerably longer than the wireless configuration; although this configuration is offset by the conductivity of metal wiring. Furthermore, electrodes can be placed directly closely facing each other, reducing the ionic path length between electrodes and enabling the use of low ionic conductivity electrolyte [38]. Wireless configurations are always monolithic and utilize the fact that the electrodes are placed on the same substrate, with the HER and OER surfaces occurring on opposite sides; which minimizes the electron path length between electrodes, but increases the ionic path length [77]. Single compartment devices suffer from potential gas mixing and possible unwanted parasitic reactions, which can pose potential safety concerns if large concentrations of hydrogen are produced [78]. Oxygen can penetrate into the cell which results in an overestimation of O_2 production; equally, it can act as an electron acceptor and be reduced at the cathode, leading to lower H_2 production. This suggests dual compartment devices have several potential advantages but can potentially suffer from increased ohmic losses due to the distance implemented between the two electrodes and use ionic separators. These ohmic losses are critical in high current density devices and increase upon the integration of a membrane for gas separation. The photoelectrode(s) can either be totally submerged in the device, which can result in optical losses when adding several refractive indices: cell windows, the photoelectrode, and the electrolyte solution; nonetheless, this can be minimized by using optically transparent materials, such as quartz

windows, but at a costly expense. Alternatively, the photoelectrode(s) may be used simultaneously as the cell window architectural support to ensure gas and liquid confinement as well as the driving the water splitting reaction.

All of these configurations and varying architectures provide additional or adjusted energetic solutions to comprise the preferred absorption, redox reactions, overpotential, and other efficiency determining characteristics. If necessary, additional electrical bias can be integrated into the circuit to correct for lacking potential to drive the water splitting reaction. These "boosted" systems otherwise known as hybrid devices, buried-junction, or PV-PEC are essentially photovoltaic materials integrated in the cell or simply buried by metal oxides for protection in aqueous environments in order to produce needed voltage to drive the reaction. A buried junction PEC generally consists of three p-i-n silicon junctions directly buried or connected to the complementary electrode (photoabsorber or metal) to complete both half reactions. Consequently building an integrated multi-junction PEC has been demonstrated by several groups: Turner, Miller, Licht, Nozik, and Nocera amongst others with integrated photovoltaics/p-i-n junctions PEC cells [12, 44, 79-91]. Likewise, dye sensitized solar cells can be linked or integrated into the photoabsorber system to produce additional bias which is also considered hybrid PEC technology [92-94]. PEC configurations other than the generally thought multi-junction PEC reactor have been patented by Gibson, Grätzel, and McNulty which all work to address current efficiency issues by optimizing gas separation, maximizing solar spectrum utilization, and resisting corrosion [29]. Nevertheless, these types of PEC are outside the view of this study due to the complexity of successive material layer processing and implementation.

Like all technologies in research and development, these conceptualized devices hold fundamental impediments, including: bubble accumulation on the electrode surfaces (increasing ohmic resistance), optical losses from solar incident angle, absorption losses when encased in protective encapsulation and/or from water refraction due to the device being encapsulated and submerged in water [29]. To further understand the possible theoretical limitations concerning photosystems for water splitting, the device configuration of the materials in the cell architecture will be discussed in while considering overall the STH efficiency.

I.4.2.1. Device Architecture and Configuration

The two main critical factors in evaluating photoelectrocatalytic water splitting schemes are the number of photoabsorbers and the number of photons needed to make one molecule of H_2. A single photoabsorber system (S) and a dual photosystem (D) can use 1, 2, or 4 photons to produce H_2 from H_2O. A PEC with one photoabsorber which absorbs a minimum of 2 photons per molecule of hydrogen (S2) has a theoretical maximum efficiency of 31%. (Suggesting one electron is transferred in the system per photon

(hν) absorbed) [39, 56, 57, 95]. For a PEC single photosystem, a system with wavelengths below 770 nm (or energies above 1.6 eV) are required to yield its maximum theoretical efficiency [42, 95-97]. The ideal band gap for a single photosystem PEC device has been suggested as 1.3 ± 0.3 eV due to additional losses which are needed to drive water oxidation; nevertheless, this is known to vary depending on the configuration and function of specific devices [63, 96, 98-100]. Displayed below in Table 1 are the theoretical efficiencies for conversion of solar radiation in the ideal limiting efficiencies PEC devices of single photosystems and dual photosystems according to Bolton [39, 56].

Scheme	**N° of photo-systems**	**Minimum N° of absorbed photons per H_2**	**Reaction**	**E per photon required (eV)**	**E_{loss} per photon (eV)**	**Max η_p (%)**	**Max η_c (%)**	**Bandgap (eV) from threshold wavelengths** λ_1	λ_2
S1	1	1	$H_2O \xrightarrow{1h\upsilon} H_2 + \frac{1}{2}O_2$	2.458	0.49	5.3	-	2.95	-
S2	1	2	$H_2O \xrightarrow{2h\upsilon} H_2 + \frac{1}{2}O_2$	1.229	0.37	30.7	-	1.6	-
					0.6	-	23.5	1.82	-
					0.8	-	17.4	2.03	-
					1	-	12.7	2.23	-
S4	1	4	$H_2O \xrightarrow{4h\upsilon} H_2 + \frac{1}{2}O_2$	0.615	0.31	30.6	-	0.925	-
D2	2	2	$H_2O \xrightarrow{h\nu_1+h\nu_2} H_2 + \frac{1}{2}O_2$	1.229	0.38*	42.4	-	1.9	1.3
D4	2	4	$H_2O \xrightarrow{2h\nu_1+2h\nu_2} H_2 + \frac{1}{2}O_2$	0.615	0.31*	41	-	1.36	0.48
					0.6	-	32.3	1.58	0.84
					0.8	-	27.1	1.72	1.1
					1	-	21.6	1.89	1.34

Table 1: Theoretical Efficiencies corresponding to Single and Dual Photosystems (*averaged E_{loss})

Comprehended from Table 1, lower photon energies and higher efficiencies are attainable if one employs two photoconverters, enabling increased absorption of the solar spectrum. A system with two photoconverters (both absorbing ≥ 2 photons per system and equal photon flux) with two different optimized E_g (e.g. 1.6 – 2.0 eV / 0.8 – 1.2 eV) calculates to a maximum efficiency limit of 42% [26, 39, 42]. Upon further studies by Bolton et al. and Weber and Dignam, it is stated that these systems will not exceed 10% for single photosystems and/or 16 – 18% for dual photosystems respectively, including losses [30, 39, 99, 101]. In reality, suitable systems for water photoelectrolysis must make accommodations for

kinetic overpotentials, material pairing, and the band bending necessary for charge separation [26, 29, 42, 56, 57, 68, 99, 102, 103]. These limitations and expectations are visually depicted in Figure 7 according to Gerischer [104] which numbered curves correspond to:

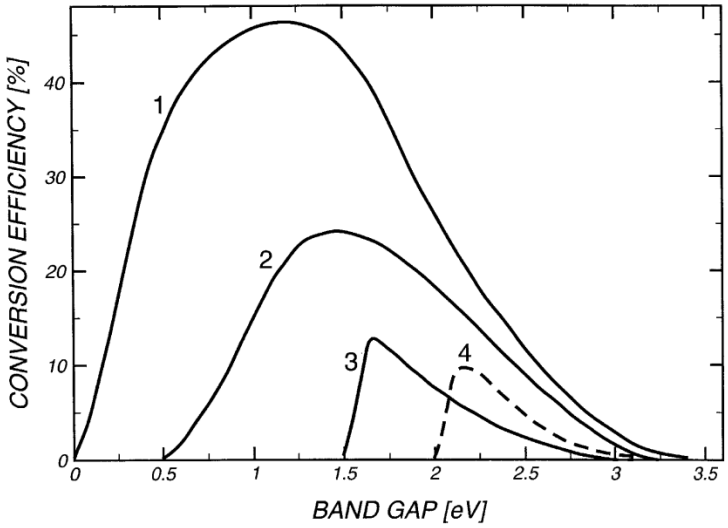

Figure 7: Conversion efficiency of solar energy vs. band gap materials in water splitting photosystems taken from Gerischer, 1979

1. hypothetical efficiency without any losses
2. efficiency including losses in semiconducting electrode
3. efficiency of PEC with two photoelectrodes
4. efficiency of PEC with one photoelectrode

Currently, the conception of a single photosystem is not highly perused due to the fact that there are little to no materials which straddle both the H^+/H_2 and O_2/H_2O redox potentials, are stable in aqueous solution, and absorb largely in the visible range of the solar spectrum. Using a single absorber to complete one of the half reaction and a metal to complete the other is commonly utilized; implementing a single photosystem with small band gap material as the photoanode and platinum as the cathode. This has been applied in conceived cells created at TU Delft, the "cappuccino cell" by EPFL, with H-cells demonstrated by Kitano et al. and Selli et al., as well as reversed engineered fuel cells [30, 38, 76, 105-108]. Single photosystems utilizing platinum as one electrode are not practical due to the high cost of platinum. Consequently, a dual photosystem with two photoabsorbers to complete the two half reactions is further sought amongst researchers concerning photoelectrocatalytic cell construction and conception on behalf of cost and efficiency for practical application. Figure 8 illustrates the band bending involved in a single photosystem of an n-type photoanode with a metal

cathode, and a dual photosystem containing an n-type photoanode and p-type photocathode. As previously discussed, Figure 8 displays the band gap (E_g), Fermi level (E_f) and pseudo Fermi level, flatband (E_{fb}), light (hv), open circuit voltage (V_{oc}), (photo)voltage applied (V_a or V_{ph}), and overpotentials needed to drive the reaction (η) of the materials.

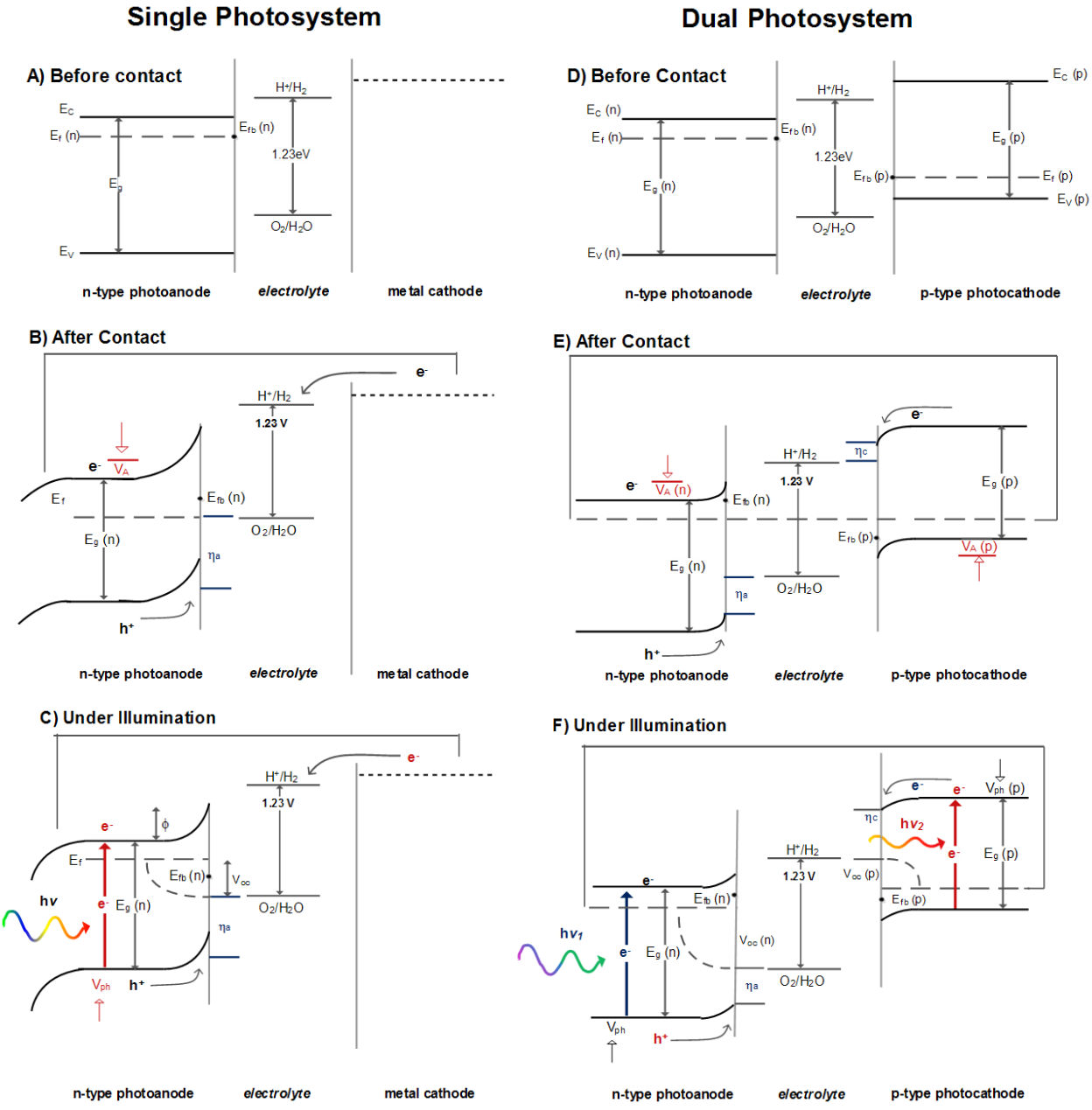

Figure 8: Band diagram for a single photosystem (A) before contact, (B) after contact, and (C) under illumination compared to a dual photosystem (D) before contact, (E) after contact, and (F) under illumination

There are several configurations applicable to the dual photosystem: back to back, parallel, or tandem (shown in Figure 9). As previously described, these can be monolithic or separate depending on the device architecture. A dual photosystem arranged with the side to side configuration is treated as two single photosystems with their area-weighted average efficiency and therefore offer little or no efficiency over single photosystems thermodynamically [39]. Experimentally, due to light absorption, this configuration has the benefit of greater absorbance compared to tandem configuration which competes for light absorbance between photoelectrodes [90]. However, the dual photosystem side to side configuration requires more area overall than the tandem configuration or monolithic devices. A back to back dual photosystem contains materials on one monolithic wireless electrode, and can be difficult in processing due to fabrication methods and techniques in deposition and thermal treatment of materials. This monolithic configuration also suffers from an increase in ionic transport distance and therefore augmented losses when the surface is larger upon scale up [109]. Therefore, considering the options of configuration of a dual photosystem, a separated tandem dual photosystem including a photoanode for oxygen production and a photocathode for hydrogen production is more appealing due to ease of material processing and assembly.

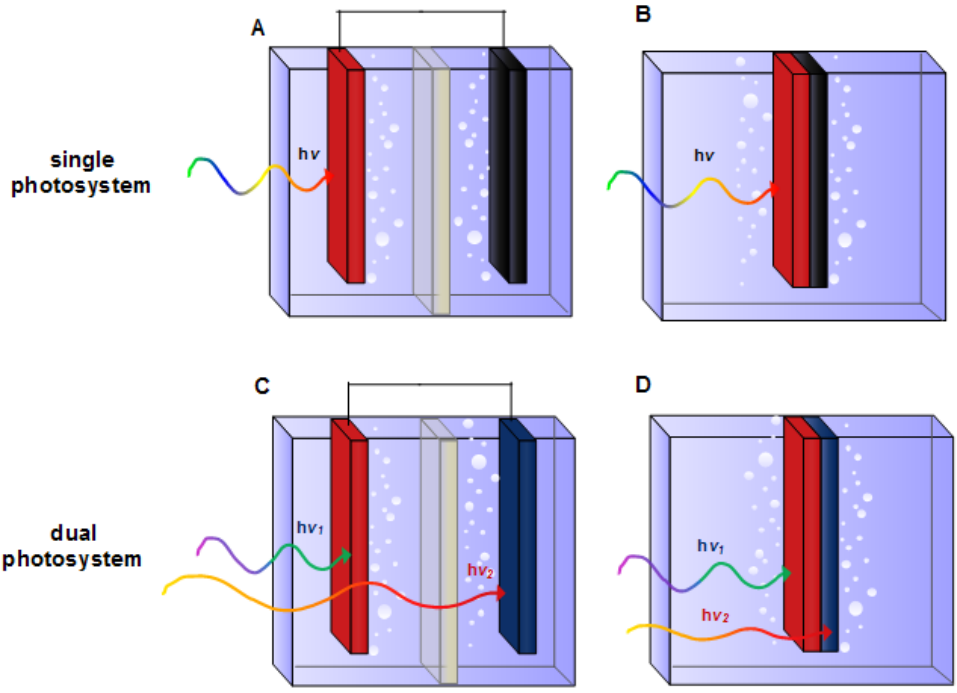

Figure 9: PEC varying architectures with a photoelectrode (red), metal counter electrode (black) or complementary photoelectrode (blue) in (A) wired dual compartment single photosystem (B) wireless single compartment single photosystem, (C) wired dual compartement dual photosystem, and (D) a wireless single compartment dual photosystem

As previously stated, photocurrent densities on the order of 15–25 mA/cm² with illumination intensity of one sun (AM1.5) are suggested for a single photoelectrode system and half these values are needed for each photoelectrode in a tandem system [45]. Ideally $E_g(n)$ and $E_g(p)$ and their flatband positions should provide enough open circuit voltage to split water while also accounting for the combined overpotentials (η_a and η_c) needed to drive the reaction [110]. The band gap lowest limit for for PEC application is determined by the energy required to split water which is determined by the photon flux (J1 – J2 in Figure 10):

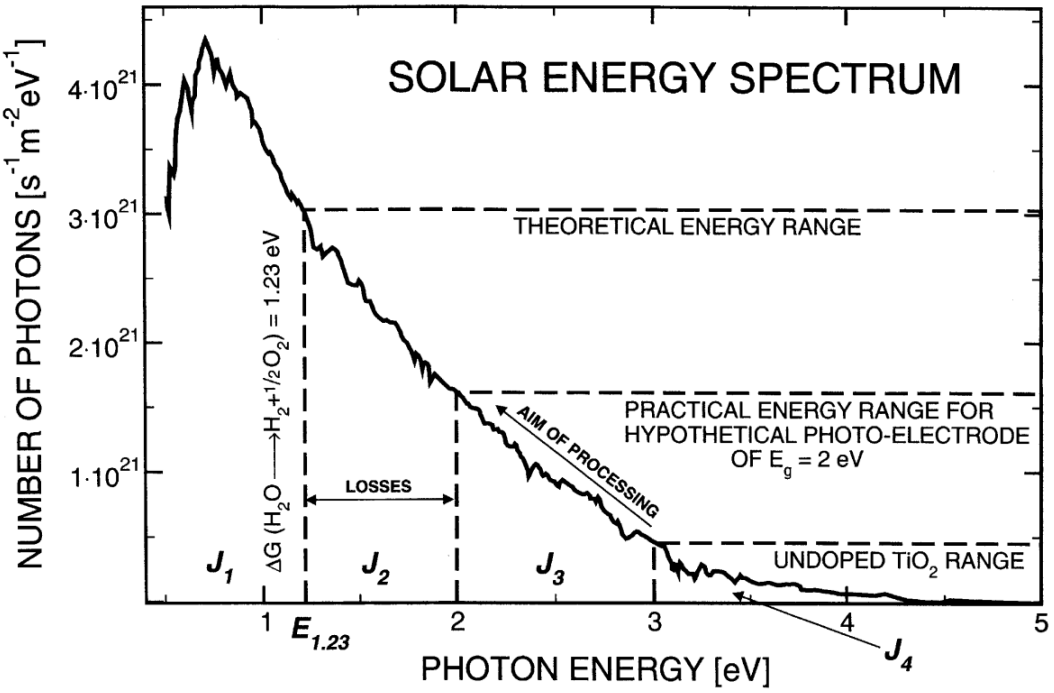

Figure 10: Solar energy spectrum (AM1.5) corresponding to theoretical energetic losses in photoelectrocatalytic materials taken from Bak, 2000

Nevertheless, in practice, this solar energy which is used for conversion is less than the theoretical energy limit due to losses previously discussed (recombination, polarization within the PEC device, resistance, voltage losses, etc.). As previously mentioned, the value of these combined losses (E_{loss}) generally measure 0.8 eV (denoted J2 – J3 in Figure 10). In consequence, a region of the solar spectrum is not available for conversion, limiting efficiency due to solar absorption constraints. In order to match materials for single photosystems in terms of solar absorbance, it is thought that the optimal energy range for a band gap measures around 2 eV (J1 – J3 in Figure 10). It has been suggested that materials with band gaps measuring between 2.0 – 2.5 eV are also conceivable [99, 111-113]. As of late, there is no certain agreement of ideal band gap combinations for tandem dual photosystems; some suggestions include: 1.7 eV and 1.1 eV, 1.9 eV and 1.2 eV, or even 3.1 eV and 1.9 eV for the photoanode and photocathode

respectively [26, 45, 114]. Other speculation states that this choice of band gaps depends largely on potential losses and use (in this case water splitting) [39]. Ultimately, materials (specifically metal oxide semiconductors) which have band gaps measuring ≤ 2 eV are highly susceptible to corrosion, which is addressed in the following section I.4.3. Photoelectrocatalytic Materials [112, 115]. Therefore, choice and optimization of materials are necessary in order to attain adequate device efficiencies and lifetimes for practical application in this chosen configuration.

The main challenge in tandem dual photosystems lies within matching the photoanode and photocathode materials to complementary absorb light to drive the water splitting reaction. A considerable optical obstacle lies within the parallel arrangement of the photoelectrodes relative to the incident light source. Accordingly one photoelectrode must attempt to share the solar spectrum, leaving the other to recover remaining unabsorbed light. Therefore complementary light absorption by the photoanode and the photocathode to achieve current matching is preferred [116]. This tandem configuration is arranged so that the photoanode with large band gap absorbs light towards the ultraviolet range of the spectrum and a small band gap photocathode recovers wavelengths in the visible to infrared region. However, this configuration involves the drawback of competing light absorption of the front and back placed photoelectrodes, compelling one photoelectrode to be relatively optically transparent for a portion of the electromagnetic spectrum while allowing the remaining light to be absorbed by the complementary photocathode.

Considering these previously discussed architectural and photoelectrode arrangement possibilities, a tandem dual photosystem employing a n-photoanode for the production of oxygen and a p-type photocathode producing hydrogen seems to be the most simple yet performant. Taking into consideration all of the previous work concerning PEC architectures and configurations with their advantages and disadvantages; implementation of a dual compartment wired device using a photoanode as the front cell window and the photocathode at the opposite end of the cell using an ionic separator for gas separation appears the most logical. This interest entails that these materials (photoelectrodes, electrolyte, membrane, and cell) are performant, abundant, stable, and inexpensive; as well as processed and implemented with ease for practical future industrial application.

I.4.2.2. State of the Art Photoelectrocatalytic Devices

To date, few tandem dual photosystems containing inexpensive, non-noble, metal oxide semiconductors for water splitting applications exist. Table 2 compares previous literature data concerning tandem dual photosystem water splitting photoelectrocatalytic cells based on metal oxide materials in attempts to realize this practical tandem dual photosystem implementation:

Year	Photoanode	Photocathode	Electrolyte	Illumination	Area	η_{STH}	Ref
2012	FTO/WO_3	Cu/Cu_2O/NiO_x	0.1 M Na_2SO_4 (pH 6)	100 mW/cm²	0.2 cm²	0.22% *(–0.6 V_{app})*	[117]
2012	FTO/$BiVO_4$/ CoO	ITO/$SrTiO_3$:Rh	0.1 mM K_2SO_4 (pH 6.9)	100 mW/cm²	4 cm²	0.06%	[118, 119]
2014	FTO/W:$BiVO_4$/ Co-Pi	FTO/Au/Cu_2O/ Al:ZnO/TiO_2/RuO_x	0.5 M Na/K SO_4 and PO_4 buffer (pH 6)	100 mW/cm²	0.28 cm²	0.5%	[120]

Table 2: Photoelectrocatalytic tandem dual photosystem water splitting devices based on metal oxides

Lin et al. apply an external bias of –0.6 V between the two photoelectrodes and therefore the system does not function without external aid (though reporting a low unassisted current of a few µA/cm²) [117]. Ideally, this tandem dual photosystem should function under AM1.5 light without external bias. Kudo and Iwashina coupled p-type 7% doped Rh:$SrTiO_3$ which is a large band gap with cobalt surface modified $BiVO_4$ for unassisted H-cell PEC but with a stable photocurrent of only 50 µA/cm² resulting in a poor STH of only 0.06%. Though the $SrTiO_3$:Rh photocathode is more of a photocatalyst electrode than a sintered thin film due to the deposition derived from powdered synthesis [118, 119]. Additionally, rhodium is a rare noble metal and should be avoided in fabrication of material based PEC cells for industrial application due to its scarcity and price. Little information was revealed as to the electrode configuration of this device (tandem or side by side), thus the results are potentially not applicable to this study. As for Bornoz et al., the complexity of the photocathode starts to become ostentatious and includes both gold and ruthenium which are also non-ideal for large scale production due to the fact that these precious metals are expensive and not abundant [120]. Regardless, this technological aspiration advances with further understanding and application using these state of the art materials.

Despite the overall architecture and configuration of the PEC device, the STH efficiency is primarily related to the semiconductor or photoelectrode photovoltaic and electrochemical properties; and more specifically, the material(s) band gap(s), which select the working voltage, stability, and limit spectral absorption [72]. In accordance with a tandem dual photosystem, the materials chosen and their performance are of great importance. Considering the thermodynamics and architectural limitations, the photoanode must be semi-transparent, n-type, and absorb near the UV region while the photocathode p-type possessing a small band gap should absorb light towards the visible and infrared region.

I.4.3. PHOTOELECTROCATALYTIC MATERIALS

The efficiency of photoelectrocatalytic devices depends on the material's efficiency to carry out the photovoltaic effect in order to create and transport charge carriers which kinetically drive the water splitting reaction. Material properties and performance are very important for the overall operation of a photoelectrocatalytic water splitting device. Positions of the conduction and valence bands in the semiconductors relative to water splitting redox potentials determine the working voltage and overpotential(s) at which this reaction is completed. The flatband voltage (E_{fb}) of each material determines the onset potential of water oxidation or proton reduction for the photoanode and photocathode respectively. Although, recombination in the space charge layer, hole trapping sites on the surface, and hole accumulation due to slow oxygen kinetics may delay this onset, resulting in lower photocurrents at lower potentials [121]. Materials with: ideal band positions for water splitting kinetics, appropriate band gaps for light absorption, strong chemical bonding for stability, and good semiconducting qualities for charge separation are the main aspirations for photoelectrocatalytic materials. These sought materials, in theory, should be inexpensive, non-toxic, easily processed/fabricated, and abundant. Finding these characteristics qualities in materials are not obvious, thus much research has been completed in order to adhere to these requirements and find new materials which possess these desired characteristics.

The three main challenges in finding suitable materials for water splitting photoelectrocatalysis are:

1. The band gap of semiconductors used for water splitting should fall in the range sufficient to achieve the energetics for electrolysis and yet allow maximum absorption of the solar spectrum. (This is 1.6–2.0 eV for single photoelectrode cells, and 1.6–2.0 eV/0.8–1.2 eV for top/bottom cells in stacked tandem configurations) [39].
2. Have a high quantum yield (>80%) across its absorption band to reach the efficiency necessary for a viable device.
3. Straddle the redox potentials of the H_2 and O_2 half reactions with its conduction and valence band edges, respectively [72]. To succeed in splitting water via solar irradiation only, the valence band of the semiconductor has to be located at a more positive potential than the chemical potential of oxygen evolution (H_2O/O_2), and the conduction band has to be located at a more negative potential than the chemical potential of hydrogen evolution (H_2/H^+). If the material does not adhere to these needs, an external bias is required [122].

The built-in potential created by the electrode material must exceed the bottom theoretical limit of 1.23 eV to split water molecules as well as overcome the electric resistance of the closed circuit [29, 73, 123]. As previously stated, the ideal material for a single semiconductor PEC hydrogen system is thought to require a band gap of 1.6 – 2.4 eV [99, 111, 112]. Thus band gap engineering and material science are necessary

in order to optimize the electrolysis as well as photovoltaic contributions for a viable hydrogen production technique. This concept of integrating two photosystems to harness maximum photo absorption can exist either with the same photovoltaic materials (homotype cell) or different materials (heterotype cell). In order to utilize the maximum solar spectrum, two different materials are proposed, ideally with different band gaps placed one behind another as to absorb the most light possible. Essentially placing one material which absorbs shorter wavelengths on the top facing the light source, and another material with the band gap which absorbs longer wavelengths recovering what is not absorbed by the first - or vice versa [39, 41]. The two layers presumably are used to drive the two half-cell reactions depending on the materials band positions. These types of photoelectrocatalytic cells are alternatively known as p-n PEC, using minority carriers in each material to reduce protons or oxidize water. A detailed schematic derived from Figure 8 of water splitting by photonic process is shown below in Figure 11, employing an n-photoanode and p-photocathode in a wired tandem dual photosystem [124, 125].

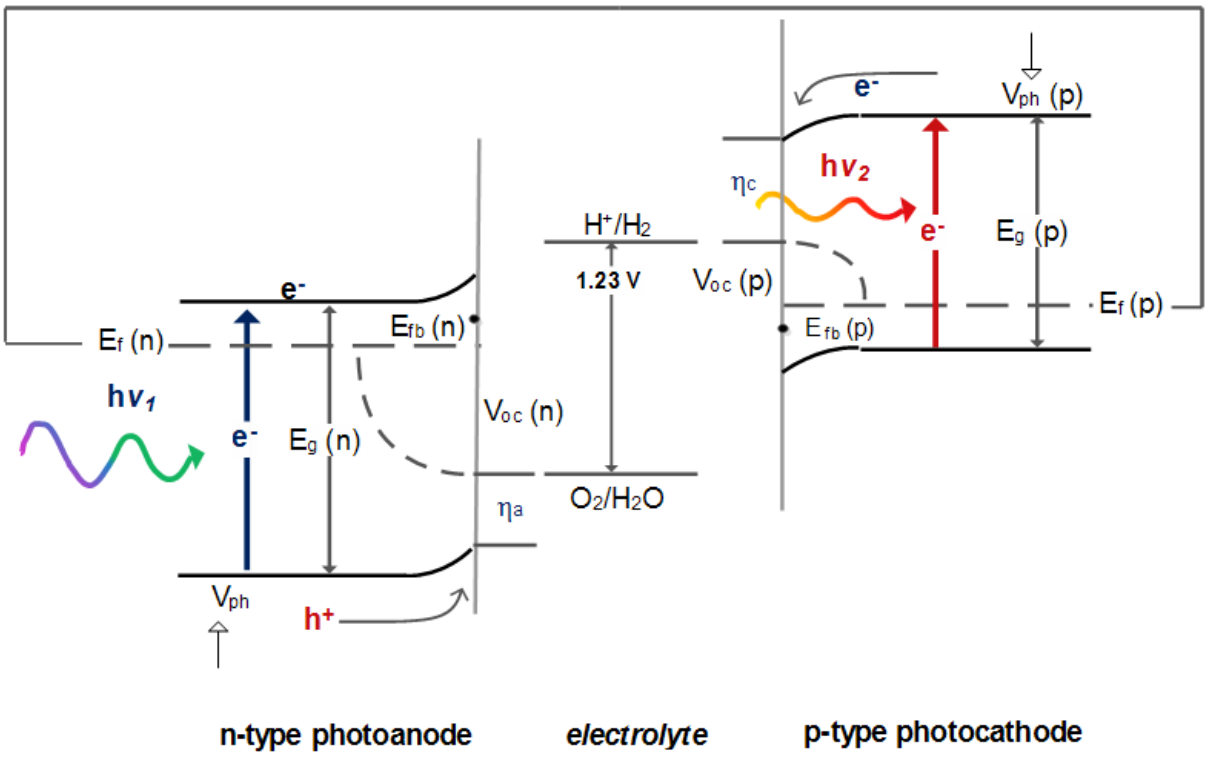

Figure 11: Tandem dual photosystem band bending diagram under working conditions

Where $h\nu_1$ and $h\nu_2$ are light wavelengths with energy greater or equal to the $E_g(n)$ and $E_g(p)$ respectively, h^+ and e^- the hole and electron pair, η_a the anodic overpotential, η_c the cathodic overpotential, E_{fb} the flat band positions of each photoelectrode, and V_{ph} the photovoltage contribution from light which drives the photovoltaic response. This can be related to the overall water splitting energetic requirements and

obstacles by the equation (35) necessitating the water splitting potential (ΔG/nF) and additional losses due to resistance in the system (iR) [84].

$$E_{g(n)} + E_{g(p)} - \left[E_{fb(p)} - E_{g(n)}\right] + \Delta E_{f(n)} - E_{f(p)} = \Delta G/nF + \eta_q + \eta_c + iR \quad (35)$$

With band gaps in the range 0.5 – 3.0 eV, semiconductors can absorb visible photons to excite electrons across the band gap, into the conduction band, where they may be collected. In photoelectrochemical water splitting devices, semiconducting materials are preferred over the dye-sensitized approach due to the fact that semiconductors can absorb wider ranges of light; whereas, dye sensitizers have narrow absorption bands [126]. The III-V compound semiconductors such as gallium arsenide (GaAs) and indium phosphide (InP) have band gaps close to the optimum (1.42 eV and 1.35 eV, respectively, at 300 K) and are favored for high efficiency cells. Nevertheless, the most widely used single junction photovoltaic solar cell material, silicon (Si), has a less favorable band gap at 1.1 eV (rendering a maximum theoretical photon to electricity conversion efficiency of 29%). Silicon is inexpensive, abundant, and mature in terms of research and development and therefore highly commercialized for photovoltaic applications. In the objective of clean hydrogen production, simply submerging photovoltaic materials in water to drive a chemical reaction is not straightforward. Most of the photoabsorber materials used in typical photovoltaic modules suffer from instability in aqueous solution due to the redox positions of their energy states. Therefore, for water splitting applications, metal oxides are considered to be more appropriate than typical photovoltaic materials [50].

To further understand the fundamental properties of metal oxides for water splitting, it is necessary to understand their electronic properties and therefore chemical bonds which form electronic properties. Where photovoltaics exhibit covalent chemical bonding, metal oxides are generally ionic or polar in nature due to the fact that oxygen is much more electronegative than any metal. Therefore, valence electrons are either fully or partially transferred from oxygen to the metal ions. This makes metal oxides more ambiguous due to their localized electron movement, as opposed to delocalized electron movement in covalently bonded materials. Thus the distinction between a direct and indirect metal oxide semiconductor is more obscure than with typical PV materials [30]. Like semiconductors, metal oxides benefit from defects in the crystal lattice, producing majority and minority carriers and exhibiting p or n-semiconductor characteristics. In oxide semiconductors, the conduction band levels of small band gap semiconductors are usually low because the deep valence bands which are formed by O 2p [127]. This is a major problem for developing visible-light-driven and stable oxide photocatalysts. Thus, it is indispensable to control the valence band with orbitals of some elements instead of O 2p.

Due to corrosive redox reactions as well as parasitic electrochemical reactions, the faradaic efficiency and stability of the photoelectrode may be hindered; thus, limiting overall device efficiency. This renders the choice of electrolyte, surface structure of the material, surface species, and potential co-catalyst addition to ameliorate the OER or HER kinetics, very important for overall STH efficiency and correct device operation. Metal oxides can contribute the OER from water (electrolyte) presence of oxygen but also from oxygen present in the crystalline lattice of the electrode, irrespective of pH [128]. This instability of metal oxides for the OER is a major obstacle for the lifetime of PEC devices. Unfortunately, Pourbaix diagrams do not always take into account this possible corrosion in metal oxides for the OER, so stability must be experimentally verified for some materials. Additionally, metals alter oxidation states during the OER and HER, which may result in increased solubility and therefore corrosion of the electrode.

Figure 12 displays the conduction and valence band positions for many state of the art researched photoelectrocatalytic water splitting materials. The red mark depicts the oxidation facility of the materials and if located below the O_2/H_2O potential is resistant to hole oxidation. Similarly for the reduction potential, if the black mark is located above the H^+/H_2 potential, the material is resistant to electron reduction (same for CB and VB). Nevertheless, there are exceptions to this simplified stability depiction, such as Cu_2O which is not in its highest oxidation state and can potentially oxidize to be more stable (e.g. CuO or $CuWO_4$). In addition, PbO, $CuWO_4$, $BiFeO_3$, and WO_3 have lower reduction potentials than H^+/H_2 but they are still stable due to the fact that their reduction potential (φ^{re}) is above the bottom of the CB level. Notably, some metal oxides do not have Nernstian behavior, such as WO_3, whose oxidation potential does not move upon change in pH, contributing to possible energy barriers, losses, and decreased stability upon increase in pH.

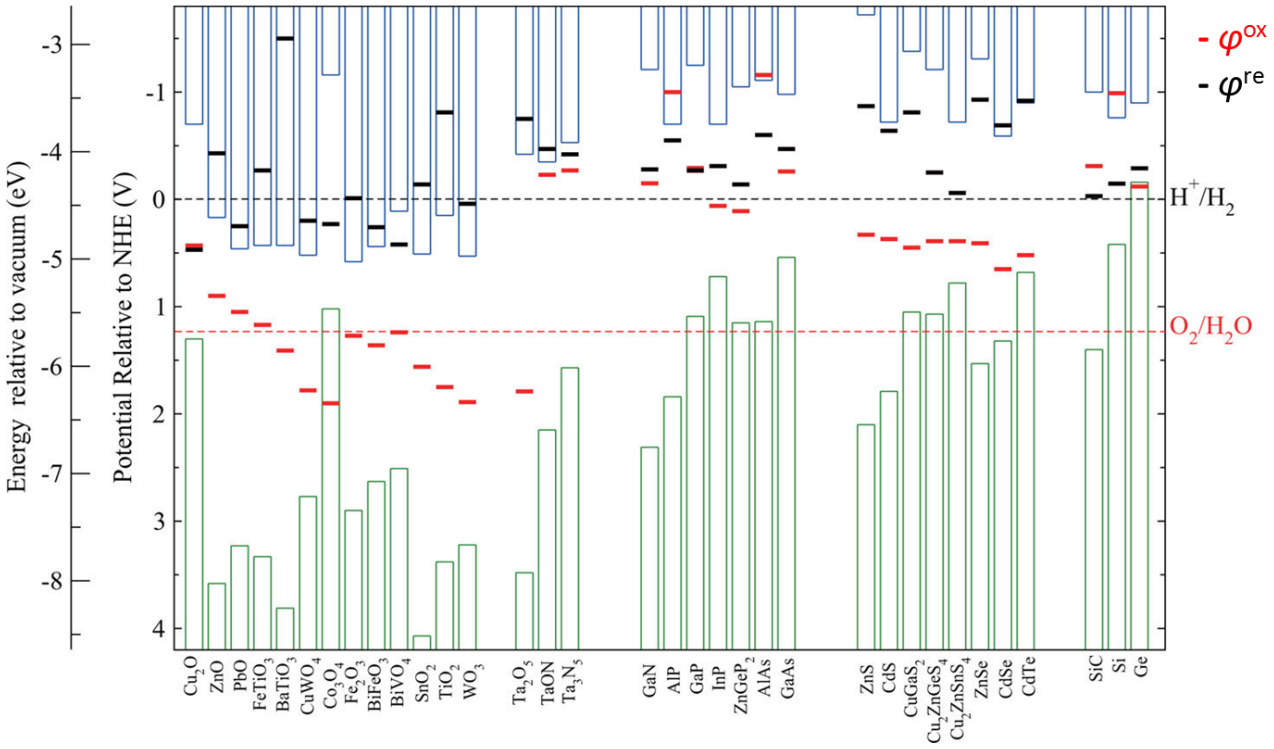

Figure 12: Corrosion potentials of potential photoelectrocatalytic materials taken from Chen, 2012

Considerable research and engineering have been accomplished in order to optimize and implement these metal oxide based photoelectrodes in hopes for better photovoltaic efficiency, water splitting kinetics, and increased stability. Unfortunately, good photoelectrocatalytic performance is rarely measured without the use of expensive precious and noble metals. In attempts to avoid this issue, abundant, lower cost materials are proposed, both for photoabsorber and co-catalyst materials which can ease the water splitting reaction kinetically. Appropriate metal oxides for the OER require low oxygen anion mobility in the bulk lattice, along with addition of co-catalysts to avoid unwanted corrosive or dissolution energetically preferred reactions; co-catalysts being the main suggested solutions to increase stability of metal oxides for water splitting applications [128].

Many factors can affect the semiconducting qualities, stability, and redox reactions in materials; such as: the overall crystal structure, surface area, lattice characteristics, and nano/microstructures. All of these factors are crucial in determining the efficiency of a semiconductor to generate and separate charges to carry out a reaction. Concerning current material engineering, 1-D configurations (nanorods, nanocones, etc.) and quantum dot technologies are suggested to enable carrier multiplication, while quantum confinement effects and hot carriers may improve charge transport and lifetime for increased performances. Semiconducting photoelectrodes are almost always doped in order to improve p or n conductivity. Doping at appropriate quantities can enhance the optical absorption of wide bandgap

semiconductors, increase the minority carrier diffusion length, or increase catalytic surface activity. Nevertheless, certain or too many defects can affect properties in negative ways such as creating midgap bulk or surface states which act as recombination centers. In photoelectrochemical cells containing metal oxides, to act like doped silicon (for improved charge carriers in practical applications), it is necessary to have shallow donors and acceptors because of the low intrinsic charge carrier mobility [30]. The concentration of dopants in metal oxides is usually limited to 1–2% at most, which corresponds to a density of states concentration of around 10^{21} cm^{-3}. It is thought that higher concentrations can lead to segregation of the dopant phase and even act as recombination centers. As of current, the most efficient electrocatalysts for photonic water splitting are based on noble metals, which are expensive and limited; therefore not ideal in industrial application [129].

The surface of the semiconductor is of high importance, as it is where the chemical reaction occurs. The surface area to volume ratio should be ideally large in the case of water splitting materials, allowing increased surface sites for this reaction. In consequence, rough, nanostructured, and porous materials are of great interest. Nevertheless, the bulk material should be in contact enough to conduct and drive charges throughout the photoelectrodes, allowing mass transport while avoiding potential recombination at grain boundaries and interparticle sites. Controversially, if the OER or HER is known to suffer from slow kinetics at the SCLJ, a larger surface area may be detrimental as it increases the surface recombination sites.

Metal oxides employed for photoelectrodes are generally deposited on indium tin oxide (ITO), fluorine doped tin oxide (FTO), or zinc oxide (ZnO) thin layers - otherwise known as transparent conducting oxides (TCO). These TCO substrates are n-type and widely recognized amongst the photovoltaic industry due their high conductivity and optical transparence [130]. This is attributed to their large band gaps ($\geq$ 3 eV) and structures, with small contribution from the Burstein-Moss shift; thus, absorbing little to no visible light and hence transparent in the visible region of the solar spectrum. Figure 13 displays the suggested band positions of FTO, ITO, and ZnO assuming Fermi levels 0.5 eV above the conduction band [131]. Due to the higher level of doping, the Fermi level of TCO materials are generally in the conduction band and therefore act as degenerate semiconductors – exhibiting metal-like behavior. The higher the Fermi level in n-type semiconductor, the higher the conductivity due to the facility of electron transfers to the conduction band from this energy level. ITO is rather expensive due to indium and is increasingly avoided for TCO use. Therefore, FTO is more commonly employed due to the greater abundance of tin, better stability, and chemical resistance [132, 133]. These materials suffer from corrosion in extremely acidic or basic conditions and should not be exposed to the solution during the water splitting reaction to avoid unwanted degradation [134].

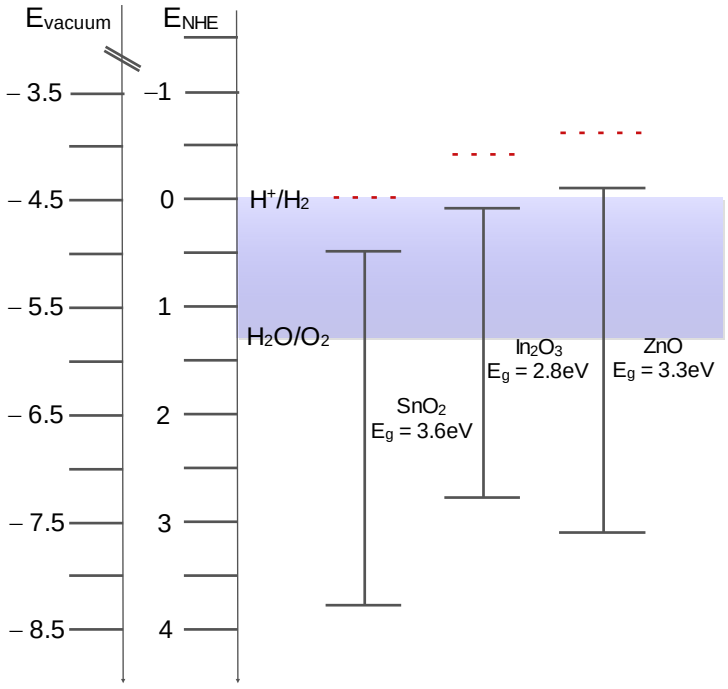

Figure 13: TCO substrate theoretical band positions

Metal oxides thin layers are deposited by several methods: chemical vapor deposition [121, 135-138], atomic layer deposition [139-144], evaporation or reactive ballistic deposition [145-148], spray pyrolysis [149-152], sputtering [85, 89, 93, 130, 153-155], electrodeposition or anodization [156-162], hydrothermal [163-167], chemical bath or solution growth [117, 141, 168, 169], spin coating [170-177], doctor blade [178-181], drop casting [182-186], and dip coating [187-192]. Heat treatments following or during the deposition process is performed in order to crystalize these materials. This step is of great importance, for this thermal treatment greatly influences the crystal structure, crystallite size, surface plane, and the possible defects or electronic transitions and electrical performance [193]. Nevertheless, materials requiring high temperatures are not practical due to the fact that substrates are typically glass and FTO which are not stable above 600°C. As previously stated, nanostructuration and implementation of porous materials are preferential in water splitting as these features enable more interaction with the electrolyte and alleviate issues of poor conductivity and charge separation efficiency arising from short diffusion length of carriers in metal oxides as well as increase light harvesting due to multiple scattering effects [194]. Increase in surface area may also increase recombination sites which occur at the SCLJ, thus requiring alternative modifications for increased surface reactivity. Fabrication methods of the photoelectrodes, thickness, morphology of nanostructured films, dimensions of the nanostructures, crystallinity, charge separation, charge transport, and recombination of the photogenerated charges all highly affect the performance of these materials in water splitting PEC devices. Therefore careful

consideration must be taken into account for each material's semiconducting and physical properties and fabrication to yield to these fundamental obstacles for overall material optimization.

Concerning materials for water splitting PEC applications, metal oxides (doped, nanostructured, and possibly containing surface catalyzers) are the common trend to date. This choice is highly influenced by the fact that metal oxides are frequently inexpensive, stable, easily prepared on a large scale, and robust under PEC operating conditions. Therefore the characterization, pairing, optimization, and correct implementation of metal oxides for a tandem dual photosystem water splitting device is crucial for correct operation and for efficient clean hydrogen production.

I.4.3.1. State of the Art Materials

Since the publication of Honda and Fujishima in 1972, the concept of water splitting photoelectrochemical cells has been a growing theme amongst the hydrogen economy and renewable energy factions [28]. Over 140 metal oxides, perovskites, and oxynitrides are known to catalyze the photochemical water-splitting reaction [195]. Materials like gallium arsenide, silicon, hematite (α-Fe_2O_3), and TiO_2 are currently amongst the most popular materials generally used in PEC cells due to solar absorption and band gap characteristics [5, 12, 196]. Since Honda and Fujishima's reaseach with rutile TiO_2, there has been a fundamental focus on anatase TiO_2 for water splitting applications [197]. Though the band gap is rather large for this application and thus visible light is not largely absorbed, limiting the photoconversion to the small portion of solar spectrum absorbed. With a large band gap of 3.2 eV (anatase), TiO_2 is favored for this application owing to its high corrosion resistance in aqueous environments [112]. Alternative materials with smaller band gaps are currently researched with the goal to harness as much sunlight energy as possible, while minimizing recombination, losses, and avoiding corrosion due to changes in pH during oxidation and reduction processes.

I.4.3.1.1. Photocathode

Typical metal oxide materials in current research for the photocathode in a dual photosystem involve NiO, Cu_2O, CuO, and several other spinel, perovskite, and delafossite compounds. These are naturally p-type owing to their O 2p characteristics resulting from an excess of oxygen vacancies [198-200]. These semiconductors typically have smaller band gaps and absorb in the visible towards the infrared region of the solar spectrum. Assuming they are placed behind a large band gap photoanode which absorbs toward the UV portion of the spectrum, the absorption of light towards the visible and IR range is ideal for a tandem dual photosystem. Unfortunately in some cases, the conduction band of these materials are much more negative than the H^+/H_2 reduction potential and generally require large overpotentials to drive the HER half reaction. Fortunately copper (I) oxide is an exception with its conduction band only slightly

negative of the proton reduction potential [201]. The abundance of copper and its narrow band gap of 1.2 eV and 2.0 eV for CuO and Cu_2O respectively make it a good candidate for photocathode materials. Both copper I and II oxides have direct band gaps and have been recently researched as photocathodes in water splitting devices [202, 203]. Cu_2O has relatively high carrier concentration, but like most metal oxides, the charge mobility and electric conductivity of Cu_2O are poor [203]. Literature reports state that Cu_2O can achieve up to −14.7 mA/cm² based on equation (24), taking into account the absorption coefficient of Cu_2O, suggesting that there are optical losses upon light absorption. The material characteristics of both copper oxides are shown below in Table 3 along with the absorbance dependent on the bandgap in Figure 14. Note that the absorption coefficients for materials were not taken into account for calculation of the maximum theoretical photocurrent achievable calculated from equation (24) in Table 3 resulting in higher estimations of achievable photocurrent [99, 113]. STH calculations assume a single photosystem; though in this case, the band gap of CuO (if actually 1.2 eV) is too small to logically calculate an STH value due to the fact that the V_{oc} can never be larger than the band gap – thus further analysis pairing it with a photoanode material is needed to calculate a genuine STH value for small band gap materials in dual photosystems.

Material	**CuO**	**Cu_2O**	**Ref**
Band Gap (eV)	1.2	2.0	[204, 205]
Wavelength (nm)	1033	620	-
j (mA/cm²) from literature		– 14.7	[143]
j (mA/cm²) calculated from eq. (24)	– 41.4	– 16	
STH Experimental Efficiency (%) from literature	-	18.1	[143]
STH Efficiency (%) calculated from eq. (30)	-	19.7	[113]
% AM1.5G Spectrum Used	75	19	[36]

Table 3: p-photocathode material characteristics

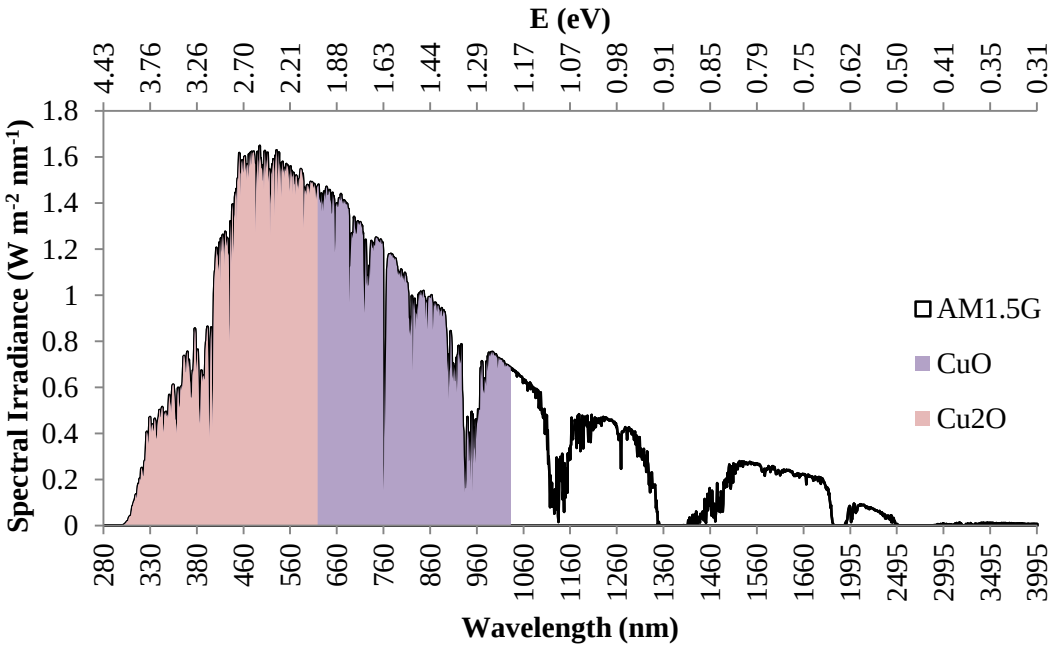

Figure 14: solar absorption of copper as a photocathode

Though CuO is also a semiconducting material, reduction of copper (II) to copper (I) can be utilized to form a p-p junction for increased charge separation due to the preferential band positions forming a CuO/Cu_2O junction. This enables copper to possess both oxidation states in a photocathode and using the varying band gaps to absorb near the infrared region as well as separated charges for increased e- concentration for the reduction of protons at the SCLJ surface [206-208]. The coupling of both copper oxidation states has been also shown to increase stability in water splitting applications [207]. A band diagram (Figure 15) suggests the theoretical positions of CuO and Cu_2O according to literature values with Fermi levels arbitrarily placed [143, 209].

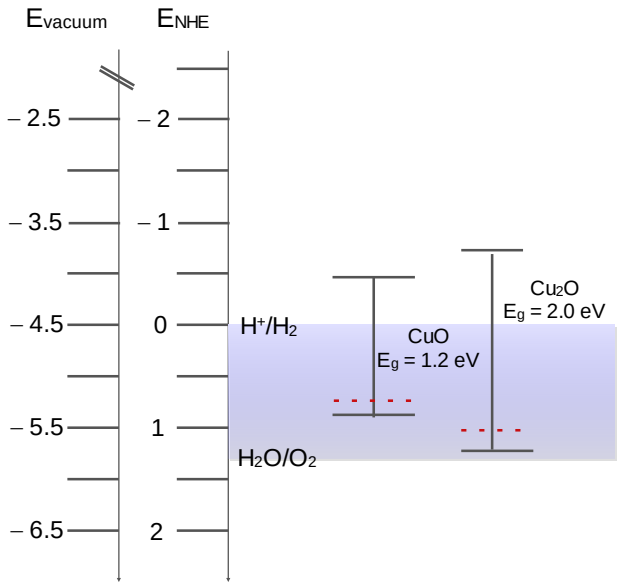

Figure 15: Band positions of p-photoanode materials

Unfortunately, one of the main drawbacks of using copper is that it is highly unstable in aqueous solutions in the cathodic region and tends to utilize electrons to reduce copper oxides to copper metal. Cuprous oxide also undergoes oxidative decomposition in air and anodic or cathodic photocorrosion (formation of CuO or Cu) as well. Copper hydroxide $Cu(OH)_2$ is metastable and easily transforms into copper oxide CuO – which is more stable either in the solid state by a thermal dehydration or at room temperature or in aqueous basic solutions [210]. The Pourbaix diagram for copper is displayed in Figure 16, suggesting its large instability in solution near the H^+/H_2 reduction potential. Both CuO and Cu_2O can react with protons at the SCLJ which may reduce these oxides into copper metal resulting in corrosion of the photoelectrode.

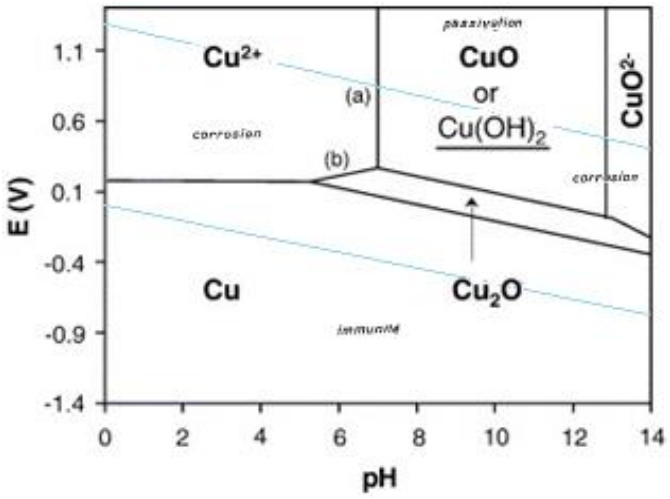

Figure 16: Pourbaix diagrams for copper adapted from Pourbaix, 1966

Cupric and cuprous oxide films for a water splitting photocathodes have been widely implemented in the field of PEC and continue to be present in several photoelectrochemical applications [203].

State of the art performances of copper based photocathodes are compared in Table 4 (the photocurrent density at the HER potential unless otherwise specified):

Year	**Photocathode**	**Cu_2O Deposition Technique**	**Cu_2O Thickness (nm)**	**Electrolyte (pH)**	**P_{in} (mW/cm²)**	**j**	**Ref**
1999	FTO/Cu_2O	electrodeposition	3000	0.5 M Na_2SO_4 (pH 7)	350	– 0.1 mA/cm²	[201]
2003	Ti/Cu_2O/TiO_2	electrodeposition	100	0.1 M sodium acetate buffer (pH 7)	700	– 0.7 mA/cm² *(at –0.4V vs. RHE)*	[211]
2011	FTO/Au/Cu_2O/ *5x*(ZnO/Al_2O_3)/ TiO_2/Pt	electrodeposition	1300	1 M Na_2SO_4 (pH 4.9)	100	– 7.6 mA/cm²	[143]
2012	Cu/CuO/NiO_x	chemical bath deposition	10000	0.1 M Na_2SO_4 (pH 6)	26 (425-660 nm)	– 4.98 mA/cm² *(at –0.02V vs. RHE)*	[117]
2012	ITO/Cu/Cu_2O/CuO	electrodeposition	-	0.05 M Na_2SO_4 (pH 6.8)	AM1.5G	– 1.54 mA/cm²	[161]
2013	ITO/CuO/$SrTiO_3$	spin coating	330	0.1 M NaOH (pH 13)	150	–1.85 mA/cm² *(at 0.1V vs. RHE)*	[175]
2013	FTO/Cu_2O/ZnO/ TiO_2/MoS_{2-X}	electrodeposition	400	(pH 1)	AM1.5	–5.7 mA/cm²	[212]
2015	Cu_2O/Ga_2O_3/TiO_2/Pt	chemical bath	3500	0.5 M Na_2SO_4 and 0.1 M KH_2PO_4 (pH 4.3)	100	– 2.95 mA/cm²	[141]

Table 4: state of the art copper based photocathodes

Though copper based photocathodes exhibit large photocurrents, the stability requires that there be protection or surface modification which can potentially affect the performance. Excessive fabrication and systems with several layers become quite intricate and inapt for industrialization like the record breaking – 7.6 mA/cm² achieved at the Ecole Polytechnique Fédérale de Lausanne which includes a gold and platinum containing photoelectrode [143]. Similarly, other attempts to passivate Cu_2O use ALD to deposit thin n-type layers to protect Cu_2O and influence charge separation by band bending, though ALD is not

suitable for upscaling of photoelectrodes, and thus impractical for industrial applications [141, 212]. Due to the large implementation of copper oxide based p-photocathodes in literature for water splitting applications, it was selected as the p-photocathode photoabsorbing material for the tandem dual photosystem to complete the HER half reaction. Copper (I) oxide is used in previous metal oxide based dual photosystems referenced in Table 2; thus allowing the comparison of state of the art performance and efficiency to our dual photosystem [117, 120, 203]. To increase stability and potentially charge carrier separation, the photocathode in this study is based on a copper (II) photoabsorber and protected by a large band gap n-type perovskite or TiO_2 as a passivation layer. This is naturally the fundamental logic for hybrid PECs, enabling the larger band gap material to protect cupric oxide from corrosion yet still conduct the hydrogen evolution reaction at the surface [175, 206, 211].

I.4.3.1.2. Photoanode

Metal oxide materials for the photoanode to date are mainly focused on n-type metal oxides TiO_2, WO_3, $BiVO_4$, and Fe_2O_3. With band gaps ranging from 3.2 to 2.1 eV these materials absorb largely towards the UV region of the solar spectrum (displayed in Figure 17). These materials solar absorption range are ideal for tandem dual photosystems as they leave much of the visible spectrum available for the photocathode to absorb; nevertheless, using larger band gaps may limit the overall efficiency of the device due the poor utilization of solar spectrum. These material's PEC characteristics based on their band gaps are compared below in Table 5.

Material	**Fe_2O_3**	**$BiVO_4$**	**WO_3**	**TiO_2**	**Ref**
Band Gap (eV)	2.2	2.4	2.7	3.2	[43, 113]
Wavelength (nm)	564	520	459	388	-
j (mA/cm²) from literature	25	7.6	3.6	1	[43]
j (mA/cm²) calculated from eq. (24)	11.9	8.6	5.4	2.1	
STH Experimental Efficiency (%)	12.9	9.2	4.8	1.3	[43, 113, 151, 213]
STH Efficiency (%) calculated from eq. (30)	14.7	10.9	6.6	2.6	
% AM1.5G Spectrum Used	30	19	12	4	

Table 5: n-photoanode material characteristics

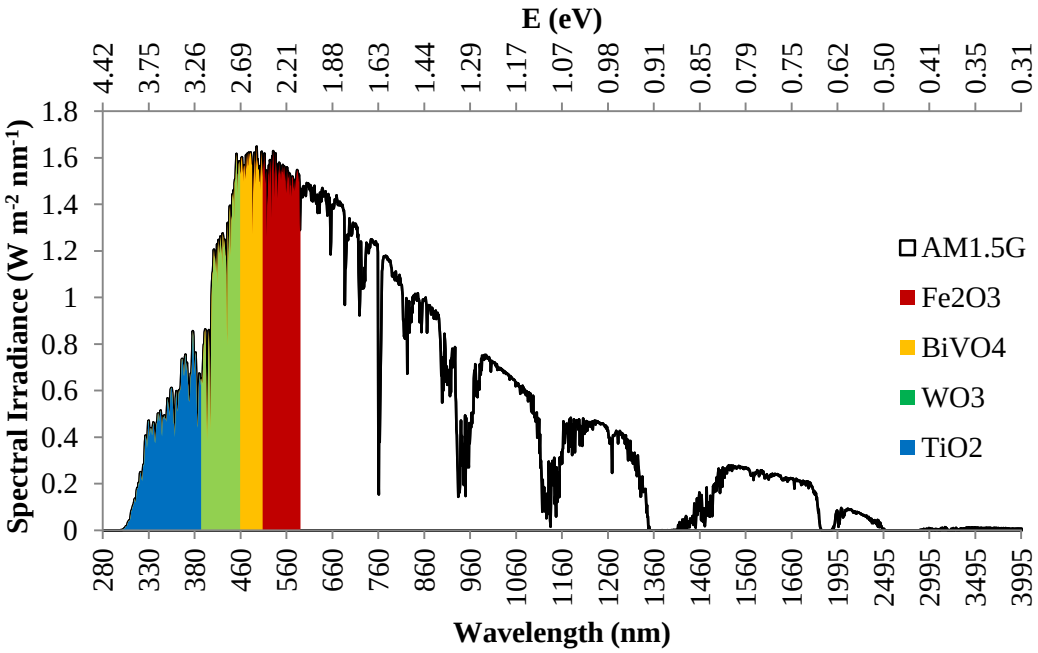

Figure 17: Solar absorption of n-photoanodes materials

Since the 1970's these materials have been milestones for water splitting photoanodes. Unfortunately TiO_2 with its large bandgap of 3.2 eV is only capable to absorb about 4% of the solar spectrum and therefore limiting the total efficiency for the OER (assuming 100% IPCE) to only 1.3% [113]. Fe_2O_3 has recently been a material of interest for water splitting applications. Hematite, the most stable form of iron oxide, is abundant and inexpensive. Yet hematite suffers from low conductivity, and bulk recombination thought to be the result due to a short hole diffusion length of around 2 – 4 nm [110]. Current efforts have focused increasingly upon WO_3 and $BiVO_4$ for water splitting applications. With band gaps of roughly 2.7 eV and 2.4 eV respectively, these materials can absorb wavelengths up to 460 and 515 nm in the visible spectrum. Figure 18 displays a diagram suggesting the theoretical band positions from several literature sources relative to the NHE (pH 0) of n-type metal oxides (with Fermi levels arbitrarily placed) [214]:

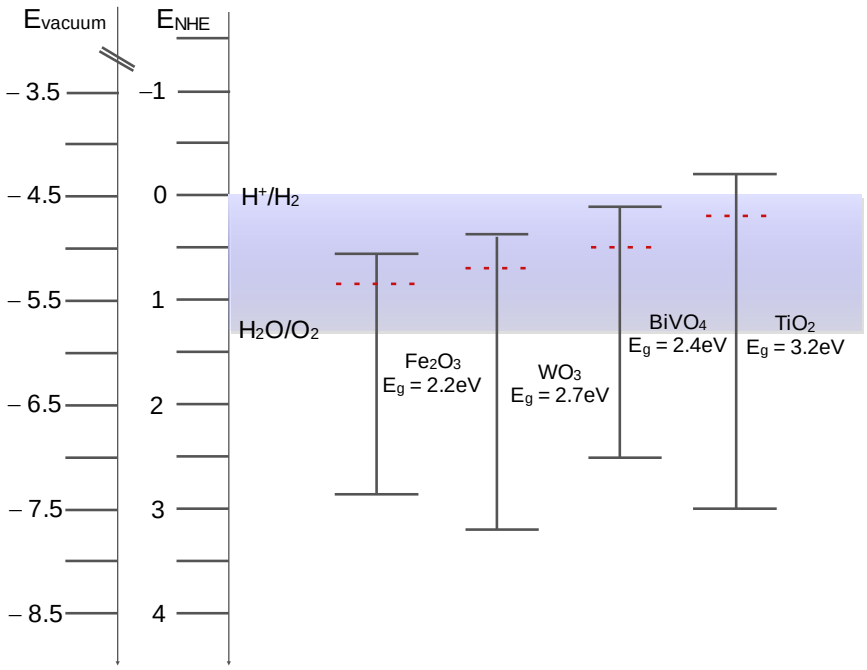

Figure 18: Band positions for n-photoanode materials

Mobility of the minority carriers to the surface is of great interest, seeing as these chargers are what carry out the OER and HER. The oxidation of water by the n-photoanode is a reaction demanding four holes to carry out this kinetically slow task, and thus is much more complex than the two-electron demanding HER. Concerning the four candidates as water splitting photoanodes, it is suggested that TiO_2 has a hole diffusion length of 10^4 nm, WO_3 150 nm, $BiVO_4$ 100 nm, and Fe_2O_3 only 2 – 4 nm [215-218]. Nanostructuration of these materials can overcome the hole diffusion length issues in WO_3 and $BiVO_4$ by increasing surface area so that holes may arrive at the surface for use in the OER. Though iron oxide suffers greatly from its inability to transport minority carriers to the surface for use and therefore engineering is needed to increase its minority carrier lifetime and overall conductivity. Introduction of dopants can be achieved with many of these materials in order to reduce the band gap for increased solar absorption or improved conductivity. Additionally, the band positions of these metal oxides are of great interest as this can affect the flatband position and therefore the onset of the photocurrent for water oxidation as well as the overpotential needed to carry out the OER. All of these considerations are taken into account upon optimization and implementation of the metal oxide for water splitting materials; as the photoabsorbing qualities are important, the kinetic water splitting reaction at the SCLJ is also of great importance for correction hydrogen and oxygen production. Thus, the electrolyte employed and/or co-catalysts increase the complexity, optimization, and characterization of the photoelectrodes.

I.4.3.1.3. Co-catalysts

Due to the fact that the photoabsorbing materials must be efficient in charge generation and separation, the surface reaction with water and electrolyte must also be efficient for overall function of the device. If charges are not utilized upon reaching the SCLJ, they risk recombining, resulting in overall performance loss. In general the $2e^-$ proton reduction for hydrogen evolution is rather fast, whereas the $4h^+$ needed to oxidize water is thought to be the kinetic bottleneck of the overall complete water splitting reaction [110]. The possible addition of co-catalysts on the photoelectrode surface may ameliorate the water splitting kinetics by providing alternative energetic pathways for charges to oxidize water or reduce protons more easily than photocorrosion, dissolution, or other parasitic reactions [219]. To date, the most efficient water splitting co-catalysts are thought to be precious metals such as platinum and ruthenium, which have good metal-proton bonding. This is displayed below in Figure 19 in volcano plots which relate the OER co-catalysts to overpotential for water splitting and the HER to metal proton bonding strength [26, 220, 221].

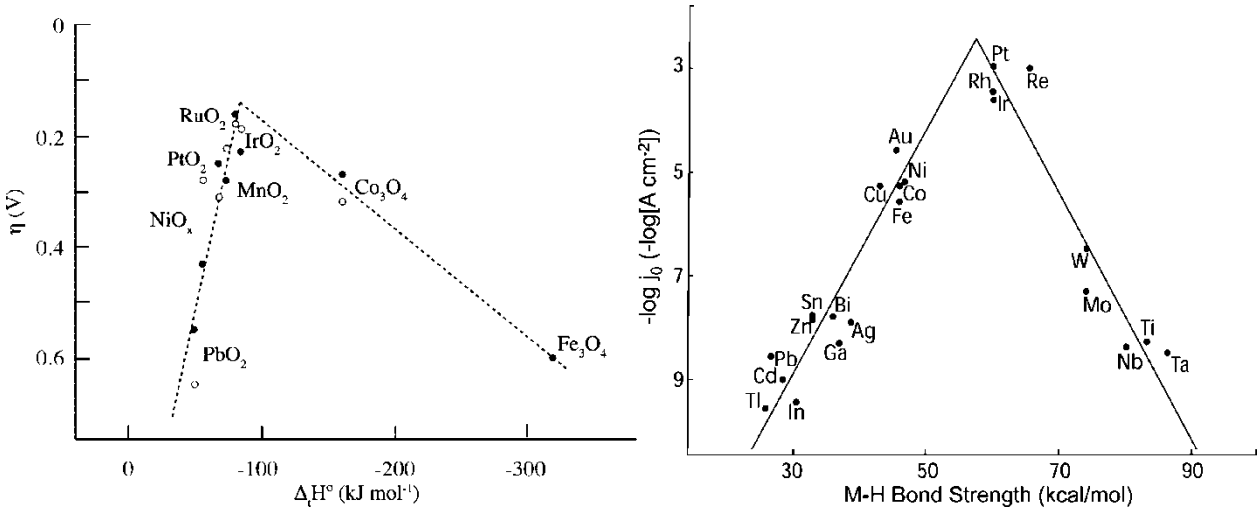

Figure 19: Co-catalysts for the Oxygen evolution reaction (left) related to overpotential and hydrogen evolution reaction (right) related to metal – proton bonding strength taken from Walter, 2010

The materials at the peak of the volcanos plots are the most ideal for the OER or HER; unfortunately, these materials are typically expensive, noble and precious metals, or non-abundant, which make them impractical for large scale application. Co-catalysts based on nickel, cobalt, manganese, molybdenum, and iron are more sought after due to their low cost and abundance [222]. General issues concerning the addition of co-catalysts are the stability in differing pH, detachment from the photoabsorber, and competing light absorption. As the pH gradient changes due to the electric field created and differing surface species (H^+ and OH^-), certain co-catalysts can become unstable or inactive as catalysts [222-224].

To date, Nocera's group has introduced the cobalt phosphate, reputably known for its "self-healing" qualities, and nickel borate which seem to be widely used by others in attempt to reduce the onset potential of the photoanode photocurrent [225-230]. Nevertheless, there is questionability concerning its stability in neutral conditions over time [223]. Many attempts are taken to find appropriate stable, self-healing, co-catalysts which ease the kinetics on the surface of n-photoanodes for the OER as it is more complicated and demanding than the HER. The hydroxide intermediates of the OER highly depend on the pH, as the increasing concentration kinetically facilitates this reaction. Energy levels associated with the co-catalysts may enable the formation of hydroxide intermediates more easily than others and display a lower overpotential for water splitting oxidation. Materials such as platinum, ruthenium, and iridium are thought to function more as metal-Schottky contacts and are considerably more stable in varying pH than other materials [231]. Nevertheless, metals which form hydroxides such as nickel and iron are highly studied in order to further understand how to alleviate the OER kinetics [224, 232-234]. It is also suggested that cobalt, nickel, iron, and manganese based co-catalysts for the OER function more as metal oxides and that the metal-oxygen bonds may give insight to the oxophilicity [233].

I.4.3.1.4. Electrolyte

The photoelectrode interacts directly with water as well as an electrolyte to transfer charges due to ionic forces in solution to energetically drive the water splitting reaction – seeing as pure water is a poor conductor and thus leads to high ohmic overpotentials. The solubility of the electrolyte highly contributes to the solution resistance, which is thought to be one of the major resistance losses in PEC devices [44]. Thus the redox potentials of water oxidation and proton reduction are not the only to consider at the SCLJ. The photovoltage achievable with a photoelectrode is decided between the energetic difference between the E_C or E_V and the electrochemical potential of the redox potential [126]. Typical electrolyzers use extremely basic or acidic solutions, which can be corrosive and thus unideal for operative conditions. These conditions offer high ionic (proton and hydroxyl) concentrations as well as charge mobility and subsequently possess low electrical resistance. Basic electrolytes are generally preferred since corrosion problems are severe with acidic electrolytes. Contrary for gas separation, ionic conducting membranes such as Nafion® – a proton exchange membrane, function more favorably in acidic conditions; thus, coupling with the right ionic transporter is of importance. In dual compartment water splitting cells, there will be a pH gradient which occurs on either side of this ionic separator due to the concentration of species which accumulate due to the Helmholtz layer at each photoelectrode [235]. This gradient can lead to highly acidic or basic localized areas and contribute to instability of each photoelectrode; thus, circulating or regenerating neutral pH conditions could potentially overcome these issues [236]. The pH of the solution plays an important role as well due to the HER and OER mechanisms which occur at electrode, preferring protons and hydroxide ions respectively. With most metal oxides, the E_C and E_V will shift along

with the water splitting potentials like in equations (10) and (11), otherwise known as the Nernstian relation: E - (0.059 × pH); however, large concentrations of hydroxide ions or protons can influence local changes in ionic species which occur in response to band bending, depletion width, and the Helmholtz layer. These are the most mobile ions in solution, yet are aggressive at large concentrations [112]. Therefore, the pH of the electrolyte can significantly alter the kinetics of both the HER and OER mechanisms. The HER is considerably fast in acidic conditions and slower in alkaline environments; whereas vice versa for the OER. The n-photoanode has a dominating role in determining the hydrogen production efficiency due to slow kinetics and four-electron reaction associated with the oxygen evolution reaction (OER) [110]. Thus employing neutral conditions is a common approach to yield to both of these kinetic concerns.

Typical cations ideal for charge transport are small and thus very mobile such as sodium (Na^+) and potassium (K^+) whose resistance becomes negligible at higher concentrations (> 3.5 M) and promote H_2 production over reduction of these species due to their very negative reduction potentials [112, 237]. Anions generally consist of phosphates (PO_4^-), sulfates (SO_4^-), chlorates ($ClO_4^{\cdot}$), chloride (Cl^-), and hydroxides (OH^-). The oxidation of these anions can energetically compete with water oxidation and lead to unwanted parasitic reactions which do not contribute to the desired O_2 production [238]. For example, Cl_2 gas may be formed from HCl electrolyte, $ClO_4^{\cdot}$ radicals from $HClO_4$ which lead to slow O_2 production, and finally surface oxo or peroxo species may be more prone to form with certain anions, which block the surface, cause great changes in pH, and can be detrimental to photoelectrode stability [158]. Energetic redox potentials for commonly used anions in water splitting reactions are shown in Figure 20.

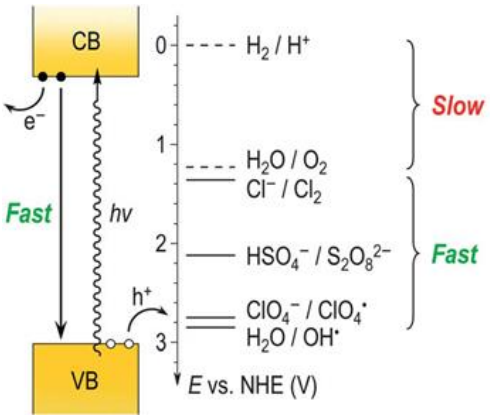

Figure 20: Redox potentials of anions/potential intermediates for the OER using WO_3, adapted from Mi, 2012

In acidic to neutral conditions, the current onset is a function of the electrolyte anion. Thus, the flat band potential becomes more positive with Cl^-, HSO_4^-, and ClO_4^- anions respectively [159]. Diffusion plays a large role in electrochemical surface reactions and thus anions which diffuse to the surface, across the surface, and then away from the surface are facilitated by high conductivity of the solution. Higher concentrations of mobile anions (such as Cl^-) can lead to more conductive solutions and thus the more effective charges can be transported between both half reaction locations [237]. In order to avoid parasitic reactions and degradation, as well as enable ionic path length between electrodes through the ionic separator; in consequence, it is imperative to employ an appropriate electrolyte at an optimal concentration.

The concentration of the electrolyte ought to be enough to transport charges efficiently, but not too concentrated to cause losses in light absorption. Directly related, the volume of electrolyte in the device must be enough to minimize ohmic losses in the solution, but again not to hinder solar absorption [109]. Considering the photoelectrocatalytic cell is under illumination, an increase in temperature will occur – though this parameter is not thoroughly studied in this thesis. Nevertheless, this increase in temperature aids to reduce both activation and ohmic overpotential as it enhances the reaction rate and reduces the electrolyte resistance.

Research effectuated concerning a PEC tandem dual photosystem employs potassium phosphate (KPi) for acidic to neutral conditions and sulfuric acid for highly acidic conditions, due to the anionic abilities to produce O_2 in place of chlorine, ethane, or CO_2 gases from electrolytes containing chlorine anions or acetate anions. Additionally, phosphate anions have been suggested as more resistant to changes in pH as well [145]. Potassium is employed as the cation, also known for its preference of photocurrent to oxygen efficiency over sodium and lithium. This is due to the high covalent nature of lithium and sodium to surface bonded oxygen in metal oxide photoelectrodes, which may absorb onto the surface and block potential O_2 production sites [238]. The concentration of electrolyte solution was chosen as 1 M for a large ionic force, and to anticipate the incorporation of a membrane and separation of compartments by an ionic separator.

I.4.3.1.5. Membrane

Many initial efforts of PEC tandem devices are based on the H-cell dual compartment cell architecture, which contains a compartment for O_2 production and another for H_2 production separated by an ionic separator [76, 105, 108, 235]. Upon implementation of a membrane for ionic separation, a pH gradient will occur on either side of the membrane, even in concentrated electrolyte, contributing to instability of materials and slowed kinetics for each half reaction [235]. Therefore, choice of electrolyte, electrolyte volume, and the ionic path length become key parameters for cell performance upon addition of a

membrane. Using ionic exchange separators for gas separation and safety contributes to the overall separation in dual compartment PEC device. To limit variables, Nafion®, a proton exchange membrane fabricated in the 1960's by DuPont, is used as a default membrane in this research as the general ionic separator to separate product gases. This material is constituted of sulfonated tetrafluoroethyelene (the ionomer of Teflon) based fluoropolymer-copolymer, which functions well upon hydration [239, 240]. Protons located on the SO_3H groups hop from one acid site to another creating conductivity exclusively to protons. Nafion® is unable to conduct anions or electrons and thus in a dual compartment tandem dual photosystem protons from one photoelectrode flow to the other by way of electrolyte through the membrane. In return, electrons flow from one photoelectrode through a metal wire to the complementary photoelectrode, completing the circuit. Nevertheless, the stability of Nafion® is considered poor in alkaline conditions, thus increased pH conditions are non-ideal for the correct functioning of this proton exchange membrane. Overall this membrane is selectively and highly permeable to water, making it a standard choice for first efforts of a dual compartment PEC device.

I.5. THESIS OBJECTIVES

Reflecting on thermodynamics and previously completed research in water splitting field, the largest theoretical efficiency for a PEC device is that of a dual photosystem, theoretically able to obtain 41% over 33% for a single photosystem [39]. Thus, the objective of this research was to construct a dual photosystem PEC device in order to carry out the HER and OER for clean hydrogen production. Architecturally, for dual PEC photosystems, the tandem configuration is theoretically thermodynamically more efficient than placing the photoelectrodes side by side. This choice additionally takes into consideration light absorption, ionic path lengths, overall PEC device area, and gas separation facilitation. Thus, a tandem configuration using dual photoelectrodes, an n-photoanode and p-photocathode for the OER and HER respectively, was deemed the most practical.

Photoabsorber materials with appropriate band gaps and photoelectrocatalytic activity were considered in order to complete both the OER and HER half reactions. The larger band gap materials generally exhibit n-type behavior, suggesting holes as the minority carrier which accumulate in the depletion zone and can be used to oxidize water to complete the OER. For several known large band gap n-type metal oxides (TiO_2, WO_3, $BiVO_4$, and Fe_2O_3), the position of the valence band allows for water oxidation. Therefore these four materials are established appropriate for use as the photoanode in a dual photosystem. Larger band gap materials absorb towards the UV region of the solar spectrum and have larger V_{oc} to drive the water splitting reaction. Thus, WO_3 and $BiVO_4$ were chosen to be implemented as n-photoanode materials for their large quantum yield and light absorption in the ultraviolet to visible range, respectively. In chapter two, these materials are synthesized, characterized, and optimized to be implemented in a water

splitting cell coupled with a p-photocathode. With the photoanode absorbing the higher energy light, the visible and infrared light are left to be absorbed by the photocathode which is placed behind the photoanode. A small band gap material exhibiting p-type behavior is needed to complete the dual photosystem as a p-photocathode, using the minority charge carriers (electrons) to reduce protons to complete the HER. Cu_2O and/or CuO are the most commonly used p-type materials for water splitting with an appropriate conduction band position relative to the HER potential and possessing a small band gap to be coupled with large band gap n-type photoanode material candidates. The choice of fabrication of materials was implemented using guidelines preferential to abundant, stable, inexpensive metal oxide materials, which potentially can be fabricated easily, at large scale, and at an energetically and financially reasonable expense.

The final focus of this research, discussed in chapter three, is the conception and construction of a complete water splitting wired dual compartment tandem dual photosystem device. Optimized materials for the n-photoanode upon integration with copper based p-photocathode are to be employed in the final photoelectrocatalytic cell. The electrolyte was chosen by aid of literature references relating to the faradaic efficiencies and conductivity to facilitate ionic transport between the photoelectrodes. Integration of a membrane for facile gas separation was aimed on employing a proton exchange membrane technology, Nafion®, in the interest of simplification of parameters. Architecture and construction of the photoelectrocatalytic cell was based on previous research and studies concerning water splitting technologies while intending to implement the least amount of materials in an innovative fashion for a functioning tandem dual photosystem PEC device.

II. PHOTOELECTROCATALYTIC MATERIALS

II.1. INTRODUCTION

This chapter investigates the optimization of materials for the n-photoanode destined for use in a complete dual photosystem tandem PEC device. Two materials were studied: tungsten trioxide and bismuth vanadate, individually and coupled, to further understand areas of amelioration for these materials in water splitting applications. In order to produce inexpensive, efficient, and practical photoelectrodes, low cost, low temperature, reproducible synthesis and deposition methods were adopted. Conscious attempts to avoid toxic, expensive, and rare earth and noble metals were implemented in mindfulness for scale up and potential industrialization for future practical application. Sol-gel synthesis was employed coupled with dip-coating deposition methods for thin film photoelectrode fabrication. These fabrication methods are chosen for the robustness, reproducibility, and ease of processing. Sol-gel synthesis enables the facile addition of additives to influence nanostructuration; congruently, augmented surface area of materials which serve to increase the amount of water splitting sites at the surface. The synthesis, characterization, and evaluation of their performances are described and discussed in the following chapter. Synthesized and researched materials will be compared to previously conferred state of the art equivalents in order to determine if sol-gel dip coating methods are practical for future application in fabrication of photoelectrodes for water splitting technologies.

The materials studied are discussed in several sections. To begin, an explanation of synthesis technique of materials for the photoanode by sol-gel process is addressed, which is intended be used in the water splitting reaction. The two deposition methods used to fabricate the thin films for water splitting applications are dip-coating and electrodeposition, chosen for their ease of processing and industrial appeal.

The second section of the chapter discusses tungsten trioxide (WO_3) fabricated by the sol-gel method, characterized, and optimized as an n-photoanode destined for use in a tandem dual photosystem. Optimization includes fabrication investigation (substrate, synthesis, temperature, thickness, nanostructuration) resulting in the best optical and photoelectrochemical performance. Photoelectrochemical measurements reveal the photocurrent at varying potentials, irradiation, and aqueous conditions, giving insight to material behavior and indicating possible areas of amelioration. The optimized thin film is then characterized by several characterization techniques to further understand the material's water splitting properties which can give insight to other possible ameliorations to increase efficiency for water splitting applications. Finally, a co-catalyst is deposited and tested on the surface in attempts to boost performance and increase faradaic efficiencies as well as stability in neutral conditions.

The third section of the chapter discusses bismuth vanadate ($BiVO_4$) as an n-photoanode material for use in neutral conditions. This material can be used individually for the OER in a tandem dual photosystem

and potentially coupled with WO_3 for increased stability and charge separation. $BiVO_4$ is fabricated, characterized, and optimized similarly to WO_3, employing sol-gel dip coating processes and similar characterization methods. Temperature, thickness, and nanostructuration are discussed and somewhat optimized for $BIVO_4$ thin films. This gives further understanding of potential areas of amelioration for implemented metal oxide use in a tandem dual photosystem.

Finally, the fourth section of this chapter discusses the attempt at combining both WO_3 and $BiVO_4$ studied to create a composite n-photoanode for the oxygen evolution reaction in a tandem dual photosystem. This is based on previous knowledge concerning the energetic positions of the conduction and valence band of both materials; suggesting the combination could increase charge separation and therefore overall water splitting performance due to their E_c and E_v relations [241]. Fabrication parameters, such as calcination temperature, thickness, and nanostructuration are studied and combined with previous results to attempt to optimize the materials and the overall performance of the composite thin film for water splitting. Finally, these composite photoanodes are characterized by the same methods as WO_3 and $BiVO_4$ in order to understand limitations in performance and potential areas of amelioration for increase future performance and efficiency. The photoelectrochemical behavior of the two materials combined reveals drawbacks, yet more importlantly, potential ameliorations to further increase overall photoanode efficiencies by combining materials for increased performance in a tandem dual photosystem PEC water splitting cell.

II.2. Fabrication Methods

Low cost, inexpensive, reproducible, scalable methods have been adopted in anticipations for industrial application of these materials for water splitting clean hydrogen future technologies. Metal-organic decomposition (MOD) techniques, referred to here as sol-gel process, are simple and allow for much variance in order to fine tune composition, dopant introduction, and material characteristics from precursor solutions which are then heated to evaporate solvents and thermally treated to pyrolyze precursors, leaving an inorganic film. Thus, sol-gel solutions, which require no extensive processing, were implemented using non-toxic organic solvents to deposit thin layers on glass/FTO substrates for the fabrication of photoelectrodes effectuating the MOD technique. Several layer depositions can be effectuated to increase the final film thickness. Annealing between layers ensures adhesion and evaporation of solvent while final calcination or thermal treatment allows control of crystallinity, oxygen stoichiometry, and particle size [242]. These layers are crystallized at relatively low temperatures of 350-450°C to keep the crystal sizes small for increased surface area while still maintaining good crystallization, conductivity, and limiting intra-particle recombination. Co-catalysts are deposited by electrodeposition techniques in efforts to aid the surface OER kinetics, increase overall stability, performance, and efficiency.

II.2.1. SOL-GEL

The sol-gel method coupled with the dip-coating is developed for the fabrication of our photoelectrodes. Sol-gel solutions are simple colloidal solutions prepared of mineral salts which form integrated networks due to polymeric linking in the solution to form a gel. Specifically, metal salts added to organic volatile solutions. Through a careful control of pH, water, and concentration in the sol-gel solution, hydrolysis and condensation reactions occur to form a sol that can be easily deposited by several means such as: spin coating, dip coating, drop casting, or doctor blade. Block co-polymers and organic additives such as poly(isobutylene -b- ethylene oxide) can be added to the solution to form and tune a nano/mesoporous microstructure. Upon final heat treatment to crystallize the metal (referred to as calcination) the carbon elements of the block co-polymer are pyrolyzed, leaving physical vacancies and thus forming a porous or mesoporous microstructure. Its decomposition should occur after the crystallization of the inorganic network occurs otherwise, the porous network will collapse. The size of the pore and the inorganic wall can be tuned and will depend on various parameters including the nature of the block-co-polymer (the contrast between hydrophilic/hydrophobic blocks) and the solvent chemistry.

Deposition of the sol-gel is done by dip coating because it is a low cost, low energy, facile method. Substrates are dipped into the sol-gel solution and upon withdrawal the organic volatile solvent evaporates, depositing a xero-gel thin layer on the substrate. Thickness of the thin film can be increased by consecutively dipping the substrate and thin films in the solution, employing an intermediate heat-treatment which is necessary to favor layer adhesion between each deposition. The thickness and the microstructure of the film will depend on: i) the concentration of metal salts in the sol-gel solution, ii) the withdrawal of the substrate from the sol-gel solution due to evaporation rate iii) the humidity, and iv) the successive deposition of thin layers onto substrates. One of the main challenges in sol-gel thin film fabrication is defining the heat treatment which reinforces the inorganic wall and avoids the decomposition of organic molecule. The different steps of the formation of the films are summarized in Figure 21.

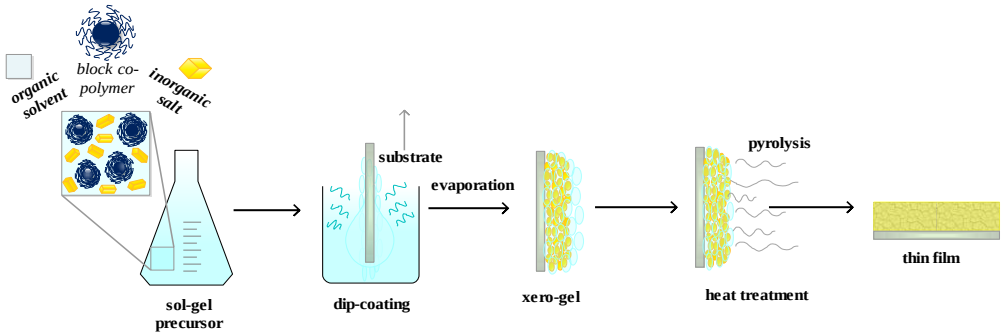

Figure 21: Sol-Gel dip coating thin film fabrication process

An example of the dip coating method is shown in Figure 22 which displays the stages of evaporation of tungsten 5+ sol-gel during dip coating withdrawal from the sol-gel precursor solution. Upon the thermal heat treatment the blue W^{5+} oxidizes in air to clear yellow W^{6+}.

Figure 22: Evaporation of tungsten sol gel onto substrate during dip coating deposition

II.2.2. ELECTRODEPOSITION

Often to ameliorate the kinetics for the OER or HER, metal-based catalysts are deposited onto the semi-conductor photoelectrodes as an amorphous thin layer or dispersed at active sites on the material's surface. This can be easily achieved by electrodeposition: a method consisting of the metal deposition onto a conductive surface by a solution of metal ions and an applied electric field. More precisely, this is effectuated by applying a current (chronopotentiometry) and monitoring the charge and/or potential measured, or alternatively by applying a voltage (chronoamperometry) and monitoring the charge and current passed. By understanding the charge or current measured during the deposition, as well as the valence number and weight of the metal deposited, Faraday's law can be applied to theoretically quantify the amount deposited. Light can be added during the electrodeposition to enforce a "photo-assisted" electrodeposition, as suggested by Nocera's group with Co-Pi [137, 243]. This concept suggests that co-catalyst deposition is received at photoactive areas of the photoelectrode, which may be more active than other surface sites of the material. This method of deposition is low cost, reproducible, and can be applied to large surface area features from the electronic field induced during deposition, thus is implemented for all co-catalyst addition in the following research as well as in previous research completed in our laboratory [244].

II.3. TUNGSTEN TRIOXIDE

II.3.1. INTRODUCTION

Tungsten trioxide was the second approach to water splitting n-photoanode materials after the photocatalytic discovery of TiO_2 for water splitting applications [245, 246]. It possesses an indirect band gap around 2.7 – 2.8 eV, can utilize 12% of the solar spectrum, and has a suitable band gap for visible light absorption to create photo-excited charge carriers in addition to its appropriately placed valence band for thermodynamic water oxidation. The valence band of WO_3 is situated near 3 V (vs. NHE) and is therefore positive enough to drive the water oxidation half reaction [215]. These physical and chemical properties enable a water splitting device with WO_3 as the n-photoanode to potentially possess an STH efficiency of 4.8% [215]. It is especially attractive due to its large incident photon to converted electron (IPCE), which enables lower overpotentials compared to iron oxide and other metal oxides [43, 247, 248]. Although the band-gap energy of WO_3 (in the monoclinic form) is larger than hematite, the photocurrent onset potential of WO_3 has shown to be lower than Fe_2O_3 for water oxidation (i.e. 0.4 V vs. RHE). This reflects the almost generally applicable rule for semiconducting oxides, whereby the decrease in band-gap is accompanied by a down-shift in the conduction band edge. This is related to the fact that the conduction band of these oxides has mainly d-band character, whereas the valence band is mainly O 2p in character [248].

Fundamentally, tungsten trioxide exists in five forms: tetragonal (α-WO_3), orthorhombic (β-WO_3), monoclinic (γ-WO_3), triclinic (δ-WO_3), and monoclinic II (ε-WO_3). Stable temperature domains of these forms occur between −43 and 740°C shown in Table 6 [215]. Hence, WO_3 generally occurs as the monoclinic phase and orthorhombic phase at room temperature and upon crystallization results in indirect semiconductors with band gaps between 2.6 – 2.8 eV for use as a water splitting photoanode [249].

Form	**Temperature domain (°C)**
tetragonal (α-WO_3)	> 740
orthorhombic (β-WO_3)	330 – 740
monoclinic (γ-WO_3)	17 – 330
triclinic (δ-WO_3)	– 43 - 17
monoclinic II (ε-WO_3)	< – 43

Table 6: Summary of tungsten trioxide crystal phases

Common synthesis of WO_3 thin films include sol-gel [178, 180, 241, 250-253] (generally deposited by dip coating, spin coating or doctor blade), hydrothermal [164-167], anodization [247, 254-258], sputtering [153, 259, 260], atomic layer deposition[139], and electrodeposition [156, 158, 215]. Thin films

fabricated by these methods result in dense, mesoporous, nanoflakes, and other various microstructures depending on synthesis conditions and substrate preparation. It is widely accepted that mesoporous and/or nanostructured WO_3 is ideal for water splitting applications due to increased electroactive surface exposure to the electrolyte [261]. Table 7 displays these state of the art WO_3 n-photoanodes in terms of photocurrent response using platinum as a counter electrode referenced to the RHE by use of a reference electrode (generally a saturated calomel or silver chloride electrode). Fabrication of WO_3 by sol-gel process is one of the most common methods due to its large scalability and low cost techniques therefore more applicable for comparison to the research concerned in this thesis. Nevertheless, it must be highlighted that anodization, hydrothermal, and sputtering techniques as well as sol-gel techniques compete with one another for WO_3 photoelectrochemical water splitting performance.

Year	**Photoanode**	**WO_3 Deposition Technique**	**Thickness (nm)**	**Electrolyte (pH)**	**P_{in} (mW/cm²)**	**j**	**Ref**
2001	FTO/WO_3	Layer by layer	2000	1 M $HClO_4$ (pH 1)	100	2.4 mA/cm²	[252, 262]
2006	W/WO3	Anodization	-	0.5 M H_2SO_4 (pH 0)	100	3.45 mA/m² (1.8V vs. RHE)	[255]
2007	ITO/WO_3	Doctor blade	2400	1 M H_2SO_4 (pH 0)	86	2.4 mA/cm²	[179, 253]
2007	FTO/WO_3	RF Magnetron Sputtering	1600	0.33 M H_3PO_4 (pH 2)	AM1.5G	2.7 mA/cm² (1.9V vs. RHE)	[153]
2008	ITO/WO_3	Doctor blade	30000	1 M $HClO_4$ (pH 1)	100	3.7 mA/cm² (1.5V vs. RHE)	[178]
2010	FTO/WO_3	Dip coating	6000	0.5 M H_2SO_4 (pH 0)	100	2.7 mA/cm² (1.4V vs. RHE)	[188]
2011	W/WO_3	Anodization	5000	1 M H_2SO_4 (pH 0)	150	3.5 mA/cm² (1.7V vs. RHE)	[257]
2011	FTO/WO_3	Drop casting	2100	1 M H_2SO_4 (pH 0)	100	3.7 mA/cm² (1.4V vs. RHE)	[182]
2011	W/WO_3	Hydrothermal	1500	0.1 M H_2SO_4 (pH 1)	-	4 mA/cm² (1.5V vs. RHE)	[166]
2012	W/WO_3	Anodization	550	1 M H_2SO_4 (pH 0)	300	3.8 mA/cm²	[247]
2012	W/WO_3	Anodization	5000	1 M H_2SO_4 (pH 0)	AM1.5	3.5 mA/cm² (1.7V vs. RHE)	[256]
2012	W/WO_3	Hydrothermal	3600	0.1 M Na_2SO_4 (pH 6)	100	2.3 mA/cm² (1.8V vs. RHE)	[165]
2013	FTO/B:WO_3	Doctor blade	1200	0.5 M NaCl (pH 2)	AM1.5	2.15 mA/cm²	[180]

Table 7: State of the art tungsten trioxide photoanodes

WO_3 suffers from stability issues arising from degradation in neutral to basic conditions and hence is generally tested in low pH conditions. The Pourbaix diagram (shown in Figure 23) for tungsten suggests stability in the anodic water splitting OER regime in acidic conditions (pH < 4). These conditions are not ideal for hydroxide intermediate formation due to the low concentration of hydroxide in solution and have been thought to favor parasitic reactions over the formation of O_2. Parasitic reactions that lead to oxidation byproducts can possibly act as a surface blocking layer, reducing the amount of available electroactive surface and eventually leading to decreased performance [58].

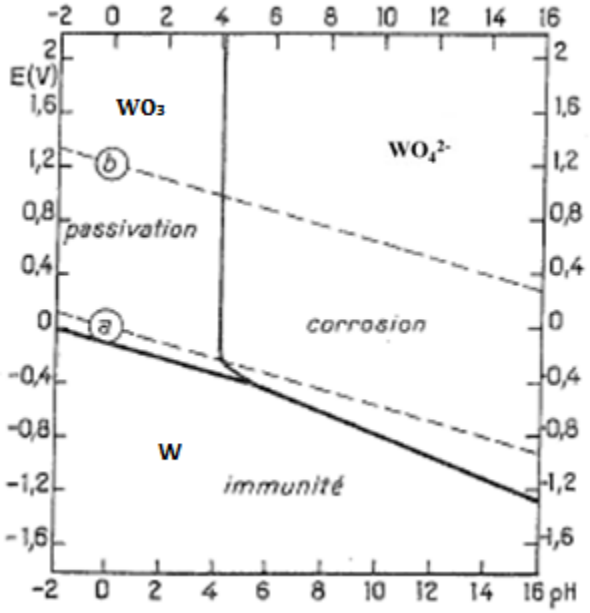

Figure 23: Pourbaix diagram of tungsten, taken from Pourbaix, 1966

WO_3 has been previously coupled with co-catalysts to increase the efficiency of the water splitting kinetics. Its valence band, which is relatively close to the H_2O/OH radical potential (seen previously in Figure 20), suggests little overpotential needed to drive the OER. Thus, addition of a co-catalyst to decrease the onset potential for the OER is unlikely. Nonetheless, several co-catalysts have been added to the surface in order to suppress peroxo formation, increase the stability in near neutral conditions, and to increase the O_2 faradaic efficiency. Cobalt in solution as well as Co-Pi have been deposited on WO_3 in order to avoid formation of peroxo species during O_2 evolution as well as stabilization in near neutral pH [261, 263]. Nonetheless, this was found to result in lower photocurrent due to interfacial states created by cobalt that shift the flat band potential and can result in increased electron-hole recombination under certain potentials [263]. Other co-catalysts such as manganese-based complexes have shown similar results, increasing the stability and preference for the formation of O_2 in near neutral conditions [139,

264]. Though many of these co-catalysts suffer from long term activity, optimization is still studied [222, 265].

Faradaic efficiencies for WO_3 vary depending on the type of electrolyte and pH. These values are rarely 100% due to the fact that parasitic reactions occur, mainly the formation of peroxo species, parasitic reactions, and dissolution or corrosion of tungsten. Several reports suggest that parasitic reactions occur from the oxidation of anions which are thermodynamically less favorable than O_2, but upon illumination the kinetics of these fast oxidation reactions predominate at the WO_3 surface [158, 159, 238]. It is suggested that neutral to basic conditions are more ideal for O_2 formation; however, WO_3 readily dissolves under these conditions. Thus, as previously stated, acidic to neutral conditions are typically imposed in sulfate or phosphate solutions ranging from pH 0 – 5 with increasing faradaic efficiencies upon increase in solution pH [238].

II.3.2. Synthesis and Characterization

WO_3 was fabricated by sol gel dip coating procedures developed within our laboratory. 4.4 mL of ethanol and 1.6 mL of THF are added together in a vial. Then 100 mg block-copolymer is added and the vial sealed and placed in an oven at 70°C for at least 45 minutes or until the polymer is dissolved. When the solution has cooled to room temperature 1 g of WCl_6 is added slowly under a fume hood to form a sol with a concentration of 0.42 M and pH of 1. Then the solution is left to spin with a magnetic stirrer at least 1 hour before use. Solution color is initially orange and changes to turquoise-blue within several minutes. Solutions employing block co-polymers are used the day of synthesis; though dense WO_3 sol precursors (without block co-polymers) are typically usable for several days. Semi-transparent thin films of WO_3 are produced by dip coating several layers of the precursor solution while thermally annealing at 350°C for 1 – 2 minutes in between layer depositions to ensure adhesion. The dip coating conditions are at room temperature with 3% relative humidity. Dip withdrawal speed measures 2.7 mm/s resulting in an average of 80 nm/layer. Finally the films are crystallized by a calcination step, varying from 400 – 550°C for 30 – 60 minutes to crystalize the xero-gel which formed on a FTO substrate from evaporation. A block-copolymer is utilized to tune a mesoporous structure due to the metal organic decomposition which occurs during calcination. The calcination step at temperatures greater than 400°C pyrolyze the carbon block-copolymers leaving voids in the material which result in a mesoporous nanostructure, increasing exposed surface to the electrolyte for increased active water splitting site to permit the OER. A total of 8 layers are deposited by dip coating resulting in WO_3 mesoporous layers of 550 – 600 nm or dense layers of 300 – 350 nm.

The thermal treatment, or calcination temperature, greatly influences the degree of crystallinity as well as the size of crystallites, the crystal structure, as well as the microstructure of a material. Since the crystallization occurs at the same time as the formation of the thin film nano/microstructure after dip coating depositions, the temperature plays a very important role. Calcination below 400°C resulted in an amorphous tungsten, verified by X-ray diffraction (XRD). Calcination treatment at 400°C for 30 – 60 minutes results in a distorted β-orthorhombic/γ-monoclinic WO_3 structure with crystal orientation preferential to the (1 0 0) plane verified by XRD and modeled from refined diffraction patterns using the orthorhombic β polymorph (Figure 24) [266, 267]. Below the XRD pattern is displayed with the associated crystal structure showing oxygen in red and tungsten in grey and blue. FTO substrate peaks are defined by a black triangle, whereas WO_3 peaks are labeled with red squares.

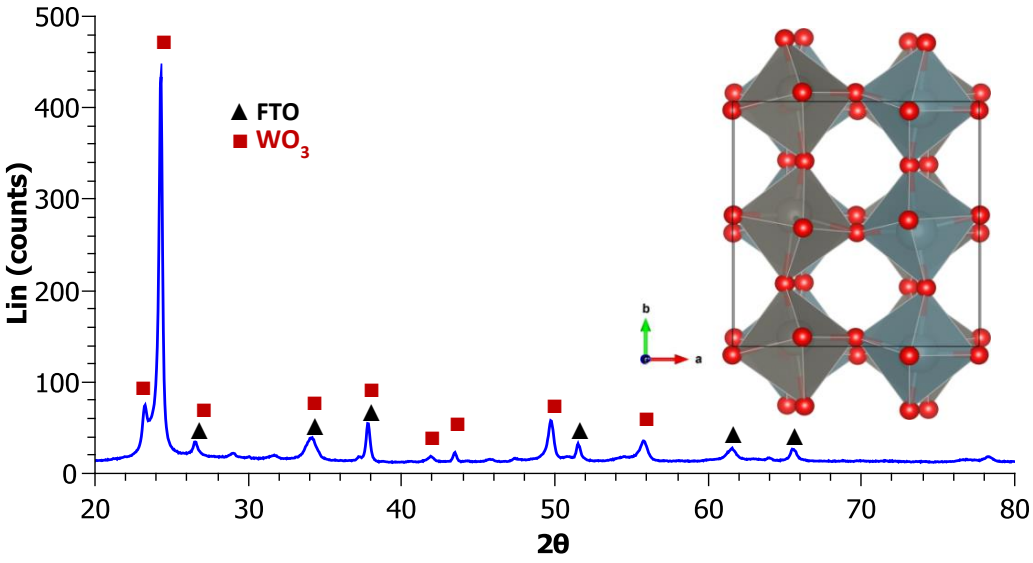

Figure 24: XRD pattern of mesoporous WO_3 and crystal structure

We applied the March's model and the March's parameter (R) has been evaluated to quantify the oriented character of the distribution of the crystallites in the layer [268]. The value attained is close to 0.5, suggesting the tungsten trioxide crystallites grow preferentially with the lattice parameter oriented normal to the sample surface. The microstructure is columnar, consisting of needle-shaped crystallites normal to their axis, and randomly oriented in the plane perpendicular to the sample surface. This simple description of the preferred orientation correction provides a very good R_{Bragg} factor (less than 3%). Although, there is a small but systematic overestimation of the calculated intensities of (2 0 2) and (2 2 0) reflections, suggesting the dimensions of the crystallites are significantly smaller than the film thickness. The average crystallite size along the a-axis for films calcinated at 400°C is roughly 50 nm whereas along the b and c-axes it is 26 nm. Lattice parameters were averaged from 5 samples based from the orthorhombic model of WO_3 to give the unit cell dimensions, the results shown in Table 8 [266].

Lattice parameters	a (Å)	b (Å)	c (Å)
WO_3	7.34	7.48	7.65

Table 8: Lattice Parameters of mesoporous WO_3

The microstructure of the films was affected by the heat treatment. Films calcined at 400°C and 500°C do not exhibit the same microstructure. The crystallite size of films treated at 400°C generally had crystallite sizes around 20 nm according to the Scherrer equation based on XRD data; while films calcinated at 500°C possessed an average crystallite size of 5 nm larger. The film calcined at 400°C exhibits a mesoporous microstructure with pores of 20 nm well-distributed onto the surface (upper left image in Figure 25). The porosity in the bulk of the film is also well distributed and connected, though more dense towards the FTO substrate due to consecutive thermal treatment (upper right in Figure 25). Modification of the pore structure is observed, accompanied with a sintering of the nanoparticle in films calcined at 500°C, which is seen in the lower left image in Figure 25. This densification seems to occur along the c-axes. Thickness of 8 layers of mesoporous WO_3 is slightly augmented by an increase in calcination temperature measuring around 550 nm and 600 nm for films calcinated at 400°C and 500°C, respectively. Thus, upon an increase of temperature or time during the calcination step, the films grew slightly larger crystal sizes and therefore a total increase in film thickness.

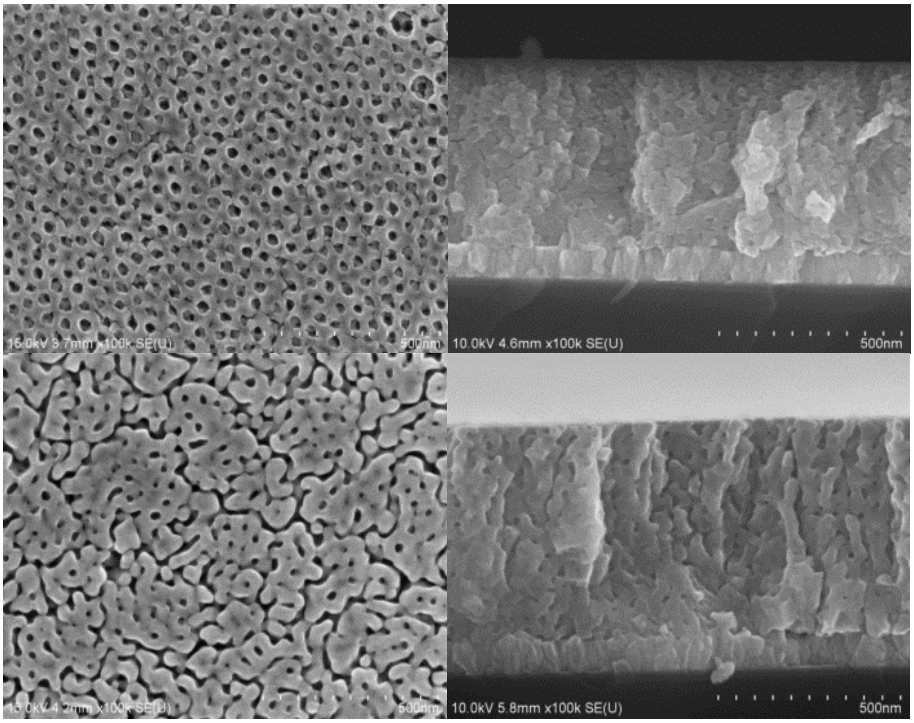

Figure 25: FEG-SEM photos of WO_3 calcinated for 30 minutes at 400°C planar (upper left), cross section (upper right), and 500°C planar (lower left) and cross section (lower right)

Further, high resolution transmission electron microscopy (TEM) was effectuated on mesoporous WO_3 to verify the pore and crystal size. This was done by scratching the thin films and dispersing the flakes in ethanol, which were then collected on a TEM grid. The pore size, like seen in FEG-SEM images measure 20 nm in diameter as seen below in the left image of Figure 26, in agreement with FEG-SEM observations.

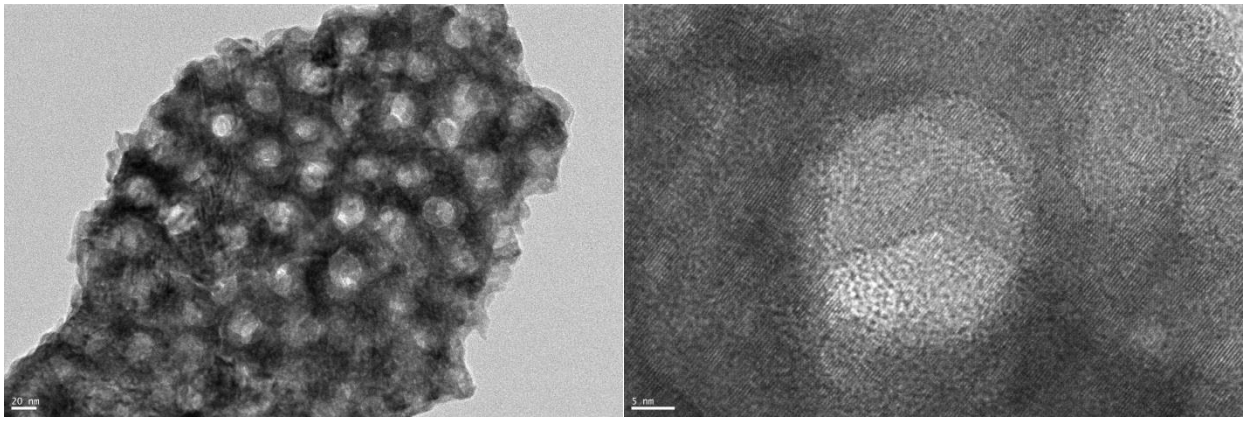

Figure 26: HR-TEM images of mesoporous WO_3 flakes calcinated at 400°C dispersed in ethanol at 50k (left) and 400k magnification (right)

X-ray photon spectroscopy (XPS) was effectuated to verify the oxidation state of tungsten as W^{6+}. The peak located at 36 eV was assigned to W 4f 7/2 and confirmed that W^{6+} was more than 98% present in the layer and that the ratio of oxygen to tungsten was effectively 3:1. This confirms a successful WO_3 composition from sol-gel dip coating techniques in agreement with literature values for other sol-gel fabricated WO_3 calcinated at 400°C [269]. The XPS spectrum of mesoporous WO_3 calcinated at 400°C for 30 minutes is shown in Figure 27 with the O 1s and W 4f peaks used to identify WO_3.

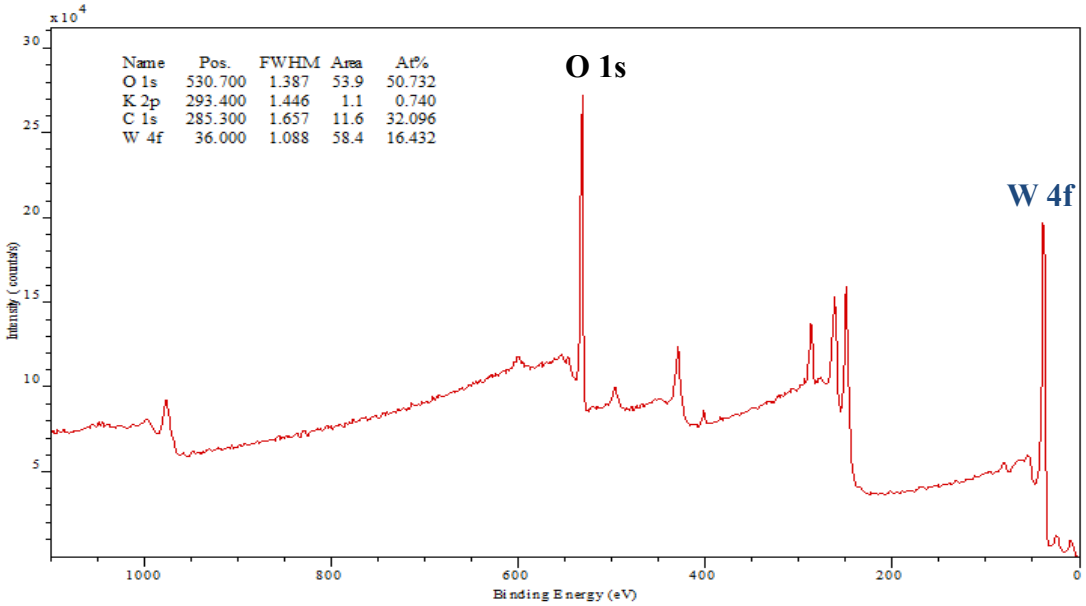

Figure 27: XPS spectrum of mesoporous WO_3 calcinated at 400°C

The band gap of WO_3 was measured from ultra-violet visible (UV-vis) near infrared spectroscopy for absorption and transmission characteristics. From the absorption edge, WO_3 is linearly extrapolated (dotted line) to possess an indirect band gap of near 2.89 eV which is displayed below in Figure 28, with the absorption in black, transmission in blue, and the associated insert Tauc plot of WO_3.

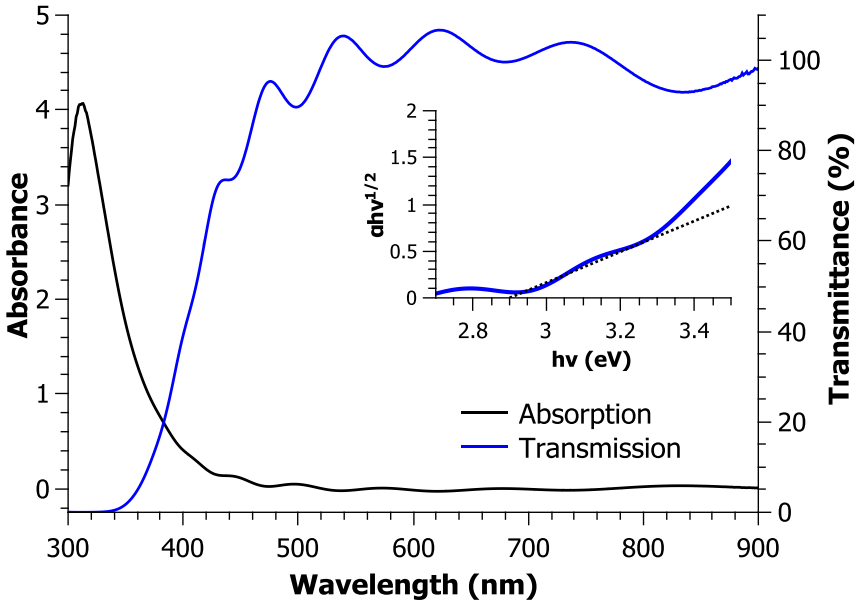

Figure 28: Absorption and Transmission Spectra of mesoporous WO_3 calcinated at 400°C with interposed Tauc plot

The absorption edge of WO_3 occurs around 400 nm confirming a large band gap. The indirect band gap of sol gel processed WO_3 was calculated from equation (16) using absorption and transmission data (shown in Figure 28) to be 2.89 eV and in agreement with the varying 2.6 – 3 eV values in literature reports [270, 271]. Fringes due to the light refraction between layers and pores in the WO_3 layersor polarons in the visible and near-infrared portion of the transmittance spectrum [260, 272]. The layer is relatively transparent until around 460 nm at which the material starts to absorb light with higher energies. This is ideal for integration in a tandem dual photosystem with the n-photoanode placed in front of the p-photocathode aiming to recover the visible and near infrared light unabsorbed by WO_3. Applied to the AM1.5G irradiation spectra, the absorption and transmission of the n-photoanode suggest that the maximum photocurrent achieved by 550 nm of mesoporous tungsten trioxide calcinated at 400°C for 30 minutes by sol-gel process is 2.13 mA/cm² in lieu of the maximum theoretical photocurrent density of 3.88 mA/cm² for a material with a band gap of 2.89 eV. Optical losses (referenced to the AM1.5G spectrum in Figure 29) therefore suggest that 55% of the theoretical photocurrent can be achieved with the fabricated mesoporous WO_3 photoanodes.

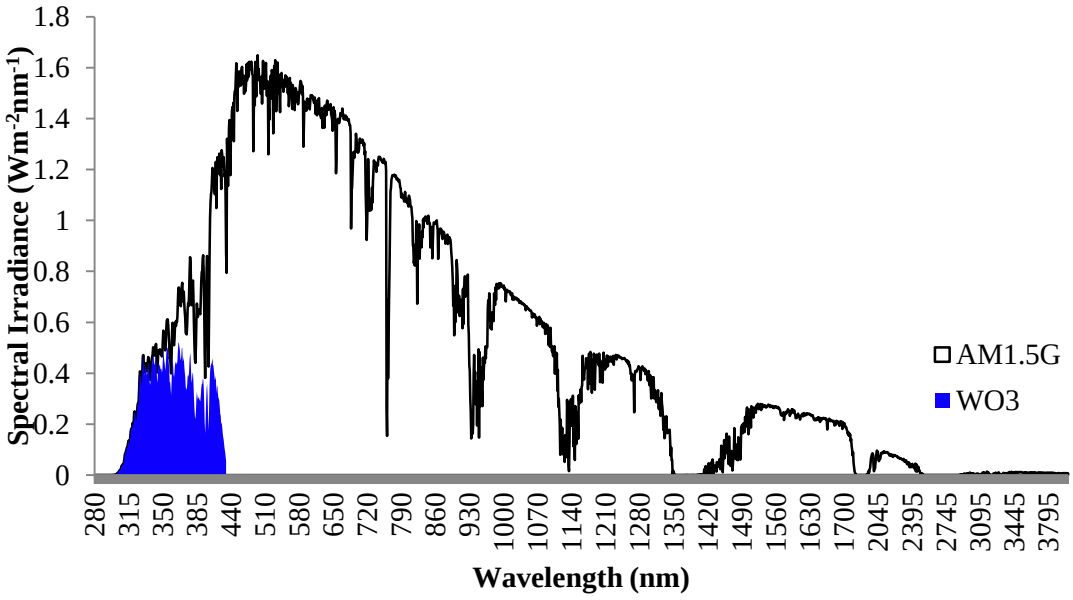

Figure 29: Empirical AM1.5 absorbance of mesoporous WO_3 photoanode calcinated at 400°C

II.3.3. ELECTROCHEMICAL CHARACTERIZATION

II.3.3.1. PRELIMINARY TEST

First, the photoelectrochemical performance of WO_3 was tested with three different types of FTO of varying conductivity (7, 15, and 100 Ω) as well as ITO. Simple photocurrent measurements revealed that

the Asahi FTO of 100 Ω *revealed the highest photocurrents and thus is used as the TCO substrate.* WO_3 *did not crystallize in the same fashion on ITO as it did on FTO; and no significant photoactivity was seen in photoelectrochemical performance and was ruled out as a potential substrate for practical reasons.*

To evaluate the photoelectrochemical performances, linear voltage sweeps using a potentiostat are measured in the anodic region for WO_3 in the dark as well as under illumination. These measurements under 300 mW/cm² illumination by a 400 – 900 nm xenon lamp resulted in photocurrents in 1 M H_2SO_4 and 1 M potassium phosphate (KPi) electrolyte (displayed in Figure 30). These measurements were completed using a 3-electrode photoelectrochemical setup; employing platinum as a counter electrode and silver chloride (Ag/AgCl KCl saturated) as a reference electrode. The FTO/WO_3 thin film was engaged as the working electrode and a linear voltage sweep with a step of 10 mV/s reveals the current diode response in the dark as well as the photodiode, or photocurrent, response upon illumination. An active area is defined by use of electrochemical scotch tape mask, exposing 0.2 cm² of the material to both the electrolyte and illumination. The dark current is largely negligible (< 10 μA/cm²) except for a first peak which is apparent in acidic conditions most likely arising from the formation of H_xWO_3 surface species occurring at 0.29 V vs. RHE, and less evident in neutral conditions [159]. Water oxidation in the absence of light begins to occur at 2.2 V vs. RHE; however, under visible light irradiation the onset potential is typically 0.6 V vs. RHE seen in Figure 30.

Initial efforts in material optimization and electrochemical characterization consist in studying the impact of microstructure onto the photoactivity of WO_3 photoelectrodes. This was done by testing 8 dip coated layers (roughly 500 – 600 nm) of WO_3 deposited on FTO with thermal treatments varying between 300 – 550° for either 30 minutes or 60 minutes, as heat-treatment (temperature and time) impact the microstructure of WO_3 films. Films calcined at 400°C exhibited the best photocurrent in 1 M H_2SO_4 as well as 1M KPi. Above 450°C, the electrochemical performance of the films slightly decreased (indicated by the 500°C-treated WO_3 black curve in Figure 30). Visually, the films treated at 500°C started to become optically opaque, diffusing light, which is not desirable for the implementation of a dual photosystem in tandem. There was little to no difference in performance between samples calcinated 30 minutes and 60 minutes; thus optimal WO_3 thin film thermal treatment conditions were considered to be 400°C for 30 minutes, in agreement with other literature for WO_3 in terms of stability and performance [249, 258].

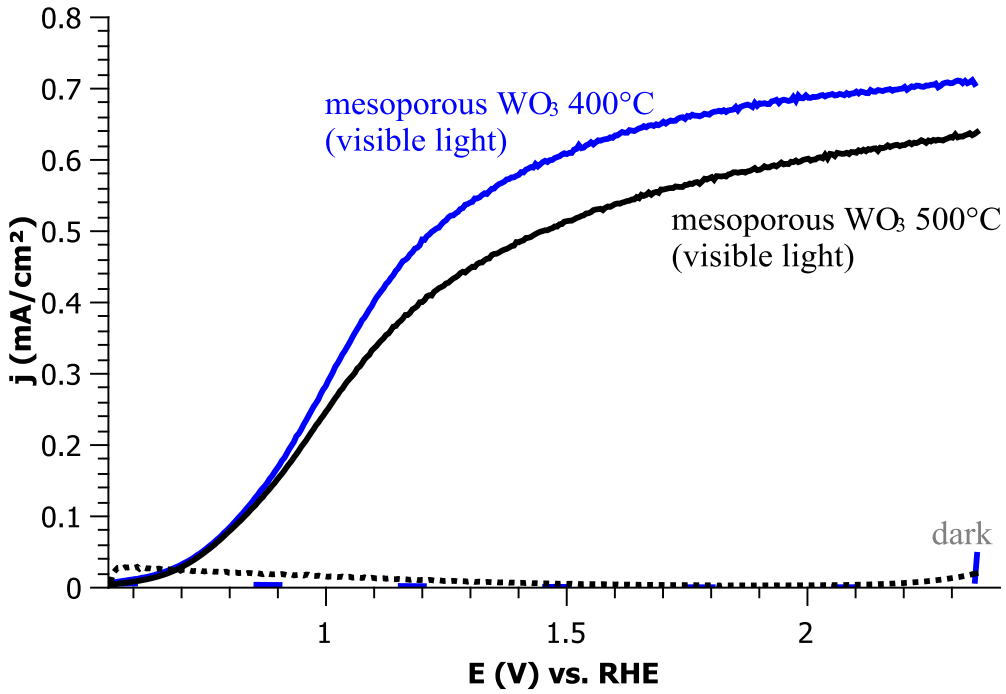

Figure 30: Photocurrent density of mesoporous 500°C heat-treated WO_3 (blue) and 400°C heat-treated WO_3 (black) under 300 mW/cm² visible (400-900 nm) light in 1 M KPi (pH 6)

To further understand the impact of the nanostructure on the photoactivity, the performance of 8 layers calcinated at 400°C of both mesoporous and dense WO_3 were electrochemically compared for their photoelectrochemical performance. Figure 31 displays the linear voltage sweep photoresponse of mesoporous (blue) and dense (black) WO_3 and associated FEG-SEM images to the right (mesoporous located at the top right and dense bottom right). It appears that mesoporous WO_3 has a larger photocurrent than dense WO_3 for water splitting applications as shown below by the linear voltage sweep curves. The photoelectrochemical performance under visible light (400 – 900 nm) with a nominal irradiation power of 300 mw/cm² in 1M KPi (pH 6) exhibits a photocurrent of 0.412 mA/cm² for mesoporous WO_3 and only 0.162 mA/cm² for dense WO_3 at 1.23 V vs. RHE; confirming that mesoporous nanostructuration is beneficial for increased PEC performance [250, 261].

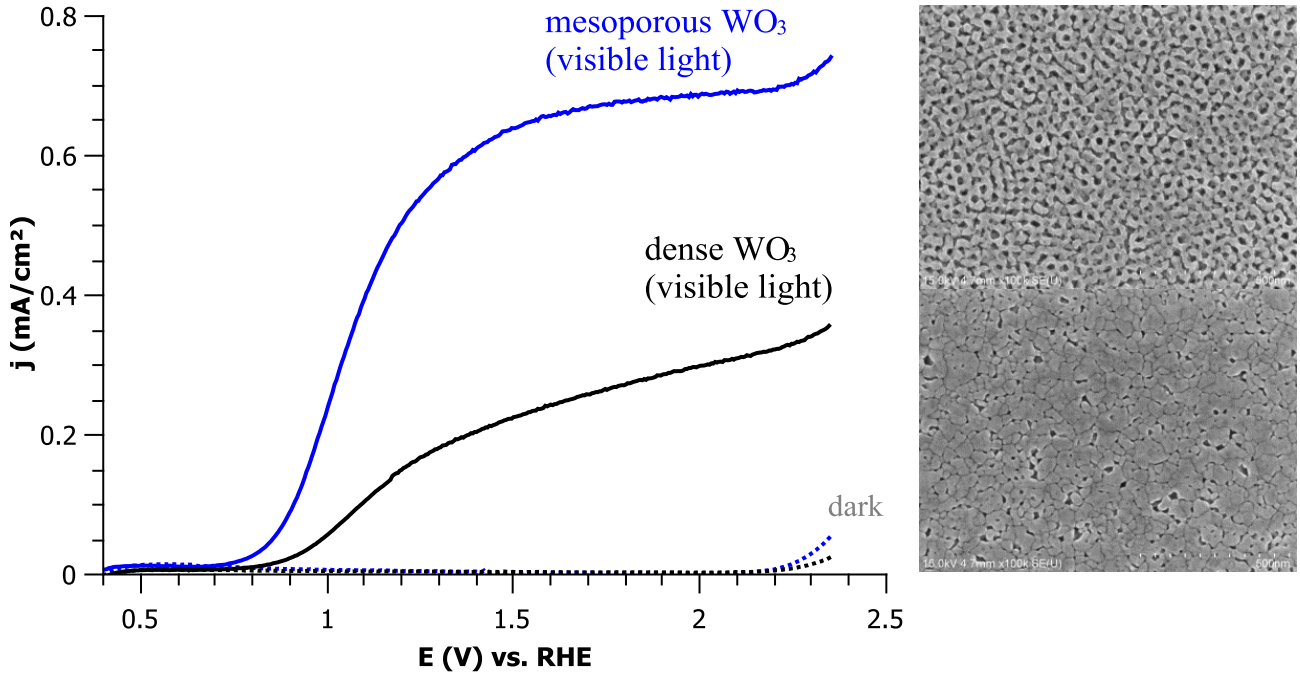

Figure 31: Photocurrent density of mesoporous WO_3 (blue) and dense WO_3 (black) under 300 mW/cm² visible (400 – 900 nm) light in 1 M KPi (pH 6) with corresponding FEG-SEM images: mesoporous (top) and dense (bottom)

II.3.4. Photoelectrochemical Performance and Stability

II.3.4.1. Photoelectrochemical Performance

Water oxidation without illumination begins to occur at 2.2 V vs. RHE; however, under 300 mW/cm² irradiation by a xenon lamp exhibiting 400 – 900 nm light, the onset potential is typically 0.6 V vs. RHE seen in Figure 32. Electrochemical impedance measurements were completed in order to determine the flat band position of WO_3 which was extrapolated to be near 0.37 V vs. RHE as seen in Figure 33. This suggests that a required overpotential of at least 0.23 V is needed to drive the OER, though addition of a co-catalyst could potentially ease the surface kinetics to account for this overpotential. The density of states (N_D) was calculated to be 4.11×10^{21}, (using $\varepsilon = 50$) [273]. This value falls within the range of values of 10^{20} – 10^{23} reported in literature for WO_3 water splitting photoanodes [178, 188, 247]. Using the flat band position and the OER potential, the open circuit voltage (V_{oc}) is considered to be around 0.6 V vs. RHE in 1 M H_2SO_4, which logically correlates with band positions and overpotential exhibited.

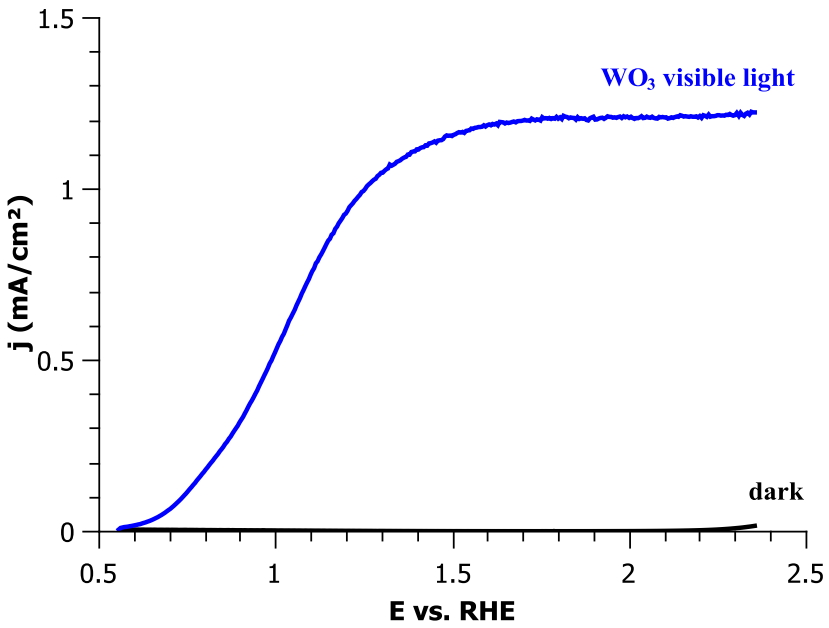

Figure 32: Dark and light linear voltage sweep of WO_3 in 1 M KPi (pH 6) under 300 mW/cm² visible light (400 – 900 nm) illumination

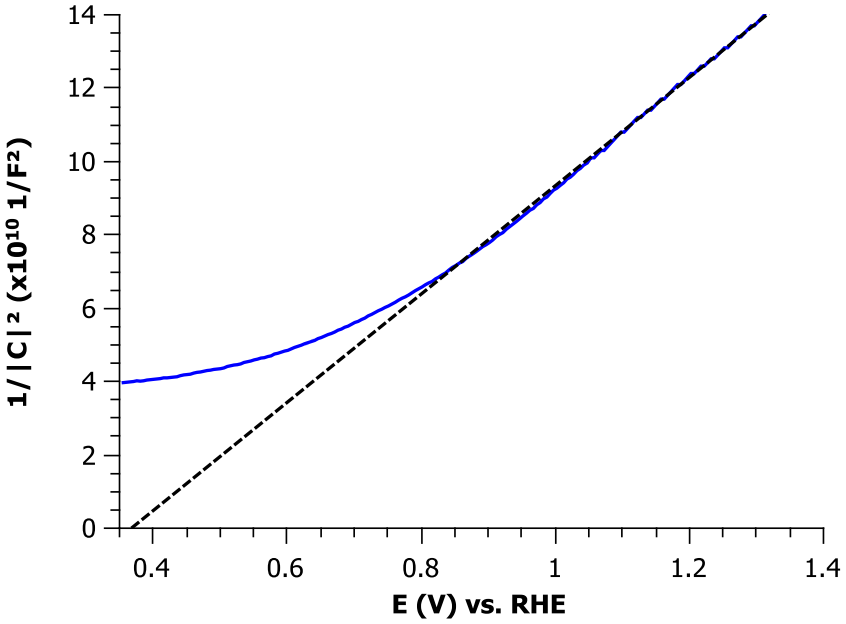

Figure 33: Mott Schottky plot of WO_3 in 1 M KPi (pH 6) 10 mV amplitude at 500 Hz

The large bandgap of 2.89 eV suggests that WO_3 absorbs light mostly in the ultraviolet portion of the solar spectrum, which was confirmed with the increase of photocurrent upon removal of the UV filter (which blocks all wavelengths below 400 nm). The photocurrent at 1.23 V vs. RHE increased from 0.53 mA/cm²

to 6.75 mA/cm² upon addition of UV light with saturation photocurrents occurring around 1.5 V vs. RHE of 0.65 mA/cm² for visible light and 8.5 mA/cm² upon ultraviolet light addition under 300 mW/cm² and 350 mW/cm² irradiation respectfully. The corresponding photodiode curves are shown below in Figure 34 of WO_3 under visible light irradiation (blue) as well as ultraviolet and visible light (dark blue).

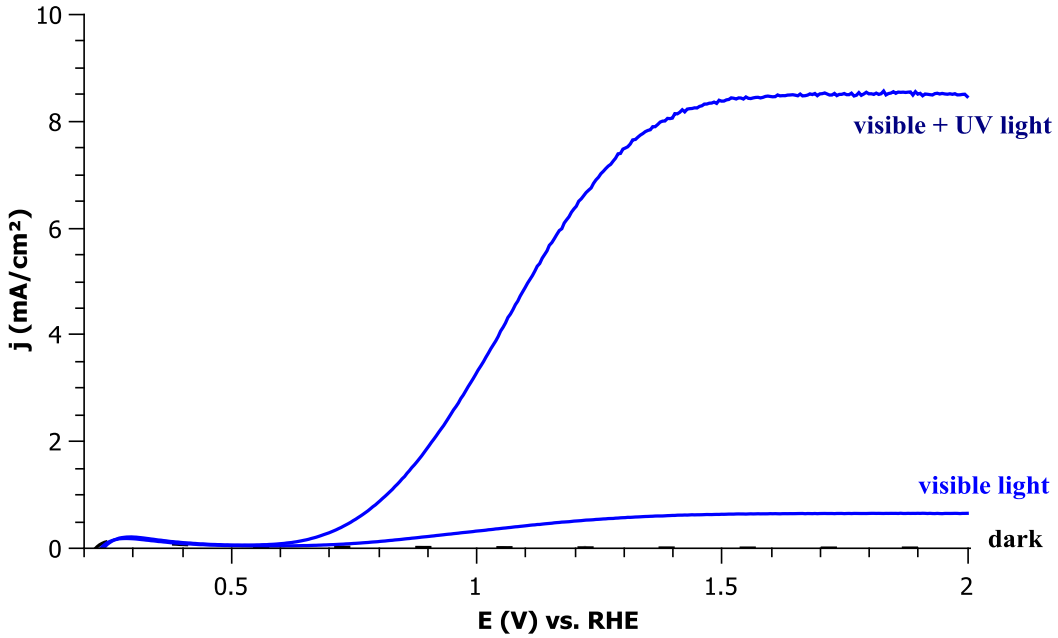

Figure 34: Photocurrent of WO_3 under 300 mW/cm² visible (400 – 900 nm) wavelength and upon addition of ultraviolet light in 1M H_2SO_4 (pH 0)

Backside illumination was found to be slightly more performant, thus samples were irradiated with the light passing through the glass and FTO before being absorbed by WO_3. Fortuitously, backside illumination is preferential for the configuration of tandem dual photosystems, having the two photoelectrodes face each other to implement the shortest ionic path length to complete the circuit. The hole diffusion length in WO_3 has been proposed to be around 150 nm: nevertheless, WO_3 is an indirect semiconductor and accordingly demands thicker films for optimum light absorption which can limit the collection of minority carriers for the OER due to the relative distance holes must travel before they recombine [215, 218]. Therefore, nanostructuration of WO_3 may be an important feature aiding in the collection of minority carriers for use of the OER at the surface.

Na_2SO_3, a sacrificial reagent which can donate electrons and requires only half the holes as the OER to oxidize the anion in solution, was added to the electrolyte solution in order to alleviate surface kinetics of WO_3. Addition of sacrificial reagents, which interact with the thin film in place of water, allow further understanding of material electrochemical behaviors at the SCLJ which potentially give insight to the

photoelectrocatalytic performance and the slow extraction of holes at the SCLJ. This method enables the calculation of the separation efficiency in the material as well as the catalytic surface efficiency as described by Dotan, et al. [274]. By using the previously calculated experimental photocurrent for WO_3 (3.88 mA/cm²) assuming no optical losses, 100% IPCE, and based on AM1.5 illumination; the empirical WO_3 absorption spectrum was applied. These calculations suggest that sol-gel dip coated WO_3 mesoporous thin films of 550 nm can achieve a photocurrent of 2.13 mA/cm² (defined as j_{abs}) or 55% of the theoretical maximum based on optical absorption. To confirm the actual photoelectrochemical performance relative to this empirically theorized photocurrent, an AM1.5 filter was employed with the xenon light source to measure the photocurrent at AM1.5G standards measuring 100 mW/cm² with and without the sacrificial reagent (1 M Na_2SO_3) added to 1 M H_2SO_4. The pH change due to the addition of Na_2SO_3 was taken into account using the Nernstian relation (0.059 × pH) described in equation (11). Equations (36) and (37) describe the efficiencies of charge separation and surface catalysis efficiency of WO_3 relevant to the water splitting photocurrent (j_{H2O}):

$$j_{H_2O} = j_{abs} \cdot \eta_{separation} \cdot \eta_{catalysis} \tag{36}$$

Addition of a sacrificial reagent (H_2O_2 or Na_2SO_3) assumes that the surface catalysis efficiency is 100% and correspondingly the photocurrent with the hole scavenger (j_{h+}) becomes:

$$j_{h^+} = j_{abs} \cdot \eta_{separation} \tag{37}$$

The photocurrent of WO_3 under AM1.5G irradiation with and without a hole scavenger at the water splitting potential is shown in Table 9. This suggests that WO_3, at water splitting potentials, possesses a separation efficiency of 18% and a surface catalysis efficiency of 85%. The separation efficiency trend in Figure 35 displays a dip between 0.6 – 0.8 V vs. RHE, though this is thought to be due to the linear voltage sweep artifact due to accumulation of protons at the surface and therefore not attributed to photocurrent activity. It is therefore, a bit misleading to the behavior of bulk separation of WO_3 working at lower potentials. The separation efficiency in the bulk remains low, suggesting that the majority of minority carriers recombine before reaching the SCLJ.

j (mA/cm²) at 1.23V vs. RHE	WO_3	
	dark	light j_{H2O}
	0,048	0,341
with 1 M Na_2SO_3	dark (h+)	light (h+) j_{h^+}
	0,049	0,398

Table 9: Photocurrent density of WO_3 under AM1.5G illumination with and without a hole scavenger

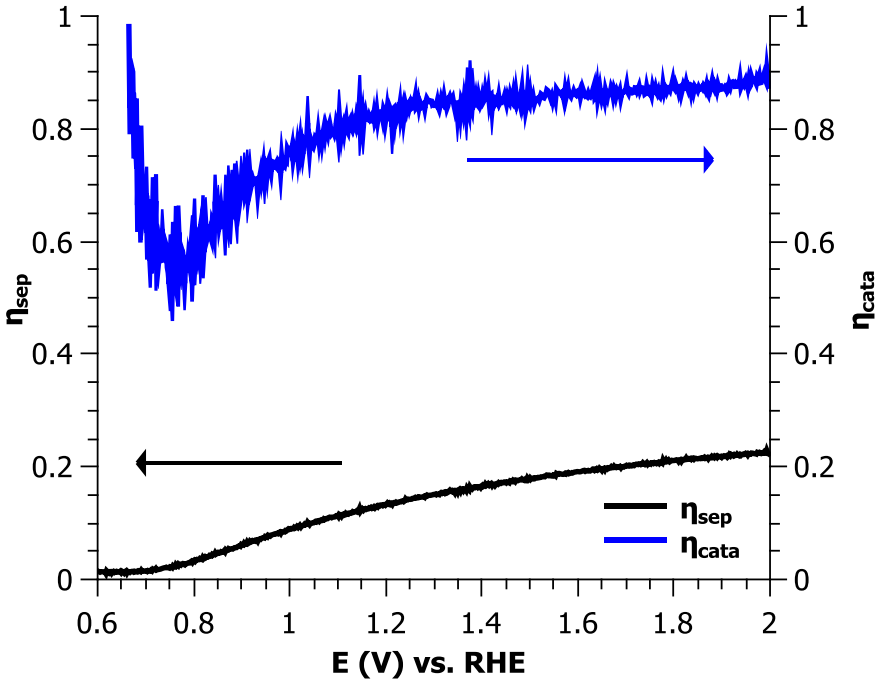

Figure 35: Separation and catalysis efficiency of WO_3 in 1 M H_2SO_4 under AM1.5 conditions

Upon variation of the light intensity, the photocurrent of WO_3 exhibits a linear trend in Figure 36, suggesting that charge carrier generation is undeniably the limiting step in efficiency towards the OER [275]. Applying a shutter at 5 second intervals to test the transient photocurrent with an illumination of 100 mW/cm² of WO_3 in 1 M KPi (pH 6) at 1.23 V vs. RHE, the light response showed no signs of anodic nor cathodic transient current (reflective of square signals in Figure 37) and showed similar phototransient response in pH 0 – 6, suggesting the SCLJ can cope with the charge carriers created upon instantaneous illumination and be successfully extracted to the electrolyte for use [276]. The addition of UV light (blue line in Figure 37) displays a large photocurrent density increase when compared to visible light irradiation (black line in Figure 37), suggesting an augmentation in performance upon illumination with higher energy wavelengths. From these results, further investigation is needed to define the performance

limitations within bulk WO_3 seeing as surface recombination is not a large factor limiting overall efficiency for these WO_3 photoanodes [277].

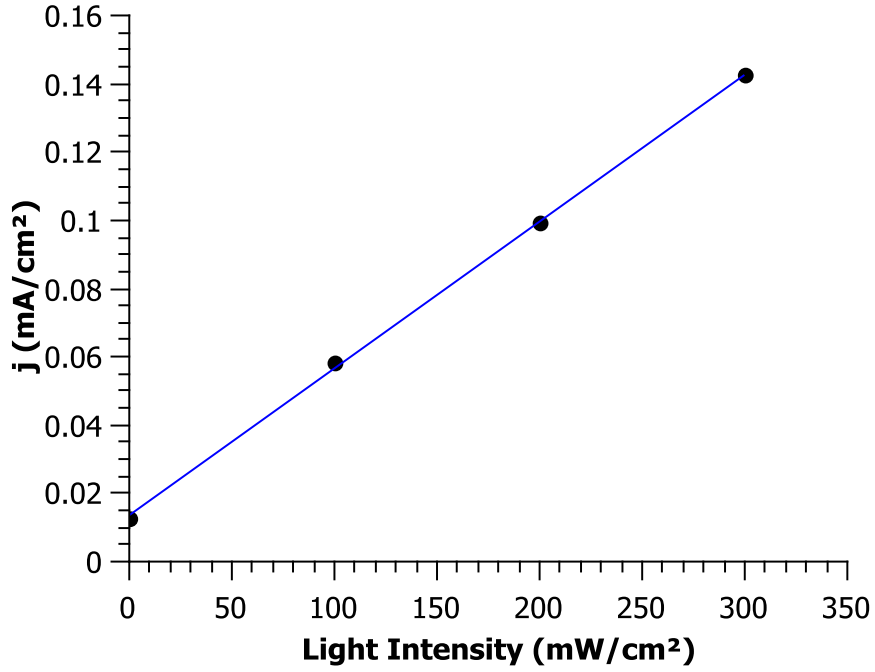

Figure 36: Photocurrent of WO_3 at 1.23 V vs. RHE at varying light intensities in 1 M KPi (pH 6)

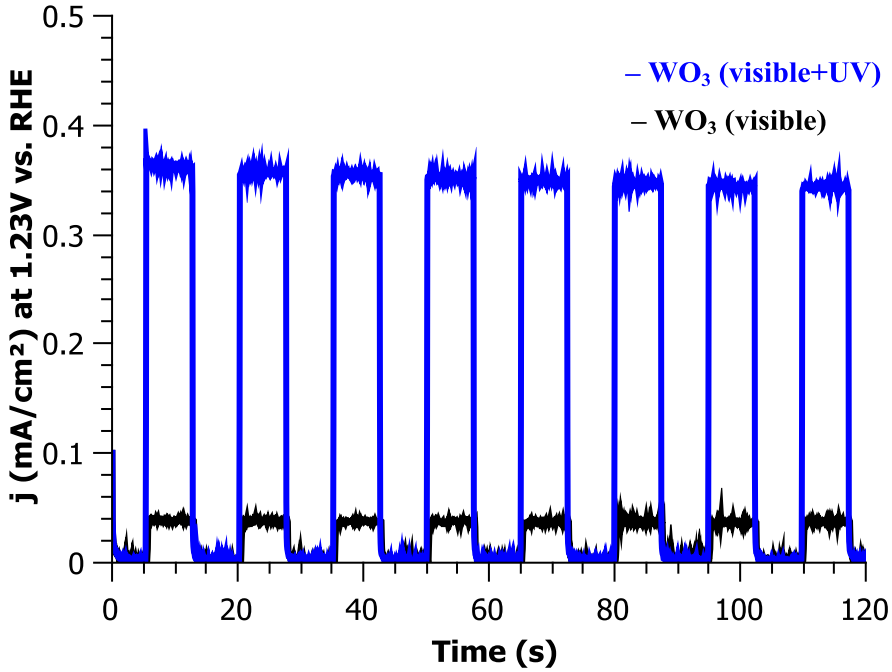

Figure 37: Photocurrent transient measurements of WO_3 at 1.23 V vs. RHE under 100 mW/cm² in 1 M KPi (pH 6) with (blue) and without (black) addition of UV light at intervals

II.3.4.2. Quantum Efficiency

To accurately quantify the number of electrons per photon usable for the OER, the incident to current photon efficiency (IPCE) was measured in 1 M H_2SO_4 between 300 – 600 nm under 300 mW/cm² light (Figure 38). 8 layer dip coated depositions of each dense WO_3 (300 nm) and mesoporous WO_3 (550 nm) were compared. The dense layer displayed a maximum IPCE at 320 nm of 57.7%, whereas the mesoporous measured 93.6% at this wavelength and showed a maximum IPCE of 95.3% at 310 nm. This confirms that nanostructuration of this material promotes minority carrier collection for use towards the OER [278-280].

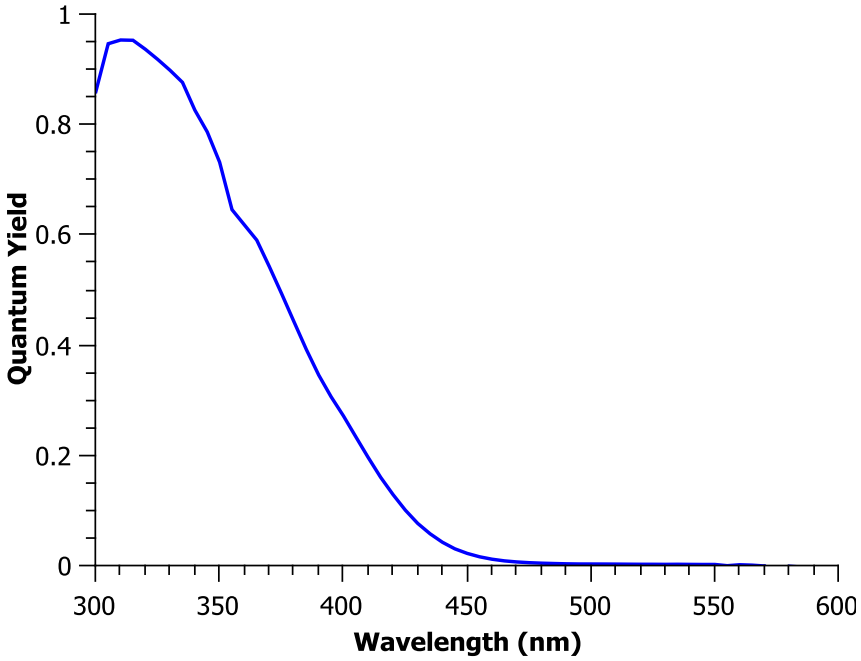

Figure 38: IPCE of dense and mesoporous WO_3 at 1.23 V vs. RHE in 1 M H_2SO_4

To further study the charge carrier dynamics of WO_3, time resolved microwave spectroscopy (TRMC) was performed on mesoporous and dense thin films of WO_3. Again, similar films as in the IPCE tests were deposited onto quartz and the films were placed under microwaves and excited with nanosecond laser pulses, emitting signals from reflected microwave power which are then detected. The change in microwave power gives insight to charge carrier dynamics within the thin films. The IPCE findings correlate with the TRMC results in that mesoporous WO_3 demonstrates longer diffusion lengths. Nevertheless, mesoporous WO_3 suffers from shorter carrier lifetimes, perhaps due to the discontinued crystal network related to the mesoporous nanostructuration. However, the diffusion length remains longer for mesoporous films than for dense films, most likely due to the difference in thickness of the samples. The two values shown for carrier lifetime (τ (ns)) and diffusion length (L_D (nm)) in Table 10 relate to the fit of the transient by a two-exponential decay curve; in example, some of the photogenerated carriers

recombine quickly while others are longer-lived. These TRMC results comparing dense and mesoporous WO_3 are presented below in Table 10. Though IPCE values are large at higher energy wavelengths, the IPCE is still quite low for near visible light. This could suggest that the diffusion length is much shorter than the light penetration depth and therefore most charge carriers are likely to recombine before they reach the interface. This is confirmed by the diffusion lengths of both dense and mesoporous WO_3 which are shorter than the overall thin film thickness.

WO_3 film type	**$\phi\Sigma\mu$ ($10^{-3}cm^2/(V\cdot s)$) at $5.9x10^{12}$ photons/cm^2/pulse**	**$\phi\Sigma\mu$ ($10^{-3}cm^2/(V\cdot s)$) at 10^9 photons/cm^2/pulse (extrapolated)**	**τ (ns)**		**L_D (nm)**	
			τ_1	**τ_2**	**L_{D1}**	**L_{D2}**
Dense ≈ 300 nm	7.8	9	91	455	46	103
mesoporous ≈ 550 nm	12.2	15	72	428	53	129

Table 10: TRMC results of dense and mesoporous WO_3

The resulting microwave conductance is given by the product of the absorbance-normalized quantum yield (ϕ) and the combined mobility of the charge carriers in the system ($\Sigma\mu$). The minimum mobility of the carriers can be obtained from the peak of the measured signal (maximum $\phi\Sigma\mu$), and the lifetime of the carriers can be taken from the decay of the signal [281]. The calculation of the diffusion length is possible by the relation: $L_D = \sqrt{D\tau}$. τ_1 and τ_2 result from short and long lived charge carriers in the material.

II.3.4.3. pH Stability

The stability of WO_3 was measured over time in different pH conditions in the dark and under illumination to verify the Pourbaix diagram (Figure 23) concerning the possible corrosion and durability of tungsten in anodic OER conditions in 1M potassium phosphate buffers of pH 2, 4, and 6. After 1 hour of electrochemical characterization at 1.5 V vs. RHE under 300 mW/cm² with UV and visible light there was a significant decrease in the photocurrent of WO_3 in all three varying pH regimes, most notably in pH 6. This confirms the Pourbaix diagram in which WO_3 corrodes to WO_4^{2-} in anodic neutral to basic conditions resulting in soluble tungsten species in pH > 4. The decrease in photocurrent over time for WO_3 in acidic conditions is potentially due to blocking of the surface by phosphate groups or even oxygen bridging peroxo species [238, 263]. It even may be the oxidation of phosphate anions to peroxydiphosphate [158]. Figure 39 displays this photocurrent during 1 hour under 350mW/cm² visible

and ultraviolet illumination at 1.5 V vs. RHE for stability testing in pH 2 (purple), pH 4 (blue), and pH 6 (black) 1 M potassium phosphate solutions.

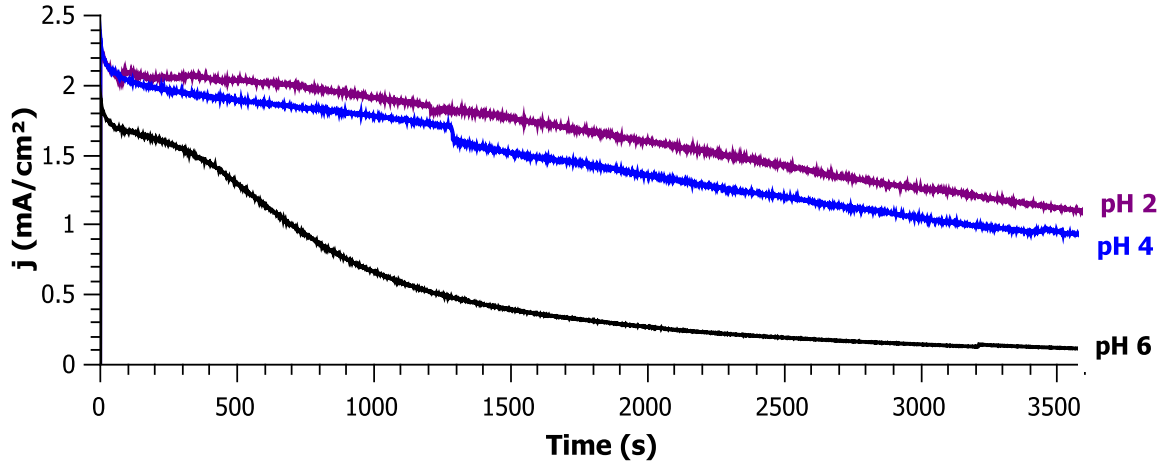

Figure 39: Photocurrent density of WO_3 at 1.5 V vs. RHE under 350 mW/cm² in varying potassium phosphate buffers

FEG-SEM images (displayed in Figure 40) were recorded before and after testing to verify the corrosion of WO_3. Visual degradation is evident for thin film of WO_3 in pH 6, confirming the corrosion of tungsten in anodic conditions. However, the microstructure seems to stay intact during 1 hour of operation in pH 2 and pH 4 with little to no degradation, confirming WO_3 is photoelectrochemically stable in strongly acidic anodic conditions for the OER.

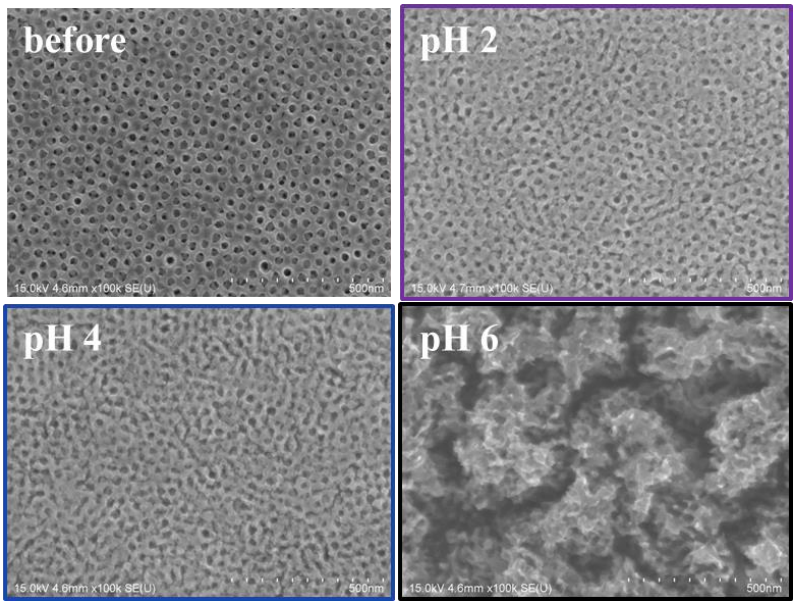

Figure 40: FEG-SEM images of WO_3 before (top left) and after 1 hour of stability testing under 300 mW/cm² irradiation at 1.5 V vs. RHE in varying potassium phosphate buffers pH 2 (top right), pH 4 (bottom left), and pH 6 (bottom right)

II.3.4.4. Faradaic efficiency

The faradaic efficiency of WO_3 was measured initially using only a gas chromatograph (GC) and a thermal conductivity detector (TCD); unfortunately these measurements revealed averages of 2 – 10% average faradaic efficiencies. According to literature for OER materials, the solubility of oxygen in solution often enables it to remain within the solution and thus fluorescent detectors or Clark electrodes are often used to quantify O_2 produced from photoanodes [238, 263]. Therefore, a Clark electrode for oxygen detection was introduced into the solution to account for the quantification of O_2 as it was found that 97% of the oxygen produced stays in the 1 M potassium phosphate buffer solutions. The faradaic efficiency detected by a Clark electrode of each WO_3 in pH 2, 4, and 6 (illuminated and at 40°C) are displayed below in Figure 41 with corresponding photocurrent in Figure 39. In accordance with OER kinetic preference in higher pH conditions, the faradaic efficiency is larger in neutral to basic pH and lower in more acidic conditions [238]. The increase of the faradaic efficiency of WO_3 in pH 4 around 1200 seconds may be due to a sudden liberation of O_2 which clings to the surface of the mesoporous photoanode, a common problem in electrolysis.

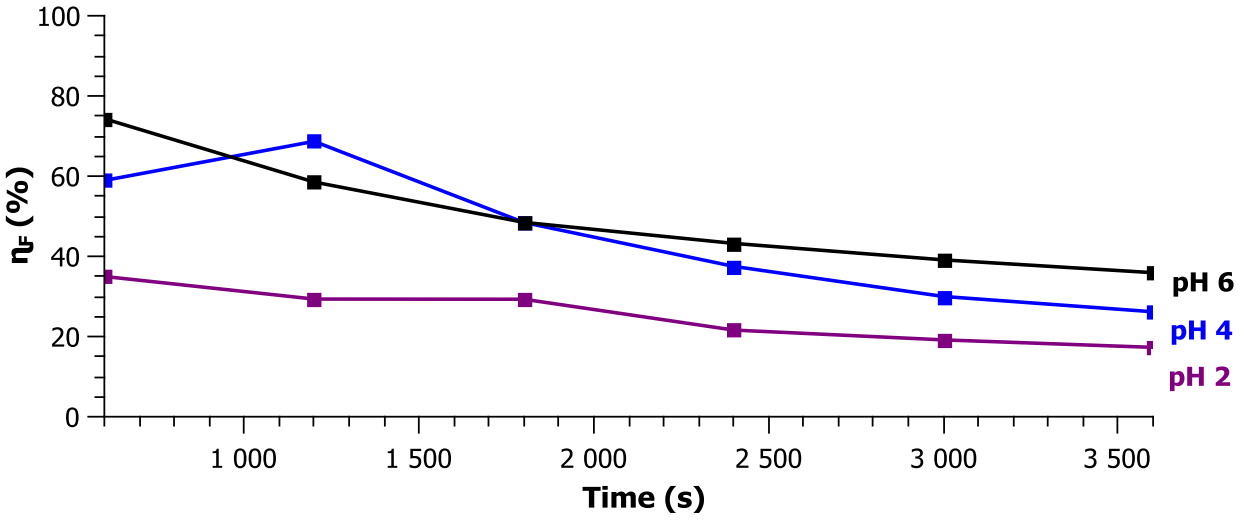

Figure 41: Faradaic efficiency of WO_3 in varying pH detected by Clark electrode at 1.5 V vs. RHE under 350 mW/cm² illumination

In pH 2, 4, and 6 the average faradaic efficiency for WO_3 in potassium phosphate is 25%, 45%, and 50% (seen by purple, blue, and black curves in Figure 41 respectively). This is an underestimation considering only a Clark electrode was used for O_2 detection (considering the soluble O_2 and poor detection limit of GC in N_2 carrier gas) and that no gas from the headspace of the cell was taken into account by GC measurements. Follow up measurements with a GC and Clark electrode coupled to detect oxygen revealed faradaic efficiencies of 66%, 47%, and 74% in 1 M phosphate buffers of pH 2, 4, and 6 respectively. The low faradaic efficiency of pH 4 may be due to poor sample preparation and thus considered and outlier. Nevertheless, the trend of O_2 faradaic efficiency in pH 6 being the largest agrees with literature values in corresponding pH conditions and preference towards OER kinetics in neutral to basic conditions [238]. pH changes in solution suggest peroxo species are present, leading to faradaic efficiencies of less than 100%, a known parasitic reaction for WO_3 [180, 238, 261, 263, 282]. The formation of OH intermediates is a known obstacle in increasing the faradaic efficiencies of WO_3 in acidic to neutral conditions [238, 283].

Unfortunately, as depicted in Figure 40, the corrosion of WO_3 occurs at pH $\geq$ 6 and therefore it is not thermodynamically suitable for the OER preferred kinetics in neutral to basic conditions. This was verified by leaving WO_3 in 1 M KPi for 19 days, after which no WO_3 remained on the FTO substrate, suggesting corrosion occurs without illumination or applied bias. Thus, in attempts to maintain the stability in neutral conditions and potentially lower the onset potential of WO_3, several co-catalysts were deposited on the surface in attempts to prevent corrosion in neutral conditions and to appeal to the OER kinetics in place of parasitic reactions.

II.3.4.5. Co-catalyst Addition

First attempts at oxygen evolution co-catalyst (OEC) deposition were conducted with ruthenium oxide and iridium oxide for use in acidic medium. Ruthenium oxide nanoparticles failed to deposit on the surface of WO_3 by wet impregnation and electroflocculation. Iridium oxide nanoparticles of 1 nm were synthesized (protocol [284]); these nanoparticles failed to deposit on the surface by wet impregnation but were successfully deposited by electroflocculation, revealing a dense layer of IrO_X measuring 25 – 75 nm in thickness. There was no cathodic shift in onset potential and the photocurrent did not increase due to this addition of IrO_X. Stability, upon addition of IrO_X, was not drastically increased for WO_3 in near neutral pH 6 potassium phosphate solutions, though slowed corrosion of WO_3. WO_3/IrO_X, like bare WO_3, exhibited a 75 -90% loss in photocurrent over an hour in 1 M KPi (pH 6) with faradaic efficiencies less than that of bare WO_3.

The well-known cobalt phosphate OER co-catalyst of Nocera's group was deposited onto the mesoporous WO_3 surface by photo-assisted electrodeposition [226]. Photo-assisted electrodeposition was done in a solution of 0.5 mM $Co(NO_3)_2$ in 0.1 M KPi (pH 6) at 0.9 V vs. Ag/AgCl (KCl sat'd) reference for 1, 5, or 10 minutes under 300 mW/cm² illumination with a xenon lamp 280 W with 400 nm UV filter with Pt grill counter electrode (2 cm² active area exposed to catalyst deposition – back illuminated). Samples were rinsed with deionized water and dried with compressed air after deposition. 5 minute depositions were found to be the most performant of the varied deposition times. This generally resulted in a 3% atomic cobalt constitution on the WO_3 thin film surface, verified by EDX measurements.

The onset potential failed to exert a cathodic shift with WO_3 and the photocurrent was not significantly enhanced. In fact the photocurrent was often slightly lower upon addition of Co-Pi, which has been experienced by other groups [263]. The samples which exhibited a slightly increased photocurrent were employed for faradaic O_2 detection measurements. The photoresponse of a successful Co-Pi 5 minute deposition is shown below in Figure 42:

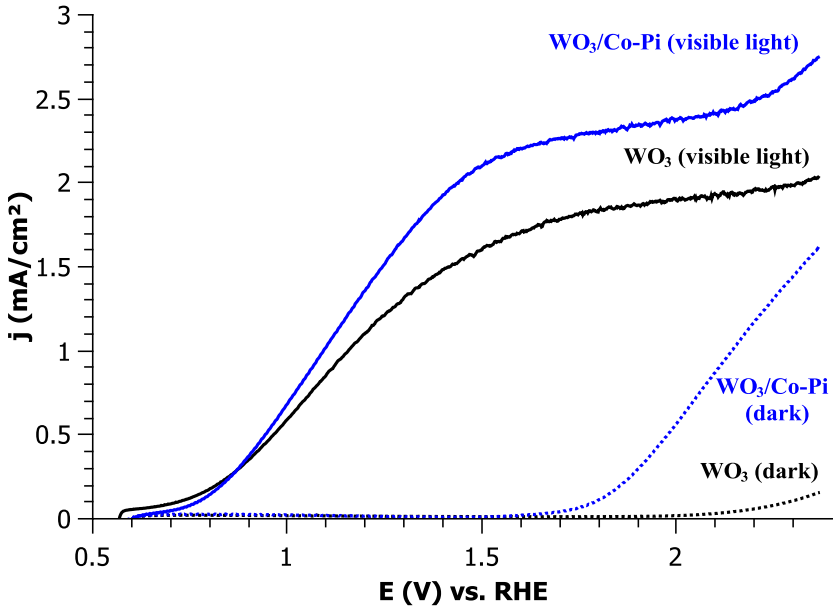

Figure 42: Linear sweep voltage dark (dotted) and photoresponse (solid) of WO_3 (black) and WO_3/Co-Pi (blue) in 1 M KPi (pH 6) under 350 mW/cm² (300 – 900 nm) illumination

Preliminary faradaic testing in 1 M KPi (pH 6) revealed similar faradaic efficiencies and slightly increased photocurrent (Figure 43), initially the Co-Pi had a larger O_2 production than bare WO_3 (blue curve in Figure 44), but after time performed more or less similar to that of the bare mesoporous WO_3. This may suggest that Co-Pi dissolves into the solution as Co^{2+} potentially acting as a homogeneous catalyst, existing on the surface of WO_3 as well as in solution [120, 223]. Slightly less corrosion occurred in near neutral conditions with Co-Pi, but no cathodic shift in onset potential, drastic increase in O_2 production, nor increase in photocurrent was consistently experienced. The Co-Pi co-catalyst did protect WO_3 more so than IrO_X over time, with an average photocurrent decrease of 30-40% with thick 70 nm layers.

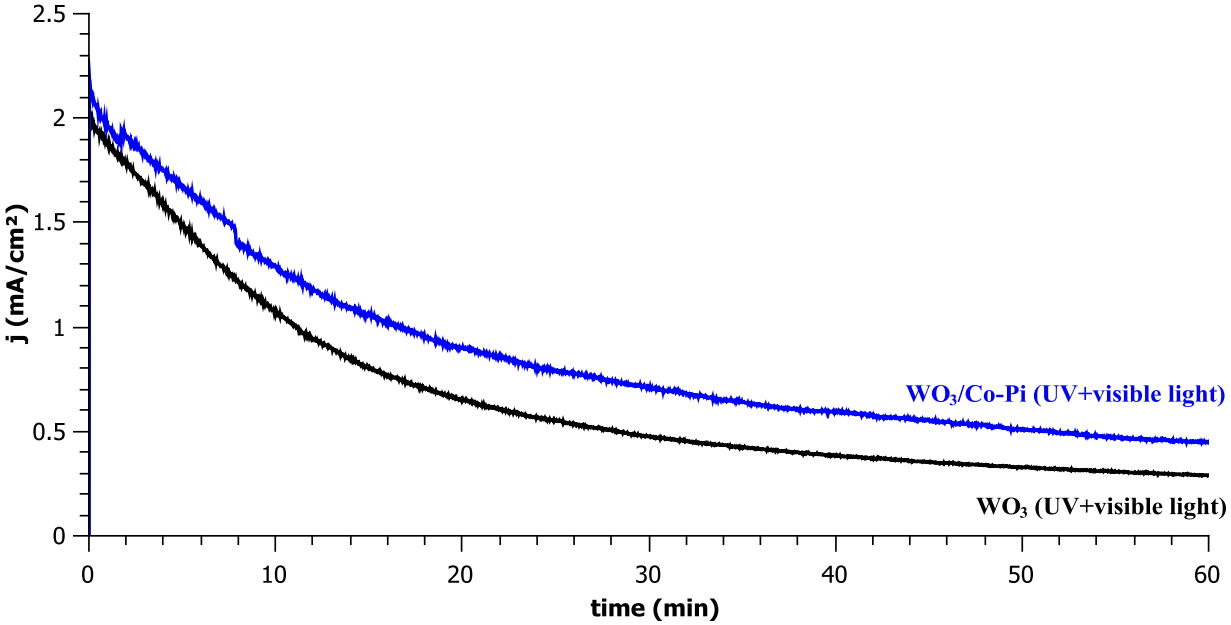

Figure 43: Photocurrent response during faradaic testing of WO_3 (black) and WO_3/Co-Pi (blue) at 1.23 V vs. RHE under 350 mW/cm² (300 – 900 nm) illumination in 1 M KPi (pH 6)

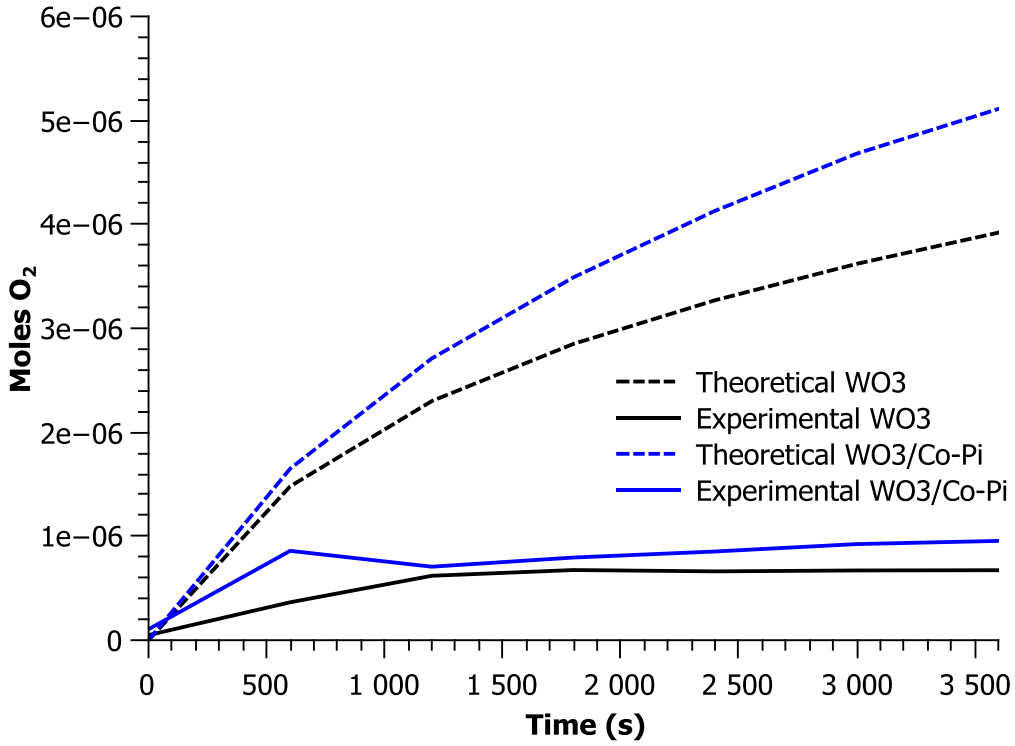

Figure 44: Moles of O_2 in solution for WO_3 and WO_3/Co-Pi photoanodes calcinated at 400°C in 1 M KPi under 350 mW/cm² illumination

II.3.5. CONCLUSIONS

Transparent thin film 550 nm WO_3 mesoporous n-photoanodes were successfully fabricated by sol-gel dip coating processes. It was found that nanostructuration of WO_3 aids significantly in the collection of minority carriers for the oxidation of water for increased performance. Despite the large IPCE value near high energy wavelengths, there is still progress to be made in the material optimization for increased performance, especially in light absorption near visible wavelengths, according to IPCE measurements. WO_3 absorption data suggests that these mesoporous thin film photoanodes can reach up to 2.13 mA/cm² instead of the 3.88 mA/cm² theoretically calculated (assuming 100% IPCE and no reflective losses). Under AM1.5G conditions, WO_3 exhibits a photocurrent at 1.23 V vs. RHE of only 0.3 mA/cm², suggesting there is still room for improvement; obtaining only 14% of the empirically theoretical photocurrent. This is most likely due to the separation efficiency in the bulk, measuring less than 20% from 0.6 – 2V vs. RHE. Though the surface catalysis efficiency is almost uniform, with an average of 85% at water splitting potentials, the OER may be hindered by peroxo species formation and parasitic reactions due to the electrolyte anion. Faradaic efficiencies are greatest in near neutral pH, measuring up to 74% in 1 M KPi of pH 6, though most of the produced oxygen remains in solution. Due to the instability of WO_3 in neutral to basic conditions, where the OER kinetics are preferred, WO_3 is unstable and thus further research on surface protection or co-catalysts are needed to increase stability and O_2 production preference. WO_3 thin films by the sol-gel method is a promising candidate for n-photoanodes in acidic conditions; though, like in neutral conditions, addition of a co-catalyst will be needed to encourage the production of O_2 over parasitic anion reactions for increased future performance.

Based on the best measured photocurrent the largest overall solar to oxygen efficiency is 0.37% for mesoporous WO_3 in pH 0 – 6 based on equation (30). This is an optimistic estimation, considering the non-ideal faradaic efficiencies and therefore is an overestimation of efficiency for a tandem dual photosystem. Compared to literature values, this small photocurrent of WO_3 by sol-gel dip coating processes is less performant than those listed in Table 7, suggesting the sol-gel route requires improvement for optimal WO_3 thin film photoanodes in water splitting technologies. Due to the fact that WO_3 is an indirect semiconductor, future implementation should assume thicker layers to reach maximum light absorption, considering many literature values present WO_3 thin films measuring microns in thickness. The UV-vis absorption confirms this hypothesis upon applying the optical absorption empirical data to the AM1.5 spectrum, revealing WO_3 only absorbs 55% of the light available for a 2.89 eV material for the AM1.5G solar spectrum. These findings signify the need for thicker layers than 550 nm for increased performance.

The instability of WO_3 in neutral to basic solutions for favored OER kinetics is an identified problem and several efforts have been taken to understand and overcome this obstacle [142, 261, 264]. As catalysts may temporarily protect the WO_3 surface, there is still a decrease in photocurrent suggesting peroxo species and parasitic reactions which block the surface and/or limit the production of O_2 occur. Addition of co-catalysts may increase the OER, though long term stability of the co-catalyst remains in question for the OER on WO_3 [223]. As previously stated, WO_3 is a possible candidate as an n-photoanode for water splitting in acidic conditions. Acidic conditions yield to both the HER and the proton exchange membrane high mobility of protons. Respectively, pairing WO_3 with a p-photocathode, which is stable in acidic conditions, must be accomplished to complete the tandem dual photosystem. The faradaic efficiency of the OER may also suffer in strongly acidic conditions due to the lack of OH^- ions in solution to influence preferential OER kinetics; thus requiring an appropriate OER co-catalyst stable in acidic conditions to aid in the preferential production of O_2. For neutral conditions, a protective layer or optimized co-catalyst must be employed for correct function as an n-photoanode concerning stability. WO_3 is envisionable in both acidic and neutral conditions with the proper suggested optimization and surface modification. More recently, protective layers have been applied such as Al_2O_3, TiO_2, and Fe_2O_3 for better faradaic yields and stability [135, 142, 259]. And most recently, WO_3 has been coupled with $BiVO_4$ for use as a composite n-photoanode for working in neutral conditions; as $BiVO_4$ is reputably stable in neutral pH, has a smaller band gap of 2.4 eV, and has suitable band positions for increased charge carrier separation. In result, these two materials combined have been the focus of many efforts as a composite n-photoanode material and is discussed in the third part of this chapter: II.4 Composite Photoanode.

II.4. BISMUTH VANADATE

II.4.1. INTRODUCTION

Recently, bismuth vanadate has been researched as a potential n-photoanode material due to its 2.4 eV band gap (absorbing up to 520 nm wavelengths of light), its suitable band positions for the OER, and its effective masses of holes and electrons which are easier to mobilize and extract than in other previously studied materials [242, 285, 286]. The conduction band of $BiVO_4$ is only slightly more negative than the water reduction potential; thus, its slightly larger than ideally suggested 2.0 eV band gap may be compensated by the band positions of $BiVO_4$ for water splitting applications [242]. With the conduction band only slightly more positive than the HER, its valence band is located around 2.4 - 2.5 eV, rendering it capable of oxidizing water [242, 285]. It is a light yellow, non-toxic pigment, first optimized by Kudo in 1998 as a n-type semiconducting metal oxide for water splitting photoanodes [287].

$BiVO_4$ exists naturally as pucherite orthorhombic crystal structure, though laboratory synthesis results in three crystalline structures: tetragonal scheelite, monoclinic scheelite, and tetragonal zircon [288, 289]. The tetragonal zircon-type phase changes irreversibly to the monoclinic scheelite-type around 397-497 °C; whereas, the monoclinic $BiVO_4$ converts reversibly to the tetragonal scheelite-type at T > 255 °C [168, 288, 290, 291]. The tetragonal and monoclinic scheelite phases have also been reported to be obtained depending on the Bi:V stoichiometric ratio in solution, suggesting an excess of Bi^{3+} leading to the tetragonal zircon-type phase [291]. Nonetheless, the monoclinic scheelite is the most photoactive and thus sought after for water splitting OER photoanode application [292, 293]. This photoactivity is thought to arise from the hybridization of Bi 6s and O 2p orbitals which shifts the top of the valence band and reduces the band gap of monoclinic $BiVO_4$ [176, 291, 294]. This is due to the structural distortion of less symmetric Bi-O bond lengths, giving rise to charge carriers in the Bi 6s states and VO_4 which forms an internal electric field, advantageous for charge separation [285]. Bi^{3+} acts as a modular agent for both structural and optical properties of the crystal. It can determine internal parameters of the lattice, influencing neighboring V and O atoms, resulting in lone pair $6s^2$ electrons [295]. It was also found that the increase in crystal size results in a decrease of band gap and a reduction of the V-O bond length, leading to a greater overlap of Bi 6s and O 2p orbitals and consequently an increase in delocalization of charge carriers and increased O_2 production [293, 296].

Walsh suggested that monoclinic $BiVO_4$ had a direct band gap of 2.4 eV; though, later Zhao et al. suggested with density functional theory (DFT) data that monoclinic scheelite $BiVO_4$ exhibits both indirect and direct band gaps at 2.1 eV and 2.4 eV respectively [285, 286]. Typical thickness of $BiVO_4$ films are rather thin, ranging from 50 – 300 nm in general to acquiesce charge carrier diffusion lengths and mobility [150, 190]. The minority carrier diffusion length has been measured to be 70 – 100 nm, as

$BiVO_4$ allegedly suffers from low intrinsic mobility and poor carrier separation due to poor electron mobility in the material [140, 149, 217, 297]. This has been confirmed by front and back illumination comparisons (depicted in Figure 45), due to the large increase in photocurrent and IPCE from back illumination; indicative of the slow transport of electrons to the back contact [146, 150, 151, 154].

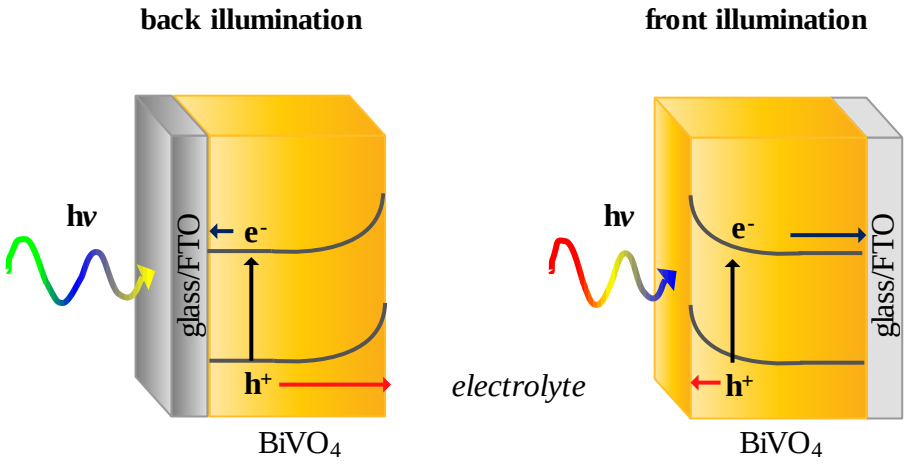

Figure 45: Back and front illumination in $BiVO_4$

The electron diffusion lengths were determined to be < 10 nm for electrodeposited films of $BiVO_4$ [190]. This is potentially due to the conduction band existing mainly of V 3d orbitals and the crystal structure which reveals that the VO_4 tetrahedra are not touching, forcing then the electrons to hop from one VO_4 tetrahedra to another [151, 286]. To increase conductivity, $BiVO_4$ is commonly doped with tungsten or molybdenum. These two metals are chosen due to their ability to possess a valence charge of 6+ acting as electron donors to increase n-type defects and potentially shifting the Fermi level. In return, this can decrease the band gap, thus increasing the charge carrier diffusion length and overall band bending [151, 170, 190, 242, 298-300]. Some literature studies show that gradient doping can be additionally beneficial for increased efficiency [149]. Doping can potentially blue shift absorption and shift the band positions of $BiVO_4$ and increase performance [213, 299]. However, the molybdenum or tungsten can replace the bismuth. Assuming a 3+ oxidation state, this potentially leads to an energetically unfavorable formation of highly charged bismuth species [301]. The effect of doping of $BiVO_4$ is not fully yet understood. DFT studies suggest that doping does not induce mobility. It instead results in local distortion of the V^{4+} resulting in the formation of small polarons and an improvement of charge separation [170, 242, 302]. TRMC results from Van de Krol's group suggest doping actually decreases charge carrier lifetimes and diffusion length. An increase of the photocurrent of W:$BiVO_4$ is then observed because intermediate-depth donor defects are introduced as carrier traps [297]. Considering film orientation and material thickness,

conductivity is a key parameter for PEC device efficiency, especially upon the implementation of thicker films for increased light absorption and efficient charge carrier collection.

Interfacial hole blocking layers, such as SnO_2 between the back contact and $BiVO_4$, have additionally been shown to increase performance. Due to potential defect state between the TCO and $BiVO_4$ which act as recombination sites, a thin layer of SnO_2 has been recently utilized in order to use the more negative position of the valence band of SnO_2 to block holes from flowing to the back contract which recombine with electrons at defect states [151, 174]. This thin layer presumably acts as a hole mirror or prevents recombination via FTO-related defect states at the FTO/$BiVO_4$ interface as shown in Figure 46 [151].

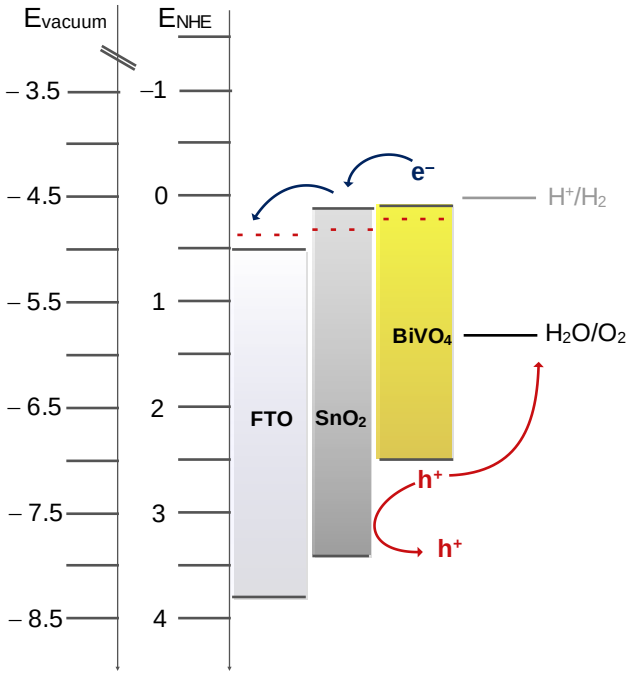

Figure 46: Band Diagram depicting SnO_2 hole mirror layer

Performance of thin films of $BiVO_4$ depends heavily on the synthesis and deposition conditions, including the Bi:V ratio introduced (as well as dopants), calcination temperature, and deposition method [291]. Many initial attempts at $BiVO_4$ were colloidal suspensions with silver nitrate or iron sacrificial agents for photocatalytic application, as the conduction band of $BiVO_4$ is not positive enough to reduce water [287, 291, 303]. The use of silver as a sacrificial reagent or surface modification has been replaced by more abundant metals since first efforts and fabrication methods beyond colloidal suspensions deposited by thin films are currently practiced. Typical $BiVO_4$ deposition methods for thin film photoanode fabrication include spray pyrolysis [149-151, 297, 304], reactive sputtering [154, 155], reactive ballistic deposition [145, 146], electrodeposition [160, 213, 305, 306], and finally MOD techniques based on colloidal and sol

gel precursors deposited by spin coating [172, 174, 176, 184, 191, 241, 307-309], drop casting [140, 147, 185], or dip coating [189, 310]. Table 11 displays the photocurrent at 1.23V vs. RHE using a reference electrode (unless otherwise stated) for state of the art $BiVO_4$ photoanodes recently fabricated employing a platinum counter electrode.

Year	Photoanode	$BiVO_4$ Deposition Technique	Thickness (nm)	Electrolyte (pH)	P_{in} (mW/cm²)	j	Ref
2006	FTO/$BiVO_4$	Spin coating	500	0.5 M Na_2SO_4 (pH 5.8)	260	1.3 mA/cm²	[176]
2011	FTO/SnO_2/W:$BiVO_4$	Spray pyrolysis	200	0.15 M K_2SO_4 (pH 7)	AM1.5	1.4 mA/cm²	[151]
2011	FTO/$BiVO_4$/FeOOH	Electrodeposition	200 - 500	0.1 M KPi (pH 7)	AM1.5	2.4 mA/cm² (0.8 V vs. RHE)	[160]
2011	FTO/Mo:$BiVO_4$/RhO_2	Spin coating	1000	0.5 M K_2SO_4 (pH 6.5)	AM1.5G	2.17 mA/cm² (1 V vs. RHE)	[311]
2012	Mo:W:$BiVO_4$/Pt	Reactive Ballistic Deposition	140	0.1 M KPi buffer (pH 6.8)	73	1.7 mA/cm²	[146]
2012	FTO/SnO_2/ W:$BiVO_4$/Co-Pi	Spray pyrolysis	200	0.1 M KPi (pH 7)	AM1.5	2.3 mA/cm²	[150, 312]
2013	FTO/W:$BiVO_4$/TiO_2	Drop casting	80 - 120	0.1 M KH_2PO_4 (pH 7)	40	0.25 mA/cm²	[185]
2014	Mo:$BiVO_4$/FeOOH	Dip coating	300	0.1 M KPi (pH 7)	100	2.77 mA/cm²	[190]
2014	$BiVO_4$/FeOOH + NiOOH	Electrodeposition	500	0.5 M KPi (pH 7)	AM1.5	2.73 mA/cm² (0.6 V vs. RHE)	[217]
2014	Ti/$BiVO_4$/CoO_x/ NiO(OH)	Drop casting particles	500	0.1 M KPi (pH 7)	AM1.5G	3.5 mA/cm²	[140]

Table 11: State of the art bismuth vanadate photoanodes

As seen in Table 11, there are several approaches and modifications done to increase the performance of $BiVO_4$. Many address the surface catalysis as the bottleneck for the OER using $BiVO_4$ while others suggest performance limitation is due to the poor bulk conductivity. Both doping and hole mirror interfacial layers together can increase the IPCE and overall performance of $BiVO_4$ [149]. However, these photocurrent values are generally lower than WO_3 state of the art photoanodes (Table 7), though $BiVO_4$ should exhibit a higher photocurrent due to its smaller band gap and ability to absorb more of the solar spectrum [178, 182]. This observation reinforces the claims of low conductivity and surface kinetic issues. While the deposition of $BiVO_4$ can be successfully accomplished, exhibiting high IPCE values, at some

point, doping, modification, and/or addition of co-catalysts is necessary to reach sufficient efficiency concerning the OER. Nanostructuration has little been reported for $BiVO_4$ as larger crystals and a continuous network is important for conductivity in $BiVO_4$ if bulk properties are considered to be limiting.

State of the art $BiVO_4$ photoanodes can reach over 3 mA/cm² under 1 sun at water splitting potentials when appropriately optimized and modified; suggesting that the theoretical photocurrent maximum of 7.6 mA/cm² is not even halfway achieved [151]. The highest reported photocurrent from Zhong et al. suggests 3.5 mA/cm², however an aluminum rear reflector is used to potentially augment AM1.5G illumination. Nevertheless using abundant cobalt and nickel as co-catalysts to increase surface catalytic activity is a promising direction for improving $BiVO_4$ photoelectrocatalytic characteristics. To date, the best performances of $BiVO_4$ photoelectrodes have been carried out by using metal–organic decomposition, facilitating doping during the preparation. The samples prepared by MOD possess good crystallinity and smaller grain size, even when sintered/calcinated under moderately high temperature [300].

Seeing as $BiVO_4$ often suffers from a large overpotential (around 0.5 V vs. RHE) and low conductivity, signifying resistive losses and high recombination rates, suspected to be exacerbated at the surface [137, 160, 217]. This has been demonstrated by adding hole accepting sacrificial reagents (electron donors) like sodium sulfite (Na_2SO_3) and hydrogen peroxide (H_2O_2) which are thermodynamically easier to oxidize than water, alleviating the slow kinetics at the surface and reducing the onset potential to 0.1 – 0.2 V vs. RHE [145, 217]. The poor surface catalytic activity of $BiVO_4$ is thought to be attributed with bismuth rich surface where the kinetics of the OER are slowed and often the surface acts as a recombination site [145, 176]. It is possible that vanadium evaporates when $BiVO_4$ is thermally treated at higher temperatures (> 500°C°), and that V^{5+} seems to dissolve into solution over time and/or upon light exposure for periods of time [176, 291]. This generally leads to a decrease in photocurrent and bismuth rich surface which may potentially help long term stability, yet at the potential expense of surface modification – which may be less ideal to achieve the OER. The stability of $BiVO_4$ is thought to be in the neutral region (pH 6 – 8), despite potential vanadium dissolution [50, 313]. Nevertheless, several groups report having degradation in photocurrent over time in neutral pH conditions, potentially due to dissolution of vanadium and photodegradation of the thin layers [145, 176]. Stability has been shown to increase upon use in appropriate electrolyte, addition of co-catalysts, or surface modification for use in neutral conditions [176, 314]. $BiVO_4$ has additionally been shown to emit stability in basic pH upon addition of an appropriate passivation layers and co-catalyst [308, 315].

Addition of co-catalysts on the $BiVO_4$ surface aims to decrease the overpotential needed to drive the OER, aid in surface kinetics preferring the production of oxygen, and finally to increase long term stability.

While dark OER catalysts, IrO_x and Co-Pi, have been suggested to not function as co-catalysts for the OER due to detrimental states at the $BiVO_4$/co-catalyst interface; in addition, platinum has been shown to exhibit instability upon $BiVO_4$ [160, 190, 316]. Accordingly, attention has been driven towards more abundant metals in recent efforts. To date, OER catalysts coupled with $BiVO_4$ for use in neutral conditions include: Co_3O_4 [317, 318], NiO_X or NiOOH [140, 319], FeOOH [155, 160, 190], NiOOH coupled with FeOOH [147, 217], while most commonly Co-Pi [147, 149, 150, 309, 320, 321]. These co-catalysts have generally succeeded in decreasing the onset potential by values of up to 150 mV with Co-Pi [298], 320 mV with CoB_i [162], 440 mV with Co-Pi [309], 500 mV with FeOOH [160]; all of which seem to aid with long term stability and exhibit an onset potential around 0 – 0.2 V vs. RHE [140, 308].

Performant $BiVO_4$ photoanodes for the OER thus require considerably more modification than WO_3 according to previous research effectuated due to poor conductivity, stability, and numerous surface issues hindering the OER. Research completed on $BiVO_4$ in this study utilizes simple sol-gel dip coating methods to fabricate thin film n-photoanodes to complete the OER in neutral conditions.

II.4.2. Synthesis and Characterization

$BiVO_4$, like WO_3, was fabricated by sol-gel dip coating process onto glass/FTO substrates [322]. The same FTO substrates were used as with WO_3 in anticipation of inserting WO_3 for a composite photoanode. Semi-transparent thin films of $BiVO_4$ onto FTO substrates were successfully synthesized for use in neutral OER conditions. The stoichiometric ratio of Bi:V of 1:1 must be obtained for correct stoichiometric crystallization of $BiVO_4$ after deposition. Vanadium salts suffer from low solubility in many organic solvents, limiting the concentration of the sol-gel and sometimes precipitating, leading to bismuth rich layers and irreproducibility between experiments. Therefore, several layers deposited by dip coating methods were effectuated to compensate for the small thickness of each layer deposited, due to lack of concentrated precursor solution. The $BiVO_4$ sol-gel precursor was adapted and optimized from Sayama et al. [176]. Typically slightly more vanadyl acetylacetonate (0.097 g in place of 0.095 g) was added due to the poor solubility of vanadium in order to keep the 1:1 stoichiometry of Bi:V. The sol is made by introducing 0.6 mL of acetic acid to 4.3 mL acetylacetone in a vial followed by 0.173 g of $Bi(NO_3)_3{\cdot}5H_2O$ and 0.095 g vanadyl acetylacetonate. (Subsequently, if dopant is introduced, this is done by replacing vanadium while keeping the total molar concentration. MoO_3 was found to be the most soluble in the solvent). $BiVO_4$ sol-gel has a solution concentration of 0.07 M and a pH of 4. The sol-gel solution is adjusted in pH to induce the correct oxidation sates for (Bi^{3+}) and vanadium (V^{5+}) to become $BiVO_4$. Adjusting the pH by use of acetic acid (weak acid) and nitric acid (strong acid) altered the microstructure as well as the stability of the sol. However, it is necessary to keep the pH lower than 5 due to the precipitation of vanadium [160]. Synthesis at pH 4 incorporating only acetic acid and acetylacetone was

found to be most ideal in terms of Bi:V stoichiometric 1:1 ratio preference. The solution is then retained in a closed vial and placed in an ultrasonic bath at 25 – 30°C and sonicated for 15 minutes. The solution is then left overnight, unexposed to light, for use the next day. This sol-gel is generally usable for 1 – 2 weeks, but had the best performance the day after synthesis. Solutions sonicated at room temperature revealed less dense microstructures than those sonicated at slightly higher 30°C temperatures.

$BiVO_4$ was dip coated at room temperature with < 3% relative humidity. Dip speed was 0.8 mm/s resulting in an average of 10 nm/layer. Optimized $BiVO_4$ requires an annealing step of at least 400°C between layers for 2 – 5 minutes and a final calcination treatment for 60 minutes at 450°C. Annealing at 450°C between layers instigates larger crystal size but requires more than 10 layers to successfully connect these large crystals and completely cover the FTO surface. Several successive annealing treatments weaken the glass substrate and will generally break the substrate; therefore annealing between layers at 400°C is more accommodating for glass substrates, but produces smaller crystal sizes.

Thermal treatment, precursor synthesis, and thickness were the main variables in thin films of $BiVO_4$ fabricated as an n-photoanode for water splitting. 5 layers of sol-gel dip coated $BiVO_4$ was thermally treated in between layers at 350°C and finally at 400 – 550°C for 30 minutes in air. Temperatures higher than 550°C were not tested, as to not reach higher temperatures and risk to induce defects and volatize vanadium or bismuth which occurs at high temperatures as well as to attain the monoclinic scheelite $BiVO_4$ which is thought to occur between 397 – 497°C [323].

Cu Kα radiation XRD spectra at 40 mA and 40 kV of $BiVO_4$ calcinated at 400 – 550°C display peaks of monoclinic bismuth vanadate, with no other apparent signs of the tetrahedral $BiVO_4$ characteristic peak at $2\Theta = 15°$, nor vanadium or bismuth oxides. $BiVO_4$ annealed between 350 – 450°C and calcinated for one hour at 400 – 450°C exhibit a monoclinic scheelite crystal structure shown in Figure 47; w here bismuth atoms are shown in purple, vanadium in blue, and oxygen in red. The XRD spectrum of $BiVO_4$ annealed at 400°C and then calcinated at 450°C for 1 hour is also shown in Figure 47 with black triangles marking FTO peaks and blue squares indicating monoclinic $BiVO_4$, the characteristic peaks corresponding to Joint Committee on Powder Diffraction Standards (JCPDS) 01-75-1867 and previous literature reports [176, 320].

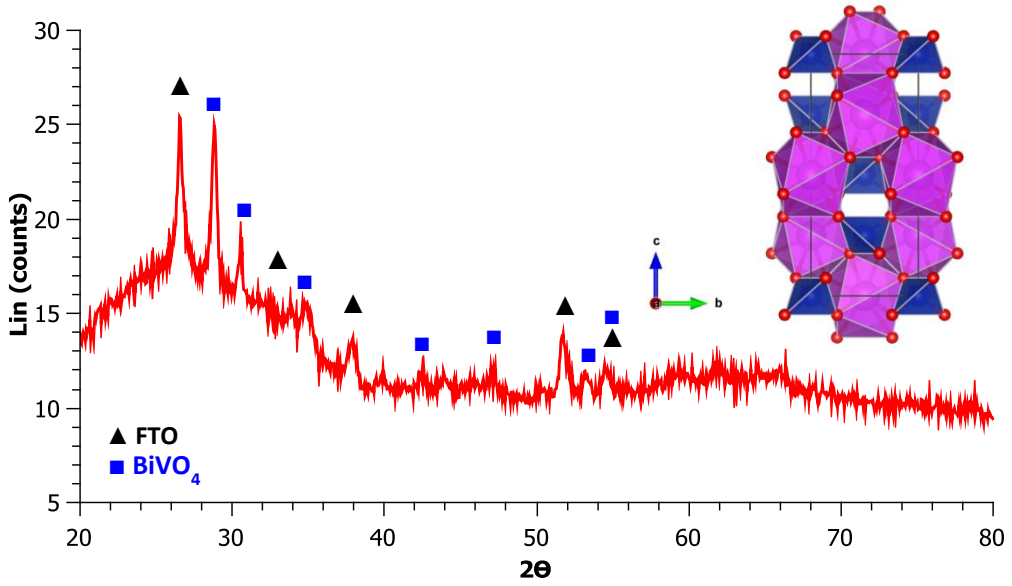

Figure 47: Cu XRD spectrum of $BiVO_4$ on FTO substrate and crystal structure

The main $BiVO_4$ scheelite peaks occur at 28.9° and 30.5, respectively indicating the (1 2 1) and (0 4 0) crystal facets in agreement with literature values [176, 324]. No tetragonal type $BiVO_4$ was detected from its characteristic peak at 24°. Thin layers of < 150 nm exhibit large signals of the glass substrate below 40°, and the peaks related to the 80 nm of FTO are easily detected. Crystallite sizes were calculated to range between 15 – 30 nm depending on the annealing and calcination temperature employed. The annealing temperature seemed to play a larger role in crystallite size definition than the final calcination temperature. The average crystallite sizes are displayed below in Table 12 for $BiVO_4$ films annealed at 350 – 450°C and calcinated at 400 – 450°C. This suggests that implementation of a higher annealing temperature and thicker layers resulted in larger crystals of $BiVO_4$.

Film Thickness (nm)	**Annealing Temperature (°C)**	**Calcination Temperature (°C)**	**Average crystallite size (nm)**
40	350	400	15
75	400	450	16
40	450	450	21
40	450	500	23
75	450	450	25
115	450	450	30

Table 12: Average $BiVO_4$ crystallite size as a function of thermal treatment and thickness

XPS peaks of the $BiVO_4$ thin films fall in agreement with other monoclinic $BiVO_4$ thin film signals (Figure 48) [154, 191, 193, 296]. The observed O 1s peak at 529.8 eV can be ascribed to the lattice oxygen in crystalline $BiVO_4$.

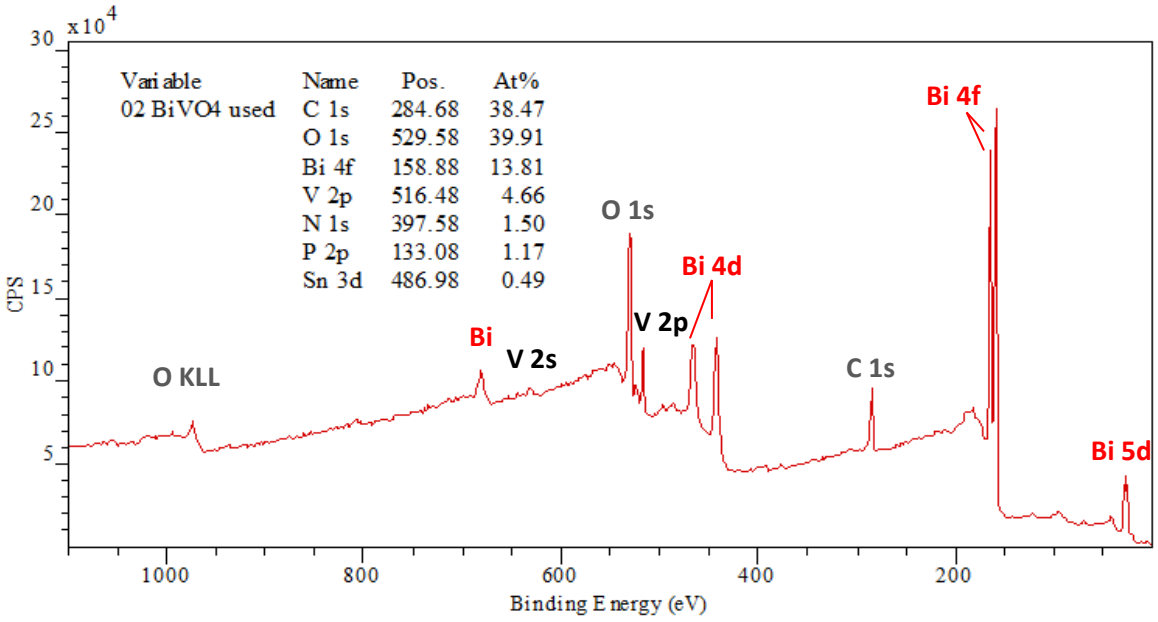

Figure 48: XPS spectrum of $BiVO_4$ annealed at 350°C and calcinated at 400°C before use

XPS measurements of $BiVO_4$ films revealed a Bi:V ratio generally ranging from 2.5 – 2.9; suggesting a bismuth rich surface [193]. Bi asymmetric 4f 5/2 and 7/2 peaks indicate the presence of Bi^{3+} ions. Before use in aqueous medium, thin films of 40 nm of $BiVO_4$ calcinated at lower temperature of 400°C possess a bismuth to vanadium ratio of 2.7.

$BiVO_4$ absorbs largely towards the UV region, and exhibits an absorption edge around 490 nm. It has two distinct transition shoulders at 320 nm and 430 nm seen in Figure 49, an indication of monoclinic scheelite structure [217, 291, 295]. The two shoulder bands have been ascribed to the charge-transfer transition involving the V-O component and Bi and V centers [171]. However, Zhao et al. suggested with DFT that these transitions are due to the photo absorption polarization along the c plane at 330 nm and along the a and c planes at 440 nm [285]. The absorption (red curve in Figure 49) and transmission (black curve in Figure 49) spectra exhibit the absorption edge at 490 nm which correlates with the Tauc plot (also shown in Figure 49) suggesting an indirect band gap of around 2.5 eV – in agreement with values for monoclinic scheelite $BiVO_4$ [176, 217, 293, 319]. However deviations in Bi:V ratios may lead to sub band gap absorbance [319]. Layers ranging from 50 – 115 nm show the same absorption and transmission features, yet layers require a minimum of 100 nm to absorb all light (0% transmission) for wavelengths below

320 nm. $BiVO_4$ transmission spectra suggest good transparence in the visible to infrared range for layers of less than 150 nm, enabling light to reach the photocathode in a dual photosystem tandem configuration. Absorption calculated from UV-vis measurements is shown below in Figure 50, suggesting 79% of the light can potentially be absorbed for a material with a band gap of 2.5 eV. The theoretical photocurrent achievable with sol-gel dip coated $BiVO_4$ in this research based on absorption data suggests 5.62 mA/cm² in place of the proposed maximum of 7.6 mA/cm², attainable from AM1.5 conditions [190]. Nevertheless, from literature data, the good optical absorbance of $BiVO_4$ is generally misleading for PEC applications due to its low conductivity and hindered OER surface kinetics which limits overall performance.

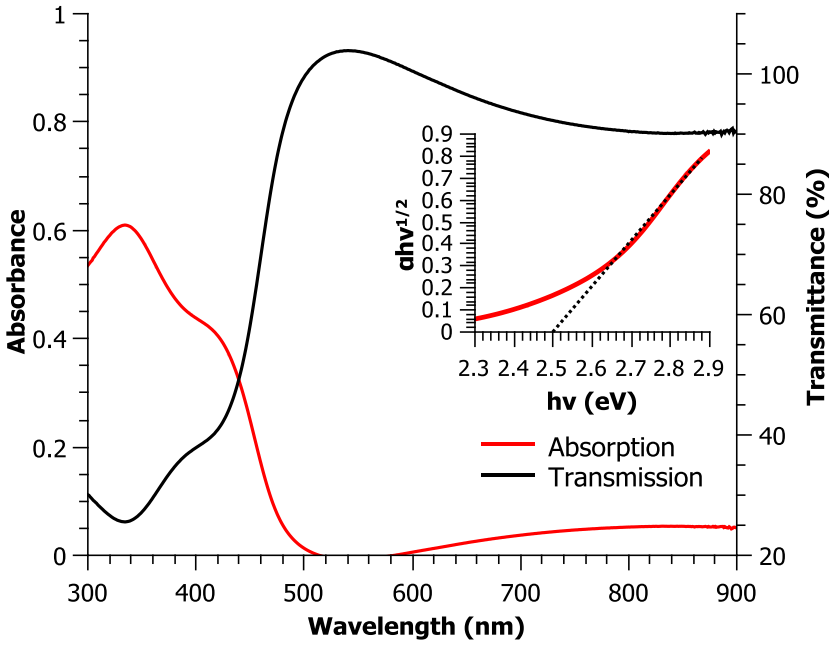

Figure 49: Absorption and Transmission of $BiVO_4$ with Tauc plot

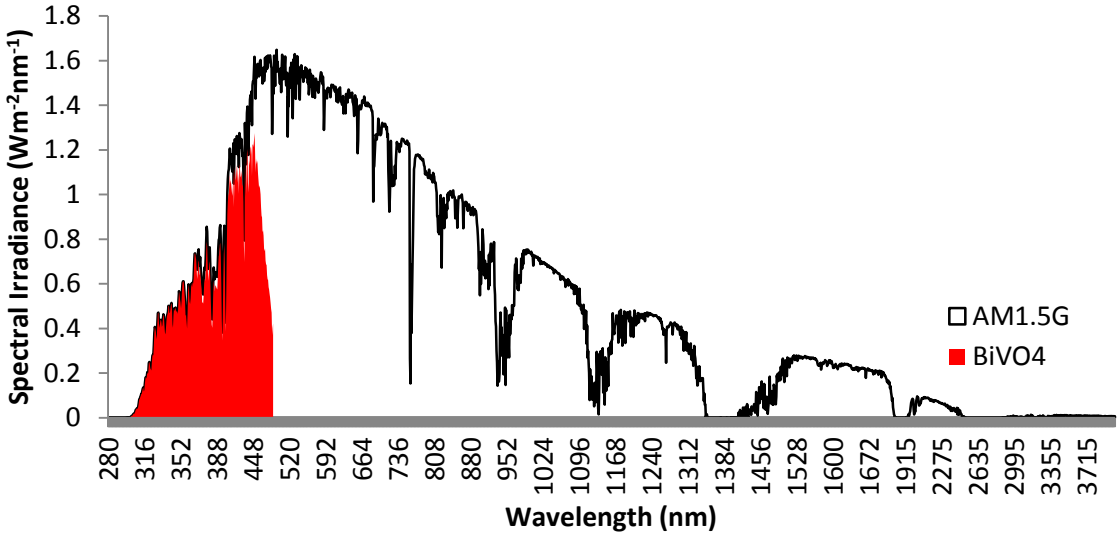

Figure 50: Empirical AM1.5 absorbance of 15 layers $BiVO_4$

II.4.2.1. Material Optimization

Material optimization of $BiVO_4$ is done first by synthesis parameters (e.g. sol concentration, pH, and inorganic salts) and then by varying thermal treatment (annealing and calcination) temperatures. Annealing and calcination temperatures are important parameters, as it greatly influences the crystallization and morphology of the thin films. Then thicknesses of the thin films are varied in order to find at which conditions $BiVO_4$ is the most performant for the OER. The linear voltage sweep measurements reveal at which potential the material starts to oxidize water in the dark and under illumination. The photocurrent density is largely important to further understand the materials behavior and the overpotential needed to split water related to the onset potential of the photocurrent density. The photocurrent density at varying potentials gives insight to the overall performance $BiVO_4$ can reach at specific conditions and is essential in calculating STH efficiencies. In optimizing $BiVO_4$, linear voltage sweeps are completed in the dark, and under illumination (300 mW/cm^2), in 1 M KPi (pH 7) for thin films calcined between 400 – 550°C in order to compare the photoactivity. These linear sweep voltage measurements are reported below with corresponding planar FEG-SEM images in Figure 51:

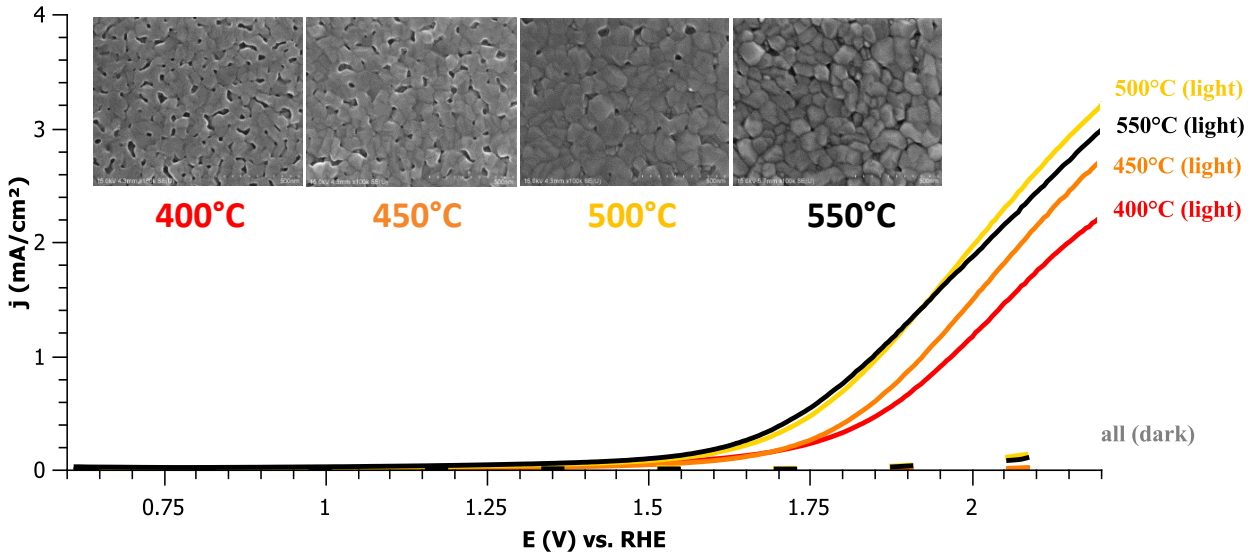

Figure 51: Linear voltage sweep of $BiVO_4$ calcinated at different temperatures under 300 mW/cm² in 1 M KPi (pH 7) with corresponding FEG-SEM images

Thermal treatments ranging above 500°C were the most performant, displaying larger photocurrents at lower potentials. The higher temperatures result in larger crystals, supposedly beneficial for O_2 production [293, 296]. However, if to be coupled with WO_3, the annealing should not exceed 400°C for previously optimized WO_3. Ultimately, further measurements were needed to understand the effect of temperature upon $BiVO_4$ for use in the oxygen evolution reaction.

TRMC measurements were performed to study the charge carrier dynamics in $BiVO_4$ films calcinated at varied temperatures. Figure 52 shows the microwave conductance transient signals of 40 nm films annealed at 350°C and calcinated at 400°C for 30 minutes and reheated at 450°C, obtained from excitation from a laser pulse of 355 nm with an intensity of 1.4×10^{14} photons/pulse·cm^2. The photon energy utilized is great than the band gap of $BiVO_4$, leading to the formation of free electrons and holes in the conduction and valence bands. As previously stated, microwave conductance is given by the product of the absorbance-normalized quantum yield (ϕ) and the combined mobility of the charge carriers in the system (denoted $\Sigma\mu$). The minimum mobility of the carriers is obtained from the peak of the measured signal (maximum of $\phi\Sigma\mu$), and the lifetime of the carriers is derived from the signal decay.

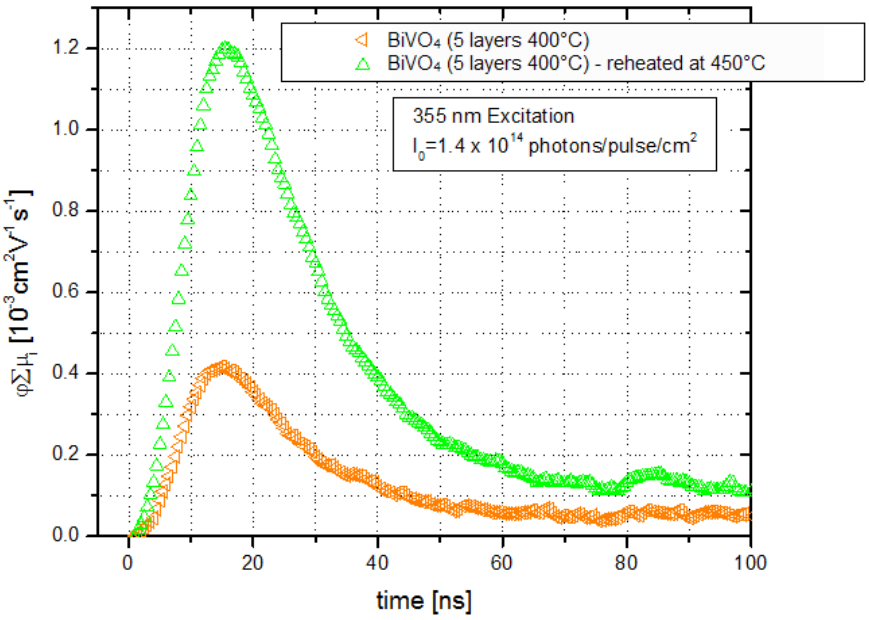

Figure 52: TRMC signals obtained from $BiVO_4$ annealed at 350°C and calcinated at 400°C (orange) and well as re-calcinated at 450°C (green)

The evolution of $\phi\Sigma\mu$ as function of time exhibit a maximum at τ = 20 ns and the value of $\phi\Sigma\mu$ is low compared to other $BiVO_4$ indicating that the photoconductivity is not optimized for films annealed at 350°C and calcinated at 400°C.

To understand the cause of the lower $\phi\Sigma\mu$ values in calcined $BiVO_4$, the TRMC signal of $BiVO_4$ calcinated at different temperatures and various thicknesses were measured at different laser pulse intensities. The resulting plot of $\phi\Sigma\mu$ as function of incident photons per pulse is shown in Figure 53. $BiVO_4$ films calcinated at 400 – 450°C are comparable to what is observed for doped $BiVO_4$ [297]. The $\phi\Sigma\mu$ initially increases with light intensity until reaching a maximum when it then decreases upon further light intensity [297]. A similar dependence of $\phi\Sigma\mu$ on the light intensity has been observed in compact and mesoporous TiO_2 films, attributing to the competition between electron trap filling and higher-order recombination [325]. The same explanation can be proposed for these $BiVO_4$ films: the concentration of electron traps is higher than the number of photon absorbed. This result indicates that $BiVO_4$ annealed and calcinated at lower temperatures (350°C and 400°C) resulted in doped $BiVO_4$ behavior (displayed as turquoise squares in Figure 53), which may be due to carbon contaminants which were not evaporated/pyrolyzed during annealing/calcination treatments. Reheating at 450°C for 12 hours increased the conductivity (as shown orange triangles in Figure 53); however, the samples still behave as doped-$BiVO_4$.

Upon increasing the annealing temperature applied between layers from 350°C to 400°C and 450°C, the doped behavior ceased. The overall conductivity of $BiVO_4$ increased substantially, due to the increase of carrier lifetime and diffusion length. This suggests that carbon contaminants are successfully expelled from the xero-gel film during the annealing step at temperatures superior to 400°C.

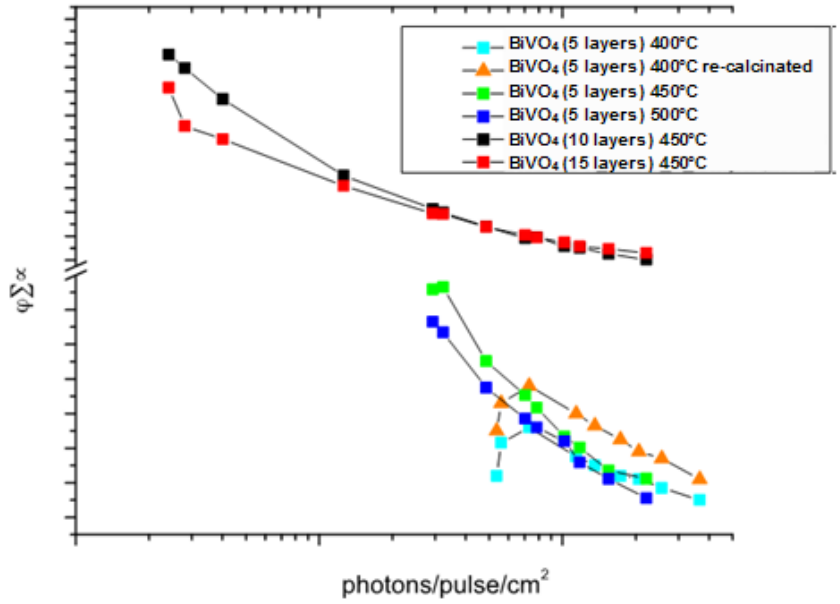

Figure 53: TRMC measurements on $BiVO_4$ calcinated at varying temperatures with increased annealing temperature and increased thickness

The impact of thickness of the films was then studied, as was the final calcination thermal treatment on the photocurrent density. The photoelectrochemical performance as a function of thickness and higher annealed $BiVO_4$ layers is shown in Figure 54. This figure indicates that 15 layers of $BiVO_4$ exhibited larger photocurrents than 10 layers. This could be allocated to the increased light absorption from increased thickness, exhibiting indirect semiconductor behavior; or more consistently, a more dense continuous crystal network for increased mass transport.

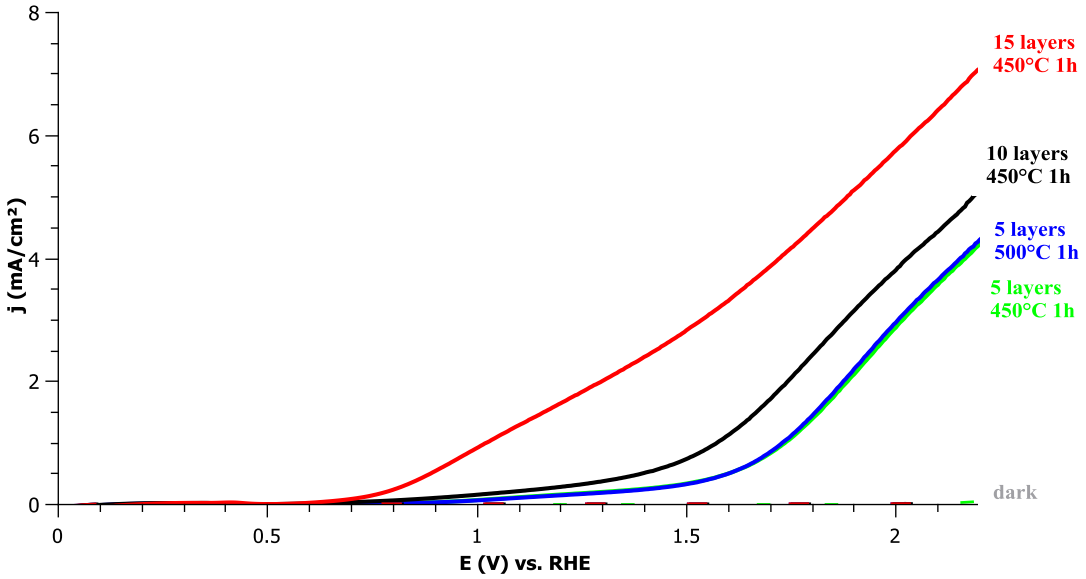

Figure 54: Photocurrent density of $BiVO_4$ as a function of thermal treatment and thickness

TRMC experiments were performed as well as SEM-FEG analyses to correlate this behavior to the microstructure of $BiVO_4$ films. The TRMC signals are reported in Figure 55, with corresponding FEG-SEM images for all $BiVO_4$ annealed at 450°C in Figure 56, and results in Table 13. Additionally, Table 13 reports the corresponding photocurrent densities in 1 M KPi under 350 mW/cm^2 at 1.23 V vs. RHE.

$BiVO_4$ film type	**Anneal Temp (°C)**	**Calc. Temp (°C)**	**Calc. Time (mins)**	**Avg. Thickness (nm)**	**$\Phi\Sigma\mu$ (10^{-3}cm^2/(V s)) at 2.93x10^{13} photons/cm^2/ pulse**	**$\Phi\Sigma\mu$ (cm^2/(V s)) at 10^9 photons/cm^2/ pulse (extrapolated)**	**τ (ns)**	**L_D (nm)**	**j (mA/cm²) at 1.23V vs. RHE**
5 layers	350	400	30	40	0.4 *(at 1.4x10^{14})*	-	20	15	0.52
5 layers *re-calcinated*	350	400 + 450	750	40	1.2 *(at 1.4x10^{14})*	-	20	25	1.78
10 layers	400	450	60	75	2.73 *(at 9.38x10^{13})*	8	18	19	2.14
5 layers	450	450	60	40	1.92	0.009	28	26	0.18
5 layers	450	500	60	50	1.73	0.007	25	22	0.17
10 layers	450	450	60	75	8.23	0.072	22	64	0.32
15 layers	450	450	60	115	7.87	0.055	21	55	1.78

Table 13: Thickness, TRMC results: carrier lifetime and diffusion length in $BiVO_4$, and corresponding photocurrent density in 1 M KPi under 350 mW/cm² (300 – 900 nm)

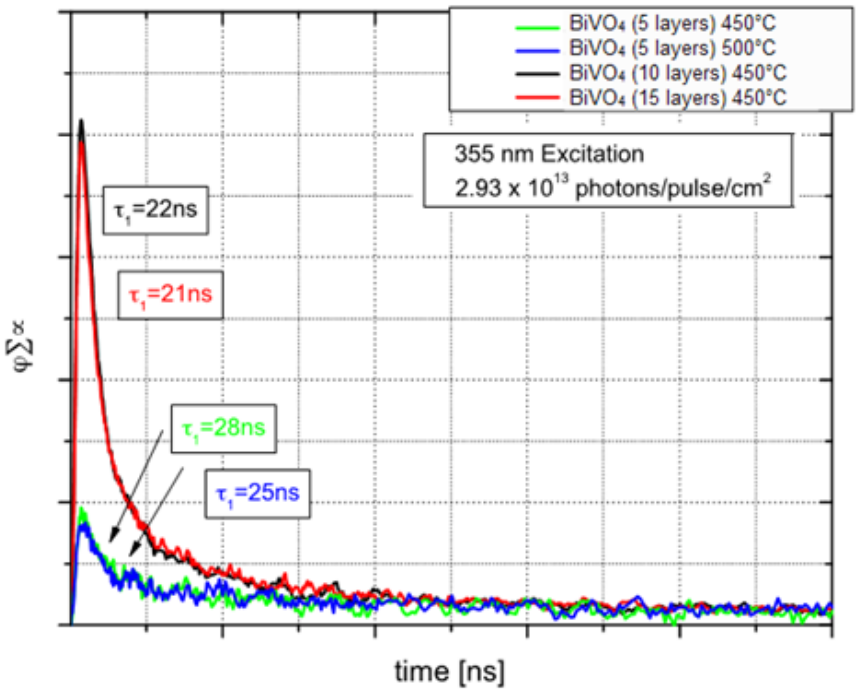

Figure 55: TRMC signals obtained from $BiVO_4$ annealed at 450°C and calcinated at 500°C (blue), and 450°C with varying thickness: 5 (green), 10 (black), and 15 (red) layers

First, the impact of film thickness on the performances is discussed, followed by impact by thermal treatments. The TRMC results, as well as the electrochemical performances of $BiVO_4$ films calcined at 450°C (annealed and final treatment), will be compared. The best electrochemical performances are achieved for the thicker layers (115 nm vs. 40 nm). A photocurrent of 1.78 mA/cm^2 at 1.23 V vs. RHE for 15 layers $BiVO_4$ was measured while a photocurrent of 0.18 mA/cm^2 at 1.23 V vs. RHE is found for 5 layers $BiVO_4$ treated at the same temperatures during fabrication. TRMC results indicate that these two samples possess identical carrier lifetime (20 ns) but exhibit different diffusion lengths. The diffusion length for the thickest film is larger, measuring 55 nm and 26 nm for 115 nm and 40 nm films, respectively. FEG-SEM images for films with various thicknesses (Figure 56) indicate a more continuous, dense with larger crystals for 15 layers $BiVO_4$ films. The best performances can then be correlated to better photoconductivity and lower recombination in samples presenting large crystals and uniform, dense microstructure [293].

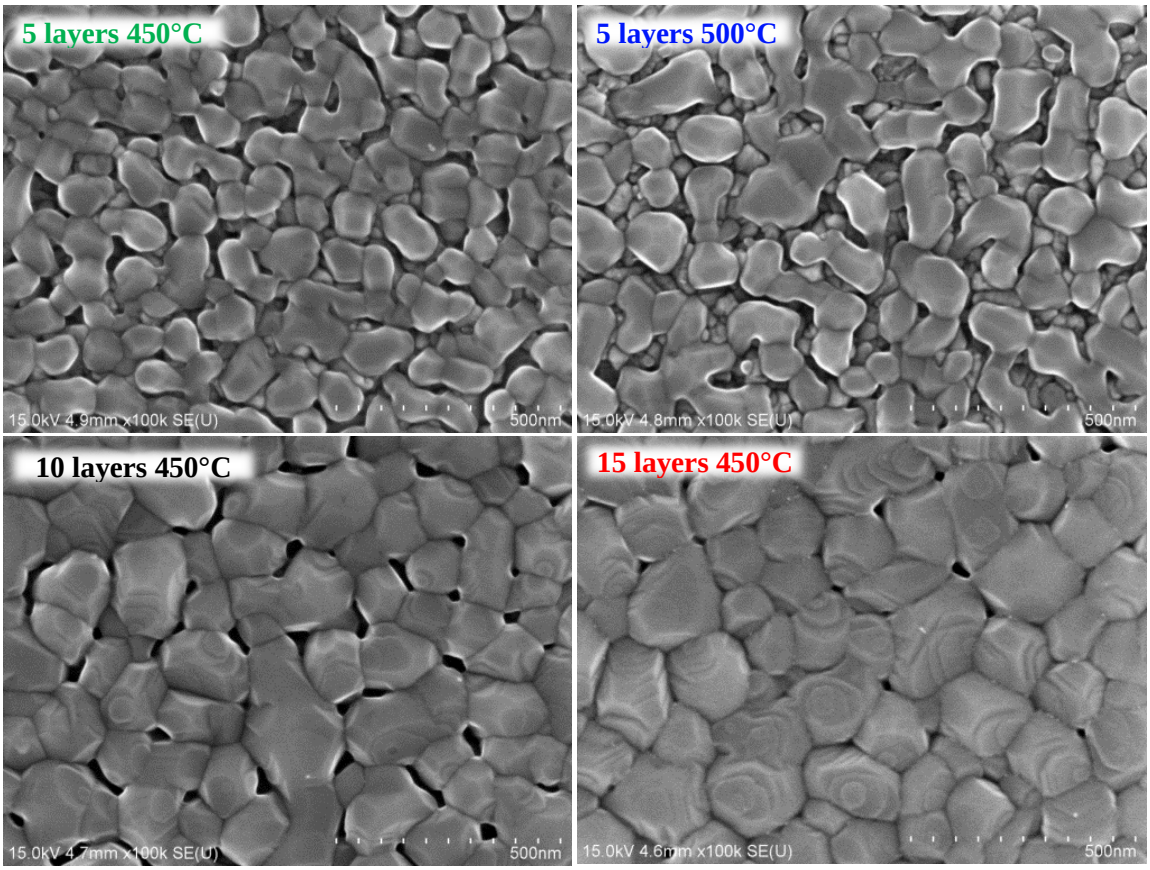

Figure 56: FEG-SEM imaged of $BiVO_4$ annealed at 450°C and calcinated at 450°C and 500°C for 1 hour with increase in thickness

Alternative syntheses conditions demonstrate that the best performances in photocurrent (2.14 mA/cm^2 at 1.23 V vs. RHE) are achieved for $BiVO_4$ annealed between layers at the lower temperature of 400°C. Comparing $BiVO_4$ with different intermediate heat treatment (400°C vs. 450°C) demonstrates that the photoelectrochemical performances are not only a question of carrier lifetime and diffusion length. SEM-FEG images (Figure 57) of 10 layers $BiVO_4$ annealed between layers at 450°C (left) and 400°C (right) both calcinated at 450°C for 1 hour, show different microstructure. Larger crystals are not seen in $BiVO_4$ annealed layers at the lower temperature of 400°C. The better electrochemical performances for these $BiVO_4$ films may be explained by increased mass transport in layers due to a well-connected crystal network in the thin films despite increased grain boundaries and smaller crystal size [193]. Thin films with an intermediate annealing temperature 450°C seem to suffer from Ostwald ripening during crystallization at higher temperatures or longer periods of time, leaving the FTO substrate exposed and breaking the continuous crystal network, necessary for mass transport [193]. This agglomeration of $BiVO_4$ crystals has been experienced by other research groups, sometimes leaving the substrate exposed [151, 185]. This suggests that annealing temperature has a large effect on the crystal growth of each layer which acts as

seeds to influence consecutively added layers [326]. To be utilized, these large agglomerate crystals must be in contact – demanding a compromise between thickness and crystal size.

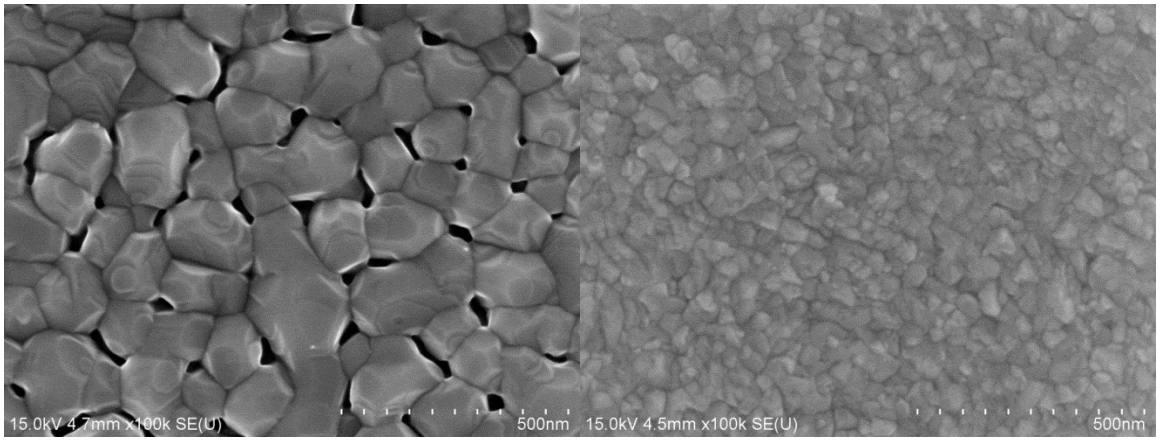

Figure 57: FEG-SEM images of 10 layers of $BiVO_4$ annealed between layers at 450°C (left) and 400°C (right) both calcinated at 450°C for 1 hour

In conclusion, these results indicate that layers which are thinner necessitate lower temperatures as to maintain smaller crystal size, forming a continuous, connected, dense network to drive charges in the layer. However, this may present more grain boundaries and sol-gel carbon contaminants if annealed under 400°C; yet, is likewise a compromise between crystal size and layer thickness; suggesting crystallite sizes should be smaller than the minority carrier diffusion length to maximize charge carrier separation efficiency [193].

II.4.3. Photoelectrochemical Performance and Stability

TRMC studies allow us to define the best conditions in term of thickness and microstructure for $BiVO_4$ films. Non-optimized $BiVO_4$ films display a large overpotential and begin to oxidize water under illumination around 1 V vs. RHE. This is reduced to 0.6 V vs. RHE (seen below in Figure 58) upon microstructure optimization: increasing the thickness, implementing higher annealing and crystallization temperatures, therefore creating a denser network of crystals in the microstructure. Photocurrents at the OER potential in 1 M KPi under 300 mW/cm² visible light (400 – 900 nm) reach over 1.2 mA/cm², upon the addition of UV light this increases to 1.8 mA/cm² (seen as dotted line in Figure 58). Despite further modifications and potential optimizations to be done, this measured photocurrent density is comparable to literature values which employ the same sol-gel process, suggesting that our optimized $BiVO_4$ by sol-gel dip coating methods are competitive with other sol-gel technique state of the art examples [176].

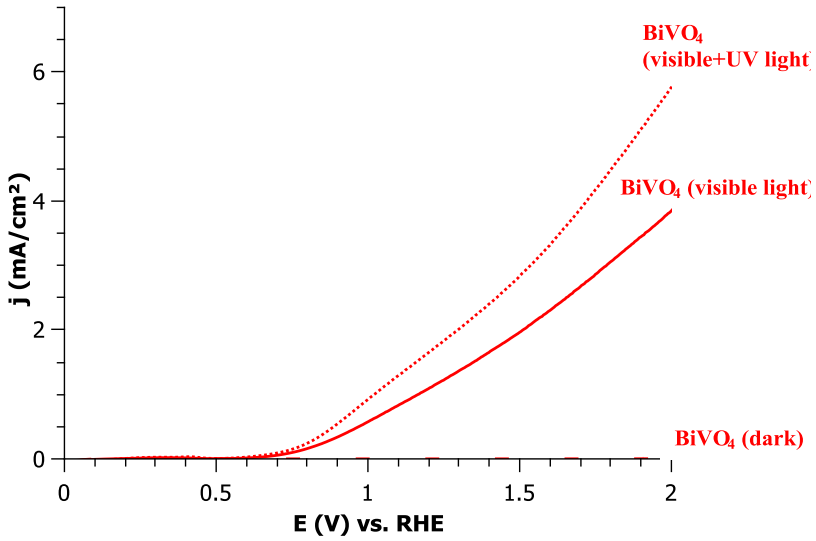

Figure 58: Photocurrent of optimized $BiVO_4$ under visible light (solid line) and upon addition of UV (dotted) light in 1M KPi (pH 7)

Upon the addition of a sacrificial agent, the photocurrent increases drastically, suggesting there is recombination which occurs at the surface of $BiVO_4$, limiting its water splitting performance. Most notably, upon the addition of Na_2SO_3, the onset potential cathodically shifts 300 mV (as shown in red in Figure 59), suggesting the surface contributes to the overpotential needed to complete the OER. Optimized photocurrent of $BiVO_4$ with a photocurrent of 1.8 mA/cm² at 1.23V vs. RHE in 1M KPi under 350mW/cm² illumination reaches 8.9 mA/cm² at the same potentials upon addition of a sacrificial reagent.

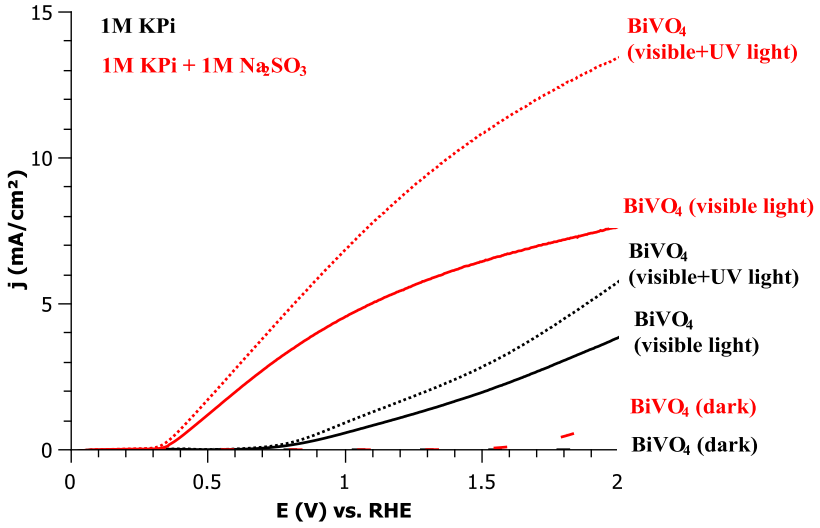

Figure 59: Photocurrent of $BiVO_4$ in 1M KPi (pH 7) under 300mW/cm² visible (solid lines) and upon addition of UV light at 350mW/cm² (dotted lines) in 1M KPi (black) and with 1M Na_2SO_3 (red)

Mott Schottky experiments were then completed in order to determine the flat band potential of these optimized $BiVO_4$ films. Mott Schottky plots were difficult to obtain with thin layers of $BiVO_4$; after the first measurement, and at higher frequencies, a horizontal line was exhibited – similar to what is observed for an insulator. This could be due to the fact that vanadium at the surface of the layer dissolves after the first measurement and a bismuth rich surface (potentially Bi_2O_3) acts as an insulator and thus the electron donors are located far from the band edge (deep donors) and slow ionization occurs [327]. Flatband initially occurs at 0.18 V vs. RHE shown in Figure 60 at frequency of 1000 Hz, which suggests the conduction band is located at a slightly lower energy level than other $BiVO_4$ values reported to be around 0.02 V – 0.1 V vs. RHE [176, 298, 313, 316]. Nevertheless, this data should be interpreted with caution as impedance masurements for Mott Schottky relations can vary and produce inaccurate results. This data collected indicate that the flatband of sol-gel dip coated $BiVO_4$ samples is more positive than literature values of −0.05 V and 0.11 V vs. RHE [176, 217]. This may explain the larger onset potential experienced in linear voltage sweep measurements. Furthermore, a cathodic shift of the onset potential is experienced upon addition of Na_2SO_3, decreasing the onset potential to 0.35 V vs. RHE. This suggests there are still ohmic losses at the SCLJ which require a minimum overpotential of around 0.17 V when the surface kinetics are completely alleviated.

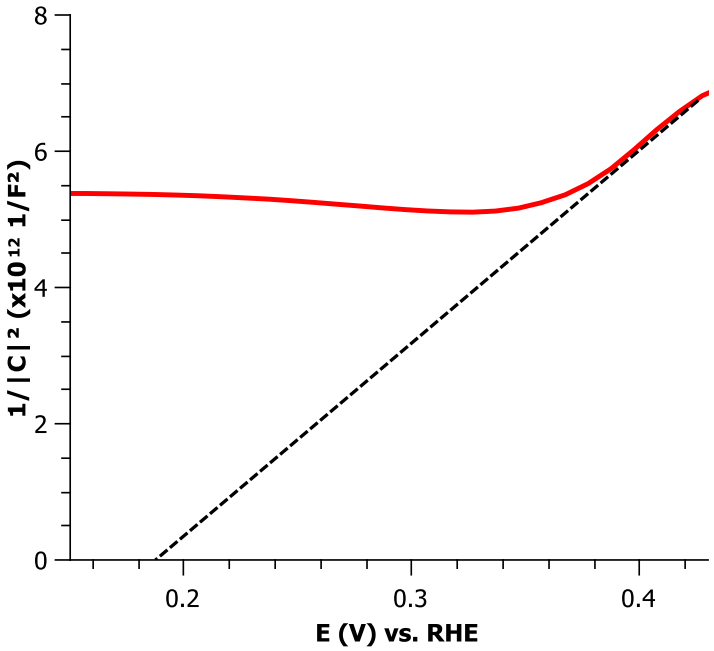

Figure 60: Mott Schottky plot of $BiVO_4$ in 1 M KPi (pH 7) 10 mV amplitude 1000 Hz

The separation and catalysis efficiency of the material was then measured as discussed before with equations (36) and (37) in II.3.3. Electrochemical Characterization. At 1.23 V vs. RHE in 1 M KPi (pH 7)

under AM1.5 illumination, with and without 1 M Na_2SO_3, $BiVO_4$ was measured to exhibit a separation efficiency of merely 30% and a surface catalytic efficiency of 8.5% (presented in Figure 61 and Table 14). The separation and catalysis efficiency at 0.5 – 2.2 V vs. RHE is displayed by the black curve in Figure 61, signifying that $BiVO_4$ is less than ideal in both surface catalysis and bulk separation for the OER. Nevertheless, at higher potentials these values increase, and notably the overall PEC performance is due to the surface catalytic properties which hinder the OER. This is possibly due to surface modification or surface blocking elements which inhibit the transfer of holes from $BiVO_4$ to the electrolyte. Its separation efficiency, (red curve) ranging from 0 – 60%, confirms hypotheses which inquire as to the poor conductivity of $BiVO_4$.

j (mA/cm²) at 1.23V vs. RHE	$BiVO_4$	
	dark	Light j_{H2O}
	0.002	0.149
with 1M Na_2SO_3	dark (h+)	light (h+) j_h+
	0.621	1.742

Table 14: Photocurrent of $BiVO_4$ at 1.23 V vs. RHE in 1 M KPi with and without 1 M Na_2SO_3 under AM1.5 illumination

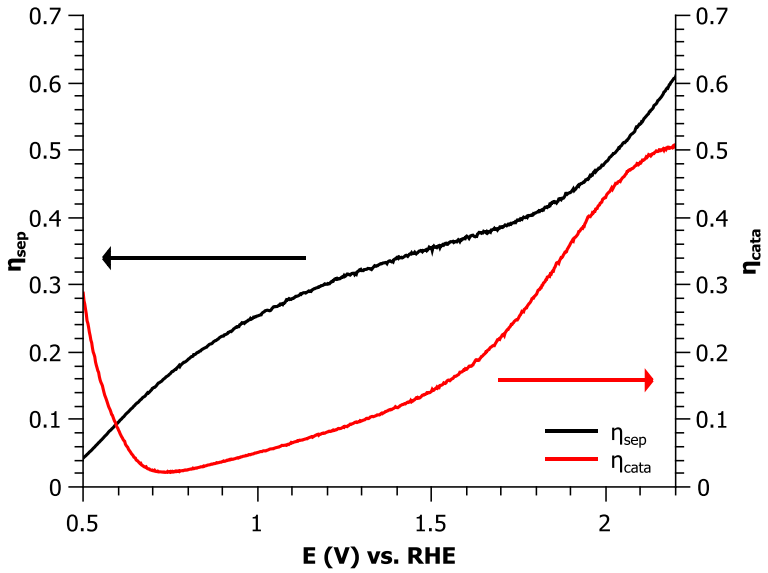

Figure 61: $BiVO_4$ separation (black) and surface catalysis (red) efficiency under AM1.5 illumination

The photocurrent as a function of illumination intensity in Figure 62 reveals a relatively linear curve, like WO_3, suggesting that charge carrier generation is additionally a limiting step in overall efficiency for the OER [275].

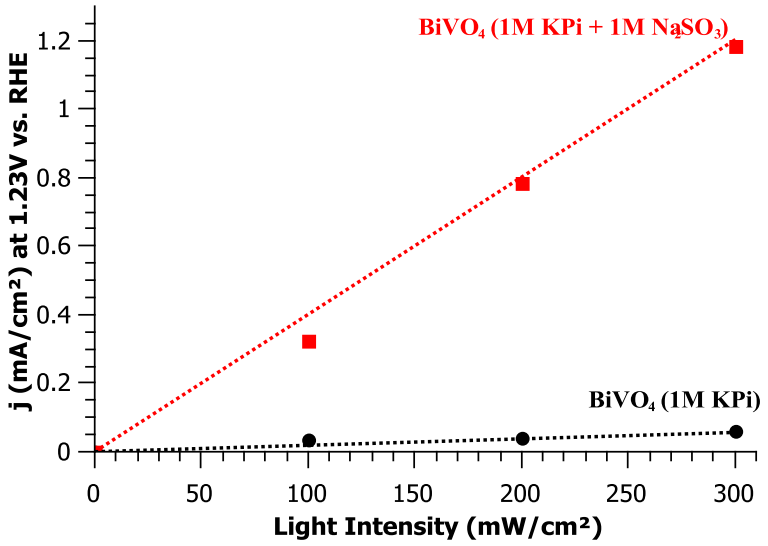

Figure 62: $BiVO_4$ photocurrent response to light intensity in 1 M KPi (black) and with 1 M Na_2SO_3 (red) (pH 7) at 1.23 V vs. RHE

The generation and separation of charge carriers is a limiting factor of $BiVO_4$ performance, requiring additional characterization measurements concerning IPCE and faradaic efficiencies give further insight to prospective progress necessary modifications to increase performance and overall efficiency of $BiVO_4$ for water splitting applications.

II.4.3.1. Quantum Efficiency

The incident photon to electron efficiency was measured at 300 W between 300 – 600 nm at 1.23 V vs. RHE in 1 M KPi (pH 7) under a 100 mW/cm² illumination (Figure 63). The response is similar to the UV-vis absorption spectra, suggesting two transitions which are very photoactive [176]. 10 layers of $BiVO_4$ annealed at 400°C and calcinated at 450°C for 1 hour possess an IPCE of 16% at 420 nm and 33.8% at 310 nm. These values are similar to those of Sayama et al., using the same sol-gel precursor and thin film deposition by spin coating deposition [176]. Chatchai et al. reproduced this process but measured considerably smaller IPCE values (<10%) [241]. Compared to literature values, a larger potential must be applied to obtain a fairly high IPCE on $BiVO_4$ photoelectrodes, which might be related to the high surface recombination of photogenerated electrons and holes; though the values obtained from sol-gel dip coating are relatively high for 1.23 V vs. RHE [300]. There is still progress to be made for the photoelectrocatalytic activity in sol-gel dip coated $BiVO_4$ considering the lower IPCE values compared to other techniques such as spray pyrolysis and electrodeposition, especially towards the visible range of the solar spectrum [217, 312]. Especially because IPCE can be misleading at low power illumination and overestimate IPCE values with $BiVO_4$ [150, 190].

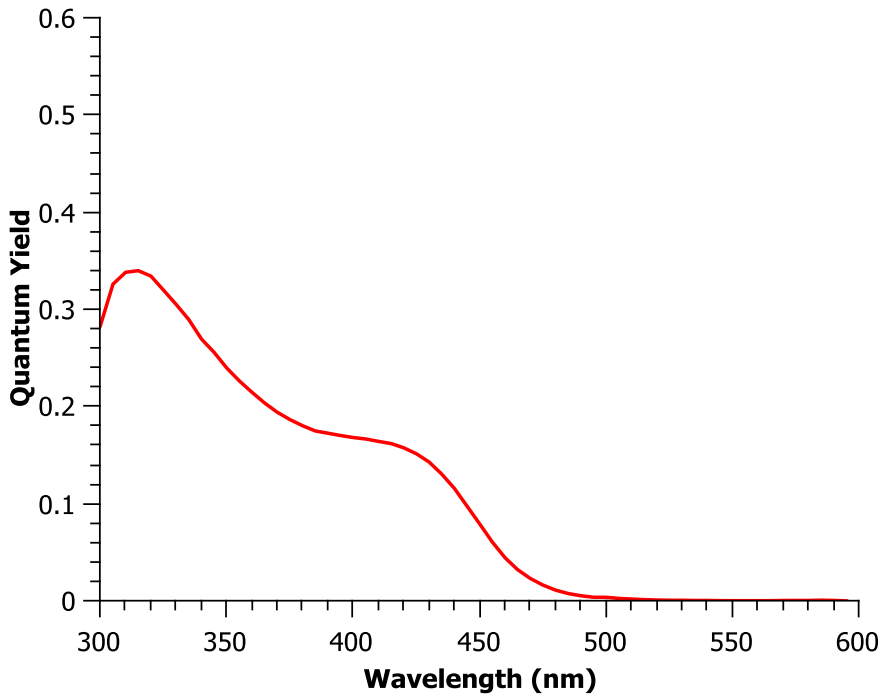

Figure 63: IPCE of optimized $BiVO_4$ calcinated at 450°C for 1 hour at 1.23 V vs. RHE in 1 M KPi (pH 7)

II.4.3.2. Stability

The stability of the photocurrent as function of time was also studied. We have seen a decrease of photocurrent over time with $BiVO_4$ in neutral conditions (1 M KPi pH 7) as seen below in Figure 64:

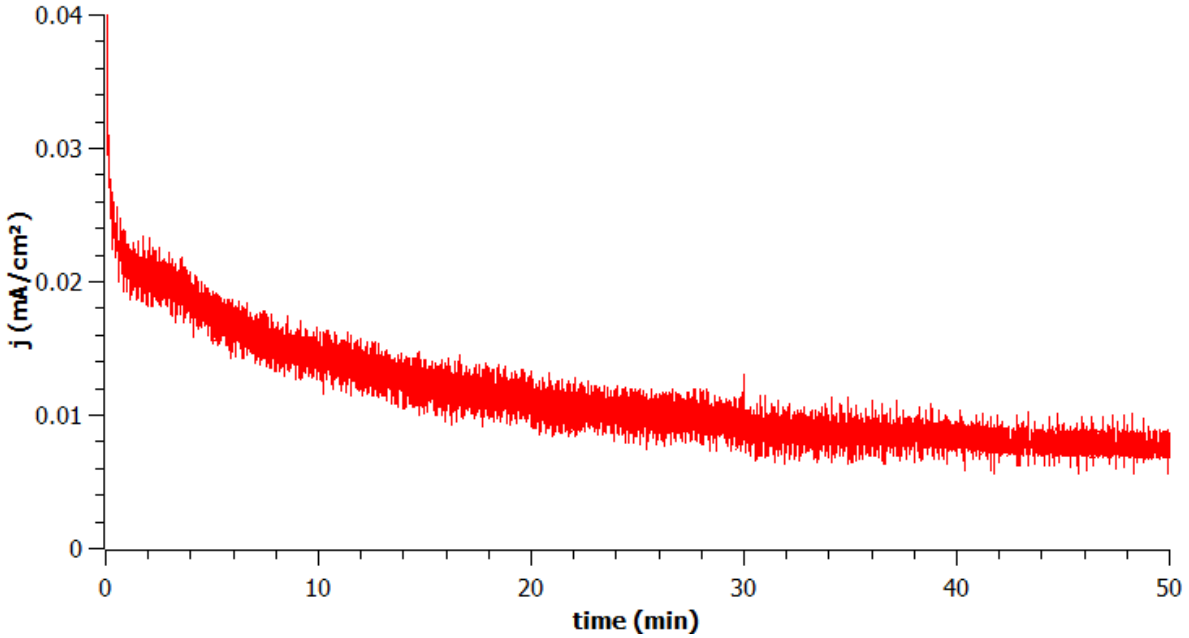

Figure 64: Photocurrent density of $BIVO_4$ at 1.23 V vs. RHE in 1 M KPi (pH 7) under 350 mW/cm²

This is potentially due to the accumulation of photogenerated holes at the surface due to poor kinetics for water oxidation resulting in severe anodic photocorrosion [160]. Decrease in photocurrent can also be attributed to bubble accumulation on the surface and a local change in pH due to the production of H^+ which may shift the redox potentials, slowing down the OER [145]. It is previously reported that the surface ratio of V:Bi decreases significantly during illumination, potentially due to the solubility of V^{5+}, resulting in a bismuth rich surface layer and a considerable reduction in photocurrent [145, 176, 193]. XPS results suggest that $BiVO_4$ after use increase in Bi:V ratio, confirming the dissolution of vanadium from the $BiVO_4$ surface, forming bismuth rich surfaces.

Controversially, upon faradaic testing and continuous irradiation at 250 mW/cm² for over an hour, $BiVO_4$ showed an increase in photocurrent, most likely to the increase in temperature from continuous illumination as well as good stability for over an hour (Figure 65). Though, this trend was not always reproducible, as discussed in the following chapter.

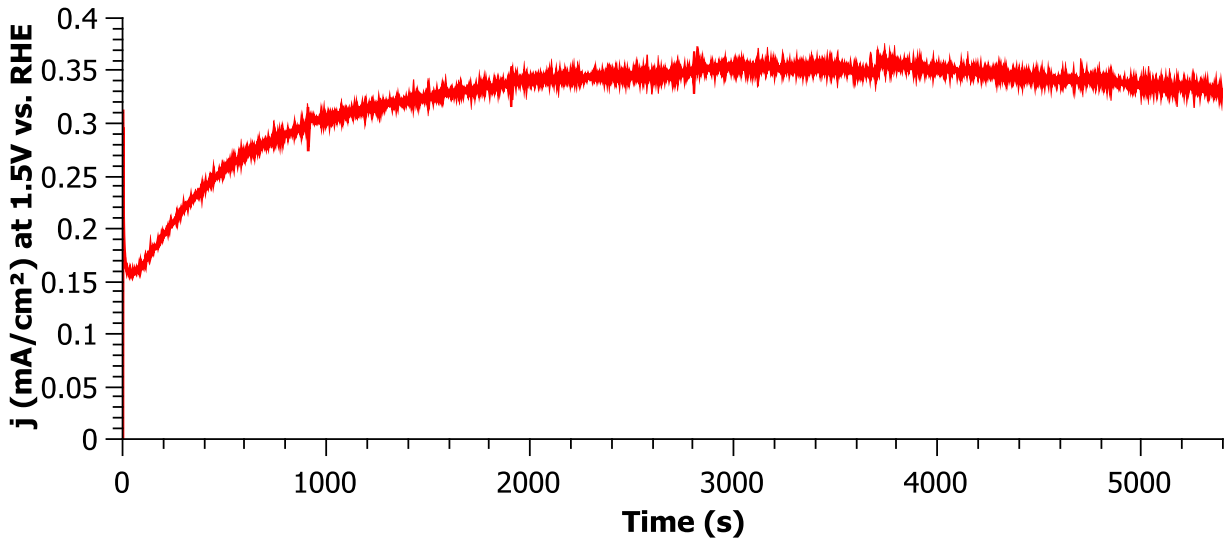

Figure 65: Photocurrent Density of 5 layers $BiVO_4$ calcinated at 400°C at 1.5 V vs. RHE in 1 M sodium phosphate (pH 7) under 250 mW/cm² illumination

II.4.3.3. Faradaic Efficiency

The faradaic efficiency of $BiVO_4$ was then measured to determine if the photocurrent exhibited by the thin films is participating in the formation of O_2 (Figure 66). Faradaic efficiency was measured with a Clark electrode and GC simultaneously to account for the O_2 dissolved in solution and present in the headspace. 5 layers of 400°C calcinated $BiVO_4$ were illuminated from the backside under 250 mW/cm² for 1.5 hours at 1.5 V vs. RHE in 1 M KPi (pH 7) which revealed large faradaic efficiencies approaching uniformity.

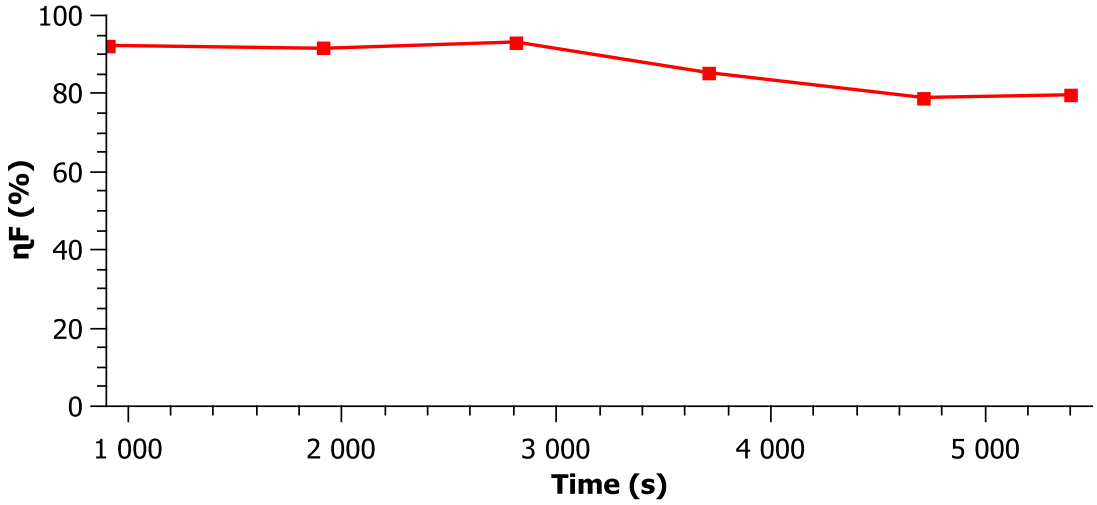

Figure 66: Faradaic efficiency of $BiVO_4$ at 1.5 V vs. RHE in 1 M phosphate buffer (pH 7) under 250 mW/cm²

(Note: the photocurrent associated with faradaic measurements is displayed in Figure 65, exhibiting stability in 1 M sodium phosphate (pH 7) solution during 1.5 hours at 1.5 V vs. RHE under 250 mW/cm² visible and ultraviolet illumination)

II.4.3.4. Modification

To improve the performances of the $BiVO_4$ electrodes, we also studied the role of the interfacial hole blocking layers, such as previously discussed SnO_2 between the back contact and $BiVO_4$. This was completed by placing a thin 10 – 20 nm layer of tin oxide between the FTO and $BiVO_4$ layers – using band gap engineering to redirect holes to the surface due to the lower energy position of the SnO_2 valence band [174]. Addition of SnO_2 in-between the FTO substrate and $BiVO_4$ was fabricated by sol-gel dip coating processes.

Ethanol and THF are added together in a vial followed by distilled water. Tin chloride is then added to the solution. The tin sol-gel has a concentration of 0.29 M and a pH of 1. The solution is left to stir with a magnetic stirrer for at least 1 day. Solution is best when used 2 – 3 days after synthesis. Solution can be used up to 1 month after synthesis. SnO_2 was dip coated at room temperature with < 3% relative humidity. Dip withdrawal speed was 1.62 mm/s resulting in an average of 10 nm/layer. 1 – 2 layer depositions of SnO_2 were generally deposited to be used as a hole blocking layer between FTO and $BiVO_4$ resulting in a dense 10 – 20 nm layer. An annealing step between layers at 350°C for 2 – 5 minutes was used, with a final calcination treatment of 400°C for 30 minutes.

This thin 10 – 20 nm of SnO_2 were successfully deposited on the FTO substrate, adopting the same crystal cassiterite structure as the commercial Asahi F:SnO_2. These dense SnO_2 layers were verified by XRD and EDX to be SnO_2. A FEG-SEM image is seen in below in Figure 67.

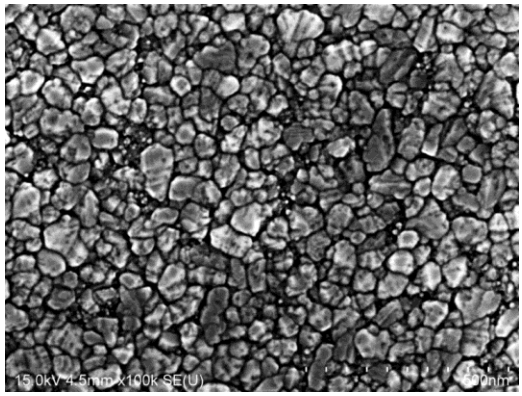

Figure 67: FEG-SEM image of dense SnO_2 on FTO by sol-gel dip coating process

These layers were very transparent, exhibiting little to no photoabsorption under visible light and measuring < 0.005 mA/cm² at 1.23 V vs. RHE in 1 M KPi (pH 7) upon addition of UV light (< 400 nm) in linear voltage sweeps. The *J-E* curves in 1 M KPi (pH 7) under 300 mW/cm² with and without UV light are reported in Figure 68 for SnO_2/$BiVO_4$ and $BiVO_4$ as black and red curves respectively. The performance results in a more diode-corrected photocurrent curve; the improvement was remarkable (shown in Figure 68); however, the onset potential of $BiVO_4$ remains rather large.

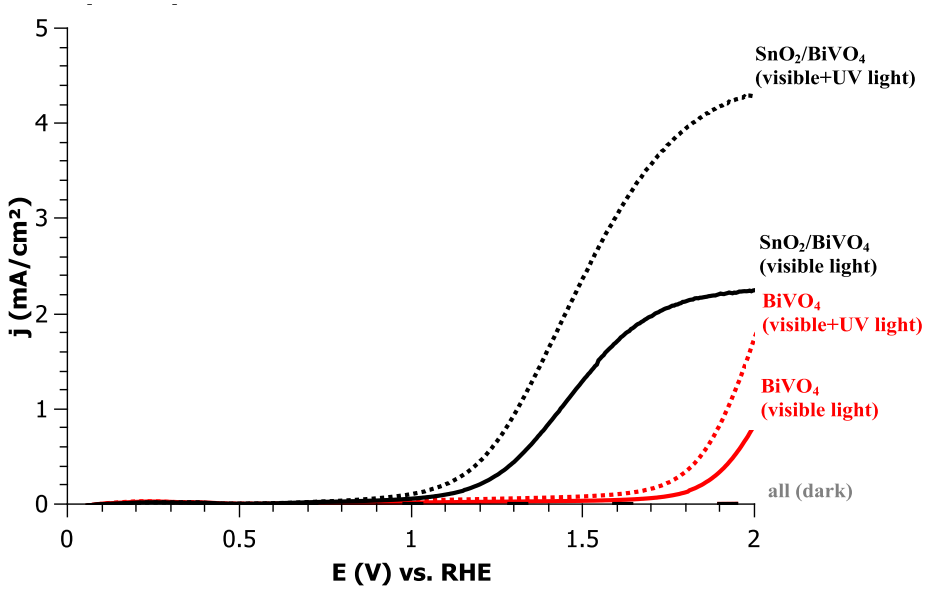

Figure 68: 5 layers of 400°C calcinated $BiVO_4$ (red) and SnO_2/$BiVO_4$ (black) in 1 M KPi (pH 7) under 300 mW/cm² with UV light (dotted) and without (solid)

Upon optimization with thermal temperature increase with annealing and calcination steps, the impact of this mirror blocking layer onto optimized $BiVO_4$ was studied. Linear voltage sweep in the dark and light of optimized $BiVO_4$ and $SnO_2/BiVO_4$ are shown below in Figure 69 in 1 M KPi (pH 7) and then in Figure 70 with sacrificial agent 1 M Na_2SO_3 under visible light at 300 mW/cm² (solid lines) and upon addition of UV light at 350 mW/cm² (dotted lines). The difference between the *J-E* curves was less important upon implementation of SnO_2 with optimized $BiVO_4$. These results indicate that upon temperature increase and optimization, this mirror blocking layer was less important, suggesting that recombination at the $BiVO_4$/FTO interface is not the most significant limiting factor for the photoactivity of $BiVO_4$ [146].

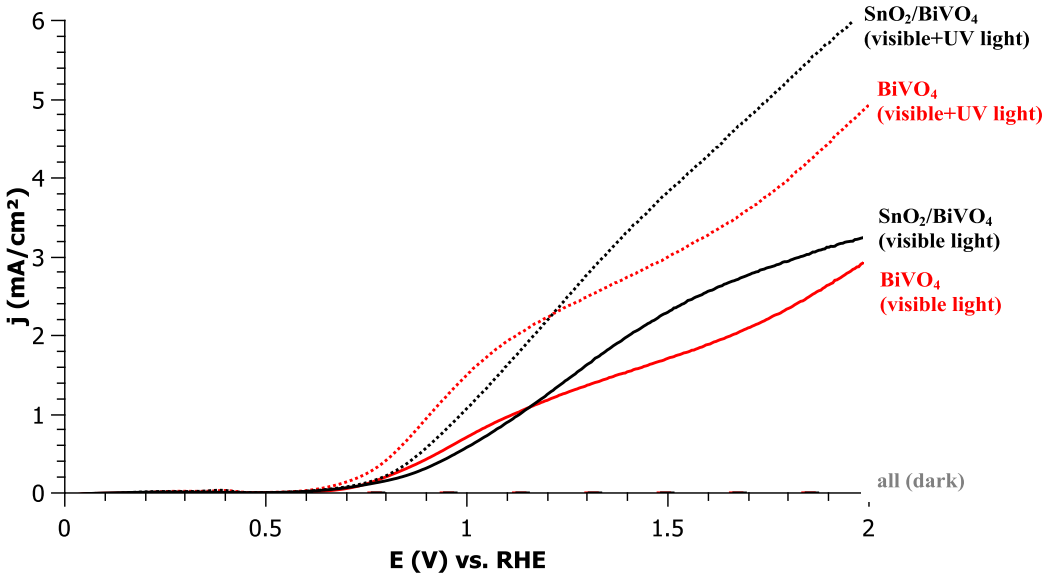

Figure 69: 10 layers $BiVO_4$ (black) and $SnO_2/BiVO_4$ (red) calcinated at 450°C for 1 hour in 1 M KPi (pH 7) under 300 mW/cm² visible (solid) and upon the addition of UV light (dotted)

Finally, adding SnO_2 layers modifies the *J-E* behavior but the surface still requires modification to ease the charge transfer to perform the OER, as seen with the photocurrent increase upon addition of a sacrificial reagent. The increase in photocurrent suggests that holes are redirected to the surface for use; though upon addition of 1 M Na_2SO_3 to relieve the catalysis efficiency, $BiVO_4$ without SnO_2 is more performant, suggesting addition of potential recombination sites between materials. This suggests that SnO_2 mass transport is slightly reduced in the composite $SnO_2/BiVO_4$ photoanode when surface kinetics are alleviated, most likely due to recombination at the $SnO_2/BiVO_4$ interface.

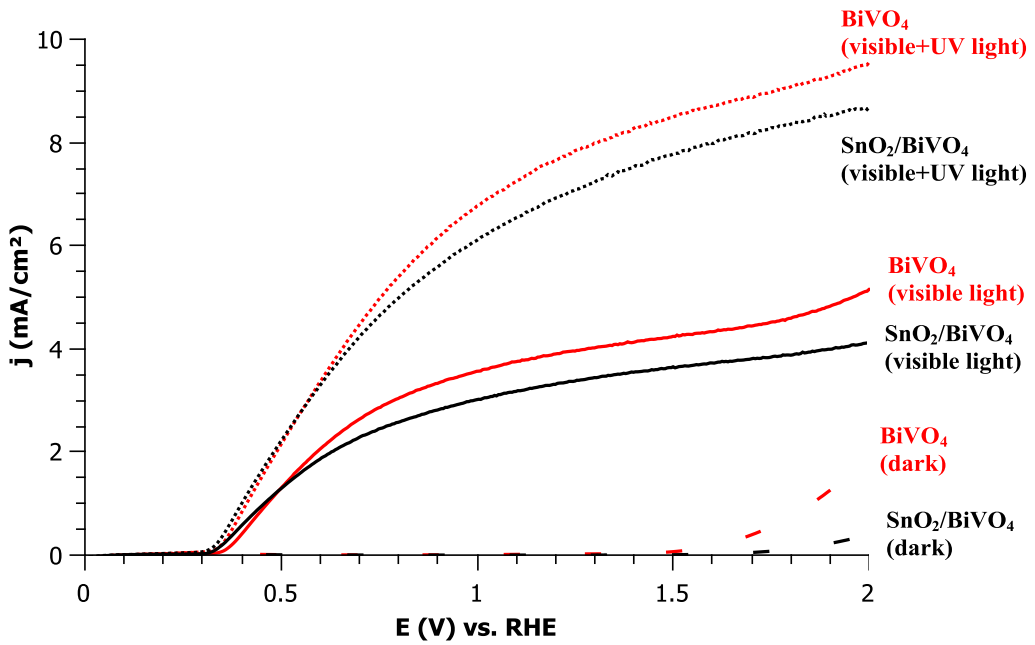

Figure 70: Optimized 10 layers $BiVO_4$ calcinated in 450°C 1 hour in 1 M KPi and 1 M Na_2SO_3 under 300 mW/cm² with and without UV light

To further understand the role of SnO_2 blocking layer, phototransient measurements were completed using a shutter for illumination at 100 mW/cm² and dark measurements for $BiVO_4$ and $SnO_2/BiVO_4$ thin films. The results are reported Figure 71 for SnO_2 (black) and $BiVO_4$ (red). The photoresponse of $BiVO_4$ possesses little to no photocurrent transient suggesting there are no large accumulation of charges or massive recombination which occurs in the material or at the SCLJ. When light reaches the sample, photogenerated holes travel to the SCLJ and accumulate because of the slow OER kinetics [150, 276], accumulation of electrons in the bulk due to slow electron transport [30], or because carriers oxidize trap states in the bulk and on the surface [110, 328]. This induces a sharp anodic current peak which decays as the accumulation process perturbs the charge distribution of the space charge region until equilibrium is reached between water oxidation and charge recombination. With $BiVO_4$ there is no cathodic transient peak observed when the light is turned off, suggesting there are no electrons diffusing from the external circuit and recombining with the accumulated holes at the SCLJ, nor accumulation of holes which act as a possible recombination mechanism [30, 329]. In general, the presence of transients diminishes at higher potentials because a larger proportion of holes have sufficient potential to oxidize water, considering an increase in potential results in larger band bending and augments the electric field in the depletion zone resulting in less charge recombination [330]. Nevertheless upon adding SnO_2 as a mirror blocking layer, transient peaks are pronounced, most likely due to the increased number of holes arriving at the SCLJ which are unable to be used due to slow OER kinetics and therefore accumulate. Upon the addition of

Na_2SO_3, these transient peaks disappear, confirming the accumulation of holes at the SCLJ due to the slow OER kinetics between $BiVO_4$ and the electrolyte [150].

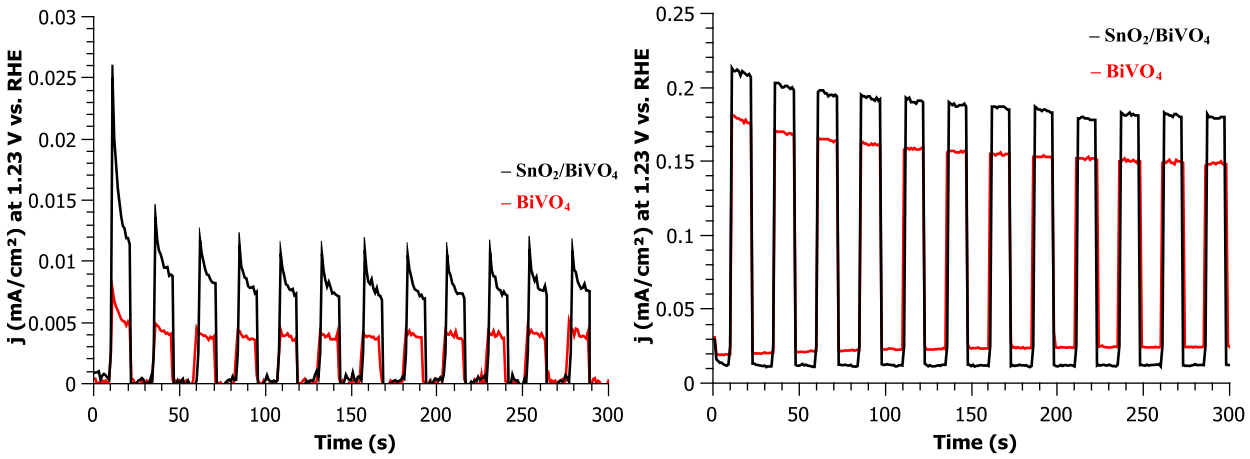

Figure 71: Photocurrent of 5 layers 400°C $BiVO_4$ and $SnO_2/BiVO_4$ at 1.23 V vs. RHE in 1M KPi (left) and with 1 M Na_2SO_3 (right) under 100 mW/cm²

These results indicate that the performances of the $BiVO_4$ layers are limited either by the poor e- conductivity in the layer or/and by the poor kinetics of holes at the $BiVO_4$/electrolyte interface. These two hypotheses are explored in the following section.

TRMC results indicate that 5 layers of 400°C treated $BiVO_4$ exhibit poor photoconductivity. To further modify this property and increase the performance of $BiVO_4$, doping with Mo and W was attempted by introducing 0 – 10% atomic amounts of either tungsten or molybdenum into the sol-gel precursor. Unfortunately, the sol-gel precursor became opaque upon addition of several tungsten and molybdenum salts, suggesting poor solubility. Several attempts at doping $BiVO_4$ with different tungsten salts were undetectable in thin sol-gel dip coated films by EDX measurements and showed little to no difference from undoped $BiVO_4$ photoanodes in photoelectrochemical performance. Therefore, doping $BiVO_4$ with tungsten was deemed unachievable by this sol-gel dip coating method. However, doping $BiVO_4$ with molybdenum was successful at variable quantities. After different attempts with variable sources of molybdenum (e.g. ammonium heptamolybdate) and different solvents, MoO_3 was found to be more soluble and successful in $BiVO_4$ doping, even if it was difficult to get reproducible results by this sol-gel dip coating method. The most successful attempts in the film synthesis revealed more dense microstructure compared to undoped $BiVO_4$ (shown in Figure 72 B). The onset potential shifted from 1.2 V vs. RHE to 0.7 V vs. RHE upon the change in composition and layer density (Figure 72 A). This improvement in performances seems simply due to the effect of doping on the crystal structure which influences a more dense crystal network.

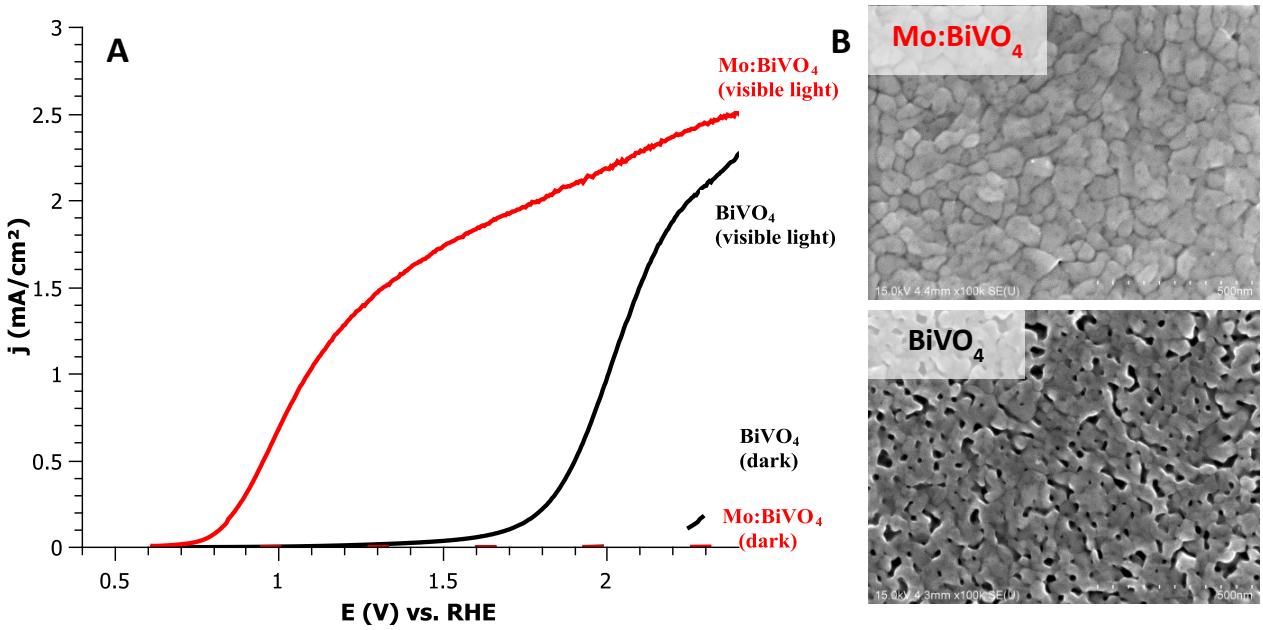

Figure 72: (A) Visible light photoresponse to $BiVO_4$ and Mo doped $BiVO_4$ in 1 M KPi (pH 7) under 300 mW/cm² illumination and (B) corresponding FEG-SEM images

Upon increased thickness and denser films, this trend was observed as well, reinforcing the hypothesis of a continuous microstructure for good charge transport throughout the film. EDX and XPS measurements suggested 3.5 – 5% atomic doping of molybdenum, when in fact excess molybdenum was added to the sol-gel precursor solution.

Thus, the doping efforts were diverted towards surface co-catalyst addition in hopes for better reproducibility to reduce recombination centers at the surface and increase $BiVO_4$ photoelectrocatalytic performance [314]. Literature reports suggest IrO_2 does not function with $BiVO_4$ and that Pt does not exhibit photostability over time [146, 316]. Therefore, cobalt, nickel, and iron were the focus for co-catalyst materials as to remain in the frame of using abundant, non–noble metals. This first attempt at catalyst deposition consisted of photo-assisted electrodeposition of Co-Pi [226]. 15 – 25 % atomic cobalt was detected by EDX referenced to $BiVO_4$. The photoelectrochemical performance did not exhibit a reduction in onset potential or an increase in photocurrent.

Following Co-Pi, we decided to test other photocatalysts such as FeOOH [147, 160, 217, 232]. FeOOH was photo-assisted electrodeposited onto $BiVO_4$ from previously reported procedure resulting in 5% atomic Fe detected by EDX on the surface [217]. Once again there was neither a decrease in overpotential nor an increase in photocurrent. Alternatively NiOOH was deposited according to the same procedure, though nickel was not detectable by EDX. The photoelectrochemical performance did not show a decrease

in onset potential, though the photocurrent was slightly increased from 0.035 mA/cm² to 0.08 mA/cm² in 1 M KPi (pH 7) under 350mW/cm² (300 – 900 nm) at 1.23 V vs. RHE (data not shown). This procedure was irreproducible, though the coupling with nickel based co-catalyst continued to be an area of interest.

Thus the nickel alternative of Co-Pi, nickel borate ($NiBO_3$ commonly denoted NiB_i), was attempted by simple means of electrodeposition [230]. No nickel was detected in XRD spectra due to its amorphous nature, though FEG-SEM images and EDX revealed porous flakes of nickel based layers on $BiVO_4$ (seen in Figure 73). UV-vis absorption revealed a slight increase in absorption and light redshift.

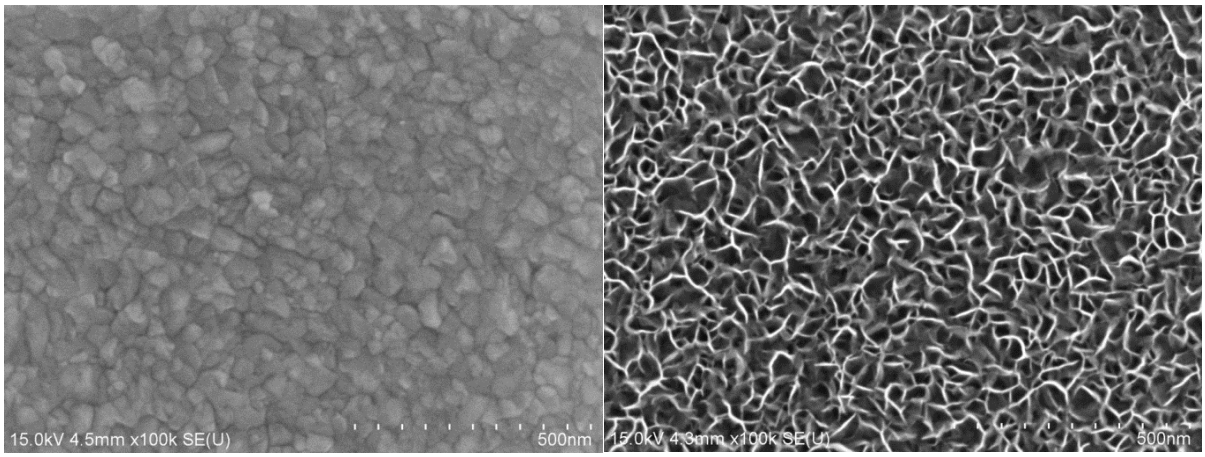

Figure 73: FEG-SEM images of $BiVO_4$ (left) and $BiVO_4/NiB_i$ (right)

The first linear voltage sweep of $BiVO_4/NiB_i$ suggests there is a 200 mV cathodic shift in onset potential (seen in Figure 74) suggested successful loading of nickel onto $BiVO_4$ [319]. This is thought to be the activation of the NiOOH, which is understood to be small nano-sized NiOOH centers [230, 331]. The second linear voltage sweep revealed that there is no reduction in onset potential and that the $BiVO_4/NiB_i$ photoanode acts similarly to the bare $BiVO_4$ photoanode; nevertheless, there is a slight increase in photocurrent seen under visible illumination in Figure 74 and upon addition of UV light seen in Figure 75. The increase of photocurrent at low potentials, suggests that nickel does help to extract charges at the SCLJ when compared to the bare $BiVO_4$ under 300 – 900 nm illumination (Figure 74). Upon faradaic testing in the complete PEC device, addition of a nickel co-catalyst suggested prolonged stability. (See chapter: III.8.1.3. $SnO_2/BiVO_4/NiB_i$ and $CuO/BaTiO_3$).

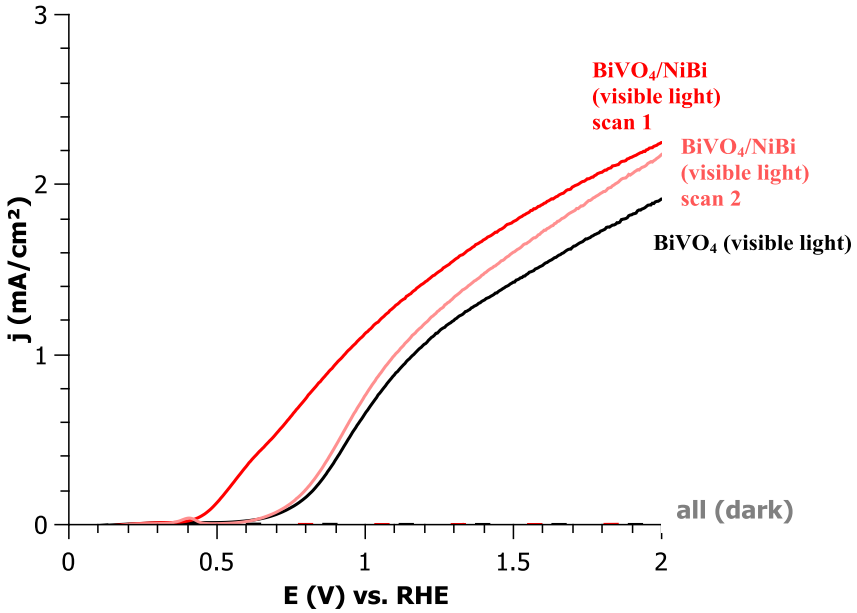

Figure 74: Linear voltage sweep of $BiVO_4$ (black) and $BiVO_4$/NiBi (red and pink) under 300 mW/cm² visible light (400 – 900 nm) in 1 M KPi (pH 7)

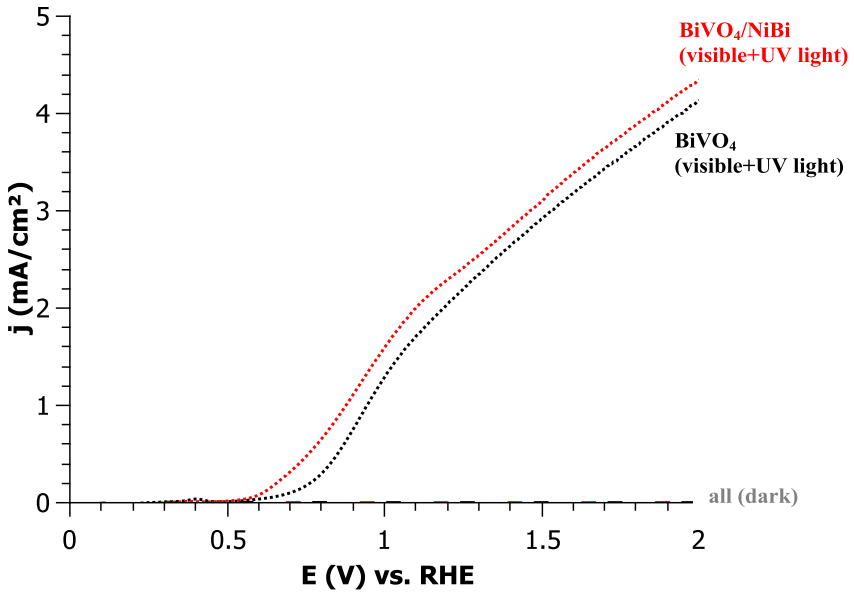

Figure 75: Linear voltage sweep of $BiVO_4$ (black) and $BiVO_4$/NiBi (red) under 350 mW/cm² visible and UV light (300 – 900 nm) in 1 M KPi (pH 7)

Additional IPCE measurements were effectuated from 600 – 300 nm to determine if the modifications concerning the SnO_2 interfacial layer and NiB_i co-catalyst had an effect on the quantum yield of $BiVO_4$ based photoanodes (displayed in Figure 76). Unmodified $BiVO_4$ reached a maximum IPCE of 33.8% at 310 nm (red curve in Figure 76), upon insertion of SnO_2 hole blocking layer this increased to 52.5% (pink

curve). Addition of a NiB_i co-catalyst on the surface increased the IPCE to 53.2% (shown in grey curve), and the combination of SnO_2 and NiBi with $BiVO_4$ increased the IPCE at 310nm to 55.9% (black curve). These values are considerable for sol-gel dip coated $BiVO_4$ compared to spin coated or sprayed $BiVO_4$ [151, 174, 176, 190, 320], though far from literature values of sputtered or electrochemically deposited $BiVO_4$, which absorb much more towards the visible range and have maximum IPCE values near unity [155, 217].

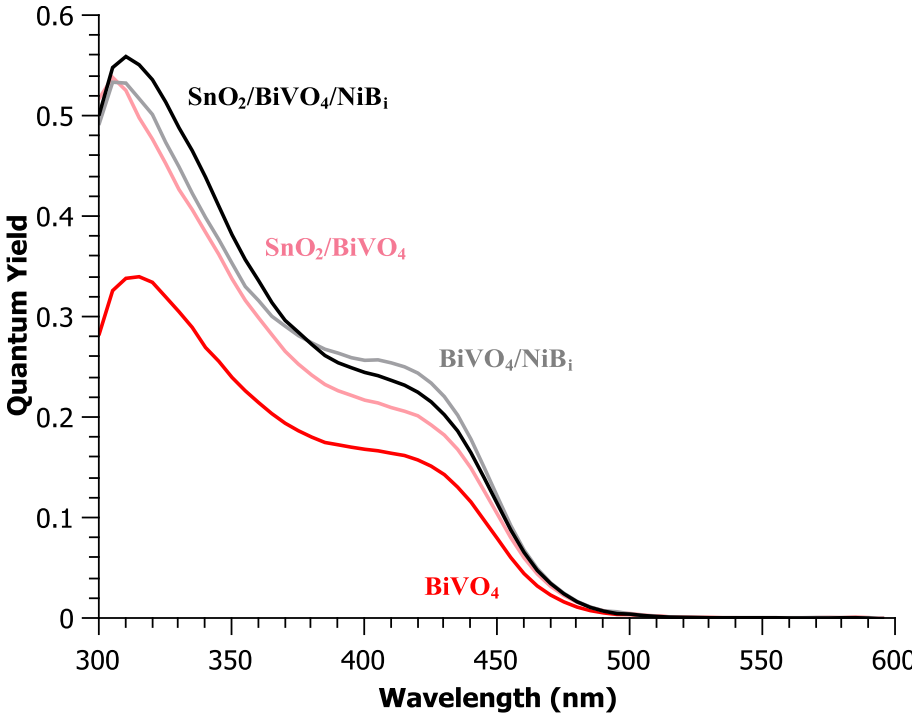

Figure 76: IPCE of $BiVO_4$ and modified $BiVO_4$ in 1 M KPi at 1.23 V vs. RHE

FEG-SEM images suggest that the NiB_i layer measures about 55 nm in thickness, slightly less than the thickness of the $BiVO_4$ layer underneath. Unfortunately, after photoelectrochemical testing in 1 M KPi (pH 7), post-mortem FEG-SEM images suggest the NiB_i is unstable and does not remain on the surface. Cross section images of $SnO_2/BiVO_4/NiB_i$ before and after use are shown below in Figure 77:

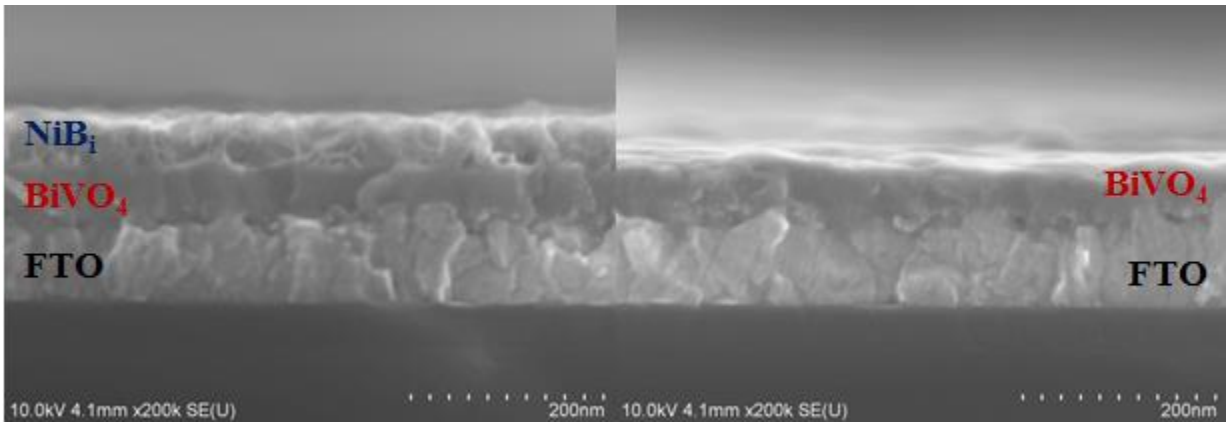

Figure 77: FEG-SEM images of $SnO_2/BiVO_4/NiB_i$ before (left) and after (right) use in 1 M KPi

Nickel borate is a promising co-catalyst for the OER, yet is more stable in basic conditions than neutral conditions [224]. Further optimization to reduce the onset potential and increase the faradaic efficiency and co-catalyst stability are still needed for $BiVO_4$. Yet, seen the initial competitive performance, our sol-gel dip coated thin films of $BiVO_4$ is a promising photoanode candidate for water splitting applications.

II.4.4. CONCLUSIONS

$BiVO_4$ was successfully fabricated by sol-gel dip coating techniques and verified by XRD, EDX, and XPS to be monoclinic scheelite possessing a band gap of 2.5 eV. These thin film electrodes are yellow and considerably transparent to light at wavelengths larger than 490 nm. $BiVO_4$ measuring an average of 75 nm for 10 layer deposition on FTO calcinated at an optimum temperature of 450°C with annealing in-between each layer at 400 – 450°C. This condition was determined to be the most active, revealing photocurrents of up to 1.8 mA/cm² in 1 M KPi (pH 7) under 350 mW/cm² Xe lamp source (300 – 900 nm) at water splitting potentials. Upon addition of a sacrificial agent, Na_2SO_3 alleviating the surface kinetic issues, this photocurrent can increase up to 8.9 mA/cm² at 1.23 V vs. RHE under the same conditions suggesting surface catalytic activity is a bottleneck for the OER using $BiVO_4$. Using equation (32) the ABPE efficiency based on the photocurrent achieved by $BiVO_4$ is 0.3%. Upon employment of a sacrificial reagent this value drastically increases to near 1.6%, suggesting that increase in surface OER kinetics hold potential for increased water splitting performance. Nevertheless, these estimations do not include the faradaic contribution and thus is an overestimate and not applicable for use with sacrificial reagents.

$BiVO_4$ suffers from a large onset potential considering its flatband position near 0.18 V vs. RHE. Denser more continuous networks of $BiVO_4$ thin films display lower onset potentials than nanostructured or non-continuous crystal, producing higher photocurrents at lower potentials. $BiVO_4$ is able to absorb 79% of the theoretical AM1.5G spectrum according to the absorption spectrum, though suffers from low conductivity and surface recombination at the SCLJ, therefore limiting its overall PEC performance. Sol-geld dip

coated thin films of $BiVO_4$, from absorption characteristics, can theoretically generate 5.6 mA/cm² under AM1.5 conditions. Nevertheless upon photoelectrochemical tests at AM1.5 irradiation in potassium phosphate, the photocurrent was 0.149 mA/cm², suggesting only 2% of the potential photocurrent is reached with these photoanodes. Charge separation efficiency is generally less than 60%, operating at 30% at water splitting potentials. The surface catalysis efficiency measured to be even less, with only 8.5% efficiency at water splitting potentials, suggesting the foremost bottleneck process in total photoanode performance. Insertion of a 10 – 20 nm SnO_2 hole mirror layer increased the saturation photocurrent of $BiVO_4$, nevertheless, it did not reduce the onset potential.

The stability of $BiVO_4$ is in question, exhibiting irreproducible stability (discussed in chapter III). The possibility of dissolution of V^{5+} may create bismuth rich surfaces and create a passivation layer which is unideal for surface catalysis and the OER [176]. Deposition of nickel borate co-catalyst slightly increased the photocurrent and improved long term stability, but failed to greatly decrease the onset photocurrent. Increasing overall photocurrent by incorporating a SnO_2 interfacial layer and NiB_i co-catalyst leads to higher IPCE values reaching 55% at 310 nm, though conductivity in the material as well as a potential bismuth rich surface could be potential limitations for IPCE and overall performance. Nevertheless the stability of NiB_i and $BiVO_4$ remain in question and further research is needed in order to ensure the long term stability of $BiVO_4$ for water splitting technologies.

Overall, the sol-gel dip coated 75 nm thin films of $BiVO_4$ deposited on FTO are promising for future photoanode water splitting tandem dual photosystem application. The films are transparent, allowing light to reach a complementary photocathode and photocurrent values upon optimization are competitive with other research groups [176]. Our fabrication process can be further optimized, including surface modification, to further increase performance and efficiency while maintaining this low cost, facile, sol-gel dip coating process; easily adjusted for scale up production for industrial application.

II.5. Composite Photoanode

II.5.1. Introduction

Seeing as WO_3 suffers from stability issues in neutral pH environments and low faradaic efficiencies, a form of passivation or protective layer can enable it to function in anodic, neutral, OER accommodating environments. This has already been illustrated by several groups using Al_2O_3, TiO_2, and most commonly $BiVO_4$ [135, 142, 147, 154, 164, 170, 172, 177, 184, 241, 259, 313, 314, 332]. WO_3 and $BiVO_4$ have the potential to be combined in a n-n tandem junction due to the position of the E_C and E_V energy levels of both materials. Placing photoabsorbers to form composite electrodes, allow for increased range of light absorption, which can surpass theoretical efficiency values previously discoursed [111]. Additionally, the E_C and E_V of WO_3 are more positive than the respective conduction and valence bands of $BiVO_4$ which can theoretically influence charge separation by diffusion; energetically directing electrons to flow to the TCO contact and arrive at the photocathode for proton reduction and in adjunction with holes traveling to the SCLJ surface to participate in the production of O_2 in neutral conditions. This band gap engineering concept is displayed in a band diagram in Figure 78. This material composite aims to utilize the high IPCE and conductivity of WO_3 in combination with the stability and increased faradaic efficiencies of $BiVO_4$. Additionally, the hole mirror concept by addition of SnO_2 between the TCO and $BiVO_4$ can be incorporated to avoid defect states between the WO_3 and $BiVO_4$ materials.

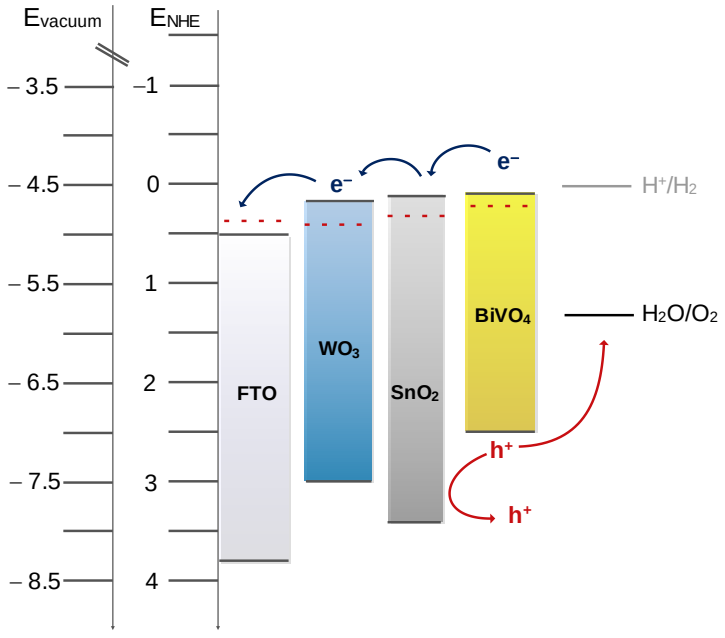

Figure 78: Coupling of WO_3, SnO_2, and $BiVO_4$ for n-n tandem photoanode

Below, Table 15 displays $WO_3/BiVO_4$ based composite photoanodes and their respective photocurrents at the OER potential of 1.23 V vs. RHE (unless otherwise stated).

Year	Composite Photoanode	Deposition Technique	Thickness (nm)	Electrolyte (pH)	P_{in} (mW/cm²)	j	Ref
2009	FTO/WO_3/$BiVO_4$	Spin coating	1100	0.5 M Na_2SO_4 (pH 5.8)	50 (> 420 nm)	0.12 mA/cm² *(1.5V vs. RHE)*	[241]
2011	FTO/WO_3/$BiVO_4$	Layer by layer	3000	0.5 M Na_2SO_4 (pH 6.6)	AM1.5	1.74 mA/cm²	[313]
2011	FTO/WO_3/$BiVO_4$	Solvothermal and spin coating	400	0.5 M Na_2SO_4	100	1.6 mA/cm²	[172]
2012	FTO/$BiVO_4$/SnO_2/WO_3 (double stacked)	Wet coating	80 / 190	0.1 M $KHCO_3$ (pH 8)	AM1.5	4.15 mA/cm²	[314]
2012	FTO/WO_3/Mo:$BiVO_4$	Hydrothermal	2000 / 50	0.5 M Na_2SO_4	AM1.5	1.7 mA/cm²	[164]
2013	ITO/WO_3/$BiVO_4$	Reactive sputtering	100 / 100	0.1 M PO_4 buffer (pH 7)	AM1.5	1 mA/cm²	[154]
2013	FTO/WO_3/$BiVO_4$	Spin coating	250	0.1 M $KHCO_3$ (pH 6.8)	AM1.5	3.43 mA/cm²	[177]
2013	FTO/WO_3/Mo:$BiVO_4$/ Co-Pi	Spin coating	600 / 550	0.1 M PO_4 buffer (pH 7)	AM1.5G	2.5 mA/cm²	[170]
2014	FTO/WO_3/$BiVO_4$	Spin coating and drop casting	2500 / 60	0.5 M KPi (pH 8)	85	3.1 mA/cm²	[184]
2014	FTO/WO_3/$BiVO_4$/ FeOOH + NiOOH	E-beam evaporation and drop casting	5500	0.5 M Na_2SO_4 (pH 7)	AM1.5G	5.35 mA/cm²	[147]
2015	FTO/WO_3/$BiVO_4$/Co-Pi	Glancing angle deposition and electrodeposition	2500 / 25	0.1 M KPi (pH 7)	AM1.5G	6.72 mA/cm²	[213, 332]

Table 15: State of the art composite $WO_3/BiVO_4$ photoanodes

The most performant composite $WO_3/BiVO_4$ photoanodes are due to the nanostructuration of WO_3. Often nanorods are fabricated to increase light absorption as well as increase charge extrapolation, adhering to the minority charge carrier diffusion length of 150 nm in WO_3 [58, 215]. The layers of $BiVO_4$ are generally thin, enough to protect WO_3 and assist in charge separation, protection of WO_3, and surface catalysis for the OER. Nevertheless, many of these composite photoanodes perform just as well as WO_3 or $BiVO_4$ alone, therefore the question of necessity of coupling these two photoelectrocatalytic materials is debatable when nanostructuration is not instigated. To fabricate composite photoanodes, both sol-gel dip

coating methods of WO_3 and $BiVO_4$ previously discussed were simply combined in order to understand if sol-gel dip coated thin films of WO_3 and $BiVO_4$ can be combined for increased performance for use as an n-photoanode in a photoelectrocatalytic dual photosystem tandem cell. These photoanodes are fabricated, characterized, and optimized according to photoelectrochemical performance.

II.5.2 Synthesis and Characterization

II.5.2.1. Synthesis

$WO_3/SnO_2/BiVO_4$ composite photoanodes were fabricated by sol-gel dip coating methods, simply integrating the optimized materials previously discussed in this chapter. Initially WO_3 and $BiVO_4$ were deposited by dipping several layers with annealing between each layer. First WO_3 is deposited onto the FTO substrate by dip coating processes (shown below as A in Figure 79), using the sol-gel process discussed in II.2. Fabrication Methods. After several layers, with annealing treatments at 350°C for 1 – 2 minutes between each layer. SnO_2 was then deposited onto the WO_3 thin film by sol-gel dip coating processes, generally 1 – 2 layers resulting in a 10 – 20 nm layer (B in Figure 79). An annealing treatment between these layers was effectuated at 350°C for 1 – 2 minutes. Finally, $BiVO_4$ was then deposited on top of the WO_3 (C in Figure 79) by dip coating methods previously discussed in chapter reference with an annealing step at 400°C for 1 – 2 minutes between layers.

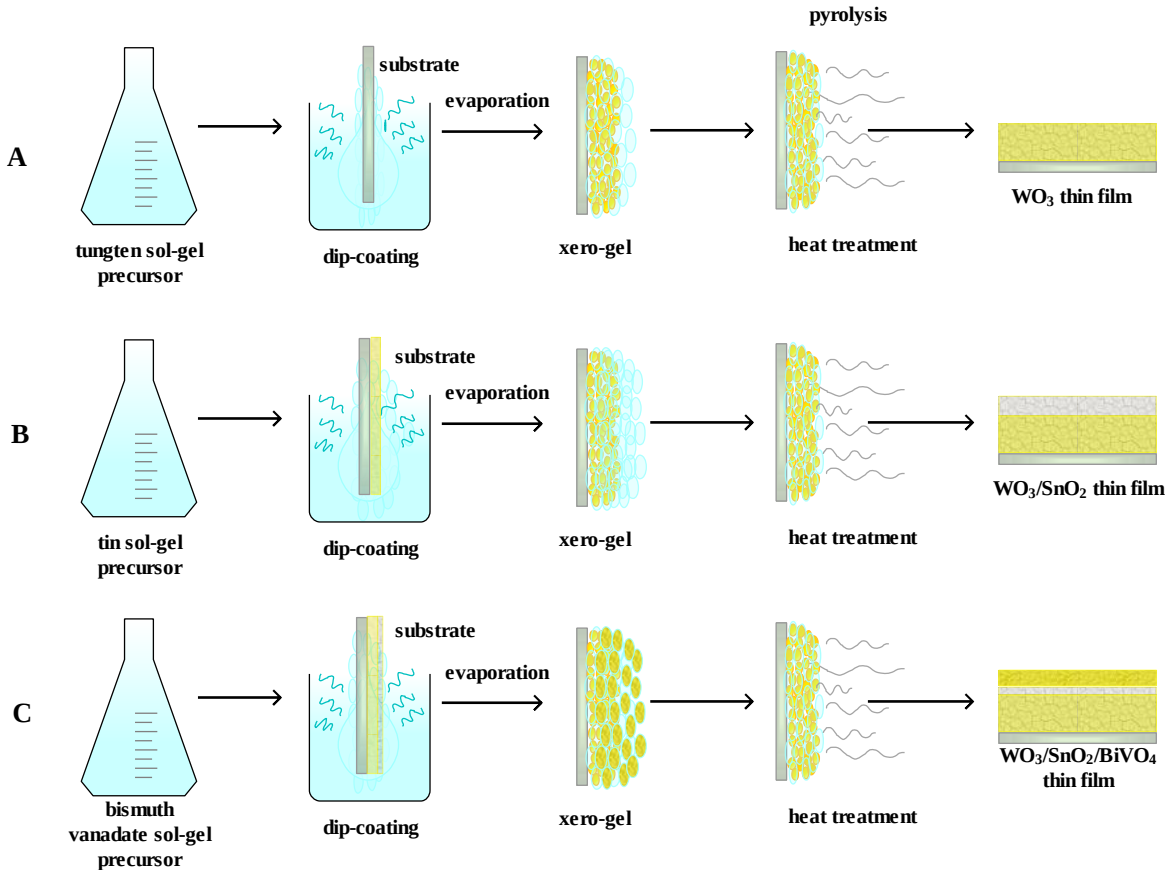

Figure 79: Sol-gel dip coating procedure schema for composite photoanodes

It was discovered that calcination of each material, after ideal thickness was achieved, performed better than one calcination treatment for all materials once in the xero-gel form on the substrate. In this combination, WO_3 does not require a mesoporous microstructure considering complete coverage of $BiVO_4$ is difficult upon a mesoporous surface and that the WO_3 is not directly exposed to the electrolyte at the SCLJ. Dense WO_3 was employed as the photoabsorber and $BiVO_4$ deposited on top to protect WO_3 from dissolution in neutral conditions while favoring the OER, preferred from O_2 detection measurements done with $BiVO_4$. Additionally, SnO_2 was layer introduced as a hole blocking layer between WO_3 and $BiVO_4$ by means of sol-gel dip coating deposition.

II.5.3. Structural Characterization

The XRD spectrum of the composite materials possesses a large WO_3 signal, indicating that WO_3 represents the majority volume of the composite photoanode thickness. This spectrum is displayed in Figure 80 along with the XRD spectra of WO_3 for comparison. The characteristic peak of $BiVO_4$ is apparent at $2\Theta = 28.9°$ and 30.5°, indicating the presence of monoclinic $BiVO_4$. FTO and the SnO_2 layer are indiscernible, yet present peaks attributed to the FTO and SnO_2 at 27°, 34°, and 38° (JCPDS 01-70-

4175). Below Figure 80 displays the XRD pattern of the composite photoanode with FTO or SnO_2 peaks labeled with a black triangle, WO_3 a blue square, and $BiVO_4$ red circle.

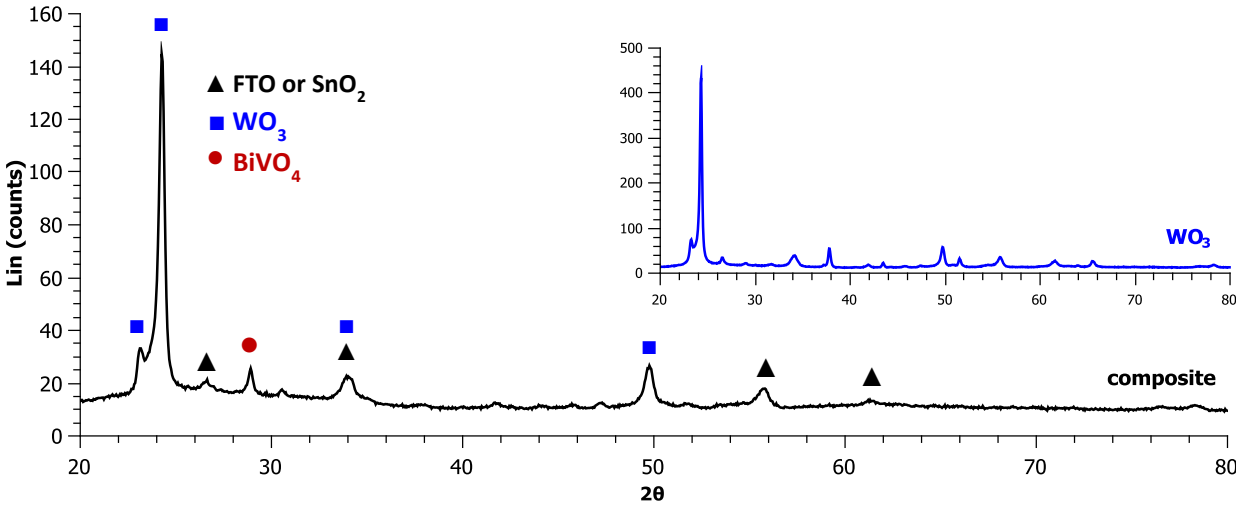

Figure 80: Cu kα XRD of composite photoanode compared to WO_3 XRD spectrum

The composition of the photoelectrode was studied by XPS experiments and the results are reported in Figure 81. XPS spectral tungsten 4d peak was located at 247 eV, suggesting the 40 nm $BiVO_4$ and 10 nm SnO_2 did not entirely cover the WO_3 thin film, leaving the WO_3 exposed. Nevertheless, the XPS peaks are similar to that of mesoporous tungsten previously studied, thus tungsten in the form of W^{6+} was most likely deposited, resulting in the form of WO_3. The signal of Bi 4f orbital split into two peaks at 159 and 164 eV while the V 2p orbital peaks appeared at 516 eV, corresponding to literature values for composite WO_3/$BiVO_4$ photoanodes [241]. All these peaks were attributed to Bi^{3+} and V^{5+} of $BiVO_4$ compound. Finally, the oxygen 1s peak appeared at a binding energy of 530 eV and was assigned to the oxygen in crystalline structure of WO_3 and $BiVO_4$ [176].

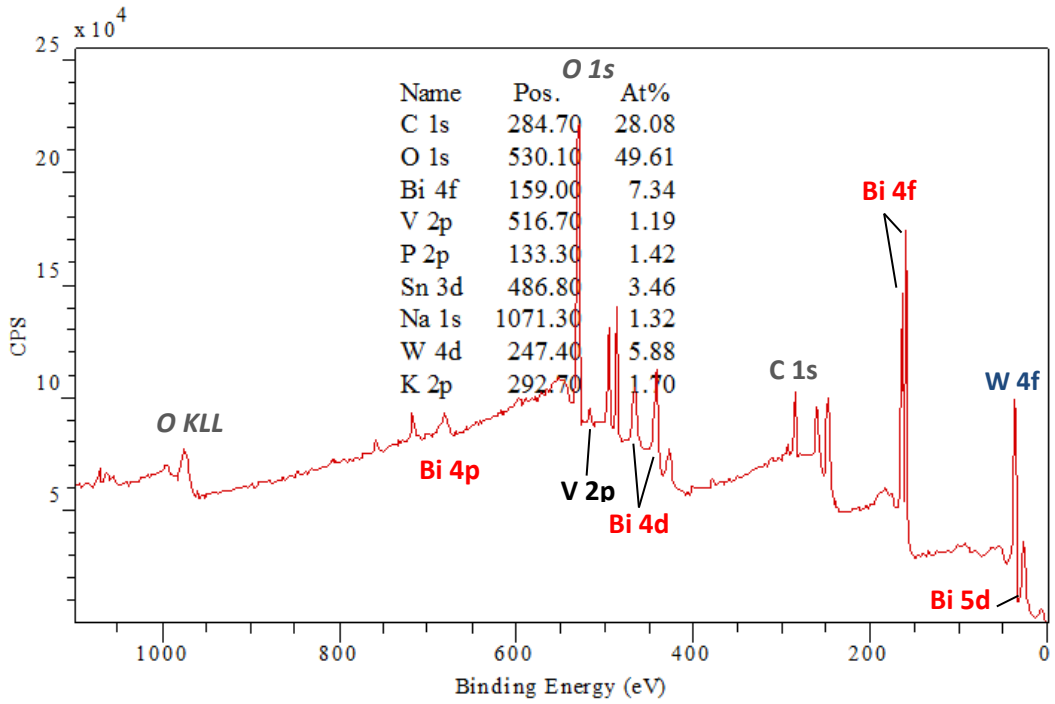

Figure 81: XPS spectrum of $WO_3/SnO_2/BiVO_4$ composite photoanode

II.5.3.1. Optical characterization

The optical properties were also studied and the results are reported in Figure 82 to understand if optical absorbance was affected by combining materials. UV-vis measurements revealed the characteristic peaks of $BiVO_4$ and WO_3 separately. The absorption edge is attributable to previously seen $BiVO_4$ with a gap of 2.5 eV. However the large absorption in the UV range resembles that of WO_3. When combined (black curve in Figure 82), the absorption edge of the composite photoanode exhibits a red shift, assuming $BiVO_4$ absorption edge and increased light absorption towards the UV, suggesting it is capable of absorbing more light in the near visible range than the material alone. The higher absorbance is thought to be due to a better deposition of $BiVO_4$ on SnO_2/WO_3 than on FTO, or variance in thickness between samples [299].

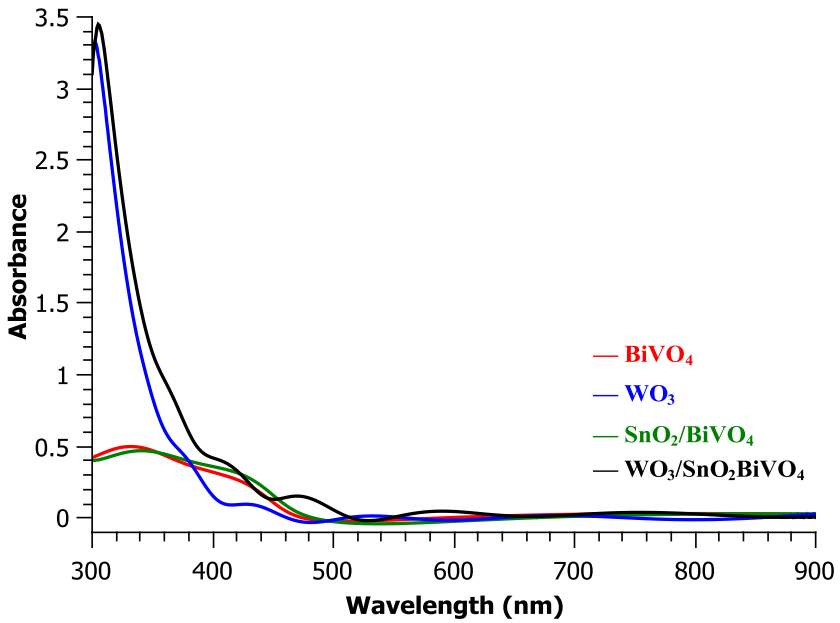

Figure 82: UV-visible absorbance spectra of $BiVO_4$, WO_3, $SnO_2/BiVO_4$ and composite photoanode

II.5.3.2. Material Optimization

The material optimization was centered on the photoelectrochemcal performances. $BiVO_4$ was optimized by calcination at 450°C for 1 hour, while WO_3 optimal calcination was considered to be 400°C for 30 minutes to an hour according to previous results. Therefore, thermal treatment on the composite photoanode was effectuated at 400°C for 30 minutes to accommodate the WO_3.

The *J-E* curves from linear voltage sweeps are reported in Figure 83 for different type of architectures: $BiVO_4$ (red curve), WO_3 (blue), $SnO_2/BiVO_4$ (green), and $WO_3/SnO_2/BiVO_4$ (black).

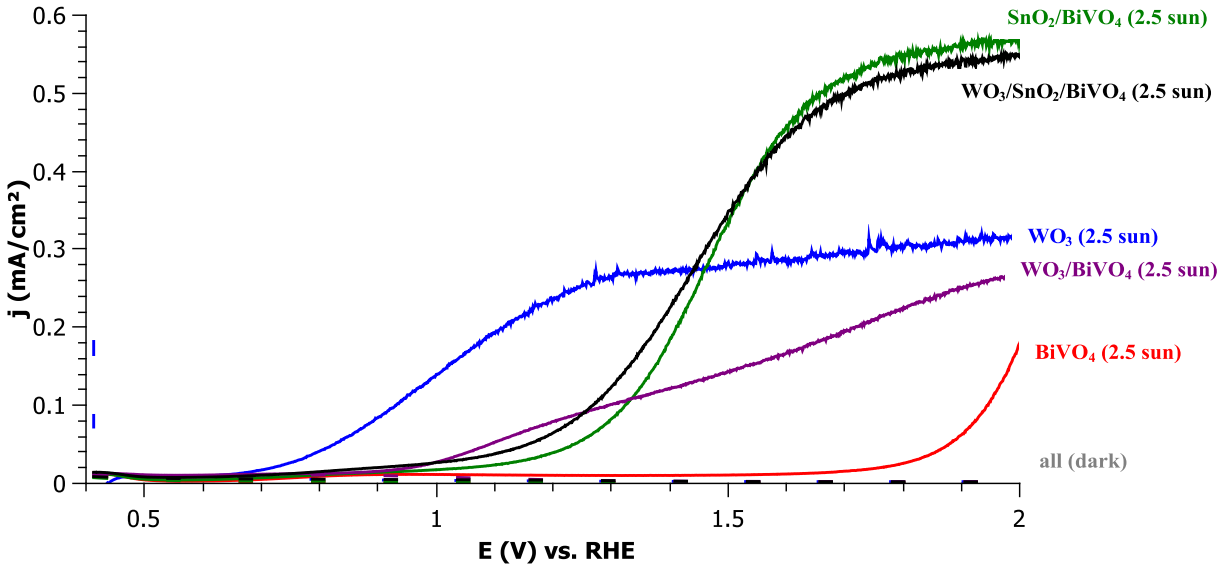

Figure 83: Linear voltage sweep of composite photoanodes with and without SnO_2 hole mirror layers in 1 M KPi under AM1.5 spectrum illumination with a power output of 250 mW/cm² illumination

Several observations can be made based on Figure 83:

- Upon incorporation of the SnO_2 layer between the WO_3 and $BiVO_4$, the saturation photocurrent increased for all composite photoanodes, suggesting better charge transfer between materials.
- Bare WO_3 photoanodes had the lowest onset potential, therefore possessing the largest photocurrent at water splitting potentials. Nevertheless, WO_3 is not stable in neutral conditions and requires protection for correct operation in neutral conditions.
- The combination of $WO_3/BiVO_4$ exhibited a more resistive diode photocurrent than either of the materials alone or upon the addition of SnO_2. The combination of $WO_3/BiVO_4$ as a composite anode performed less well than $WO_3/SnO_2/BiVO_4$; conceivably due to the interfacial transfer of charges between the materials seen the band positions of SnO_2 which let the electrons flow from $BiVO_4$ to SnO_2 and then WO_3 towards FTO.
- Bare $BiVO_4$ possesses the largest onset potential; therefore, exhibiting the lowest photocurrent at water splitting potentials. Upon the addition of SnO_2 layer, the performance increased (cathodic shift of the overpotential and better photocurrent), limiting recombination of photon excited charges at the FTO/$BiVO_4$ interfaces. The $SnO_2/BiVO_4$ photodiode curve was similar to the composite $WO_3/SnO_2/BiVO_4$ photoanode, giving indication of band positions of SnO_2 – suggesting it aids in electron diffusion to the contact but blocks holes diffusing from WO_3 to $BiVO_4$ due its large band gap and higher valence band.

- Composite photoanode exhibited large onset potential somewhat ameliorated by addition of WO_3, however not consistently upon reproducing experiments

These results highlight the benefit of combining different materials to engineer the bands of several materials in order to achieve good performances in terms of photocurrent and onset potential. The $WO_3/SnO_2/BiVO_4$ assembly demonstrates an interesting photocurrent of 0.123 mA/cm^2 at 1.23 V vs. RHE.

We then studied the impact of the density of the films on the performances of $WO_3/SnO_2/BiVO_4$ architecture. Composite photoanodes containing mesoporous WO_3 did not perform as well as with dense WO_3, seeing as it is not exposed to the electrolyte. The photocurrent *J-E* curves are shown below in Figure 84 with dense WO_3 (purple) and mesoporous WO_3 (grey) in composite photoanodes in 1 M KPi (pH 7) under 350 mW/cm² xenon arc lamp illumination. Mesoporous WO_3 incorporated into the composite structure reaches 0.12 mA/cm² at 1.23 V vs. RHE, whereas using dense WO_3 resulted in a photocurrent of 0.66 mA/cm² under the same conditions. It is highly possible that the SnO_2 and $BiVO_4$ layers are not defined and sink into the pores at the surface, acting more as $WO_3/BiVO_4$ photoanodes which display considerably lower photocurrents.

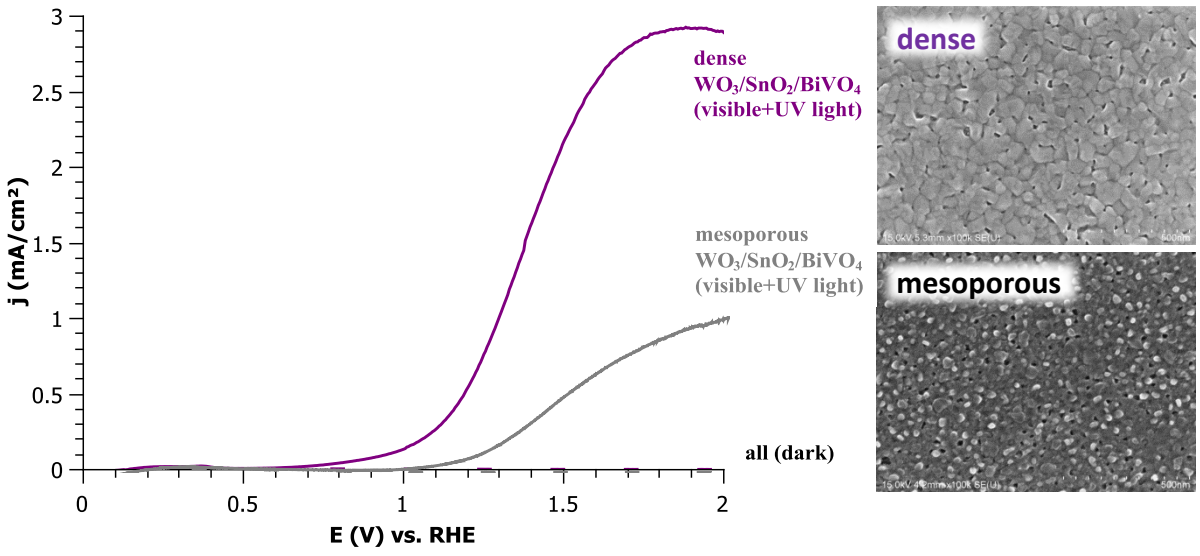

Figure 84: Linear voltage sweep of mesoporous WO_3 (gray) and dense WO_3 (purple) layers in 350 mW/cm² illumination (300 – 900 nm) with corresponding FEG-SEM images

Upon employing dense WO_3 as the absorber, it was concluded that calcination of each material before addition of the next was more performant than completing one simultaneous calcination step for all materials at the end of deposition, suggesting longer calcination times lead to better crystallization and

overall conductivity and performance. The photocurrent responses are displayed in Figure 85 with simultaneous calcination in grey and separate calcination in green:

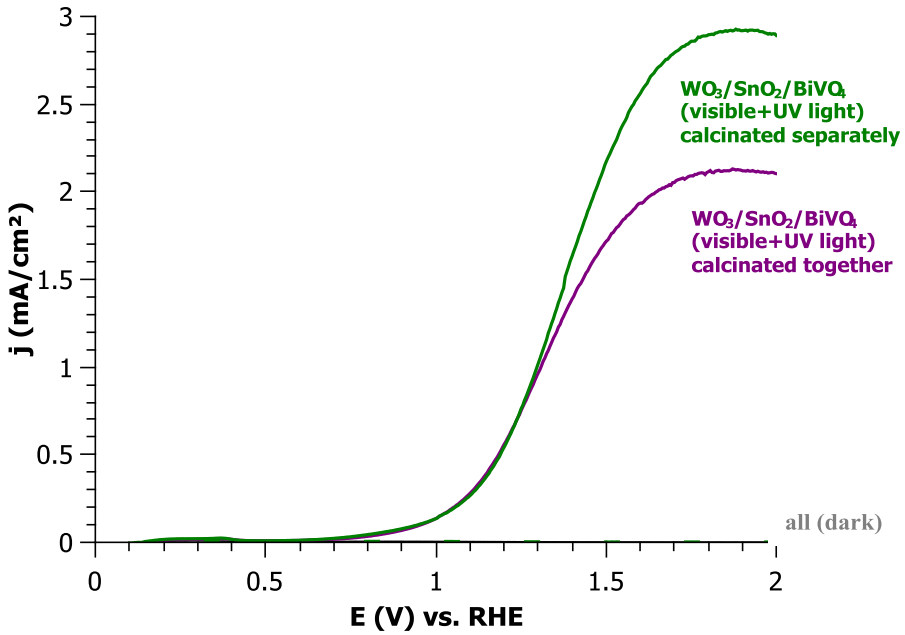

Figure 85: Composite photoanode linear voltage sweep in 1 M KPi under 350 mW/cm² (300 – 900 nm) illumination calcinated separately (green) and together (purple)

This effect was not reproducible and when compared to $BiVO_4$ alone and WO_3 alone; WO_3 alone performed better at water splitting potentials than composite photoanodes due to its large UV response and lower onset potential than composite photoanodes (seen in Figure 86) . However, upon the addition of Na_2SO_3 (shown in Figure 87), $BiVO_4$ was the most performant, suggesting that the surface recombination is a major factor limiting the performance of the OER with photoanodes utilizing $BiVO_4$ for use in neutral conditions as well as the overall thickness of photoanodes. WO_3 layers were generally 300 – 350 nm, SnO_2 layers 10 – 20 nm, and $BiVO_4$ 50 – 60 nm. (Note WO_3 was not tested with Na_2SO_3 due to degradation in pH < 7; though from previous tests performs similarly with and without addition of sacrificial reagents).

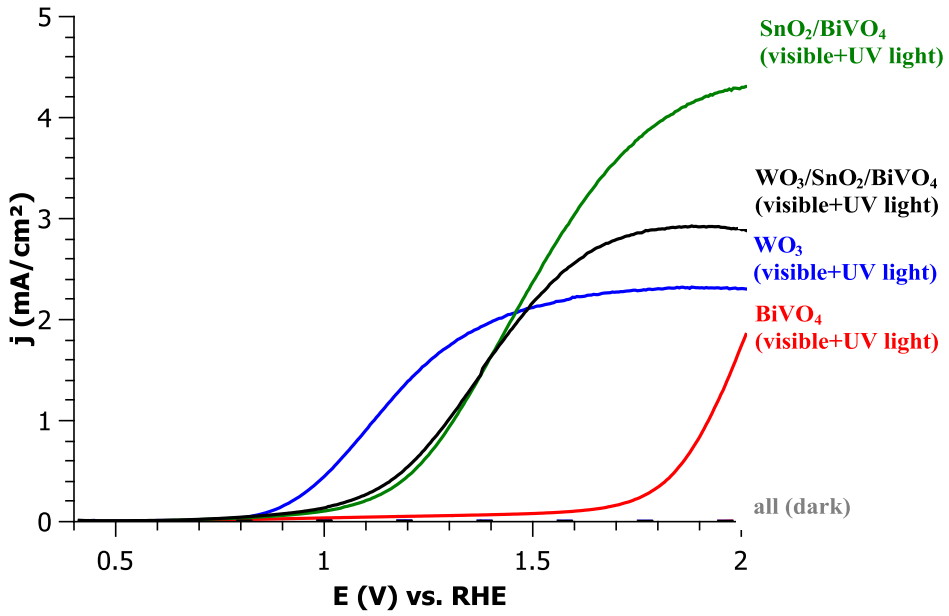

Figure 86: Linear voltage sweep of $BiVO_4$, WO_3, $SnO_2/BiVO_4$, and composite photoanodes in 1 M KPi under 350 mW/cm² (300 – 900 nm)

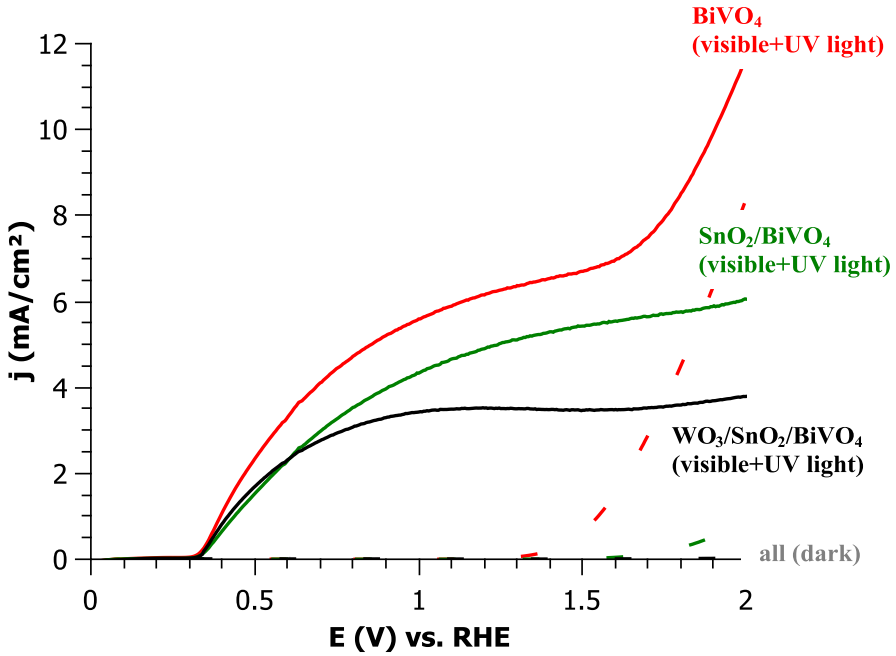

Figure 87: Linear voltage sweep of $BiVO_4$, WO_3, $SnO_2/BiVO_4$, and composite photoanodes in 1 M KPi with 1 M Na_2SO_3 under 350 mW/cm² (300 – 900 nm) illumination

Supplementary, Figure 87 indicates that upon addition of the hole acceptor, Na_2SO_3, $BiVO_4$ consistently performed better (followed by SnO_2, then composite photoanodes). This is possibly due to the

introduction of more recombination centers between each material at the interfaces. This was verified by placing another SnO_2 layer between the FTO and WO_3 in the composite electrode, in attempts to redirect the holes towards the SnO_2 and then $BiVO_4$ layers to be used for the OER. Photocurrent measurements shown in Figure 88 reveal that inserting WO_3 at the FTO/SnO_2 interface does not improve the performance, signifying the positions of both the valence and the conduction bands of the coupled materials. The samples with several layers deposited perhaps exhibited decreased photocurrent due to interfaces at differing materials, validating the hypothesis of addition of interfacial recombination centers between layers. The SnO_2 conduction band is less positive than WO_3, potentially blocking the electrons from reaching the FTO contact, resulting in losses and decreased performance. Without the SnO_2 layer between the FTO and WO_3, electrons flow from $BiVO_4$ to SnO_2 and WO_3 which are then successfully collected at the FTO contact. By this logic, the holes created in WO_3 are blocked at the SnO_2 interface due to the positive position of its valence band. Thus, the only holes to participate in the OER are those formed in the $BiVO_4$ layers and are collected at the $BiVO_4$/electrolyte interface in $WO_3/SnO_2/BiVO_4$ composite photoanodes.

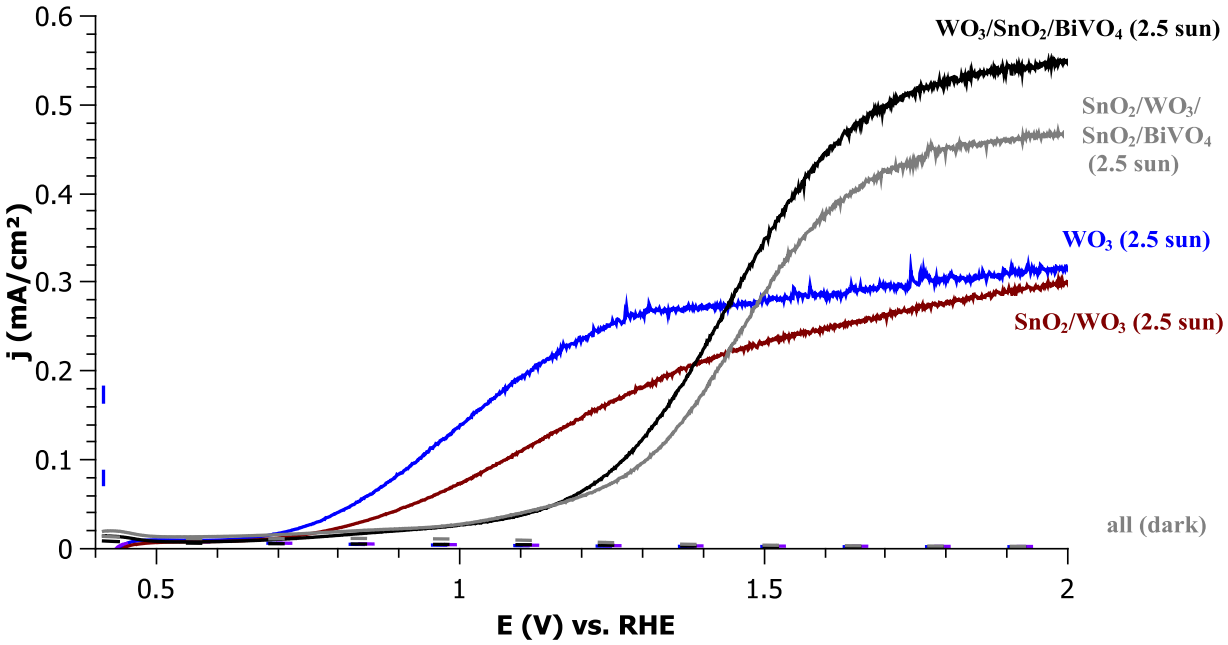

Figure 88: Linear voltage sweep responses of composite photoanodes upon addition of SnO_2 layers between FTO and WO_3 under AM1.5 illumination at 250 mW/cm² in 1 M KPi (pH 7)

Previous results highlight the benefit of incorporating WO_3 in the electrode for performances improvement. Due to the position of SnO_2, the valence band position can potentially block the holes generated by WO_3, therefore rendering them unavailable for the OER. Accordingly, one may ask if the

hole generated in WO_3 participates in the OER process. So we then studied the impact of the WO_3 thickness in the electrochemical performances (see Figure 89). Varying the thickness of the WO_3 verified that the holes created in WO_3 do not contribute to the OER suggested by similar photocurrent responses in Figure 89. This is due to the more positive SnO_2 valence band between $BiVO_4$ and WO_3. This result proposes that WO_3 merely helps with electron separation with $BiVO_4$ and fails to transfer holes to the $BiVO_4$ surface for water oxidation [313].

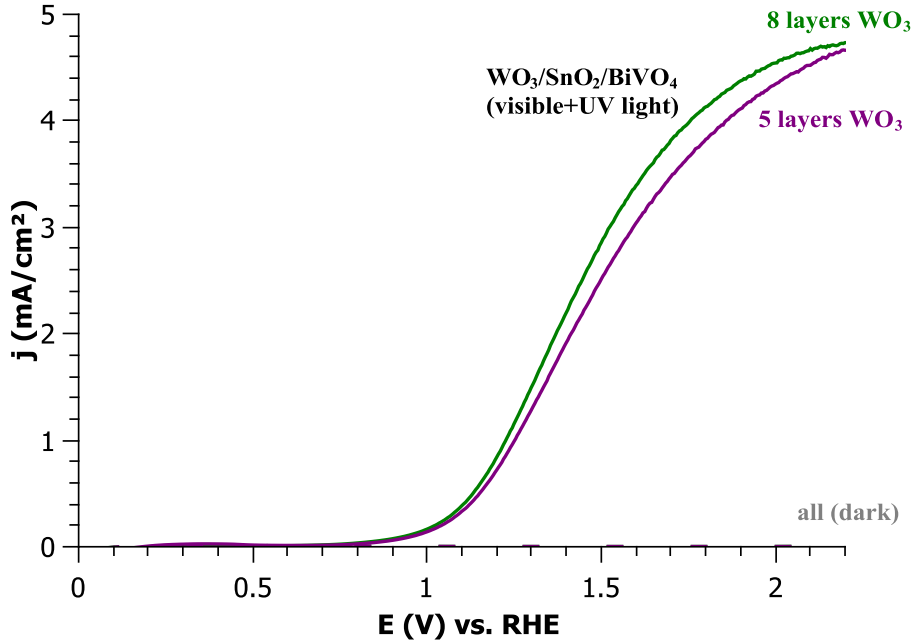

Figure 89: Linear voltage sweep of composite photoanodes with varied WO_3 thickness: 350 nm (green) and 200 nm (purple) in 1M KPi under 350 mW/cm² (300 – 900 nm) illumination

The somewhat optimized composite photoanode consisted of 8 layers of dense WO_3 (350 nm), 2 layers of SnO_2 (18 nm), and 7 layers of $BiVO_4$ (50 nm). A FEG-SEM cross section image is displayed below in Figure 90 and a photo of the FTO substrate, WO_3, composite photoanodes, $BiVO_4$,and $SnO_2/BiVO_4$ are shown, presenting the yellow transparent thin films fabricated during this research in Figure 91.

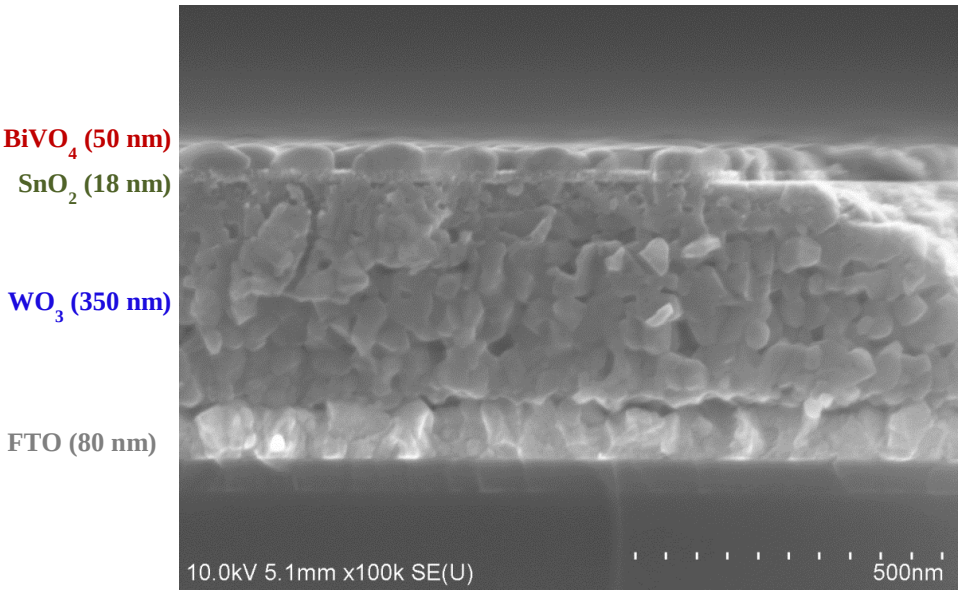

Figure 90: FEG-SEM cross section image of composite photoanode calcinated at 450°C for 1 hour

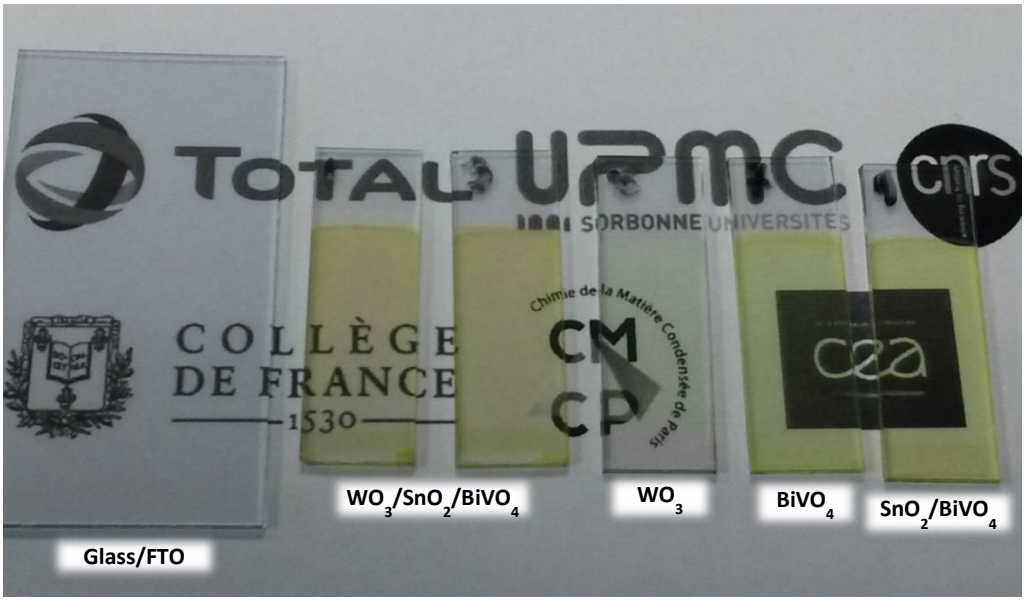

Figure 91: Photo of glass/FTO substrate, composite, WO_3, $BiVO_4$, and $SnO_2/BiVO_4$ photoanodes

Previously, we have demonstrated that the thermal treatment impacts the microstructure of $BiVO_4$ and its performance. Thus the impact of the heat-treatment on the composite $WO_3/SnO_2/BiVO_4$ photoanode was studied. The photoelectrochemical performances are reported in Figure 92 for $BiVO_4$ (red) and composite photoanodes calcinated at 400°C (green) and 450°C (black). The composite photoanode calcinated at 400°C displayed the best performance at 1.23 V vs. RHE of 2.35 mA/cm², compared to the composite

photoanode calcinated at 450°C with a photocurrent of 1.05 mA/cm² and $BiVO_4$ alone 0.534 mA/m². Higher calcination temperatures did not necessarily benefit the composite performance.

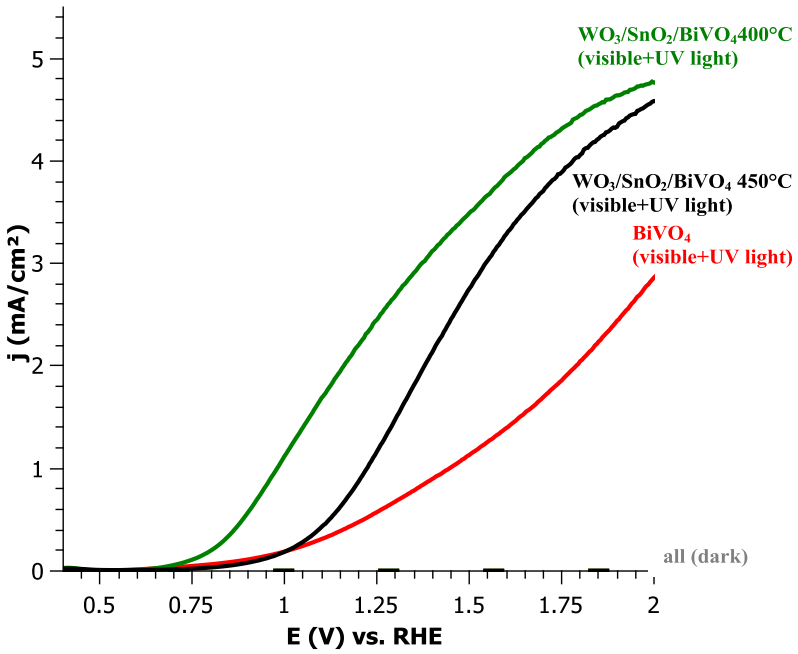

Figure 92: Photocurrent of $BiVO_4$ (red) and composite $WO_3/SnO_2/BiVO_4$ photoanodes calcinated at 400°C (green) and 450°C (black) in 1 M KPi (pH 7) under 350 mW/cm² illumination

This is probably due to the large crystals of $BiVO_4$ which did not form a continuous network; necessary for good conductivity and overall performance as seen with $BiVO_4$ previously (shown below in Figure 93). Much like the $BiVO_4$ thin films alone, those which completely covered the SnO_2 and had a continuous dense network performed better than agglomerated networks of larger crystals of $BiVO_4$.

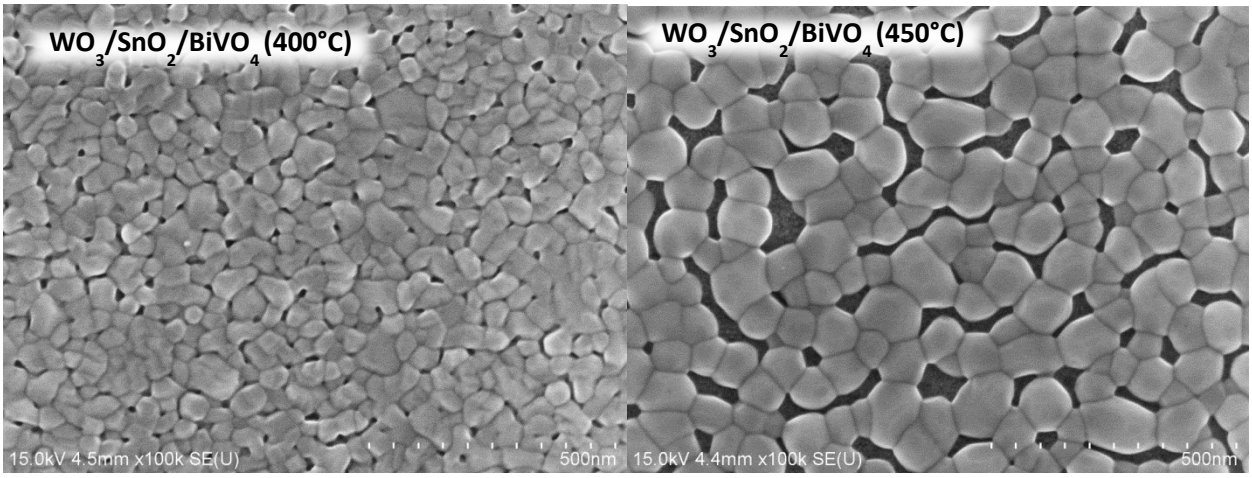

Figure 93: FEG-SEM image of composite photoanodes calcinated at 400°C (left) and 450°C (right)

Upon the addition of Na_2SO_3, $BiVO_4$ exhibited the largest photocurrent of 7.72 mA/cm² at 1.23 V vs. RHE, compared to the two composite photoanodes reaching 4.88 mA/cm² and 3.86 mA/cm² (shown in Figure 94), like all previous experiments concerning composite and $BiVO_4$ photoanodes.

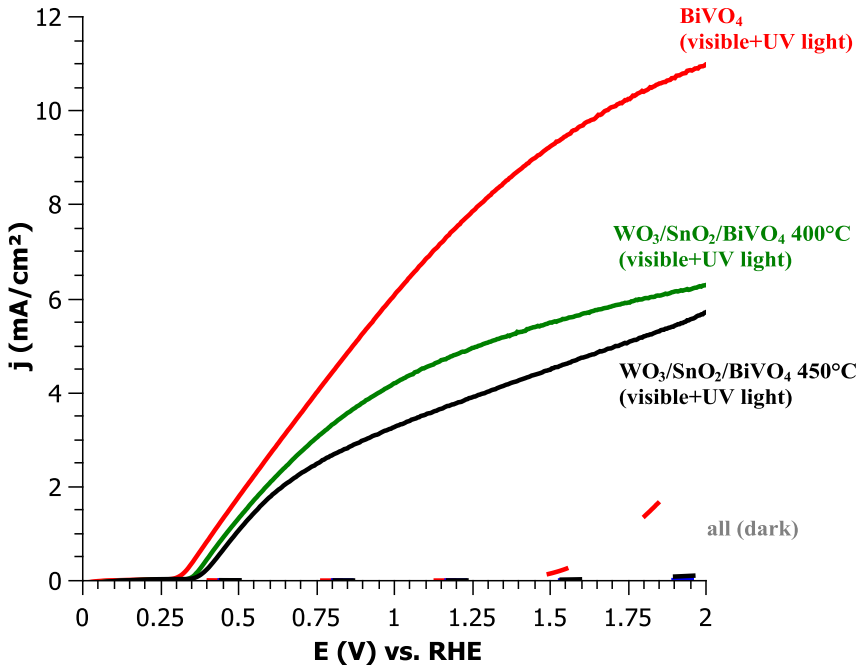

Figure 94: Photocurrent of $BiVO_4$ (red) and composite $WO_3/SnO_2/BiVO_4$ photoanodes calcinated at 400°C (green) and 450°C (black) in 1 M KPi with 1 M Na_2SO_3 (pH 7) under 350 mW/cm² illumination

This incites that when the slow surface kinetics are relieved, the conductivity and charge separation and transport become more crucial in the performance of the photoelectrode. Thus the addition of sacrificial reagents can give insights to bulk versus surface limiting performances. Mass transport becomes critical upon the addition of sacrificial reagents which alleviate the OER, making the best performing photoanodes in phosphate solution considerably less performant relevant to $BiVO_4$ individually [193].

II.5.4. Conclusions

The attempt at a composite photoanode, based on the large IPCE and good conductivity of WO_3 and the surface OER and stability in neutral conditions of $BiVO_4$, experienced several obstacles potentially leading to increased recombination throughout the composite photoanode. Several photoelectrochemical measurements revealed the composite photoanode can reach higher photocurrents at 1.23 V vs. RHE than $BiVO_4$ photoanodes due to the contribution of a lower onset potential most likely due to WO_3. Nevertheless, the total photocurrent achieved by the composite photoanode was significantly lower than

literature values and less performant than $SnO_2/BiVO_4$ or WO_3 photoanodes alone. Under visible light irradiation the composite photoanodes perform better at 1.23 V vs. RHE than single material photoanodes. However, upon the addition of ultraviolet light, dense and mesoporous WO_3 have large photoactive responses and despite the lower saturation current, has a lower photocurrent onset potential, reaching higher photocurrents at the OER potential than composite and $BiVO_4$ photoanodes. The composite photoanode therefore failed to outperform mesoporous WO_3 in terms of photocurrent at the OER potential.

The combination of materials potentially adds recombination centers and thus future efforts to optimize composite $WO_3/BiVO_4$ photoanodes should optimize the interfaces between layers for better charge transfer. Like literature examples, the incorporation of nanostructured (i.e. nanorods) of WO_3 should be implemented to increase its role in charge separation for overall increased performance [147].

Seen the lower performance of the composite photoanodes by sol-gel dip coating procedures, $SnO_2/BiVO_4$ and mesoporous WO_3 were chosen to be the n-photoanode materials tested in the tandem dual photosystem water splitting cell for neutral and acidic conditions respectively – which is discussed in the following chapter.

III. PHOTOELECTROCATALYTIC CELL

III.1. INTRODUCTION

The conception and construction of photoelectrocatalytic cells for water splitting technologies have, and currently are, researched and conceptualized by several groups. Many initial attempts, implementing wired planar electrodes, were effectuated with "H-cell" architecture, named for the shape of the cell which is formed as the letter H [76, 108, 235]. As previously discussed, the implementation of a dual photosystem is theoretically more efficient than a single photoabsorber [39]. An H cell employing two photoelectrodes in a tandem configuration competes for light and contains several obstacles in terms of optics, resistance, and gas separation. This type of cell easily enables the separation of the two half reaction compartments for easy gas separation by an ionic separator. Nevertheless, this adds even more complexity to the system, increasing ohmic losses through the ionic separator and creating a pH gradient which occurs on either side of the separator at each photoelectrode [236]. Considering and taking example from previous research accomplished on photoelectrocatalytic water splitting cells, a laboratory-scale cell was constructed to measure the photoelectrode materials previously optimized to be employed in a complete tandem dual photosystem photoelectrocatalytic cell. This cell, though experimentally scaled, can give insight to future improvements, as well as scale up obstacles and materials needed for future application.

Though the tandem dual photosystem competes for light absorption between electrodes, it can theoretically achieve higher efficiencies than that of a side-by-side dual photosystem configuration. Thus, in consideration of thermodynamic theoretical values for overall efficiency, a wired dual compartment tandem dual photosystem device is the aim in this research towards construction and use of a photoelectrocatalytic cell for water splitting. Seeing though WO_3 is unstable in neutral conditions, two cell conditions were adopted: acidic and neutral conditions. WO_3 was paired with copper based p-photocathode for use in 1 M H_2SO_4 (pH 0) employing a CuO based photoabsorber with HER co-catalyst (MoS_3), which is stable and highly active in acidic conditions [212, 333-335]. Neutral conditions in 1 M potassium phosphate (pH 7) were employed for use with SnO_2/$BiVO_4$ photoanodes which are recognized to be somewhat stable in neutral conditions [50, 313]. These photoanodes were also paired with a CuO based photocathode.

III.2. DESIGN AND CONSTRUCTION

Initial design of the PEC device was based on the concept of an H-cell with gas input and output for O_2 and H_2 detection. Seeing the architecture and configuration a wired dual tandem photosystem, it is theoretically more efficient thermodynamically and more compact in area to place one photoelectrode in front of the other [39]. Photoelectrodes were employed as windows to the cell; therefore limiting materials and potential optical losses for cell enclosure.

Alike other cells for water splitting, the structure consisted of several pieces which are pressed together for easy assembly and disassembly. The cell was constructed using white polyamide [PA 6] Ertalon® 6 SA manufactured by Quadrant plastics, chosen for its high chemical resistance and low oxygen permeability. The cell consisted of 4 hollow elliptical pieces of 6 mm thickness to separate the two photoelectrodes and membrane. This defined the spacing between the two photoelectrodes to be 12 mm when placed in the cell in order to decrease ohmic losses [30]. The distance between electrodes was not varied during experimentation with fabricated materials in this study; though this could potentially increase or decrease performance due to ionic path length between the photoelectrodes and volume of electrolyte included in the reaction [38]. The outer dimensions of the substrates for the photoelectrocatalytic cell were 4.5 x 2.5 cm. The outer sections encapsulated the photoelectrodes, functioning as a frame for the entire cell. Whereas, the inner sections incorporated the inlet and outlets for gas as well as an optional inlet for reference electrodes. The two inner sections also act as a membrane frame. The active area was defined by a hole in the elliptical sections, measuring 2.01 cm^2 or 1.6 cm in diameter, exposing this defined area (active area) of the photoelectrodes to both light and the electrolyte for the OER and HER; therefore ensuring the photoanode and photocathode had equal active areas. The design ensures that the active area wetted by the electrolyte is the equivalent to the illuminated area. The pieces, once placed together, are kept by stainless steel screws and nuts with o-rings between each piece to ensure a hermetically sealed cell in the defined active area containing the electrolyte. The entire volume of the cell with all 4 pieces employed is cylindrical and measures 2.41 cm^3; enabling the cell to contain roughly 2.4 mL of liquid between the two electrodes. This suggests 1.2 mL of electrolyte on either side of the ionic separator/membrane for the HER and OER when added. The gas inlets and outlets for gas collection and/or detection as shown in each side of the inner pieces are displayed in Figure 95 and Figure 96. Electrolyte was added into cell by the gas outlets before being sealed with o-rings and polypropylene X8 GE HiTrap™/HiPrep™ threaded connectors containing PEEK tubing which was connected to a gas chromatograph for detection. Often, air leaks occurred due to these inlet and outlets, which were attempted to be sealed with silicone paste to reduce leaks. Unfortunately electrolyte inputs and outputs enabling circulation of electrolyte was not employed in this initial cell design with the aim to avoid pH gradients occurring at the photoanode and photocathode – potentially increasing future stability of the photoelectrode materials.

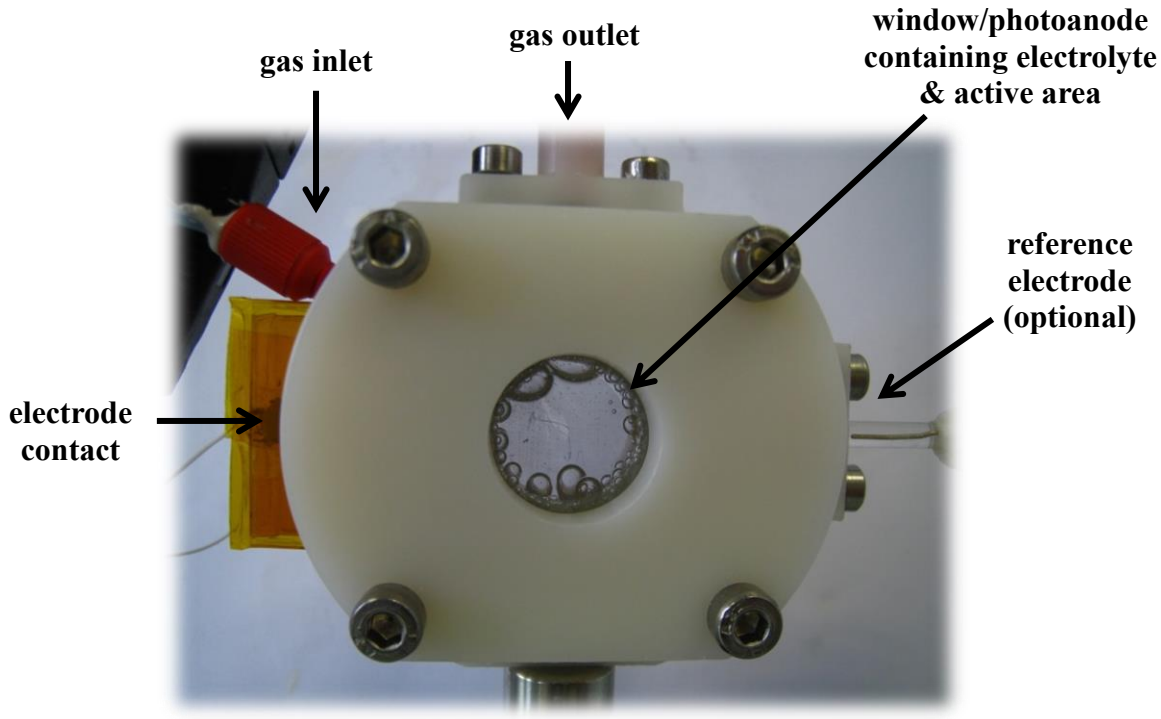

Figure 95: Photo of PEC face with inlet and outlet indications

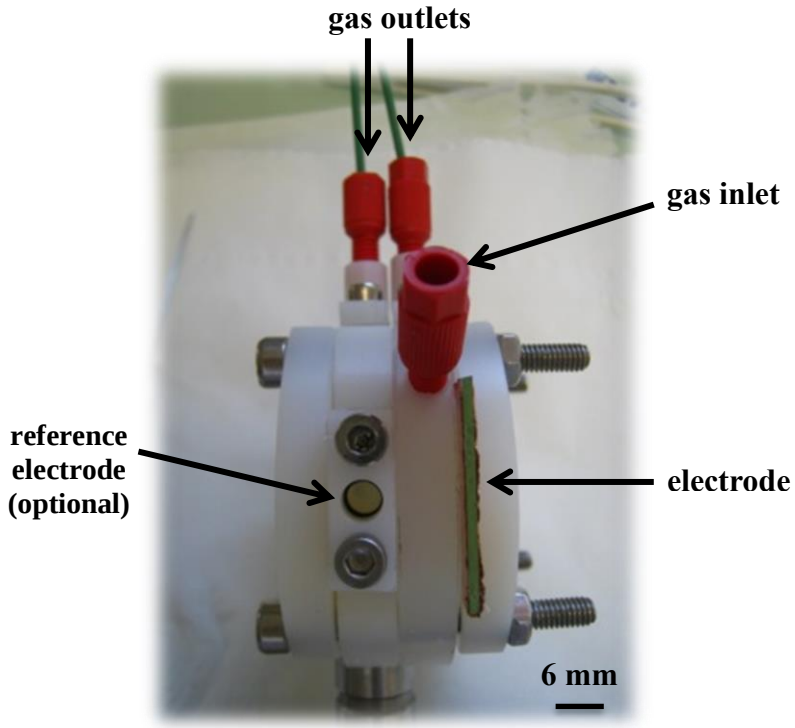

Figure 96: Photo of PEC side with inlet and outlet indications (symmetrical to other side)

III.3. Cell Operation and Membrane Addition

The cell was tested with FTO electrodes for solution resistance by electrochemical impedance measurements. FTO Asahi substrates (used for photoelectrodes) were used as the counter and working electrodes for electrochemical impedance spectroscopy measurements. The frequency was swept from 200 kHz to 0.1 Hz in 1 M KPi (pH 7) with amplitude of 10 mV and fitted with an equivalent circuit (shown in Figure 97 with corresponding cell cross section) in order to determine the solution and membrane contribution to the cell. By this method, the solution resistance can be found by reading the real axis value at the high frequency intercept. The resistance ($R_{ct,a}$) depicts the charge transfer resistance associated with the anode. This is in parallel with the double layer capacitance, previously introduced as the Helmholtz layer. The cathode is modeled equivalently with $R_{ct,c}$ and $C_{dl,c}$. A simplified equivalent circuit models the photoelectrocatalytic cell, employing the photoanode and its double layer capacitance, the membrane and electrolyte solution, as well as the complementary photocathode and its respective double layer capacitance. The double layer capacitance depends on many variables: electrode potential, temperature, ionic concentrations, types of ions, oxide layers, electrode roughness, and impurity adsorption, etc. The solution resistance (and membrane when added) is referenced as R_s.

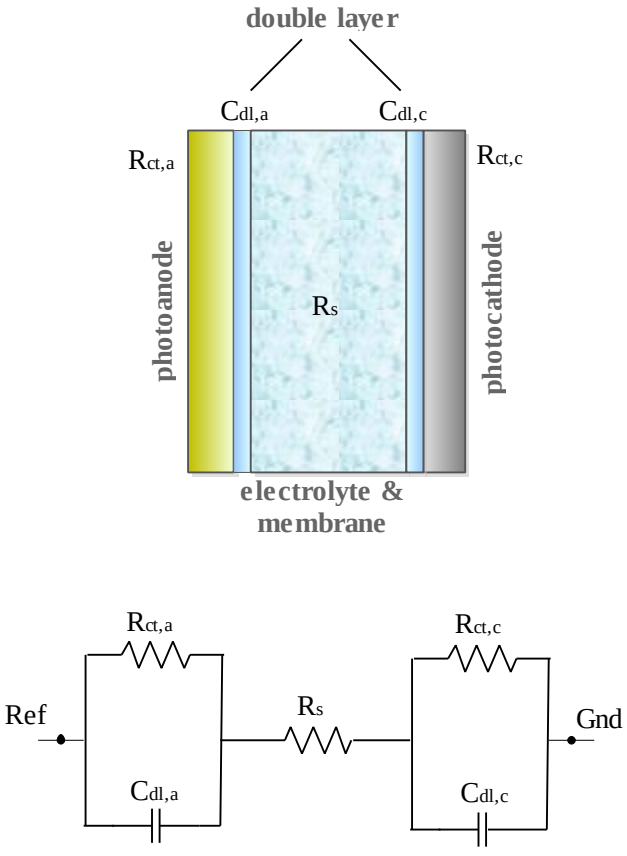

Figure 97: PEC schema and equivalent circuit model

This equivalent circuit is very basic and potentially not the most accurate depiction. In a more complex modeling of the circuit, Warburg element for each photoelectrode to model diffusion at lower frequencies, bulk contact resistances, and wiring element should be included.

There are resistance contributions in the system due to the FTO electrodes and solution. During the impedance measurements the FTO at the cathode tin reduced, potentially altering resistance and capacitance in the system. The major source of loss in the system is most likely due to an ohmic drop in the electrolyte, which remains one of the largest obstacles in cell construction and conception [235]. The entire cell averaged ohmic resistance of 340 – 480 Ω with 1 M KPi (pH 7) electrolyte. On average, the solution resistance in of 1M KPi with 12 mm distance between electrodes is 70 – 75 Ω. 0.1 M possessed higher resistance, with an average of 85 Ω. When center section is removed, the distance between electrodes decreased from 12 mm to 6mm. With a distance of 6 mm between the FTO substrates, the 0.1 M KPi the resistance decreased, suggesting that placing the photoelectrodes closer may lessen ohmic resistance in the cell. Nevertheless, modeling with this equivalent circuit may not be very accurate considering several electrochemical reactions are not taken into account in the model.

The addition of a Nafion® NRE-212 membrane was done by first activating the membrane in boiling sulfuric acid and boiling water. The membrane was integrated by placing it in between the two middle sections of the cell. Initial tests with CuO/TiO_2 and WO_3 revealed little to no O_2 or H_2 produced by the photoelectrodes, accompanied by a very small photocurrent in the cell. This could be due to increased resistivity in the system upon the addition of the membrane, or the fact that the photoelectrodes are not stable and materials dissolve into solution. Nevertheless, impedance tests upon addition of the membrane added slight resistance to the system, increasing the solution and membrane resistance by 2 Ω for 12 mm spacing with 1 M KPi. The Nyquist plot for 1 M KPi with and without membrane is displayed below in Figure 98, suggesting the increase in cell resistance upon integration of a membrane.

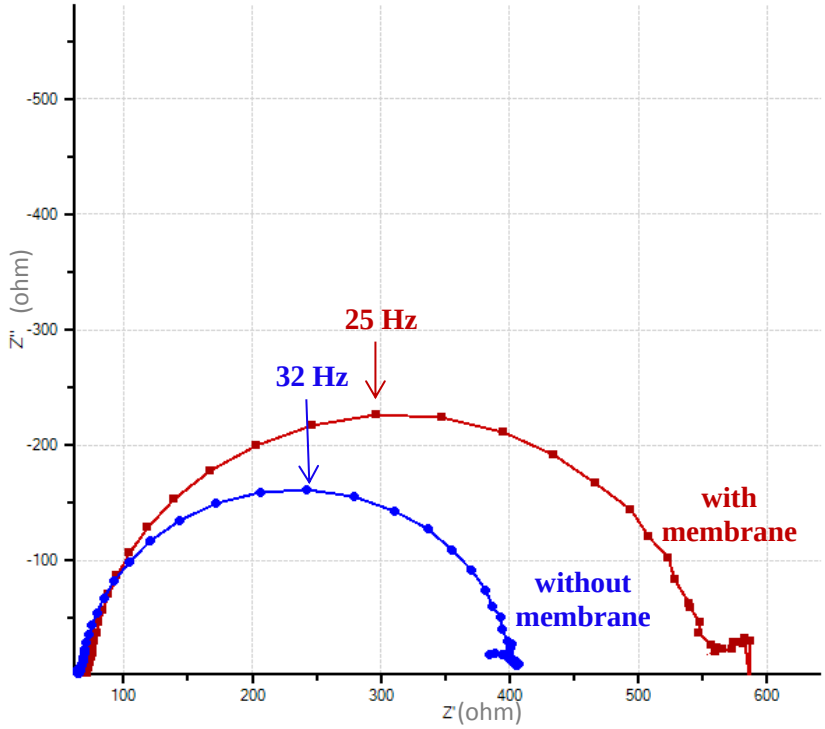

Figure 98: Nyquist plot of cell with 1 M KPi with (red) and without (blue) membrane

The resistance of the solution was greater with 0.1 M, thus 1 M KPi was used as the final electrolyte to decrease ohmic losses in the cell. The device behaved as expected with the most resistance occurring with the largest distance between electrodes (12 mm) and the membrane. The least resistance occurred with 6 mm spacing between FTO electrodes. Figure 99 displays the Nyquist plot of the cell behavior with 6 mm (green) spacing between electrodes, 12 mm (blue), and 12 mm with Nafion® membrane (red).

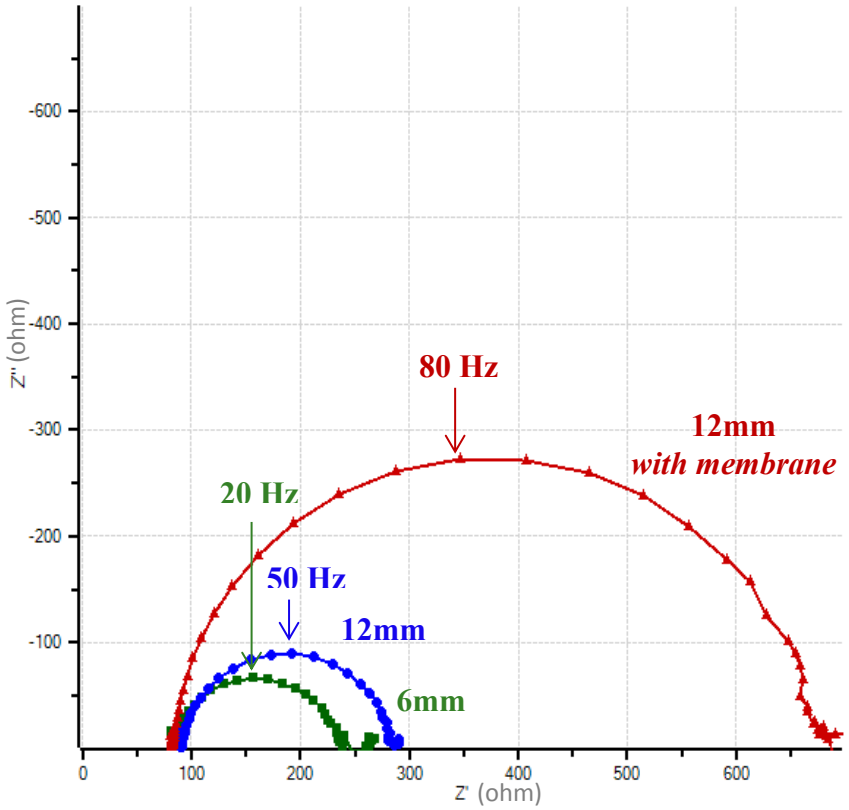

Figure 99: Nyquist plot of cell with 0.1 M KPi with 6mm between electrodes (green) and 12 mm (blue) and at 12 mm with membrane (red)

Associated data concerning the resistance of the electrolyte (and membrane) are shown below in Table 16. The resistance of the solution (R_s) was calculated from fitting with the equivalent circuit (shown in Figure 97) and with Modulab semi-circle fit. These values were relatively close, suggesting the equivalent circuit is representative of the system. The values are estimations with large error possibility which are difficult to compare due to the FTO electrodes reducing at the cathode and affecting the overall cell resistivity. In general, the electrolyte 0.1 M – 1 M KPi and spacing of electrodes of 6 – 12 mm results in an ohmic loss of 67 – 95 Ω.

KPi concentration	**fit**	**solution resistance (Ω)**		
		6mm	**12mm**	**12mm + membrane**
1 M	eq. circuit	73	67	76
	circle	71	67	74
0.1 M	eq. circuit	86	92	85
	circle	85	91	83

Table 16: Solution (and membrane) resistance measured in cell and fitted from equivalent circuit model and circle model

Upon applying 4 mA/cm² to the cell during impedance testing, the potential measured was 2.5 V. Ohm's law thus suggests that the polarization resistance of the cell is 625 Ω; larger than what the Nyquist plot suggests. This could be due to other processes not taken into account during the data fitting; such as corrosion of FTO, wire resistance, and unknown chemical processes which may be occurring.

In terms of optical losses, UV-vis transmission measurements with photoanodes were completed to define what wavelengths the photocathode would receive after passing through the photoanode, electrolyte, and Nafion® NRE-212 (50.8 µm) membrane. Upon addition of 1 M KPi electrolyte the refractive index of the glass/FTO/SnO_2/$BiVO_4$ photoanode is reduced and more light is received at the photocathode side of the cell than in air medium. Upon addition of a membrane the UV-vis transmission is similar than with the electrolyte, suggesting there are little losses in optical transparency throughout a dual compartment cell divided by a Nafion® NRE-212 50 µm membrane. At wavelengths 600 – 900 nm the average transparency is 80%, suggesting that the photocathode can receive the majority of light in the visible to infrared region. The transmittance in neutral conditions with a glass/FTO/SnO_2/$BiVO_4$ photoanode with 1 M KPi is shown in Figure 100 and for acidic conditions with glass/FTO/WO_3 photoanode with 1 M H_2SO_4 in Figure 101, suggesting that the volume or concentration of electrolyte in the cell does not hinder light absorption [109].

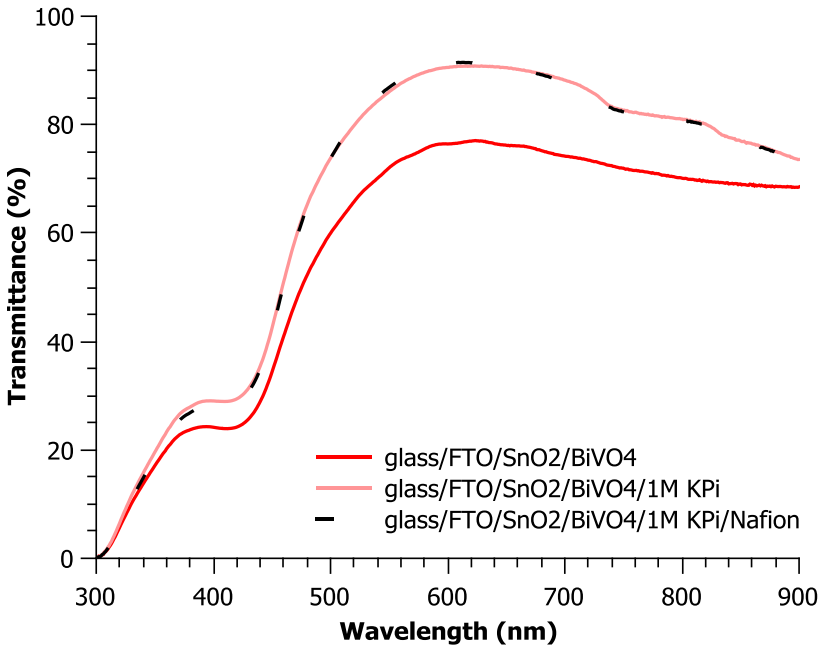

Figure 100: UV-vis transmission spectra of photoelectrocatalytic cell with SnO_2/$BiVO_4$ and 1 M KPi for neutral conditions

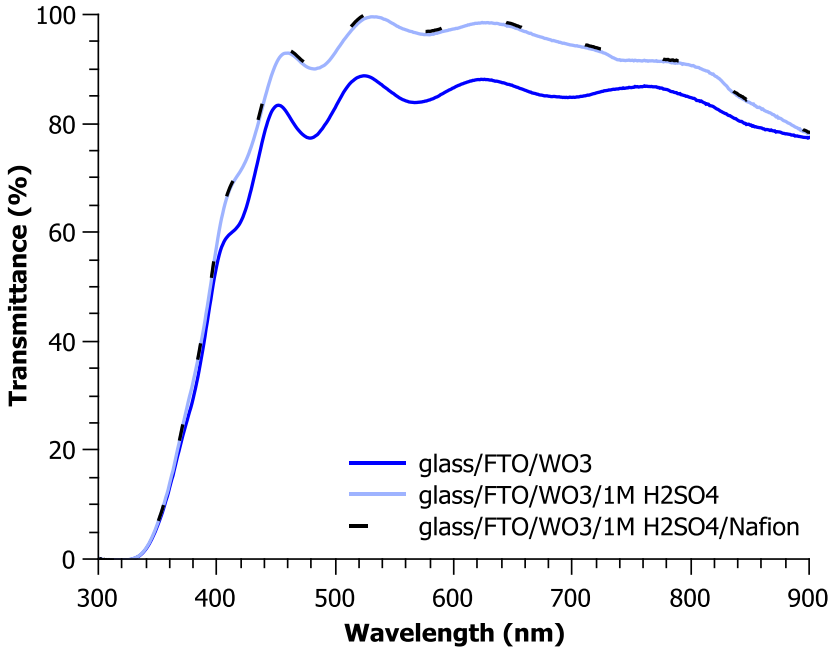

Figure 101: UV-vis transmission spectra of photoelectrocatalytic cell with WO_3 in 1M H_2SO_4 for acidic conditions

In terms of optical losses, quartz is a more ideal substrate than glass for the substrate for the photoanode; nevertheless, quartz is much more expensive than glass and should be taken into account for the increased cost in large scale application. Alternatively, fused silica may replace glass in the future for the photoanode application for an increase in optical efficiency of the device [30]. This may increase future functioning of materials due to increased UV light absorption.

III.4. Gas Detection

Unlike previous faradaic measurements, done by injection, gas detection for the complete photoelectrocatalytic cell was continuously measured by a micro gas chromatograph using a flow of 5 mL/min of argon gas and solution air-tight Schlenck liquid guards to avoid injection of electrolyte into the µGC column. The PEEK tubes were employed to house the gas measured and the volume of the guards. A small pump in the µGC was used to ensure collection and quantification of the gas produced in the cell, which tentatively added to air detection and thus leaks into system and overestimation of O_2 produced in some experiments. Gas detection from the photoelectrocatalytic cell constructed was done by an SRA µGC with high limits of detection for O_2 using argon as a carrier gas instead of previously used nitrogen, which is more difficult to detect oxygen with seeing the very close thermal conductivity values of N_2 and O_2 [273]. Nitrogen was always detected by the µGC, suggesting either it is present in low quantities in the argon carrier gas (which is unlikely seen its purity of 99.9995%), or there were small

leaks in the cell and/or solution guards due to the pump in the µGC pulling gas into the column. Hydrogen and oxygen were able to be detected simultaneously, enabling a stoichiometric ratio of hydrogen to oxygen to be calculated from faradaic experiments.

III.5. Copper Based p – Photocathodes

For the hydrogen evolution reaction, copper based p-photocathodes were fabricated by sol-gel dip coating methods. Due to the oxidation that occurs during the calcination treatment, it is impossible to keep the copper (I) oxidation state to produce Cu_2O by this method; therefore CuO was the main photoabsorber. Due to the photocorrosion of copper it was protected by TiO_2 and $BaTiO_3$ which were also synthesized and deposited by sol-gel dip coating procedures. The TiO_2 and $BaTiO_3$ layers were less than 100 nm in thickness as to work as protective layers and increase charge separation. MoS_3 was deposited to increase the kinetics of water reduction in acidic conditions and measured to be 60 – 70 nm in thickness [333].

III.6. Device Testing

Optimized photoanode materials from the previous chapter were used in the photoelectrocatalytic cell constructed and coupled with copper based photocathodes fabricated in parallel with a scientific partner (Thesis of Johanna Toupin). This cell (seen in Figure 102) was constructed to perform at atmospheric pressure and temperatures of 25 – 80°C (due to heating overtime upon constant illumination) which could potentially improve photoelectrode performance [336]. Three different tests were completed with WO_3 functioning as the n-photoanode in acidic conditions: with 1 M H_2SO_4 (pH 0) as the electrolyte. Three further tests were completed with $SnO_2/BiVO_4$ functioning as the n-photoanode but in neutral conditions: with 1 M KPi (pH 7). Copper based photocathodes were employed equally as the photocathode in the photoelectrocatalytic cell, both in acidic and neutral conditions.

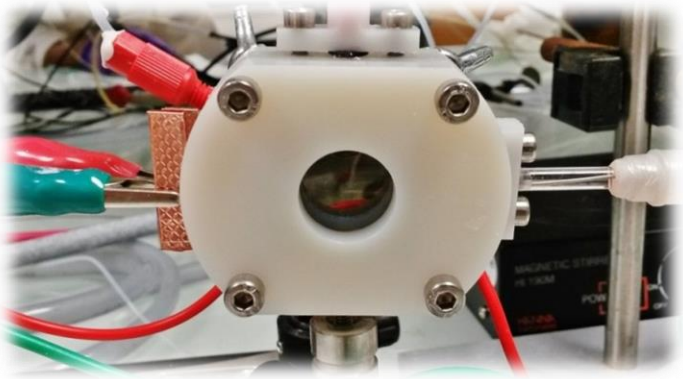

Figure 102: Photo of PEC during use

Testing conditions were effectuated with and without external bias. Generally there was little to no photocurrent produced from the two materials and an external bias was added by aid of a potentiostat for guaranteed gas detection. When external bias was applied, the photoanode was employed as the working electrode with the photocathode as the counter electrode, as well as reference electrode. Upon addition of an external bias via potentiostat, an Ag/AgCl KCl saturated reference electrode was employed using the optional reference electrode input in the cell side compartment. When no external bias was applied, the reference electrode was connected directly to the counter electrode.

Illumination was undertaken with xenon arc lamp functioning at 280 W with an output of 350 mW/cm² coupled with a liquid infrared filter, emitting wavelengths of 300 – 950 mW/cm². The cell was placed 20 cm from the lamp source and light power measured by a photodiode to ensure accurate calculations for the solar to hydrogen or applied bias photon to current efficiency. These calculations were done according to equations (32) and (33); taking into account the faradaic efficiency which was measured simultaneously with a micro-gas chromatograph. Gas detection was done by flowing argon through the cell at 5 mL/min which acted as a carrier gas leading to the μGC which was able to detect H_2 and O_2 simultaneously. There was approximately 1.5 m of PEEK tubing (with an internal diameter of 0.3 mm) between the cell and GC for detection, along with a liquid guard which measured 13 mm in diameter and 150 mm long to avoid liquid being introduced to the GC column, equaling a total volume from the cell to the μGC of 20.96 cm^3. This suggests, at 5 mL/min flow, that the gas takes slightly over 4 minutes to reach the GC. Measurements were taken every 60 seconds employing an injection (with the aid of a pump for 20 seconds) of 50 ms or 40 μL of gas. There was much error in gas detection due to potential leaks in many areas of the setup (shown below in Figure 103) and upon employment of the liquid guard. The micro-gas chromatograph error was stated to be ± 2%.

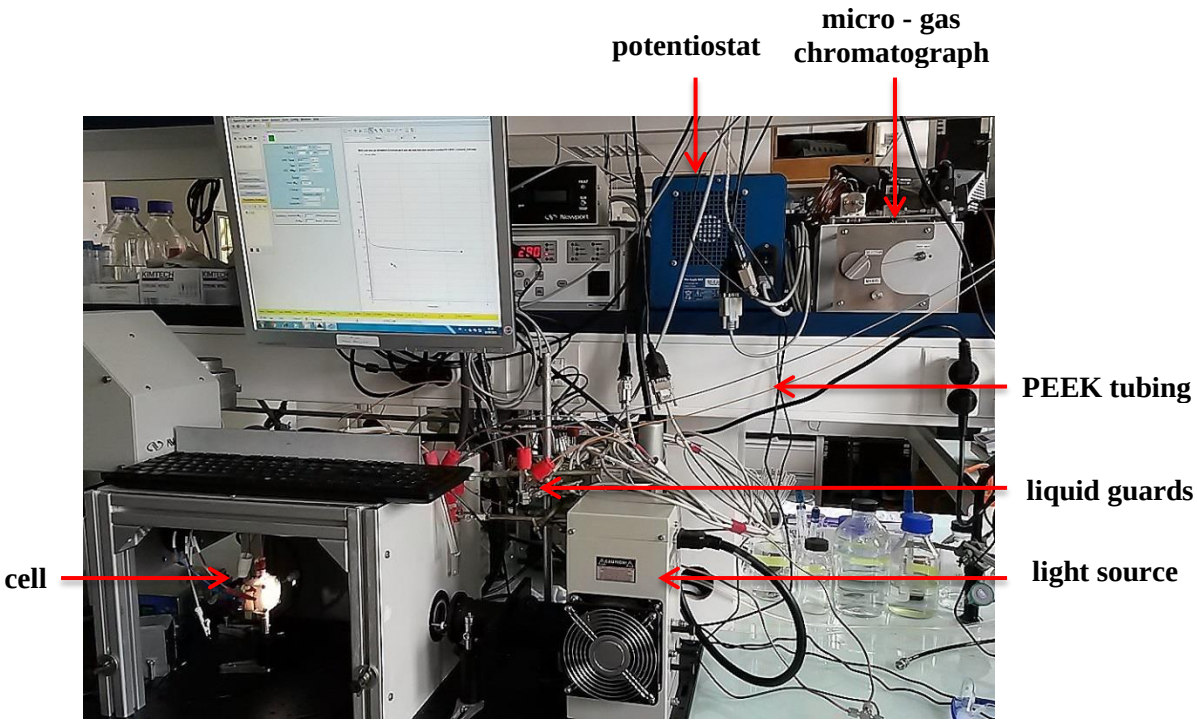

Figure 103: Photoelectrocatalytic cell measurement bench setup

III.7. Acidic Conditions

As previously discussed, WO_3 is an appropriate material as an n-photoanode in a dual photosystem for the OER. Therefore an optimized mesoporous (previously characterized and discussed in chapter II.2. Tungsten Trioxide) thin film photoelectrode of WO_3 was tested alone in the device with a platinum counter electrode deposited onto FTO by evaporation (followed by calcinated at 450°C for 2 hours to ensure adhesion). This single photosystem test was completed to ensure functioning of the photoelectrocatalytic device, followed by complete metal oxide dual photosystem attempts coupled with copper based photocathodes for use in acidic medium.

These three tests were effectuated under articulated conditions with CuO based photoabsorber p-photoanodes with modifications shown below in Table 17:

n- photoanode	p-photocathode	electrolyte	illumination	membrane
FTO/WO_3	FTO/Pt	1 M H_2SO_4 (pH 0)	350 mW/cm² (300 – 900 nm)	no
FTO/WO_3	$FTO/CuO/MoS_3$			no
FTO/WO_3	$FTO/CuO/TiO_2/MoS_3$			yes
FTO/WO_3	$FTO/CuO/BaTiO_3/MoS_3$			no

Table 17: PEC materials and tests in acidic conditions

The MoS_3 HER co-catalyst deposited on the photocathodes is known to function in acidic conditions, thus the measurements were effectuated in pH 0 with 1 M H_2SO_4, due to the stability of the co-catalyst [212, 333-335]. Wavelengths 300- 950 nm of a xenon arc lamp without ozone coupled with an Oriel infrared water filter was employed as a light source approximately 20 cm away from the cell with a light power output of 350 mW/cm² at the photoanode. The photoanode was illuminated from the backside as to be facing the photocathode; and in accordance, the photocathode was illuminated from the front side.

III.7.1. PEC TANDEM DUAL PHOTOSYSTEM TESTS IN ACIDIC CONDITIONS

III.7.1.1. WO_3 and Pt

The first test was completed with WO_3 as a photoanode and platinum as a cathode in a single photosystem to ensure no electrolyte or gas leaking, and that the device could function properly as intended. Unfortunately after 80 minutes of use, some of the electrolyte was displaced into the tubing from the flow of the carrier gas leading to the gas chromatograph, leaving an air pocket in the cell which contacted the electrodes and increased the ohmic resistance in the device. Results from the gas chromatograph showed a potential leak due to faradaic efficiencies being larger than 100%; therefore, data was only treated using the measured gas and charge before the leak was detected. This suggests that the gas chromatograph system (PEC gas inputs and outputs, tubing, and connectors) is not optimized and thus a large source of error in the following experiences.

To ensure gas detection, 1.03 V vs. Ag/AgCl KCl saturated reference electrode was administered to the cell, therefore surpassing potential needed to split water with WO_3 as a photoanode. Despite the obstacles with the setup, the faradaic efficiency of WO_3 was large in acidic medium, measuring almost 92%. The gas chromatograph measured a smaller faradaic efficiency for the platinum counter electrode employed of around 66%. This suggests a H_2:O_2 ratio of 1.44:1 which is stoichiometrically incorrect for ideal functioning of a PEC for water splitting. Therefore either H_2 is capable of leaking out of the cell/gas detection system, reverse reactions occurred, or some H_2 bubbles were stuck on the electrode surface or at nucleation sites in the cell and therefore not detected. Seeing as there is no electrolyte flowing through the cell, only argon as a carrier gas perturbs the system in order to dislocate bubble accumulation at places in the cell. Gas bubbles that do not dislocate from the electrode surface, otherwise known as the "bubble effect" is a known problem within the water electrolysis community [337]. The stability of the system was confirmed by the stabilized photocurrent of roughly 1.6 mA/cm² for over an hour. Visually, neither the WO_3 photoanode nor the platinum counter electrode displayed any signs of dissolution or degradation after removing it from the cell. No applied bias to photon efficiency for hydrogen was calculated for this test due to the fact that platinum is not photoactive, only a single photosystem was tested. Using the

faradaic efficiency of the photoanode, ABPE for the photoanode single photosystem calculated to be 0.083%. Data acquired during this preliminary test is displayed in Table 18 and Figure 104:

Total Q (C)	**Theoretical moles of gas produced**		**Detected moles of gas produced**		**Average j (mA/cm²)**	**Faradaic Efficiency (%)**		**ABPE *(O_2)* (%)**
14.80	H_2	O_2	H_2	O_2	1.60	H_2	O_2	0.083
	$7.67x10^{-5}$	$3.83x10^{-5}$	$5.06x10^{-5}$	$3.51x10^{-5}$		65.97	91.49	

Table 18: Performance of WO_3 vs. platinum in PEC under 350 mW/cm² in 1 M H_2SO_4 with 1.03 V external bias

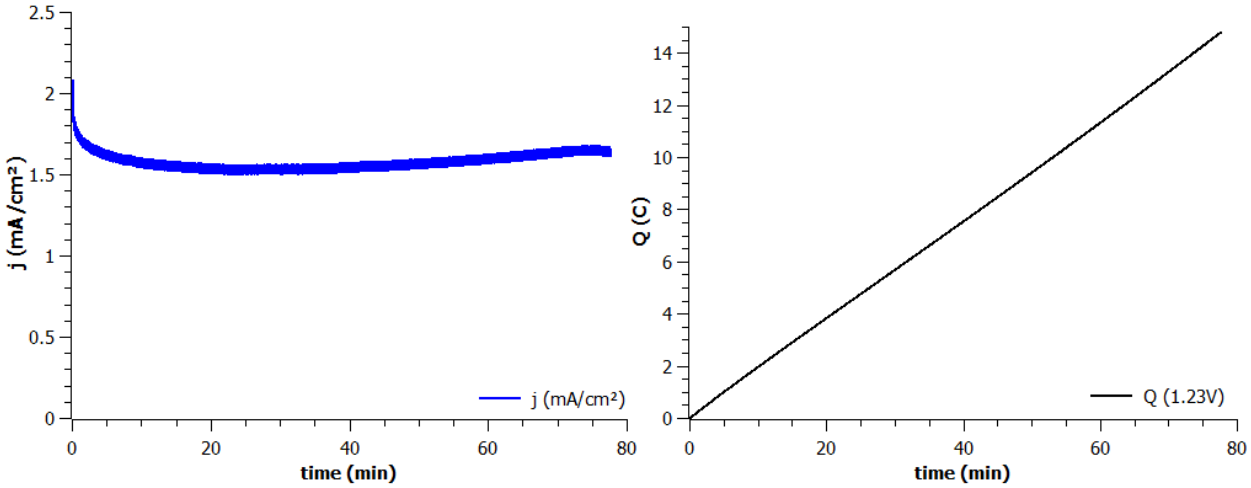

Figure 104: Photocurrent density and charge passed in WO_3 vs. platinum PEC device under 350 mW/cm² in 1 M H_2SO_4 (pH 0) with 1.03 V external bias

This preliminary test suggests that the cell functions relatively well with the exception of gas collection setup. The stability of WO_3 is rather good in acidic conditions and exhibited a steady photocurrent for over an hour. The steady state photocurrent of 1.6 mA/cm² corresponds to previously measured values for smaller samples (1 × 3 cm) for WO_3 at 1.23 V vs. RHE, suggesting the material functions similarly in varying cells, ensuring that the fabricated photoelectrocatalytic cell, despite some losses, functions properly electrochemically.

III.7.1.2. WO_3 and CuO/MoS_3

To measure a genuine solar to hydrogen efficiency, no external bias was added to the PEC containing a WO_3 photoanode and CuO/MoS_3 photocathode for testing in acidic conditions. Nevertheless, upon illumination of 350 mW/cm², the photocurrent displayed was very low and congruently no hydrogen was evolved or simply not detected. The total charge passed after an hour was only 0.02 C and the average photocurrent in the system was 0.002 mA/cm². This suggests that the copper photocathode may have

limited the WO_3 photoanode in terms of photocurrent and overall performance, as the previous experiment with WO_3 and platinum implied that WO_3 was the limiting photoelectrode in terms of performance in determining the operational (photo)current. Data corresponding to the unbiased measurements of WO_3 and CuO/MoS_3 are shown below in Table 19 and Figure 107:

Total Q (C)	**Theoretical moles of gas produced**		**Detected moles of gas produced**		**Average j (mA/cm²)**	**Faradaic Efficiency (%)**		**STH (%)**
0.02	H_2	O_2	H_2	O_2	0.002	H_2	O_2	0
	8.56×10^{-8}	4.28×10^{-8}	0	2.29×10^{-6}		0	5357*	

Table 19: Performance of WO_3 vs. CuO/MoS_3 in PEC under 350 mW/cm² in 1 M H_2SO_4 (*signifies leak in gas detection system)

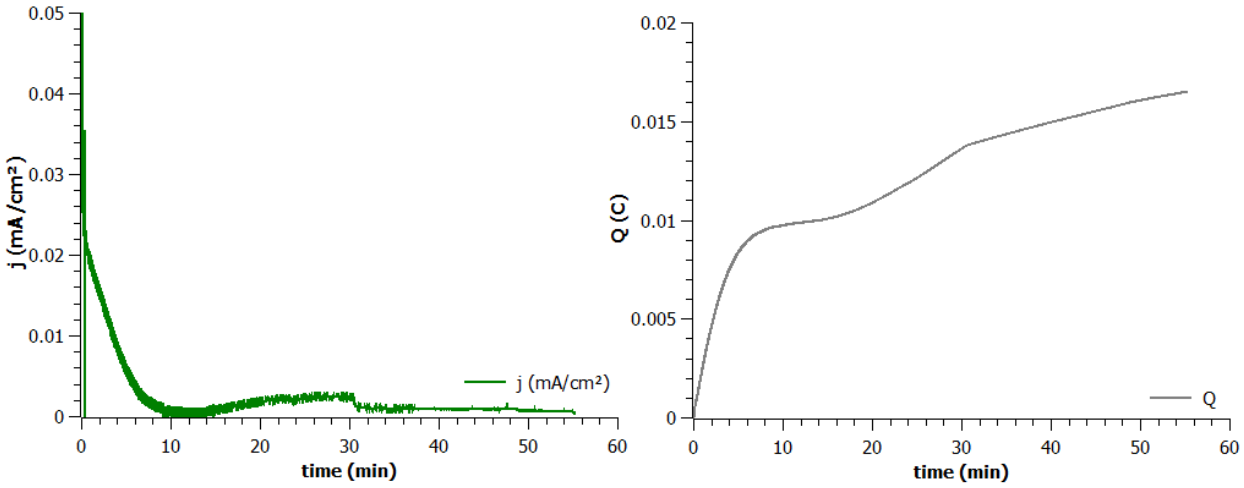

Figure 105: Photocurrent density and charge passed in WO_3 vs. CuO PEC device under 350 mW/cm² in 1 M H_2SO_4 (pH 0) with no external bias

Removal of the photoelectrodes form the cell after testing revealed that the CuO/MoS_3 photocathode had completely dissolved in the acidic conditions, Figure 106 reveals a photo of the absence of black CuO.

Figure 106: Photo of CuO/MoS_3 photocathode after use

The grey-black copper layer is completely gone and the MoS_3 layer seems to be somewhat still intact, suggesting the electrolyte came into contact with the copper despite the 70 nm layer of MoS_3 covering it. The CuO/MoS_3 photocathodes suffered in terms of stability which is either due to incomplete coverage of the CuO layer or piercing of the layer when clamped into the cell for use. In contrast, the WO_3 photoanode, like before remained untouched and visually showed no signs of degradation. Thus, it seems the system may need external bias in order to function correctly; suggesting that the open circuit voltage provided by the photoanode and photocathode combined is not sufficient to split water under 350 mW/cm² illumination.

III.7.1.3. WO_3 and $CuO//TiO_2/MoS_3$

Testing of materials in acidic conditions with a *proton* exchange membrane is more logical than in neutral conditions due to the concentration of protons in solution. However, upon integration of Nafion® NRE 212, there were complications with this system as no hydrogen was detected even with an external bias of 0.6 V added. The voltage detected by the potentiostat was 0.4 V, suggesting the working potential of the system was decreased by 33% throughout the device. Due to no hydrogen being detected the APBE was 0%. Data associated with the measurements made are shown in Table 20 and Figure 107:

Total Q (C)	Theoretical moles of gas produced		Detected moles of gas produced		Average j (mA/cm²)	Faradaic Efficiency (%)		ABPE (%)
0.17	H_2	O_2	H_2	O_2	0.026	H_2	O_2	0
	8.89×10^{-7}	4.45×10^{-7}	0	4.96×10^{-6}		0	1114*	

Table 20: Performance of WO_3 vs. $CuO/TiO_2/MoS_3$ in PEC under 350 mW/cm² in 1 M H_2SO_4 with 0.6 V external bias and Nafion® Membrane (*signifies leak in gas detection system)

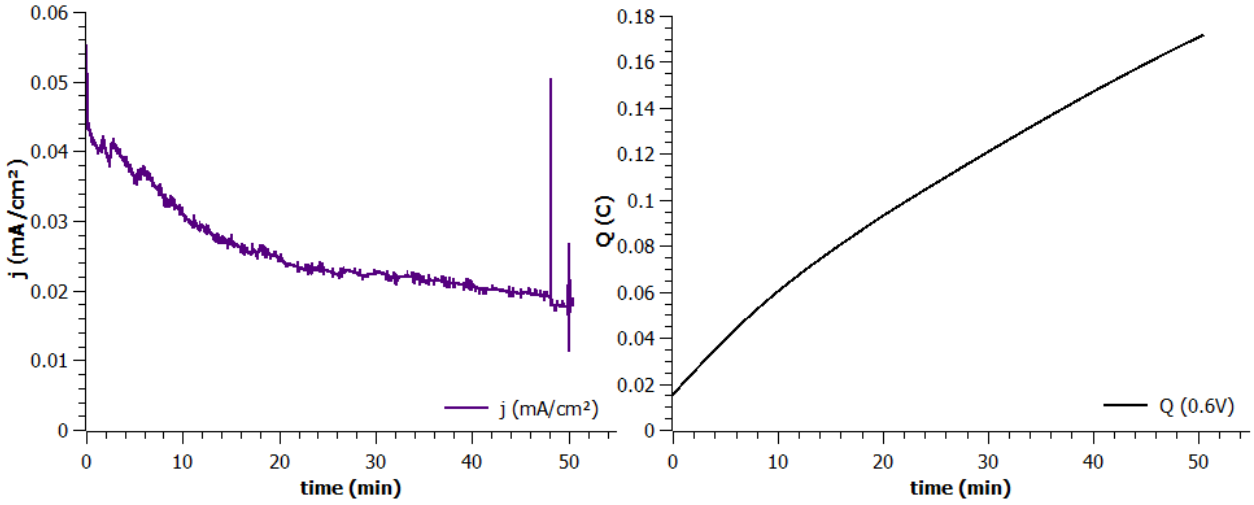

Figure 107: Photocurrent density and charge passed in WO_3 vs. CuO/TiO_2 PEC device under 350 mW/cm² in 1M H_2SO_4 (pH 0) with 0.6 V external bias and Nafion® NRE-212

The fact that no H_2 was detected could be due to the fact that the TiO_2 did not protect the copper photocathode and the CuO reduced to Cu_2O and potentially even to elemental copper, which corrodes according to the Pourbaix diagram in Figure 16 and dissolved into solution during testing. The degradation of copper over time proposes that the electrolyte was in contact with the copper at some point and eventually reduced by the protons in solution.

III.7.1.4. WO_3 and $CuO//BaTiO_3/MoS_3$

Seeing as the test without external bias for acidic conditions did not produce H_2 and demonstrated a small photocurrent, an external bias of 0.6 V vs. Ag/AgCl reference electrode was applied for the WO_3 vs. $CuO/BaTiO_3/MoS_3$ sample. A cross section FEG-SEM image of the photocathode is shown in Figure 108 indicating that the CuO layer measures 500 nm, the $BaTiO_3$ varies with an average thickness around 80 nm, and finally the MoS_3 top layer of 60 nm.

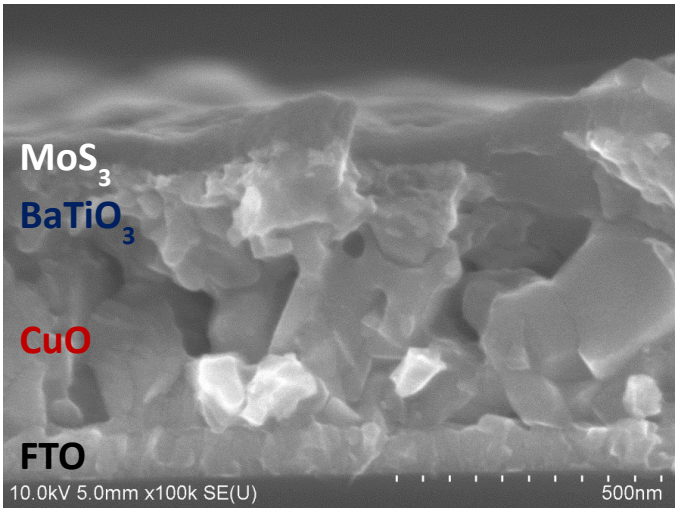

Figure 108: FEG-SEM cross section image of FTO/CuO/$BaTiO_3$/MoS_3 photocathode

Addition of a membrane was excluded in this test due to the previous results, suggesting the drop in voltage in the cell due to membrane addition may contribute to malfunctioning or significant losses in the system. This test, employing WO_3 as a photoanode and CuO/$BaTiO_3$/MoS_3 as a photocathode showed a slight loss in photocurrent overtime, but with an overall stable response after 20 minutes of functioning. Poor faradaic efficiencies of 28.34% and 21.41% for the HER and OER were measured respectively. While there seemed to be no leak in the system which let air into the cell or GC, there is always a continuous detection of nitrogen (an average detection of 2.5×10^{-8} moles).

The argon used as the carrier gas is very pure 99.9995% thus there must be some air which enters the GC detection system at some point – the origin has not yet been identified. Nevertheless, the small faradaic efficiencies of the photoelectrodes could be due to the fact that parasitic reactions occur with WO_3 leading to other products than O_2 and reverse reactions occurring due to the possibility of mixing of gases since there was no membrane included in the system to separate the product gases. Accordingly, O_2 may have been reduced at the photocathode and H_2 oxidized back to water at the photoanode resulting in lower gas production and/or detection [26, 338, 339]. The applied bias photon efficiency was calculated to be 0.019%. Data associated with this test is displayed below in Table 21 and Figure 111:

Total Q (C)	Theoretical moles of gas produced		Detected moles of gas produced		Average j (mA/cm²)	Faradaic Efficiency (%)		ABPE (%)
4.221	H_2	O_2	H_2	O_2	0.367	H_2	O_2	0.019
	2.19×10^{-5}	1.09×10^{-5}	6.20×10^{-6}	9.37×10^{-6}		28.34	21.41	

Table 21: Performance of WO_3 vs. $CuO/BaTiO_3/MoS_3$ in PEC under 350 mW/cm² with 0.6 V external bias in 1 M H_2SO_4

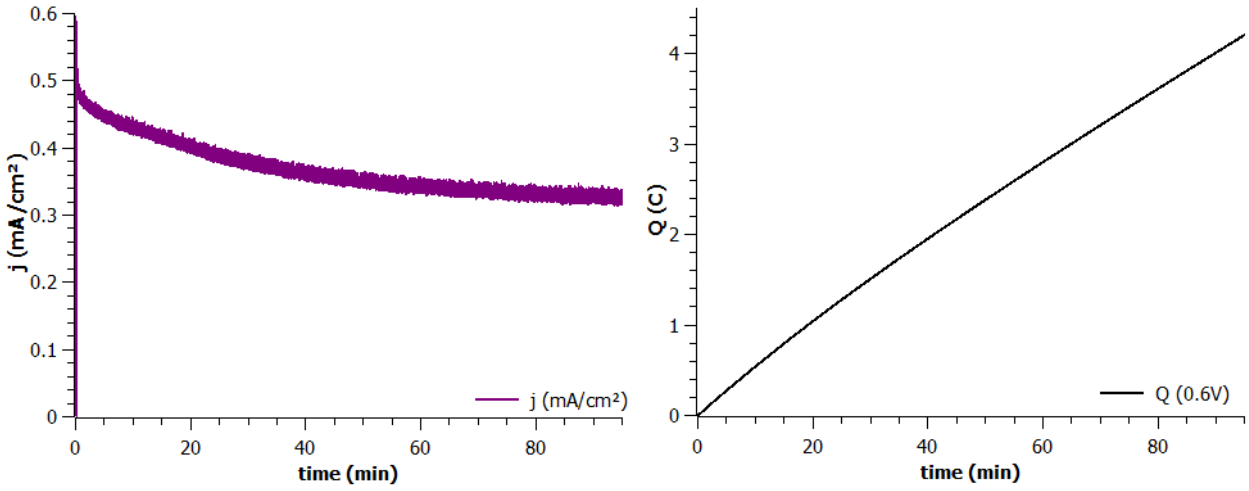

Figure 109: Photocurrent density and charge passed in WO_3 vs. $CuO/BaTiO_3$ PEC device under 350 mW/cm² in 1 M H_2SO_4 (pH 0) with 0.6 V external bias

After the experiment, the photoelectrodes were removed and rinsed with distilled water. The copper thin film which remained on the surface of the photocathode quickly detached and dissociated completely from the FTO substrate, suggesting this poor contact was likely the source of the decrease in photocurrent. The WO_3 photoanode visually seems untouched and very stable in these conditions, like all previous photoelectrocatalytic cell tests with WO_3 suggesting good stability in strongly acidic conditions. This was confirmed by FEG-SEM images (displayed below in Figure 110), suggesting the WO_3 photoanodes are stable in strongly acidic conditions.

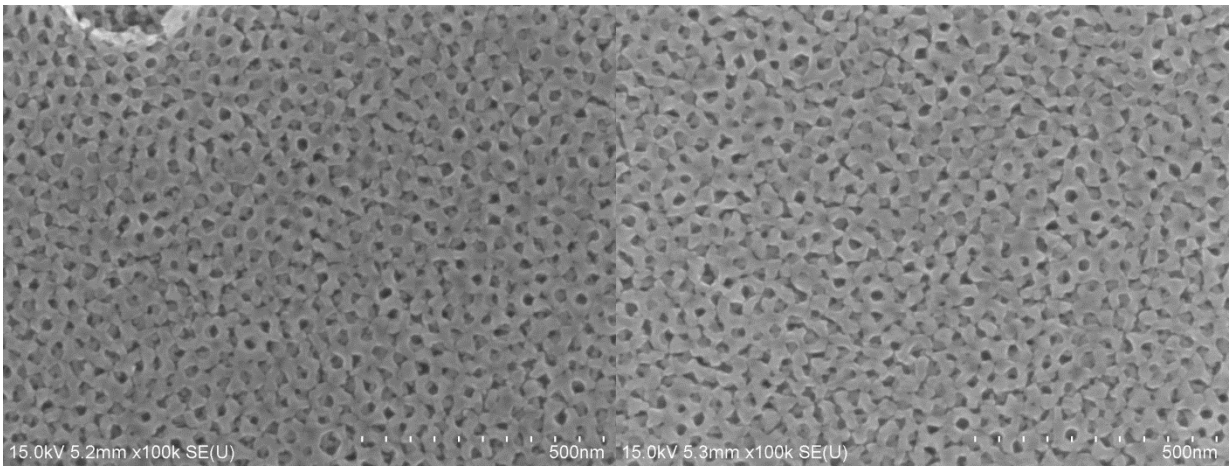

Figure 110: FEG-SEM images of WO_3 (left) before 95 minutes use in 1 M H_2SO_4 with copper photocathode under 350 mW/cm² illumination and (right) after use

A photo of the photoelectrodes after 95 minutes of use under 0.6 V external bias under 350 mW/cm² illumination and 1 M H_2SO_4 is shown below in Figure 111:

Figure 111: Photo of CuO/$BaTiO_3$ (left) and WO_3 (right) after testing in photoelectrocatalytic cell

The black seen in the photocathode active area of Figure 111 is on the back of the sample due to dip-coating techniques. The layer of $BaTiO_3$ and CuO seemed to be intact, thus suggesting reduction occurred at the TCO interface, reducing the layer of copper which dissolved to dissociate the thin layer and its protection all together. This detachment of the copper oxide layer from the substrate advocates that the electrolyte interacted with the copper layer, reducing it and instigating the detachment of the copper absorber layer and protective layer eventually. Hypothetically it is possible that upon tightening the cell to avoid electrolyte leaks, the o-ring pierces the thin layer and leaves opening for electrolyte to penetrate around the edges of the thin film. Therefore, the $BaTiO_3$ protective/composite layer may in fact protect CuO thin films at the SCLJ for water splitting technologies in acidic conditions but to no avail if

electrolyte finds it way around this layer; nevertheless, overall stability is still an issue for copper based photocathodes in this cell due to inadvertent exposure to the electrolyte in acidic conditions.

III.8. NEUTRAL CONDITIONS

$BiVO_4$, measured to be somewhat stable in neutral conditions during previous faradaic testing, was employed as an n-photoanode in the tandem dual photosystem photoelectrocatalytic cell for the OER. This photoanode was complemented by a CuO based p-photocathode like in previous acidic conditions. The CuO and protected CuO based photocathodes were fabricated by sol-gel dip coating methods and modified as denoted in Table 22.

n- photoanode	**p-photocathode**	**electrolyte**	**illumination**	**membrane**
$FTO/SnO_2/BiVO_4$	FTO/CuO	1 M KPi (pH 7)	350 mW/cm² (300 – 900 nm)	no
$FTO/SnO_2/BiVO_4$	$FTO/CuO/TiO_2$			no
$FTO/SnO_2/BiVO_4/NiB_i$	$FTO/CuO/BaTiO_3$			no

Table 22: PEC materials and tests in neutral conditions

Similar to the tests in acidic conditions, the neutral condition tests were effectuated in 1M KPi in place of sulfuric acid under the same settings: using wavelengths 300- 950 nm of a xenon arc lamp without ozone coupled with an Oriel infrared water filter was employed as a light source approximately 20 cm away from the cell with a light power output of 350 mW/cm² at the photoanode. The photoanode was again illuminated from the backside as to be facing the photocathode; leaving the photocathode to be illuminated from the front side.

III.8.1. PEC TANDEM DUAL PHOTOSYSTEM TESTS IN NEUTRAL CONDITIONS

III.8.1.1. $SnO_2/BiVO_4$ and CuO

The first test effectuated in neutral conditions was with $SnO_2/BiVO_4$ (annealed at 400°C and calcinated at 450°C for 1 hour) as a photoanode and unprotected CuO as a photocathode in 1M KPi (pH 7). An external bias (of 0.6 V vs. reference) was added due to the large overpotential exhibited by the large onset potential in the photocurrent responses for $BiVO_4$. FEG-SEM images of the $SnO_2/BiVO_4$ and CuO photoelectrodes are displayed in Figure 112 and Figure 113 before use. FEG-SEM images suggest that the CuO crystals are large and leave some areas of the FTO exposed. The overall thickness is around 80 nm for the FTO and 500 nm for the CuO as expressed by FEG-SEM cross section images in Figure 114).

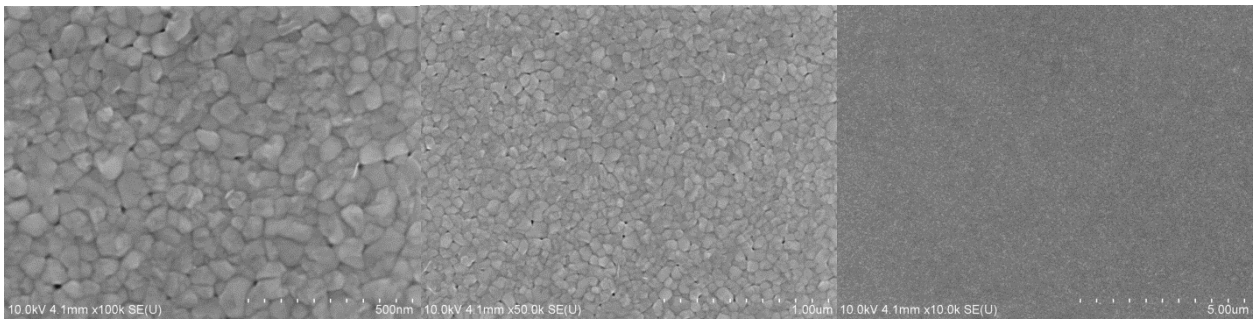

Figure 112: FEG-SEM images of FTO/SnO_2/$BiVO_4$ photoanodes under 100k, 50K and 10k magnification

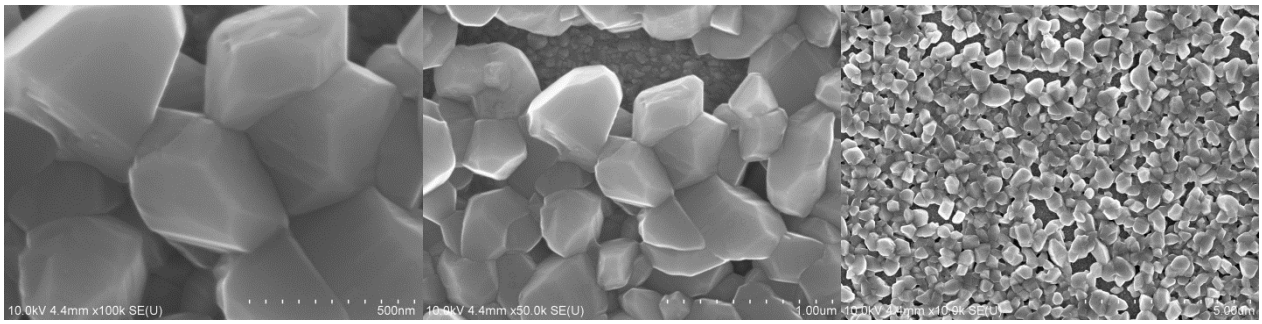

Figure 113: FEG-SEM images of FTO/CuO photocathode at 100k, 50K and 10k magnification

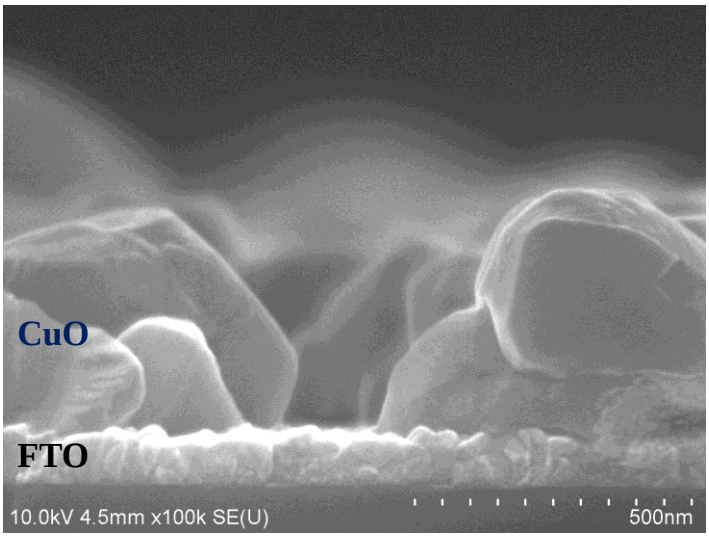

Figure 114: FEG-SEM cross section image of CuO on FTO substrate

The photocurrent of the SnO_2/$BiVO_4$ and CuO coupled tandem dual photosystem decreased significantly with an overall average of 0.27 mA/cm² with a total charge of 7.655 coulombs passed after 3.6 hours of use. The photocurrent decreased significantly, suggesting instability or increase in resistance between the photoelectrodes employed. The faradaic efficiency of the photocathode was measured to be 72%; however

the oxygen detected by the GC suggested a leak somewhere in the system, measuring a faradaic efficiency of almost 360%. The gas detection once again shows great error in the O_2 detection most likely due to a leak in the connection line from the cell to the GC. Nitrogen detected by the GC averaged a persistent 3.3 x 10^{-8} moles throughout the measurements. The applied bias to photon efficiency based on the production of hydrogen was calculated to be 0.037%; a rather low efficiency, even with an external bias applied. Data associated with this experiment is displayed in Table 23 and Figure 115.

Total Q (C)	**Theoretical moles of gas produced**		**Detected moles of gas produced**		**Average j (mA/cm²)**	**Faradaic Efficiency (%)**		**ABPE (%)**
7.655	H_2	O_2	H_2	O_2	0.268	H_2	O_2	0.037
	3.97×10^{-5}	1.98×10^{-5}	2.85×10^{-5}	7.10×10^{-5}		71.88	357.88*	

Table 23: Performance of $SnO_2/BiVO_4$ vs. CuO in PEC under 350 mW/cm² in 1 M KPi with 0.6 V bias (*signifies leak in gas detection system)

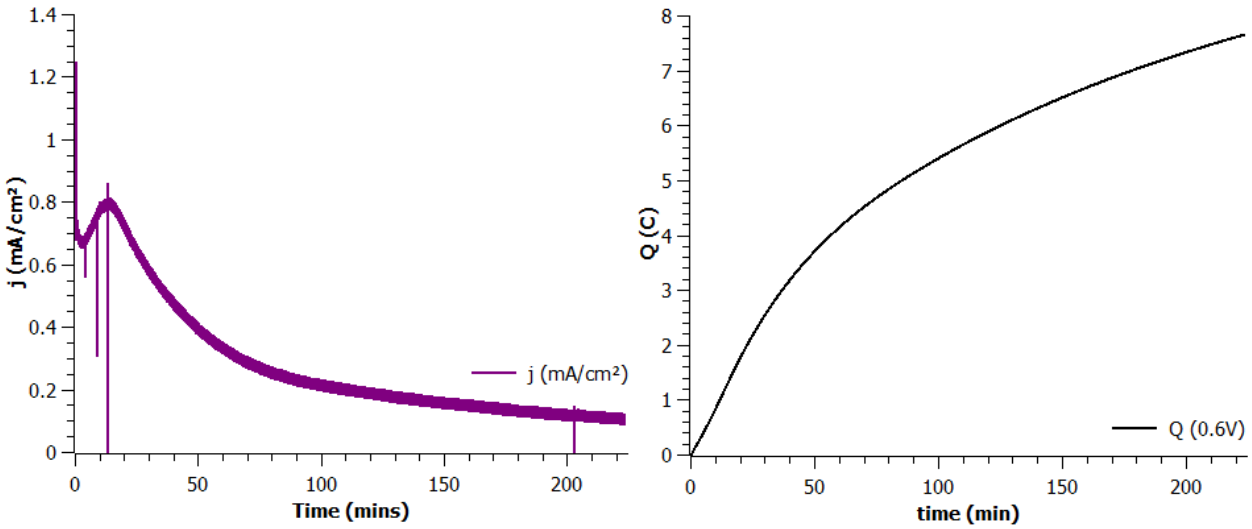

Figure 115: Photocurrent density and charge passed in $SnO_2/BiVO_4$ vs. CuO PEC device under 350 mW/cm² in 1 M KPi (pH 7) with 0.6 V external bias

The photos taken of the photoelectrodes after use indicate dissolution of the $BiVO_4$ and reduction of the black CuO to bronze colored Cu_2O or even elemental copper. These post-test photos (Figure 116) illustrate that copper based photocathode stability is increased in neutral conditions compared to acidic conditions; which may confirm that the corrosion is somewhat delayed when the concentration of protons is fewer in the electrolyte.

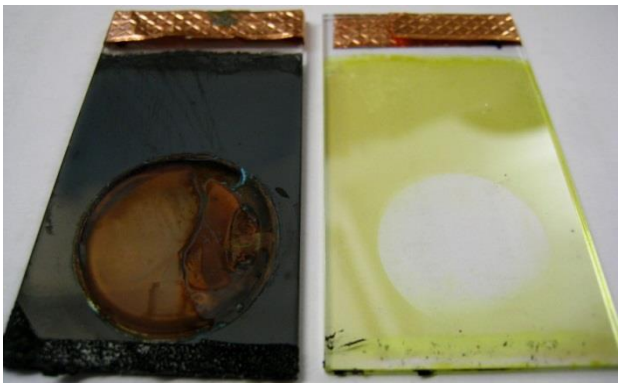

Figure 116: Photo of CuO (left) and $SnO_2/BiVO_4$ (right) after testing in photoelectrocatalytic cell

III.8.1.2. $SnO_2/BiVO_4$ and CuO/TiO_2

In attempts to calculate a STH value for neutral conditions in the photoelectrocatalytic cell, $SnO_2/BiVO_4$ and CuO/TiO_2 were used in a 2-electrode setup to attempt operation without external bias. Upon illumination, the photocurrent in neutral conditions with $SnO_2/BiVO_4$ photoanode and CuO/TiO_2 photocathode without bias (Figure 117) was close to zero; therefore, an external bias of 0.6 V was applied to the cell to ensure to drive the water splitting and detection of product gases.

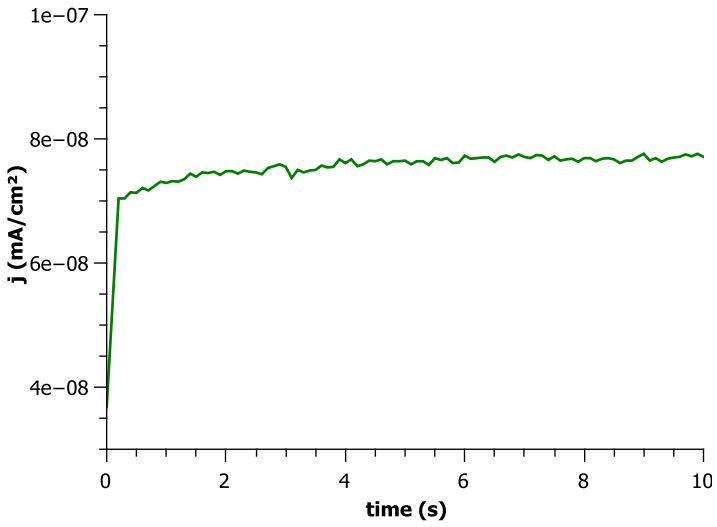

Figure 117: Photocurrent density and charge passed in $SnO_2/BiVO_4$ vs. CuO/TiO_2 PEC device under 350 mW/cm² in 1 M KPi (pH 7) without external bias

FEG-SEM images were taken of CuO/TiO_2 (shown in Figure 118) suggesting that some of the CuO in the CuO/TiO_2 photocathodes may be more exposed than in other areas, potentially affecting the long term stability.

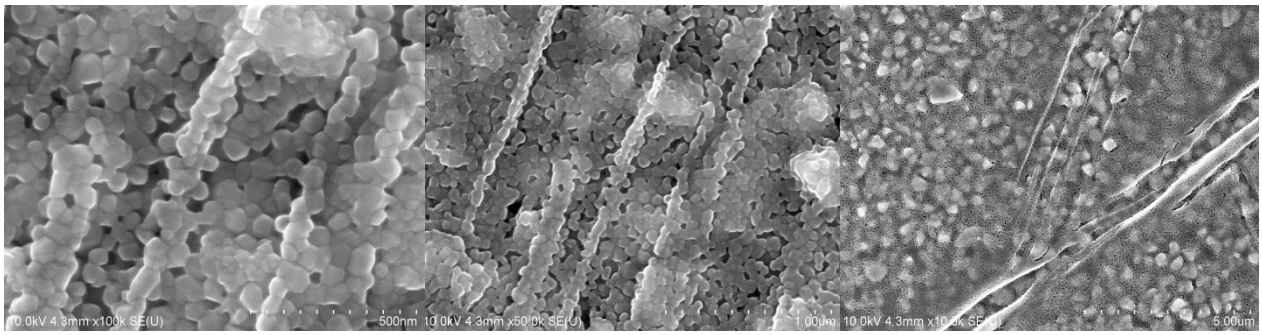

Figure 118: FEG-SEM images of FTO/CuO/TiO_2 photocathode at 100k, 50K and 10k magnification

After 75 minutes of testing in pH 7, the experiment was stopped due to the pronounced decrease in photocurrent. The detection of hydrogen was very small and oxygen very large, suggesting another leak in the GC setup. The ABPE was calculated to be 0% due to the lack of detection of hydrogen. Like in acidic conditions with CuO/TiO_2, little to no hydrogen was detected by the GC. Thus this could also be due to TiO_2 n-type behavior on the surface of CuO as previously seen with WO_3 and CuO/TiO_2 in acidic conditions. Further investigation for photocathode stability and performance are required to understand complete tandem dual photosystem sources of loss. The data associated with SnO_2/$BiVO_4$ coupled with CuO/TiO_2 in neutral conditions are displayed in Table 24 and Figure 119.

Total Q (C)	Theoretical moles of gas produced		Detected moles of gas produced		Average j (mA/cm²)	Faradaic Efficiency (%)		ABPE (%)
2.325	H_2	O_2	H_2	O_2	0.268	H_2	O_2	0.000
	1.20×10^{-5}	6.02×10^{-6}	1.28×10^{-8}	4.94×10^{-5}		0.11	819.64*	

Table 24: Performance of $SnO_2/BiVO_4$ vs. CuO/TiO_2 in PEC under 350 mW/cm² in 1 M KPi with 0.6 V external bias (*signifies leak in gas detection system)

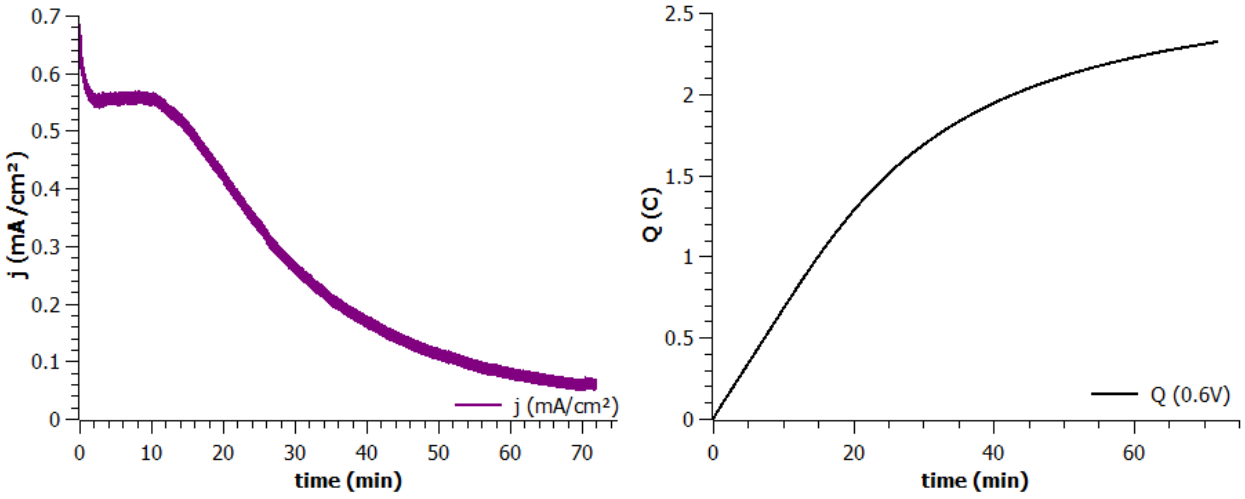

Figure 119: Photocurrent density and charge passed in $SnO_2/BiVO_4$ vs. CuO/TiO_2 PEC device under 350 mW/cm² in 1 M KPi (pH 7) with 0.6 V external bias

Once again, after removal of the two photoelectrodes, it seems the major decrease in photocurrent was due to degradation of the materials. Even with the TiO_2 protective layer, the copper was reduced by protons in the copper oxide photoabsorber layer. FEG-SEM images in Figure 121 shows the CuO/TiO_2 photocathode microstructure before (left) and after use (right) displaying an exposed copper photocathode and thus the TiO_2 inability to successfully passivate the copper. This is also visually evident by the color change of the active area from grey-black CuO color to the copper orange Cu_2O or elemental copper shown in Figure 120. $BiVO_4$ also indicated dissolution of the layer (seen to the right in Figure 121) which is no longer present where the material was exposed to the electrolyte. This is potentially due to the thin layer (roughly 75 nm) and the V^{5+} potentially dissolving in electrolyte [176, 193, 291, 307]. The slightly thicker portion of the $BiVO_4$ thin film, due to dip-coating evaporation artifacts, still remains on the surface of the $SnO_2/BiVO_4$ film. Thus, the thinner area of $BiVO_4$ seems to have dissolved into solution either by photodegradation, photocorrosion, or dissolution.

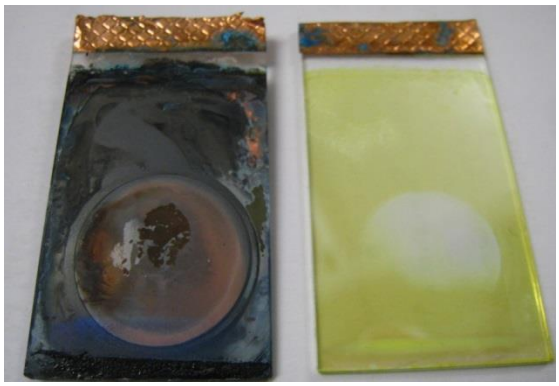

Figure 120: Photo of CuO/TiO_2 (left) and $SnO_2/BiVO_4$ (right) after testing in photoelectrocatalytic cell

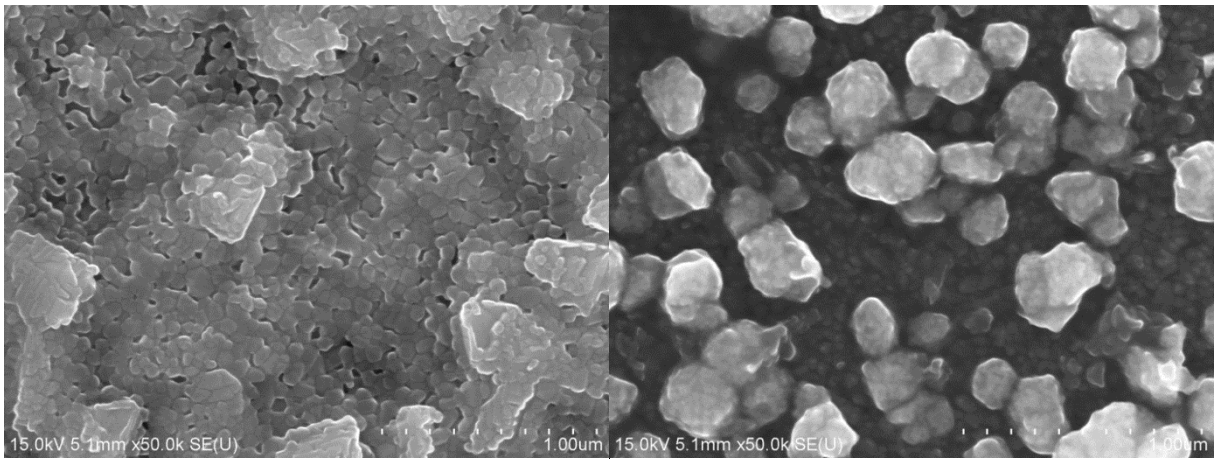

Figure 121: FEG-SEM images of CuO/TiO_2 (left) before use for 75 minutes in 1 M KPi with copper photocathode under 350 mW/cm² illumination and (right) after use

These results suggest that even with protection, CuO/TiO_2 photocathodes are not stable, most likely due to incomplete coverage of the TiO_2 layer thus failing to protect CuO from the electrolyte, which reduces CuO into Cu_2O and potentially Cu, producing the orange bronze coloration and eventual dissolution. Even though CuO photocathodes are more stable in neutral pH than in acidic conditions, the $BiVO_4$ photoanode also suffers from instability. Thus further optimization or addition of co-catalysts is needed for practical application.

III.8.1.3. $SnO_2/BiVO_4/NiB_i$ and $CuO/BaTiO_3$

Finally, in attempts to ameliorate the stability of the photoanode, $SnO_2/BiVO_4$ with co-catalyst NiB_i was paired with $CuO/BaTiO_3$ for use in neutral conditions in the cell. Below in Figure 122 and Figure 123 the FEG-SEM images of the two materials at three different magnifications are shown of $SnO_2/BiVO_4/NiB_i$ (Figure 122) and of $CuO/BaTiO_3$ (Figure 123). It is seen that the NiB_i did not deposit as uniformly as previously shown (Figure 73) and seemed to form large clusters of nickel oxides dispersed amongst the

$BiVO_4$ surface, verified by EDX. The ratio of Ba:Ti was verified to be 1:1 by EDX measurements at 10 kV tension, assuring that the both amorphous and crystalline deposited layer on the CuO was indeed $BaTiO_3$.

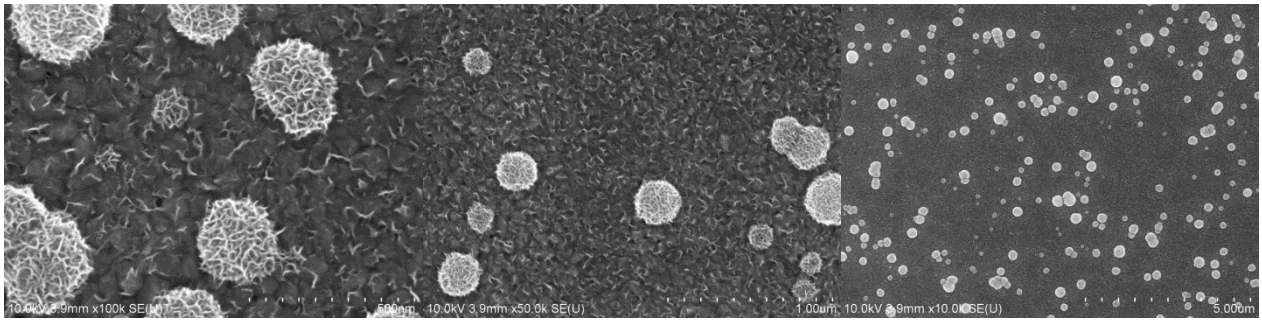

Figure 122: FEG-SEM images of FTO/SnO_2/$BiVO_4$/NiB_i photoanodes at 100k, 50K and 10k magnification

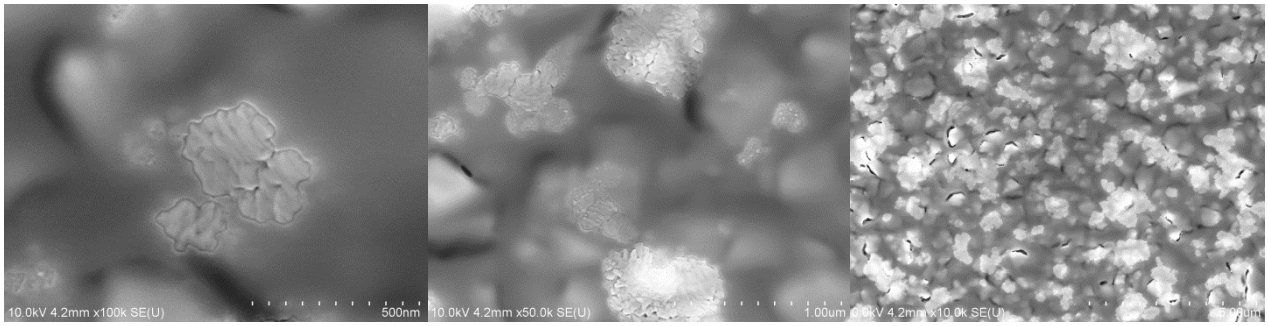

Figure 123: FEG-SEM images of FTO/CuO/$BaTiO_3$ photocathode at 100k, 50K and 10k magnification

Under 350 mW/cm² illumination without external bias, the average photocurrent of this combination was 0.018 mA/cm². This is only slightly less than previously reported results using copper absorbing photocathodes, but with WO_3 as the photoanode [117]. Unfortunately, the liquid guards and gas connections to the cell suggested leaking, as the faradaic efficiency for O_2 was larger than 100% and for H_2 was quite low: 0.44%; ultimately resulting in an STH efficiency of 0% (calculated based on the detection of H_2 and not O_2). The solar to oxygen efficiency was calculated to be 0.01%, though this is an overestimation considering the leak resulting in faradaic efficiency of O_2 being over 100%. These values along with associated data are shown below in Table 25. Associated photocurrent density and charge measured in the cell are displayed in Figure 124.

Total Q (C)	Theoretical Moles of Gas (moles)		Detected Moles of Gas		Average j (mA/cm²)	Faradaic Efficiency (%)		STH (%)
0.122	H_2	O_2	H_2	O_2	0.018	H_2	O_2	0.000
	6.33×10^{-7}	3.17×10^{-7}	2.76×10^{-9}	5.25×10^{-7}		0.44	165.88*	

Table 25: Performance of $SnO_2/BiVO_4/NiB_i$ vs. $CuO/BaTiO_3$ in PEC under 350 mW/cm² in 1 M KPi (*signifies leak in gas detection system)

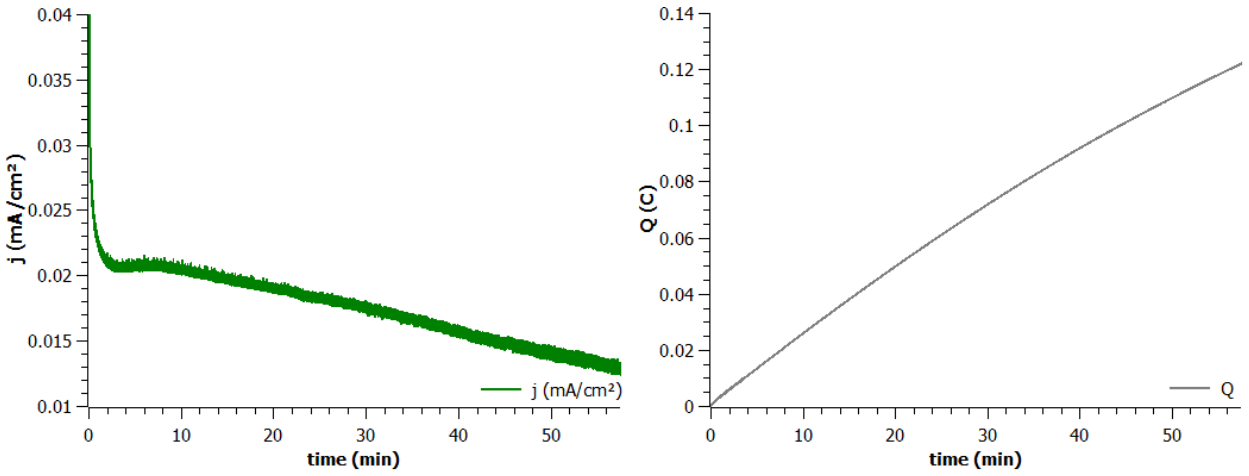

Figure 124: Photocurrent density and charge passed in $SnO_2/BiVO_4/NiB_i$ vs. $CuO/BaTiO_3$ PEC device under 350 mW/cm² in 1 M KPi (pH 7) with no external bias

After the 1 hour of testing with no external bias, 0.6 V was applied to the cell in order to see if the materials performed better. It is possible that the copper was partially dissolved by this point. Nevertheless, the faradaic efficiency of the photocathode increased upon applying and external bias and again the faradaic efficiency of the photoanode measured much larger than 100%. This photocurrent measurement during this applied bias test, though slowly decreasing over time, was the highest measured for $BiVO_4$ and CuO coupled photoelectrodes in neutral conditions. The applied bias efficiency (based on H_2) was calculated to be 0.023%; suggesting the materials function better with external applied bias. Associated data are shown in Table 26 and Figure 125:

Total Q (C)	Theoretical Moles of Gas (moles)		Detected Moles of Gas		Average j (mA/cm²)	Faradaic Efficiency (%)		ABPE (%)
3.224	H_2	O_2	H_2	O_2	0.348	H_2	O_2	0.023
	1.67×10^{-5}	8.35×10^{-6}	6.00×10^{-6}	2.20×10^{-5}		35.91	263.41*	

Table 26: Performance of $SnO_2/BiVO_4/NiB_i$ vs. $CuO/BaTiO_3$ in PEC under 350 mW/cm² with 0.6 V external bias (*signifies leak in gas detection system)

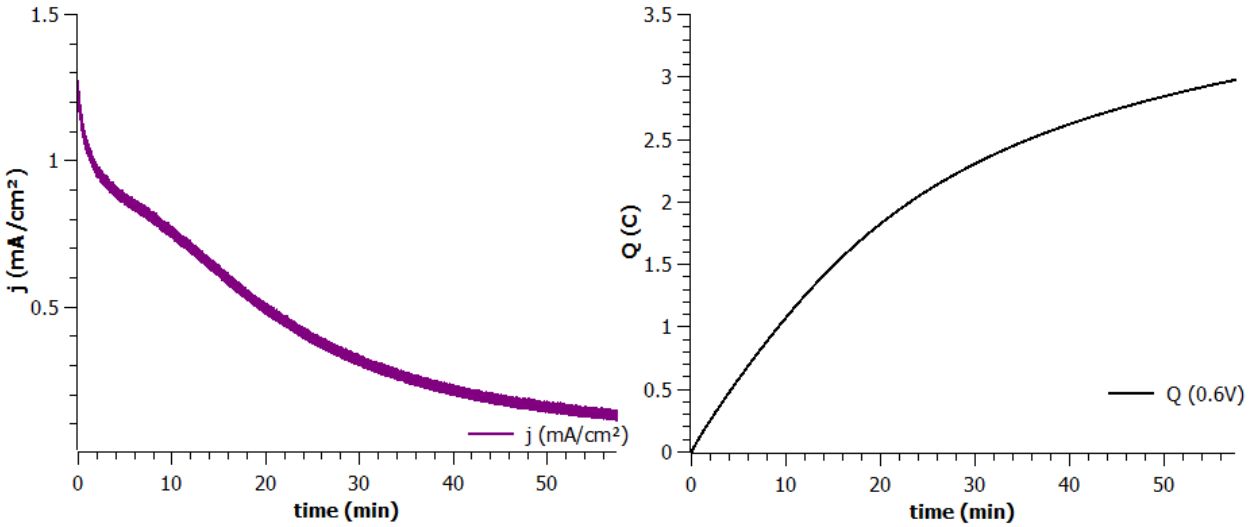

Figure 125: Photocurrent density and charge passed in $SnO_2/BiVO_4/NiB_i$ vs. $CuO/BaTiO_3$ PEC device under 350 mW/cm² in 1M KPi (pH 7) with 0.6 V external bias

The decrease in photocurrent was due to the dissolution of $BiVO_4$ and CuO, which again suffered from instability even with protection from $BaTiO_3$. This is shown in the photo shown in Figure 126 which displays the copper photocathode (left) and $BiVO_4$-based photoanode (right) after at least 2 hours of testing under 350 mW/cm² illumination (with and without external bias) in 1 M KPi (pH 7). Like with TiO_2, the CuO may have been reduced at the FTO contact due to exposure by non-uniform coverage or piercing the layer with the cell, while somewhat still protected by the $BaTiO_3$ at the SCLJ. Nevertheless, it is visibly clear that instability occurs for both materials under these conditions for the active area, whether reduced at the FTO substrate or from photodegradation or dissolution upon exposure to the electrolyte and light. However, the $BiVO_4/NiB_i$ seems to degrade slower than previous tests with $BiVO_4$ that did not contain NiB_i, suggesting NiB_i aids in the stability, or at least prolongs the lifetime of $BiVO_4$ photoanodes for water splitting applications.

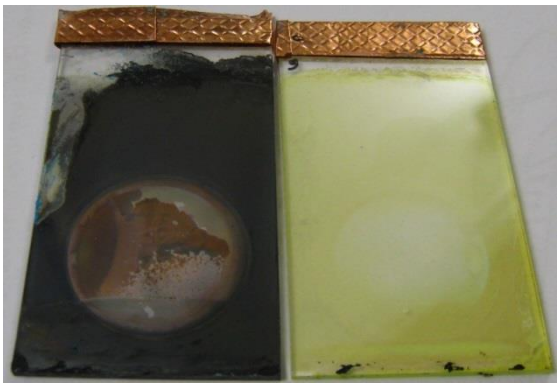

Figure 126: Photo of $CuO/BaTiO_3$ (left) and $SnO_2/BiVO_4/NiB_i$ (right) after testing in photoelectrocatalytic cell

$SnO_2/BiVO_4/NiB_i$ photoanodes visually advocate to be have somewhat dissolved in the solution. Upon inspection with FEG-SEM post mortem images, the $BiVO_4$ is still present, but the NiB_i layer is not. The FTO can be seen below the $BiVO_4$ in the right of Figure 127 suggesting that some of the layer has dissolved into solution.

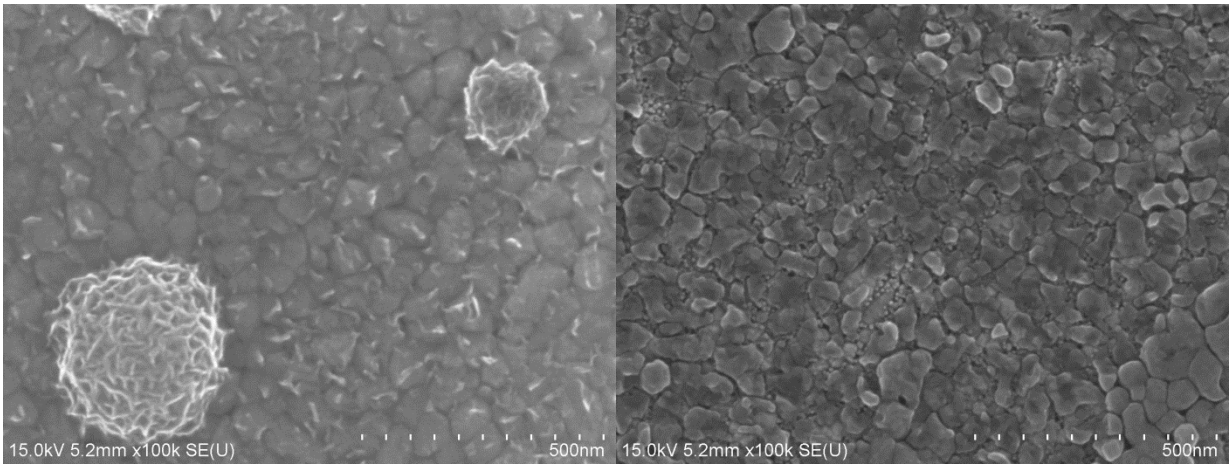

Figure 127: FEG-SEM images of $SnO_2/BiVO_4/NiB_i$ (left) before use for 60 minutes in 1 M KPi with copper photocathode under 350 mW/cm² illumination and (right) after use

These results suggest that stability is a great obstacle in overcoming in the conception, construction, and use of a tandem dual photosystem photoelectrocatalytic cell.

III.9. CONCLUSIONS

These studies demonstrate that the gas detection setup is obviously in need of optimizing for accurate gas detection. PEEK tubing enable the secure transfer of gas to the GC but connection between the cell and tubing, solution guards and tubing, and the gas chromatograph are most likely the largest sources of error.

It is possible that some gas bubbles stayed on the photoelectrodes and nucleated at sites in the cell as shown in (Figure 128). Nevertheless, most GC results insisted a leak in the system as there was an overestimate of oxygen concerning the faradaic efficiency. In addition, nitrogen was always detected by the GC. The pump employed with the GC for accurate gas detection could easily force air to be pulled into the GC, being detected in the TCD as well. This pump was imperative for gas detection, as 5 mL/min gas flow was the minimum flow for gas detection in the column and not many products were generally detected. The employment of a pump enabled the detection of product gas but may have been too violent for the small PEEK tubing, introducing air into the system creating error in gas detection measurements. It was found after testing that one of the gas outlets was cracked along the plastic, suggesting a source of gas leaking. Thus when threaded gas connectors were tightened to ensure hermetic sealing, the plastic became fragile overtime and eventually fissured.

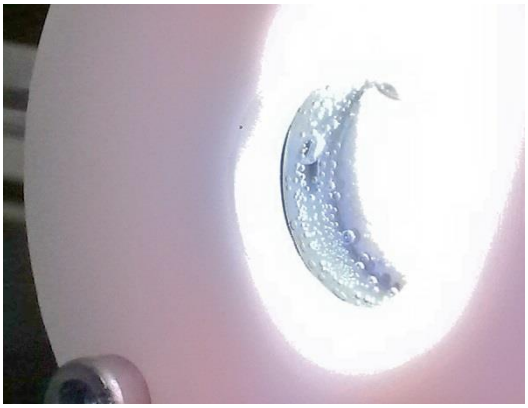

Figure 128: photo of gas bubbles at nucleation sites in the cell and on electrodes

Considering the architecture, the device uses materials resourcefully, maintaining the photoelectrodes as the cell walls simultaneously. However the cell dimensions, material, and electrode separations still need optimization, seeing as there was a large voltage drop over the system seen by EIS measurements, unrelated to the membrane integrated.

The cell may exhibit a higher performance upon employing quartz or fused silica as the photoanode substrate in place of glass in order to recover more ultraviolet light; though at the expense of an increased manufacturing cost. The compromise of light between the photoanode and photocathode seemed to be only a small problem due to the similar refractive indices of the glass substrates and electrolyte employed. Figure 100 and Figure 101 suggest that more than 80% of the incident light is received by the photocathode at wavelengths larger than 420 nm for WO_3 and 500 nm for $BiVO_4$ photoanode implementation. The AM1.5G spectrum has an output power of 683.65 W/m² for wavelengths 300 – 900 nm. If this photoelectrocatalytic cell was used under AM1.5G conditions employing 300 – 900 nm the

incident power which reaches the photocathode would be 59.5 mW/cm² (86% of the incident light power after passing through the photoanode) with WO_3 or 50 mW/cm² (73% incident light) with $BiVO_4$ as the photoanode. Therefore the transparency of photoanode materials, electrolyte, and membrane were not significantly detrimental to the optical aspects of the tandem dual photosystem configuration of the cell.

A significant issue concerning the architecture of the device was the lack of headspace available for gas accumulation and collection. There was little to no area for the carrier gas flowing in to collect, thus a small volume of electrolyte was displaced and flowed through the gas collection tubing and into the liquid guards to avoid being absorbed into the GC column. This generally resulted in increased resistance of the cell due to contact of the photoelectrodes with air. The displacement of electrolyte left an air bubble of roughly 0.19 cm^3 which increases resistance in the cell due to the carrier and product gases in contact with the photoelectrodes. This reduces the electrolyte volume from 2.4 mL to 2.2 mL therefore decreasing the time it takes to produce a pH gradient and instigating potential degradation and hindering overall stability of the materials. Taking into account the refractive indexes of the substrates and air from Figure 100 and Figure 101, the gas bubble which forms in the cell can greatly reduce solar absorption over 0.24 cm² (or 12% of the active surface) of the photoelectrodes, limiting overall performance and efficiency. A typical example of this is shown below in Figure 129:

Figure 129: Photo of gas headspace that accumulates in PEC active area

Thus, incorporation of headspace complicates the manufacturing of the device, as it should assume more of an H-form to keep the ionic separator exposed to the electrolyte for gas separation but employing areas above each photoelectrode for gas collection. Employment of a membrane was unsuccessful and thus requires further tests to implement an ionic separator for increased formation of product gases. Use of thinner membranes could result in faster diffusion of the neutral acid or base across the membrane and result in smaller steady-state pH gradients and therefore possess lower losses due to pH gradients in the

system [235]. Electrolyte flow and implementation of bi-polar membranes could be potential solutions for maintaining stability for the photoelectrodes [340-342]. Though this technology is not yet optimized for photocatalytic water splitting to accommodate the optical transparency, electronic conductivity and kinetics of water dissociation [342].

Concerning the integration of materials, CuO photoabsorber photocathodes were stable longer in neutral pH, most likely due to the lower concentration of protons available to reduce the copper at the SCLJ. Even with protection, the copper was reduced and often dissociated from the substrate. Photocathodes with TiO_2 or $BaTiO_3$ as a passivation/composite layer did not protect the CuO photoabsorber layer from reduction due to contact with the electrolyte. This was verified by the color change in material. This could possibly be due to the materials processing/optimization and integration of the photoelectrode in the cell. Pressing of photoelectrodes in the cell when securing them for use may pierce or damage the thin films; thus, accelerating degradation due to exposure. Nonetheless, $BiVO_4$ photoanodes seemed to be the limiting factor in terms of stability in neutral conditions. The $BiVO_4$ thin films were absent after an hour of use. This may be due to dissolution of vanadium at the surface and/or the thin layer which dissolves overtime due to this dissolution [176]. Tungsten trioxide seemed to be the only photoelectrode which was continuously stable; exhibiting little to no dissolution or degradation for more than an hour under accelerated conditions (350 mW/cm^2 with applied bias in concentrated electrolyte: 1 M H_2SO_4). Future efforts concerning the use of WO_3 in acidic medium should be concentrated on applying appropriate, stable, OER co-catalysts to increase O_2 faradaic efficiencies.

Overall, there are still several obstacles in material optimization and implementation in a PEC tandem dual photosystem containing only metal oxide thin films. This research contributes to knowledge on possible points of amelioration, both for laboratory cell architecture and material performance. The cell itself requires modifications for correct implementation of a membrane, gas detection, and to decrease losses by dimensioning and electrolytes. Placing the photoelectrodes closer and employing a headspace in laboratory destined cells are some of several ameliorations possible for future forms of the cell. Finally, implementation of flowing electrolyte (which can hypothetically replace the carrier gas flowing to the GC in laboratory cells) can potentially recover gases and prevent pH gradients occurring when the cell materials are optimized and stable, for eventual operation including a membrane for a wired dual compartment tandem dual photosystem water splitting cell.

CONCLUSIONS AND PERSPECTIVES

WO_3, SnO_2, and $BiVO_4$ thin film n-photoanodes for the OER half reaction in a water splitting cell were fabricated by sol-gel dip coating processes. Mesoporous WO_3 was deposited on glass/FTO substrates for use in acidic and neutral conditions as a photoanode for the OER. The microstructure of WO_3 was mesoporous due to the incorporation of block-copolymer in the sol, increasing the thickness, quantum yield, and surface area exposed to the electrolyte for overall increased performance. WO_3 performed with a large quantum yield in the UV light range, possessing a band gap of 2.8 eV. Nevertheless, sol-gel dip coated mesoporous WO_3 was less performant than other fabrication methods concerning state of the art WO_3 water splitting photoanodes. The photocurrent density of WO_3 suggested it can achieve applied bias to photon efficiencies of 0.3%. Though stable in acidic conditions, WO_3 suffers from peroxo species formation, which decreases the faradaic O_2 efficiency for water splitting applications. Near neutral conditions, the OER kinetics seem to be more favorable for O_2 production, but WO_3 is thermodynamically unstable in pH > 4. Co-catalyst surface modification efforts to stabilize the WO_3 in neutral conditions were unsuccessful and non-optimized. Thus, WO_3 mesoporous thin films without co-catalysts were deemed appropriate to test in a tandem dual photosystem cell under acidic conditions. An increase in thickness is potentially needed to increase absorption in the near visible region, but overall the WO_3 by sol-gel dip coating processes is a promising candidate due to the facile synthesis and deposition techniques. More research for appropriate abundant co-catalysts to function in acidic conditions with WO_3 is needed to increase the O_2 production and reduce the formation of parasitic peroxo formation for practical application.

Similarly, transparent yellow $BiVO_4$ thin films were synthesized by sol-gel dip coating processes, exhibiting good visible light transmittance for implementation in a tandem dual photosystem and possessing a band gap of 2.5 eV. It was discovered that the annealing temperature between deposition layers by dip-coating has a large role in determining the microstructure and conductivity. If annealed below 400°C between layers, the organic solvent in the sol stays in the layer, potentially doping the $BiVO_4$ with remaining carbon. Annealing between layers at 400°C with a final calcination at 450°C revealed thin but dense films possessing 10 – 40 nm crystals which exhibited high photoactivity and a lower onset potential for $BiVO_4$. Annealing at 450°C with final calcination at 450°C revealed larger 100 – 200 nm crystals which exhibited much larger minority carrier lifetime and diffusion lengths. Nevertheless, the larger crystals were less connected, limiting mass transport throughout the thin films; therefore, requiring thicker films for these higher temperature conditions. Findings suggest larger crystals are necessitated for increased conductivity (possessing larger minority carrier diffusion lengths and times), but in return, require thicker films for efficient performance. Thinner dense films can be annealed at slightly lower temperatures and exhibit good photocurrents despite the thin layer and several grain boundaries. The ABPE efficiency based on the photocurrent achieved by $BiVO_4$ in 1M KPi (pH 7) was calculated to be

0.3%. Upon employment of a sacrificial reagent, this value drastically increases to near 1.6%, suggesting that surface OER kinetics are a limiting factor in performance for $BiVO_4$. To increase this performance, 10 – 20 nm SnO_2 thin films were fabricated and deposited by sol-gel dip coating processes and were used to block back flow of holes to the TCO contact, increasing the amount of holes at the surface to participate in the OER. Upon optimization of the $BiVO_4$, this effect became less evident, suggesting the FTO/$BiVO_4$ interface is not a primary performance limiting obstacle. Faradaic efficiencies of $BiVO_4$ were measured in neutral pH to be above 70%; suggesting potential parasitic reactions or degradation is involved. Stability is questionable, due to the irreproducible tests in varying cells. Though, like many other groups, it is suspected that the dissolution of V^{5+} is the potential source of instability in neutral aqueous solutions. This dissolution leads to a bismuth rich surface, which may not be ideal for the OER due to surface OH bonding with vanadium [343]. The addition of co-catalysts suggested nickel is one of the most promising, though it did not succeed in greatly reducing the onset potential of $BiVO_4$ - which is a large obstacle in $BiVO_4$ optimization. The stability of nickel on $BiVO_4$ is not optimized in neutral pH, and requires further development. Overall, $BiVO_4$ by sol-gel dip coating methods can potentially be utilized for water splitting applications in the near future.

WO_3 was combined with $BiVO_4$ to form a composite photoanode for operation in neutral conditions, seeing as WO_3 has poor surface OER kinetics and is not stable in OER favored conditions. The WO_3 aided in electron transfer to the FTO but none of the WO_3 minority charge carriers could be harnessed at the SCLJ from the photovoltaic effect in the WO_3. This is most likely due to the positive position of SnO_2 valence band which lies between WO_3 and $BiVO_4$. Nevertheless, addition of an interfacial SnO_2 layer increased overall performance, suggesting the holes of $BiVO_4$ are redirected to the SCLJ instead of recombination defect states between the WO_3 and $BiVO_4$ layers. These composite photoanodes were less performant than individually employed mesoporous WO_3 in acidic conditions or SnO_2/$BiVO_4$ in neutral conditions; for it seems, according to state of the art WO_3/$BiVO_4$, nanostructuration of the tungsten layer is more beneficial than dense layers. Addition of SnO_2 layers between each photoabsorber confirmed that sol-gel composite photoanodes are potentially unideal in terms of interfacial charge transfer between materials. Thus sol-gel templating or even other forms of deposition to form thin films of WO_3 nanorods and nanostructures could be potentially advantageous in the composite WO_3/$BiVO_4$ photoanode.

A photocatalytic cell was constructed with white polyamide Ertalon® 6 SA, derived from the H-cell idea employing the complementary photoelectrodes as the cell windows. This cell was tested with optimized WO_3 photoanodes in acidic conditions in 1 M H_2SO_4 (pH 0) complemented by CuO based photocathodes for the HER. SnO_2/$BiVO_4$ was employed for use in 1 M KPi (pH 7) neutral conditions, which was also complemented by CuO photocathodes. Overall, the materials, with the exception of WO_3, suffered greatly

from stability issues. The large decrease in operating photocurrent was generally due to the degradation of photoelectrodes. CuO reduced to Cu_2O and eventually elemental copper and $BiVO_4$ suffered from (photo) dissolution, indicated by the absence of the thin yellow layer after use. CuO was very unstable in acidic conditions, most likely due to poor coverage of protective layers (MoS_3, TiO_2, and $BaTiO_3$) which permitted penetration of the proton rich electrolyte leading to the reduction and deactivation of CuO for the HER. Neutral conditions exhibited similar electrolyte exposure issues, but at a slower rate of photocathode degradation due to the lower concentration of protons in solution contributing to the reduction of copper oxides. Faradaic efficiencies have not yet reached unity due to poor detection techniques and potential parasitic reactions related to peroxo species and degradation for WO_3 and $BiVO_4$ respectively which restrict the efficient production of both H_2 and O_2 gases from water. Further research on co-catalysts is needed to increase the OER kinetics in acidic conditions for WO_3 and increase the stability and surface reaction kinetics of $BiVO_4$ in neutral conditions.

The PEC suffered from large potential drop in the electrolyte between the photoelectrodes. Addition of a membrane did not drastically increase resistance in the system thus was considered suitable, but was ineffectual when employed in acidic conditions. More research is needed in cell dimensions and spacing to fully understand how to suitably integrate a membrane and reduce ohmic drops in the cell. The large drop in resistance is most likely due to the electrolyte and spacing between the photoelectrodes and cell dimensions, which should be altered in future models [235]. The laboratory PEC constructed should be redesigned to encompass a headspace for gas collection. In an optimized upscaled version of this PEC, headspace is less of a concern – assuming the photoelectrodes function at the appropriate stoichiometric 2:1 hydrogen to oxygen ratio. A membrane or ionic separator for gas separation should be included in the cell once the source of potential drop has been identified and rectified. Flowing electrolyte could even replace the carrier gas in an industrialized cell, enabling the collection of produced gases for separation and treatment while avoiding bubble accumulation on the top photoelectrode in the cell. Finally, this laboratory cell operates in a vertical orientation, which does not take into account the optimal inclination relevant to the solar zenith for photovoltaics; therefore, tilted tandem dual photosystem industrialized cells should have less resistance and be tilted for increased absorption and accordingly overall performance [99].

Overall, the research effectuated on water splitting photoelectrocatalytic materials and cell proved advancement in the aim of producing clean hydrogen via abundant, low cost, non-toxic means. It is the first tandem dual photosystem cell encompassing only metal oxides as photoelectrodes to complete the water splitting reaction. The methods used to fabricate these metal oxide thin film photoelectrodes included purely sol-gel, dip coating, and electrodeposition methods. These methods are attractive due to

the facile, non-energetically demanding processing. No noble metals or unabundant materials were used to construct the photoelectrodes. This proves that water splitting photoelectrocatalysis can potentially be completed using abundant metal oxides, and using low cost manufacturing, in the near future. Nonetheless, there is still much progress to be made in terms of material performance, stability, and implementation before being integrated in a tandem dual photosystem PEC for sustainable application.

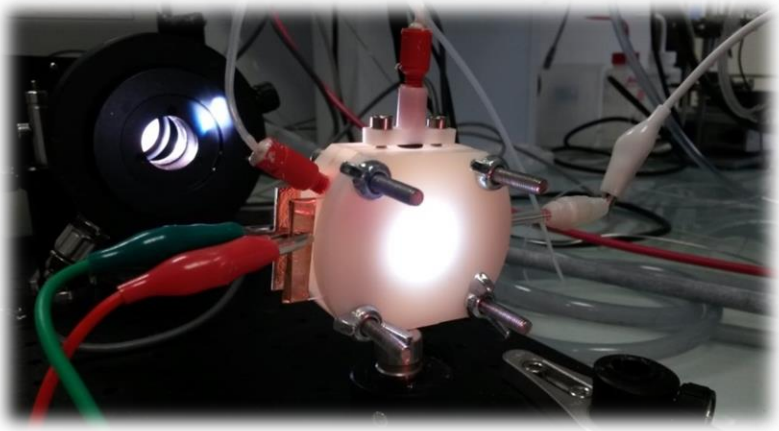

REFERENCES

1. Winter, C.-J., *Hydrogen energy — Abundant, efficient, clean: A debate over the energy-system-of-change.* International Journal of Hydrogen Energy, 2009. **34**(14): p. S1-S52.
2. Jain, I.P., *Hydrogen the fuel for 21st century.* International Journal of Hydrogen Energy, 2009. **34**(17): p. 7368-7378.
3. Haber, F. and R.L. Rossignol, *Production of ammonia*. 1916, Google Patents: United States Patent Office.
4. Riis, T., et al., *Hydrogen Production and Storage*. 2010, Organisation for Economic Co-operation and Development, International Energy Agency, Hydrogen Implementation Agreement: 9 rue de la Fédération, 75739 Paris Cedex 15, France.
5. Holladay, J.D., et al., *An overview of hydrogen production technologies.* Catalysis Today, 2009. **139**: p. 244-260.
6. Ulleberg, O., *Modeling of advanced alkaline electrolyzers: a system simulation approach.* International Journal of Hydrogen Energy, 2003. **28**: p. 21-33.
7. Cerri, I., et al., *Scientific Assessment in support of the Materials Roadmap enabling Low Carbon Energy Technologies*, in *JRC Scientific and Technical Reports*. 2012, European Commission, Joint Research Centre, Insitute for Energy and Transport, SETIS. p. 62.
8. Koroneos, C., et al., *Life cycle assessment of hydrogen fuel production processes.* International Journal of Hydrogen Energy, 2004. **29**: p. 1443-1450.
9. Altmann, M., et al., *Potential for Hydrogen as a Fuel for Transport in the Long Term (2020 - 2030)*, in *Technical Report Series*, H. Hernandez, Editor. 2004, Institute for Prospective Technological Studies. p. 174.
10. Tributsch, H., *Photovoltaic hydrogen generation.* International Journal of Hydrogen Energy, 2008. **33**(21): p. 5911–5930.
11. Peharz, G., F. Dimroth, and U. Wittstadt, *Solar hydrogen production by water splitting with a conversion efficiency of 18%.* International Journal of Hydrogen Energy, 2007. **32**: p. 3248-3252.
12. Khaselev, O., A. Bansal, and J.A. Turner, *High-effciency integrated multijunction photovoltaic/electrolysis systems for hydrogen production.* International Journal of Hydrogen Energy, 2001. **26**: p. 127-132.
13. Bilgen, E., *Solar hydrogen from photovoltaic-electrolyzer systems.* Energy Conversion and Management, 2001. **42**(9): p. 1047-1057.
14. Lehman, P.A., et al., *Operating experience with a photovoltaic-hydrogen energy system.* International Journal of Hydrogen Energy, 1997. **22**(5): p. 465–470.
15. Hollmuller, P., et al., *Evaluation of a 5 kW p photovoltaic hydrogen production and storage installation for a residential home in Switzerland.* International Journal of Hydrogen Energy, 2000. **25**(2): p. 97–109.
16. Hancock-Jr., O.G., *A photovoltaic-powered water electrolyzer: its performance and economics.* International Journal of Hydrogen Energy, 1986. **11**(3): p. 153-160.
17. Gibson, T.L. and N.A. Kelly, *Optimization of solar powered hydrogen production using photovoltaic electrolysis devices.* International Journal of Hydrogen Energy, 2008. **33**(21): p. 5931–5940.
18. Kelly, N.A. and T.L. Gibson, *Design and characterization of a robust photoelectrochemical device to generate hydrogen using solar water splitting* International Journal of Hydrogen Energy, 2006. **31**(12): p. 1658-1673.
19. Bansal, A., O. Khaselev, and J.A. Turner, *Photoelectrochemical System Studies*, in *Proceedings of the 2000 DOE Hydrogen Program Review*. 2000, NREL. p. 17.
20. Bonke, S.A., et al., *Renewable fuels from concentrated solar power: towards practical artificial photosynthesis.* Energy & Environmental Science, 2015. **8**: p. 2791-2796.

21. Shockley, W. and H.J. Queisser, *Detailed Balance Limit of Efficiency of p-n Junction Solar Cells* Journal of Applied Physics, 1961. **32**(3): p. 510-520.
22. Daous, M.A., M.D. Bashir, and M.M.A. El-Naggar, *Experiences with the safe operation of a 2 kWh solar hydrogen plant.* International Journal of Hydrogen Energy, 1994. **19**(5): p. 441–445.
23. Vidueira, J.M., A. Contreras, and T.N. Veziroglu, *PV autonomous installation to produce hydrogen via electrolysis, and its use in FC buses.* International Journal of Hydrogen Energy, 2003. **28**(9): p. 927 – 937.
24. Ghosh, P.C., et al., *Ten years of operational experience with a hydrogen-based renewable energy supply system.* Solar Energy, 2003. **75**(6): p. 469–478.
25. M.Grätzel and A.J. McEvoy. *Hydrogen Production by Solar Photolysis of Water*. in *American PhysicalSociety Symposium Basic Research for the Hydrogen Economy*. 2004. Montreal, Canada: EcolePolytechnique Fédérale de Lausanne.
26. Walter, M.G., et al., *Solar Water Splitting Cells.* Chemical Reviews (ACS Publications), 2010. **110**(11): p. 6446-6473.
27. Zhu, F., et al., *Amorphous Silicon Carbide Photoelectrode for Hydrogen Production from Water using Sunlight*, in *Solar Hydrogen*. 2010, InTech. p. 353-374.
28. Fujishima, A. and K. Honda, *Electrochemical Photolysis of Water at a Semiconductor Electrode.* Nature, 1972. **238**: p. 37-38.
29. James, B.D., et al., *Technoeconomic Analysis of Photoelectrochemical (PEC) Hydrogen Production*. 2009, Directed Technologies: Arlington, Virginia USA.
30. Van-de-Krol, R., et al., *Photoelectrochemical Hydrogen Production*. Electronic Materials: Science & Technology, ed. H.L. Tuller. 2012, Springer New York Dordrecht Heidelberg London: Springer.
31. Zoulias, E., et al., *A Review on Water Electrolysis.* TCJST, 2004. **4**(2): p. 41-71.
32. Harrison, K.W., et al., *Hydrogen Production: Fundamentals and Case Study Summaries*, in *18th World Hydrogen Energy Conference*. 2010, NREL: Essen, Germany. p. 21.
33. Pourbaix, M., *Atlas of electrochemical equilibria in aqueous solutions*. 1966, Oxford, New York: Pergamon Press. 644.
34. Gueymard, C.A., D. Myers, and K. Emery, *Proposed reference irradiance spectra for solar energy systems testing.* Solar Energy, 2002. **73**(6): p. 443–467.
35. Gueymard, C.A., *The sun's total and spectral irradiance for solar energy applications and solar radiation models.* Solar Energy, 2004. **76**(4): p. 423-453.
36. ASTM, *Reference Solar Spectral Irradiance: Air Mass 1.5*, in *SMARTS2 (vesion 2.9.2)* 2003, American Society for Testing and Materials.
37. Green, M.A., et al., *Solar cell efficiency tables (Version 45).* Progress in Photovoltaics: Research and Applications, 2015. **23**: p. 1-9.
38. Bosserez, T., et al., *Design of Compact Photoelectrochemical Cells for Water Splitting.* Oil & Gas Science and Technology, 2015. **IFP Energies nouvelles**.
39. Bolton, J.R., S.J. Strickler, and J.S. Connolly, *Limiting and realizable efficiencies of solar photolysis of water.* Nature, 1985. **3116**: p. 495-500.
40. Hu, S., et al., *An analysis of the optimal band gaps of light absorbers in integrated tandem photoelectrochemical water-splitting systems.* Energy & Environmental Science, 2013. **6**: p. 2984-2993.
41. Seger, B., et al., *2-Photon tandem device for water splitting: comparing photocathode first versus photoanode first designs.* Energy & Environmental Science, 2014. **7**: p. 2397-2413.
42. Bard, A.J. and M.A. Fox, *Artificial Photosynthesis: Solar Splitting of Water to Hydrogen and Oxygen.* Accounts of Chemical Research, 1995. **28**: p. 141-145.
43. Prévot, M.S. and K. Sivula, *Photoelectrochemical Tandem Cells for Solar Water Splitting.* Journal of Physical Chemistry C, 2013.
44. Cox, C.R., et al., *Ten-percent solar-to-fuel conversion with nonprecious materials.* Proceedings of the National Academy of Sciences, 2014. **111**(39): p. 14057–14061.

45. Woodhouse, M. and B.A. Parkinson, *Combinatorial approaches for the identification and optimization of oxide semiconductors for efficient solar photoelectrolysis.* Chemical Society Review, 2009. **38**: p. 197-210.
46. Onda, K., et al., *Wet Electrons at the H2O/TiO2 (110) Surface.* Science, 2005. **308**(5725): p. 1154-1158.
47. Seferlis, A.K. and S.G. Neophytides, *On the kinetics of photoelectrocatalytic water splitting on nanocrystalline TiO2 films.* Applied Catalysis B: Environmental 2013. **132-133**: p. 543-552.
48. Miller, E. and R. Rocheleau. *Photoelectrochemical Production of Hydrogen*. in *Proceedings of the 2002 U.S. DOE Hydrogen Program Review*. 2002. Golden, Colorado USA.
49. Wu, H. and Z. Zhang, *Photoelectrochemical water splitting and simultaneous photoelectrocatalytic degradation of organic pollutant on highly smooth and ordered TiO2 nanotube arrays.* Journal of Solid State Chemistry, 2011. **184**: p. 3202-3207.
50. Chen, S. and L.-W. Wang, *Thermodynamic Oxidation and Reduction Potentials of Photocatalytic Semiconductors in Aqueous Solution.* Chemistry of Materials, 2012. **24**: p. 3659−3666.
51. Gerischer, H., *The Role of Semiconductor Structure and Surface Properties in Photoelectrochemical Processes.* Journal of Electroanalytical Chemistry and Interfacial Electrochemistry, 1983. **150**: p. 553-569.
52. Kudo, A., *Development of photocatalyst materials for water splitting.* International Journal of Hydrogen Energy, 2006. **31**: p. 197-202.
53. Department of Energy, U.S., *Technical Plan-Production*, in *Fuel Cell Technologies Program Multi-Year Research, Development and Demonstration Plan*. 2011, Office of Energy Efficiency and Renewable Energy (EERE), US Department of Energy (DOE), Hydrogen, Fuel Cells and Infrastructure Technologies Program. p. 47.
54. Agency, I.E., *Advanced Materials for Waterphotolysis*, in *Hydrogen Implementing Agreement 2010 Annual Report* 2010, Organisation for Economic Co-operation and Development.
55. Luzzi, A. *Hydrogen production by water photolysis?* 2004. **50**/**51**, 8.
56. Bolton, J.R., *Solar photopdroduction of hydrogen: A review.* Solar Energy, 1996. **57**(1): p. 37-50.
57. Bolton, J.R., *Solar Photoproduction of Hydrogen*, in *IEA Technical Report*. 1996, IEA, University of Western Ontario: London, Ontario Canada. p. 51.
58. Bignozzi, C.A., et al., *Nanostructured photoelectrodes based on WO3: applications to photooxidation of aqueous electrolytes.* Chemical Society Review, 2013. **42**: p. 2228-2246.
59. Reichman, J., *The current-voltage characteristics of semiconductor-electrolyte junction photovoltaic cells.* Applied Physics Letters, 1980. **36**(7): p. 574-577.
60. Hoffmann, M.R., et al., *Environmental Applications of Semiconductor Photocatalysis.* Chemical Reviews (ACS Publications), 1995. **95**: p. 69-96.
61. Baruch, P., et al., *On some thermodynamic aspects of photovoltaic solar energy conversion.* Solar Energy Materials and Solar Cells, 1995. **36**: p. 201-222.
62. Nelson, J., *Photons In, Electrons Out: Basic Principles of PV*, in *The Physics of Solar Cells: Photons In, Electrons Out*. 2003, Imperial College Press. p. 17-39.
63. Parkinson, B.A., *On the Efficiency and Stability of Photoelectrochemical Devices.* Accounts of Chemical Research, 1984. **17**: p. 431-437.
64. Nozik, A.J. and R. Memming, *Physical Chemistry of Semiconductor-Liquid Interfaces.* Journal of Physical Chemistry, 1996. **100**: p. 13061-13078.
65. Buhl-Jr., M.L., et al., *Thermodynamic limits on conversion of solar energy to work or stored energy—Effects of temperature, intensity and atmospheric conditions.* Solar Energy, 1984. **32**(1): p. 75-84.
66. Bolton, J.R., *The photochemical conversion and storage of solar energy: An historical perspective.* Solar Energy Materials & Solar Cells, 1995. **38**: p. 543-554.
67. Liao, C.-H., C.-W. Huang, and J.C.S. Wu, *Hydrogen Production from Semiconductor-based Photocatalysis via Water Splitting.* Catalysts, 2012. **2**: p. 490-516.

68. Chen, Z., et al., *Accelerating materials development for photoelectrochemical hydrogen production: Standards for methods, definitions, and reporting protocols.* Journal of Materials Research, 2010. **25**(1): p. 3-16.
69. Rajeshwar, K., *Hydrogen Generation from Irradiated Semiconductor-Liquid Interfaces*, in *Solar Hydrogen Generation: Toward a Renewable Energy Future*, K. Rajeshwar, R. McConnell, and S. Licht, Editors. 2008, Springer. p. 167-228.
70. Miller, E.L., *Photoelectrochemical Hydrogen Production: DOE PEC Working Group Overview*. 2009, Hawaii Natural Energy Institute University of Hawaii at Manoa.
71. Archer, M.D. and J.R. Bolton, *Requirements for Ideal Performance of Photochemical and Photovoltaic Solar Energy Converters.* Journal of Physical Chemistry, 1990. **94**(21): p. 8028-8036.
72. Holladay, J.D., et al., *An overview of hydrogen production technologies.* Catalysis Today, 2009. **139**: p. 244–260.
73. Wang, Z., et al., *Comparison of thermochemical, electrolytic, photoelectrolytic and photochemical solar-to-hydrogen production technologies.* International Journal of Hydrogen Energy, 2012. **37**: p. 16287-16301.
74. Jing, D., et al., *Efficient solar hydrogen production by photocatalytic water splitting: From fundamental study to pilot demonstration.* International Journal of Hydrogen Energy, 2010. **35**: p. 7087-7097.
75. Sayama, K., et al., *Stoichiometric water splitting into H2 and O2 using a mixture of two different photocatalysts and an IO3-/I- shuttle redox mediator under visible light irradiation.* Chemical Communications, 2001: p. 2416–2417.
76. Selli, E., et al., *A photocatalytic water splitting device for separate hydrogen and oxygen evolution.* Chemical Communications, 2007: p. 5022-5024.
77. Ronge´, J., et al., *Monolithic cells for solar fuels.* Chemical Society Reviews, 2014. **43**: p. 7963-7981
78. Schröder, V., et al., *Explosion Limits of Hydrogen/OxygenMixtures at Initial Pressures up to 200 bar.* Chemical Engineering & Technology, 2004. **27**(8): p. 847-851.
79. Miller, E.L., et al., *Optimization of Hybrid Photoelectrodes for Solar Water-Splitting.* Electrochemical and Solid-State Letters, 2005. **8**(5): p. A247-A249.
80. Nocera, D.G., *The Artificial Leaf.* Accounts of Chemical Research, 2011. **45**(5): p. 767–776
81. Turner, J.A., J. Manassen, and A.J. Nozik, *Photoelectrochemistry with p-Si electrodes: Effects of inversion.* Applied Physics Letters, 1980. **37**: p. 488-491.
82. Licht, S., *Multiple Band Gap Semiconductor/Electrolyte Solar Energy Conversion.* Journal of Physical Chemistry B, 2001. **105**: p. 6281-6294.
83. Licht, S., et al., *Over 18% solar energy conversion to generation of hydrogen fuel; theory and experiment for efficient solar water splitting.* International Journal of Hydrogen Energy, 2001. **26**(7): p. 653-659.
84. Nozik, A.J., *Photochemical diodes.* Applied Physics Letters, 1977. **30** (11): p. 567-569.
85. Miller, E.L., et al., *Development of reactively sputtered metal oxide films for hydrogen-producing hybrid multijunction photoelectrodes.* Solar Energy Materials & Solar Cells, 2005. **88**: p. 131-144.
86. Mettee, H., J.W. Otvos, and M. Calvin, *Solar induced water splitting with p/n heterotype photochemical diodes: n-Fe2O3/p-GaP.* Solar Energy Materials, 1981. **4**(4): p. 443-453.
87. Yamane, S., et al., *Efficient Solar Water Splitting with a Composite "n-Si/p-CuI/n-i-p a-Si/n-p GaP/RuO2" Semiconductor Electrode.* Journal of Physical Chemistry C, 2009. **113**(32): p. 14575–14581.
88. Ohashi, K., J. McCann, and J.O.M. Bockris, *Stable photoelectrochemical cells for the splitting of water* Nature, 1977. **266**(610-611).
89. Rocheleau, R.E., E.L. Miller, and A. Misra, *High-Efficiency Photoelectrochemical Hydrogen Production Using Multijunction Amorphous Silicon Photoelectrodes.* Energy & Fuels, 1998. **12**: p. 3-10.

90. Ding, C., et al., *Solar-to-hydrogen efficiency exceeding 2.5% achieved for overall water splitting with an all earth-abundant dual-photoelectrode.* Physical Chemistry Chemical Physics, 2014. **16**: p. 15608-15614.
91. Han, L., et al., *Efficient Water-Splitting Device Based on a Bismuth Vanadate Photoanode and Thin-Film Silicon Solar Cells.* ChemSusChem, 2014. **7**(10): p. 2832–2838.
92. Brillet, J., M. Grätzel, and K. Sivula, *Decoupling Feature Size and Functionality in Solution-Processed, Porous Hematite Electrodes for Solar Water Splitting.* Nano Letters, 2010. **10**(10): p. 4155–4160.
93. Brillet, J., et al., *Highly efficient water splitting by a dual-absorber tandem cell.* Nature Photonics, 2012. **6**: p. 824-828.
94. Brillet, J., et al., *Examining architectures of photoanode–photovoltaic tandem cells for solar water splitting*. Journal of Materials Research, 2010. **25**(1): p. 17-24.
95. Cowan, A.J. and J.R. Durrant, *Long-lived charge separated states in nanostructured semiconductor photoelectrodes for the production of solar fuels.* Chemical Society Review, 2013. **42**: p. 2281-2293.
96. Heller, A., *Conversion of sunlight into electrical power and photoassisted electrolysis of water in photoelectrochemical cells.* Accounts of Chemical Research, 1981. **14**(5): p. 154-162.
97. Nozik, A.J., *Efficency of Converting Solar Irradiance into Electrical or Chemical Free Energy*. 2005, NREL, University of Colorado Boulder.
98. Tryk, D.A., A. Fujishima, and K. Honda, *Recent topics in photoelectrochemistry: achievements and future prospects.* Electrochimica Acta, 2000. **45**: p. 2363-2376.
99. Varghese, O.K. and C.A. Grimes, *Appropriate strategies for determining the photoconversion efficiency of water photoelectrolysis cells: A review with examples using titania nanotube array photoanodes.* Solar Energy Materials & Solar Cells, 2008. **92**: p. 374-384.
100. Lewis, N.S., *Chemical Control of Charge Transfer and Recombination at Semiconductor Photoelectrode Surfaces.* Inorganic Chemistry, 2005. **44**(20): p. 6900-6911.
101. Weber, M.F. and M.J. Dignam, *Efficiency of Splitting Water with Semiconducting Photoelectrodes.* Journal of the Electrochemical Society, 1984. **131**(6): p. 1258-1265.
102. Murphy, A.B., et al., *Efficiency of solar water splitting using semiconductor electrodes.* International Journal of Hydrogen Energy, 1999. **31**(14): p. 1999-2017.
103. Rauh, R.D., et al., *Design and Evaluation of New Oxide Photoanodes for the Photoelectrolysis of Water with Solar Energy.* Journal of Physical Chemistry, 1979. **83**(17): p. 2221-2226.
104. Gerischer, H., *Solar photoelectrolysis with semiconductor electrodes*, in *Solar Energy Conversion*. 1979, Springer Berlin Heidelberg. p. 115-172.
105. Lopes, T., et al., *Characterization of photoelectrochemical cells for water splitting by electrochemical impedance spectroscopy.* International Journal of Hydrogen Energy, 2010. **35**(20): p. 11601-11608.
106. Seger, B. and P.V. Kamat, *Fuel Cell Geared in Reverse: Photocatalytic Hydrogen Production Using a TiO2/Nafion/Pt Membrane Assembly with No Applied Bias.* Journal of Physical Chemistry C, 2009. **113**(43): p. 18946–18952.
107. Ampelli, C., et al., *Synthesis of solar fuels by a novel photoelectrocatalytic approach.* Energy & Environmental Science, 2010. **3**: p. 292-301.
108. Kitano, M., K. Tsujimaru, and M. Anpo, *Decomposition of water in the separate evolution of hydrogen and oxygen using visible light-responsive TiO2 thin film photocatalysts: Effect of the work function of the substrates on the yield of the reaction.* Applied Catalysis A: General, 2006. **314**: p. 179–183.
109. Haussener, S., et al., *Modeling, simulation, and design criteria for photoelectrochemical water-splitting systems.* Energy & Environmental Science, 2012. **5**: p. 9922-9935.
110. Dare-Edwards, M.P., et al., *Electrochemistry and photoelectrochemistry of iron(III) oxide.* Journal of the Chemical Society, Faraday Transactions 1, 1983. **79**: p. 2027-2041.

111. Weber, M.F. and M.J. Dignam, *Efficiency of Splitting Water with Semiconducting Photoelectrodes.* Journal of the Electrochemical Society, 1984. **131**(6): p. 1258-1265.
112. Bak, T., et al., *Photo-electrochemical hydrogen generation from water using solar energy. Materials-related aspects.* International Journal of Hydrogen Energy, 2002. **27**(10): p. 991-1022.
113. Murphy, A.B., et al., *Efficiency of solar water splitting using semiconductor electrodes.* International Journal of Hydrogen Energy, 2006. **31**(14): p. 1999-2017.
114. van-de-Krol, R., Y. Liang, and J. Schoonman, *Solar hydrogen production with nanostructured metal oxides.* Journal of Materials Chemistry, 2008. **18**: p. 2311-2320.
115. *The Book of Photon Tools: Stephen J. Dearden*. 1999: Oriel Instruments.
116. Tong, L., et al., *Sustained solar hydrogen generation using a dye-sensitised NiO photocathode/BiVO4 tandem photo-electrochemical device.* Energy & Environmental Science, 2012. **5**: p. 9472-9475.
117. Lin, C.-Y., et al., *Cu2O|NiOx nanocomposite as an inexpensive photocathode in photoelectrochemical water splitting.* Chemical Science, 2012. **3**: p. 3482–3487.
118. Jia, Q., K. Iwashina, and A. Kudo, *Facile fabrication of an efficient BiVO4 thin film electrode for water splitting under visible light irradiation.* Proceedings of the National Academy of Sciences, 2012. **109**(29): p. 11564-11569.
119. Iwashina, K. and A. Kudo, *Rh-Doped SrTiO3 Photocatalyst Electrode Showing Cathodic Photocurrent for Water Splitting under Visible-Light Irradiation.* Journal of the American Chemical Society, 2011. **133**(34): p. 13272–13275.
120. Bornoz, P., et al., *A Bismuth Vanadate−Cuprous Oxide Tandem Cell for Overall Solar Water Splitting.* Journal of Physical Chemistry C, 2014. **118**(30): p. 16959–16966.
121. Tilley, S.D., et al., *Light-Induced Water Splitting with Hematite: Improved Nanostructure and Iridium Oxide Catalysis.* Angewandte Chemie, 2010. **122**.
122. Guo, J., *Electronic structure characterization and bandgap engineering of solar hydrogen materials*. 2007, Lawrence Berkeley National Laboratory: Berkeley, CA.
123. Osterloh, F.E. and B.A. Parkinson, *Recent developments in solar water-splitting photocatalysis*, in *Materials Research Society*. 2011. p. 17-22.
124. Nozik, A.J., *p-n photoelectrolysis cells.* Applied Physics Letters, 1976. **29**: p. 150-153.
125. Nozik, A.J., *Photoelectrochemisty Applications to Solar Energy.* Annual Reveiw Physical Chemistry, 1978. **29**: p. 189 - 222.
126. Kamat, P.V., et al., *Beyond Photovoltaics: Semiconductor Nanoarchitectures for Liquid-Junction Solar Cells.* Chemical Reviews (ACS Publications), 2010. **110**: p. 6664-6688.
127. Scaife, D.E., *Oxide semiconductors in photoelectrochemical conversion of solar energy.* Solar Energy, 1980. **25**(1): p. 41-54.
128. Binninger, T., et al., *Thermodynamic explanation of the universal correlation between oxygen evolution activity and corrosion of oxide catalysts.* Scientific Reports, 2015. **5**(12167): p. 1-7.
129. Artero, V. and M. Fontecave, *Light-driven bioinspired water splitting: Recent developments in photoelectrode materials.* Comptes Rendus Chimie, 2011. **14**: p. 799-810.
130. Klein, A., et al., *Transparent Conducting Oxides for Photovoltaics: Manipulation of Fermi Level,Work Function and Energy Band Alignment.* Materials, 2010. **3**: p. 4892-3914.
131. Hamberg, I., et al., *Band-gap widening in heavily Sn-daped In2O3.* Physical Review B, 1984. **30**(6): p. 3240 - 3249.
132. Gordon, R.G., *Criteria for Choosing Transparent Conductors*, in *MRS Bulletin*. 2000.
133. Goto, K., T. Kawashima, and N. Tanabe, *Heat-resisting TCO films for PV cells.* Solar Energy Materials & Solar Cells, 2006. **90**(18-19): p. 3251-3260.
134. McKone, J.R., N.S. Lewis, and H.B. Gray, *Will Solar-Driven Water-Splitting Devices See the Light of Day?* Chemistry of Materials, 2013. **26**(1): p. 407-414.
135. Sivula, K., F. Le-Formal, and M. Grätzel, *WO3-Fe2O3 Photoanodes for Water Splitting: A Host Scaffold, Guest Absorber Approach.* Chemistry of Materials, 2009. **21**: p. 2862-2867.

136. Kay, A., I. Cesar, and M. Grätzel, *New Benchmark for Water Photooxidation by Nanostructured a-Fe2O3 Films.* Journal of the American Chemical Society, 2006. **128**: p. 15714-15721.
137. Zhong, D.K., et al., *Photo-assisted electrodeposition of cobalt–phosphate (Co–Pi) catalyst on hematite photoanodes for solar water oxidation.* Energy & Environmental Science, 2011. **4**: p. 1759-1764.
138. Alarcon-Llado, E., et al., *BiVO4 thin film photoanodes grown by chemical vapor deposition.* Physical Chemistry Chemical Physics, 2014. **16**: p. 1651-1657.
139. Liu, R., et al., *Water Splitting by Tungsten Oxide Prepared by Atomic Layer Deposition and Decorated with an Oxygen-Evolving Catalyst.* Angewandte Chemie International Edition, 2011. **50**: p. 499-502.
140. Zhong, M., et al., *Surface Modification of CoOx Loaded BiVO4 Photoanodes with Ultrathin p-Type NiO Layers for Improved Solar Water Oxidation.* Journal of the American Chemical Society 2015. **137**(15): p. 5053-5060.
141. Li, C., et al., *Positive onset potential and stability of Cu2O-based photocathodes in water splitting by atomic layer deposition of a Ga2O3 buffer layer.* Energy & Environmental Science, 2015. **8**: p. 1493-1500.
142. Kim, W., et al., *Promoting water photooxidation on transparent WO3 thin films using an alumina overlayer.* Energy & Environmental Science, 2013. **6**: p. 3732–3739.
143. Paracchino, A., et al., *Highly active oxide photocathode for photoelectrochemical water reduction.* Nature Materials, 2011. **10**: p. 456-461.
144. Strandwitz, N.C., et al., *Photoelectrochemical Behavior of n ‑type Si(100) Electrodes Coated with Thin Films of Manganese Oxide Grown by Atomic Layer Deposition.* Journal of Physical Chemistry C, 2013. **117**(10): p. 4931−4936.
145. Berglund, S.P., et al., *Photoelectrochemical Oxidation of Water Using Nanostructured BiVO4 Films.* Journal of Physical Chemistry C, 2011. **115**(9): p. 3794–3802.
146. Berglund, S.P., et al., *Incorporation of Mo and W into nanostructured BiVO4 films for efficient photoelectrochemical water oxidation.* Physical Chemistry Chemical Physics, 2012. **14**: p. 7065-7075.
147. Shi, X., et al., *Efficient photoelectrochemical hydrogen production from bismuth vanadate-decorated tungsten trioxide helix nanostructures.* Nature Communications, 2014. **5**.
148. Ahn, K.-S., et al., *The effect of thermal annealing on photoelectrochemical responses of WO3 thin films.* Journal of Applied Physics, 2007. **101**: p. 093524-1-4.
149. Abdi, F.F., et al., *Efficient solar water splitting by enhanced charge separation in a bismuth vanadate-silicon tandem photoelectrode.* Nature Communications, 2013. **4**(2195).
150. Abdi, F.F. and R. van de Krol, *Nature and Light Dependence of Bulk Recombination in Co-Pi-Catalyzed BiVO4 Photoanodes.* Journal of Physical Chemistry C, 2012. **116**(17): p. 9398–9404.
151. Liang, Y., et al., *Highly Improved Quantum Efficiencies for Thin Film BiVO4 Photoanodes.* Journal of Physical Chemistry C, 2011. **115**(35): p. 17594–17598.
152. Shinde, S.S., et al., *Physical properties of hematite a-Fe2O3 thin films: application to photoelectrochemical solar cells.* Journal of Semiconductors, 2011. **32**(1).
153. Marsen, B., et al., *Progress in sputtered tungsten trioxide for photoelectrode applications.* International Journal of Hydrogen Energy, 2007. **32**: p. 3110-3115.
154. Chen, L., et al., *Reactive Sputtering of Bismuth Vanadate Photoanodes for Solar Water Splitting.* Journal of Physical Chemistry C, 2013. **117**(42): p. 21635–21642.
155. Chen, L., et al., *Mo-Doped BiVO4 Photoanodes Synthesized by Reactive Sputtering.* ChemSusChem, 2015. **8**: p. 1066 – 1071.
156. Mao, A., et al., *Hematite modified tungsten trioxide nanoparticle photoanode for solar water oxidation.* Journal of Power Sources, 2012. **210**: p. 32-37.
157. McDonald, K.J. and K.-S. Choi, *Photodeposition of Co-Based Oxygen Evolution Catalysts on a-Fe2O3 Photoanodes.* Chemistry of Materials, 2011. **23**(7): p. 1686–1693.

158. Mi, Q., et al., *A quantitative assessment of the competition between water and anion oxidation at WO3 photoanodes in acidic aqueous electrolytes.* Energy & Environmental Science, 2012. **5**: p. 5694-5699.
159. Mi, Q., et al., *Photoelectrochemical oxidation of anions by WO3 in aqueous and nonaqueous electrolytes.* Energy & Environmental Science, 2013.
160. Seabold, J.A. and K.-S. Choi, *Efficient and Stable Photo-Oxidation of Water by a Bismuth Vanadate Photoanode Coupled with an Iron Oxyhydroxide Oxygen Evolution Catalyst.* Journal of the American Chemical Society, 2012. **134**: p. 2186−2192.
161. Zhang, Z. and P. Wang, *Highly stable copper oxide composite as an effective photocathode for water splitting via a facile electrochemical synthesis strategy.* Journal of Materials Chemistry, 2012. **22**: p. 2456–2464.
162. Ding, C., et al., *Visible light driven overall water splitting using cocatalyst/BiVO4 photoanode with minimized bias.* Physical Chemistry Chemical Physics, 2013. **15**: p. 4589--4595.
163. Xi, L., et al., *A novel strategy for surface treatment on hematite photoanode for efficient water oxidation.* Chemical Science, 2013. **4**: p. 164-169
164. Zhang, K., et al., *Photoelectrochemical cells with tungsten trioxide/Mo-doped BiVO4 bilayers.* Physical Chemistry Chemical Physics, 2012. **14**: p. 11119-11124.
165. Qin, D.-D., et al., *Dense layers of vertically oriented WO3 crystals as anodes for photoelectrochemical water oxidation.* Chemical Communications, 2012. **48**: p. 729-731.
166. Amano, F., et al., *Facile Preparation of Platelike Tungsten Oxide Thin Film Electrodes with High Photoelectrode Activity.* ACS Applied Materials & Interfaces, 2011. **3**(10): p. 4047–4052.
167. Biswas, S.K. and J.-O. Baeg, *A facile one-step synthesis of single crystalline hierarchical WO3 with enhanced activity for photoelectrochemical solar water oxidation.* International Journal of Hydrogen Energy, 2013. **38**(8): p. 3177-3188.
168. Neves, M.C. and T. Trindade, *Chemical bath deposition of BiVO4.* Thin Solid Films, 2002. **406**(1-2): p. 93-97.
169. Shen, S., et al., *Physical and photoelectrochemical characterization of Ti-doped hematite photoanodes prepared by solution growth.* Journal of Materials Chemistry A, 2013. **1**: p. 14498–14506.
170. Jeong, H.W., et al., *Strategic Modification of BiVO4 for Improving Photoelectrochemical Water Oxidation Performance.* Journal of Physical Chemistry C, 2013. **117**(18): p. 9104–9112.
171. Luo, H., et al., *Structural and Photoelectrochemical Properties of BiVO4 Thin Films.* Journal of Physical Chemistry C, 2008. **112**(15): p. 6099-6102.
172. Su, J., et al., *Nanostructured WO3/BiVO4 Heterojunction Films for Efficient Photoelectrochemical Water Splitting.* Nano Letters, 2011. **11**: p. 1928–1933.
173. Lin, F., B.F. Bachman, and S.W. Boettcher, *Impact of Electrocatalyst Activity and Ion Permeability on Water-Splitting Photoanodes.* Journal of Physical Chemistry Letters, 2015. **6**(13): p. 2427–2433.
174. Chatchai, P., et al., *FTO/SnO2/BiVO4 Composite Photoelectrode for Water Oxidation under Visible Light Irradiation.* Electrochemical and Solid-State Letters, 2008. **11**(6): p. H160-H163.
175. Choudhary, S., et al., *Nanostructured CuO/SrTiO3 bilayered thin films for photoelectrochemical water splitting.* Journal of Solid State Electrochemistry, 2013. **17**: p. 2531-2538.
176. Sayama, K., et al., *Photoelectrochemical Decomposition of Water into H2 and O2 on Porous BiVO4 Thin-Film Electrodes under Visible Light and Significant Effect of Ag Ion Treatment.* Journal of Physical Chemistry B, 2006. **110**(23): p. 11352-11360.
177. Fujimoto, I., et al., *WO3/BiVO4 composite photoelectrode prepared by improved auto-combustion method for highly efficient water splitting.* International Journal of Hydrogen Energy, 2013. **39**(6): p. 2454-2461.
178. Yagi, M., et al., *Preparation and photoelectrocatalytic activity of a nano-structured WO3 platelet film.* Journal of Solid State Chemistry, 2008. **181**: p. 175-182.

179. Yang, B., et al., *Strong photoresponse of nanostructured tungsten trioxide films prepared via a sol–gel route.* Journal of Materials Chemistry, 2007. **17**: p. 2722-2729.
180. Barczuk, P.J., et al., *Structural and photoelectrochemical investigation of boron-modified nanostructured tungsten trioxide films.* Electrochimica Acta, 2013. **104**: p. 282-288.
181. Han, S., et al., *Enhancing photoelectrochemical activity of nanocrystalline WO3 electrodes by surface tuning with Fe(III).* International Journal of Hydrogen Energy, 2012. **37**(22): p. 16810-16816.
182. Kim, J.K., et al., *Synthesis of transparent mesoporous tungsten trioxide films with enhanced photoelectrochemical response: application to unassisted solar water splitting.* Energy & Environmental Science, 2011. **4**: p. 1465–1470.
183. Wang, G., et al., *Facile Synthesis of Highly Photoactive a-Fe2O3-Based Films for Water Oxidation.* Nano Letters, 2011. **11**: p. 3503-3509.
184. Rao, P.M., et al., *Simultaneously Efficient Light Absorption and Charge Separation in WO3/BiVO4 Core/Shell Nanowire Photoanode for Photoelectrochemical Water Oxidation.* Nano Letters, 2014. **14**: p. 1099−1105.
185. Eisenberg, D., H.S. Ahn, and A.J. Bard, *Enhanced photoelectrochemical water oxidation on bismuth vanadate by electrodeposition of amorphous titanium dioxide.* Journal of the American Chemical Society, 2014. **Just Accepted**.
186. Zhao, J., E. Olide, and F.E. Osterloh, *Enhancing Majority Carrier Transport in WO3 Water Oxidation Photoanode via Electrochemical Doping.* Journal of The Electrochemical Society, 2015. **162**(1): p. H65-H71.
187. Bica, E., et al., *Characterization of some tungsten trioxide thin films obtained by dip-coating.* Journal of Optoelectronics and Advanced Materials, 2009. **1**(6): p. 1011-1014.
188. Li, W., et al., *Photoelectrochemical and physical properties of WO3 films obtained by the polymeric precursor method.* International Journal of Hydrogen Energy, 2010. **35**(24): p. 13137-13145.
189. Xie, B., et al., *Preparation of monoclinic BiVO4 thin film by citrate route for photocatalytic application under visible light.* Thin Solid Films, 2010. **518**(8): p. 1958–1961.
190. Seabold, J.A., K. Zhu, and N.R. Neale, *Efficient solar photoelectrolysis by nanoporous Mo:BiVO4 through controlled electron transport.* Physical Chemistry Chemical Physics, 2014. **16**: p. 1121-1131.
191. Zhou, B., et al., *Fabrication and photoelectrocatalytic properties of nanocrystalline monoclinic BiVO4 thin-film electrode.* Journal of Environmental Science, 2011. **23**.
192. Herrmann-Geppert, I., et al., *Surface aspects of sol–gel derived hematite films for the photoelectrochemical oxidation of water.* Physical Chemistry Chemical Physics, 2013. **15**: p. 1389-1398.
193. Sinclair, T.S., et al., *Factors affecting bismuth vanadate photoelectrochemical performance.* Material Horizons Communication, 2015. **2**: p. 330–337.
194. Li, G., D. Zhang, and J.C. Yu, *Ordered Mesoporous BiVO4 through Nanocasting: A Superior Visible Light-Driven Photocatalyst.* Chemistry of Materials, 2008. **20**(12): p. 3983–3992.
195. Ismail, A.A. and D.W. Bahnemann, *Photochemical splitting of water for hydrogen production by photocatalysis: A review.* Solar Energy Materials and Solar Cells, 2014. **128**: p. 85-101.
196. Turner, J.A., et al., *Photoelectrochemical Water Systems for H2 Production*, in *2007 DOE Hydrogen, Fuel Cells, and Infrastructure Technologies Program Review*. 2007, NREL, Hawaii Natural Energy Institute.
197. Ni, M., et al., *A review and recent developments in photocatalytic water-splitting using TiO2 for hydrogen production.* Renewable and Sustainable Energy Reviews, 2007. **11**: p. 401-425.
198. Koriche, N., et al., *Photocatalytic hydrogen evolution over delafossite CuAlO2.* International Journal of Hydrogen Energy, 2005. **30**: p. 693-699.

199. Joshi, U.A., A.M. Palasyuk, and P.A. Maggard, *Photoelectrochemical Investigation and Electronic Structure of a p-Type CuNbO3 Photocathode.* Journal of Physical Chemistry C, 2011. **115**(27): p. 13534-13539.
200. Choi, J., N. King, and P.A. Maggard, *Metastable Cu(I)-Niobate Semiconductor with a Low-Temperature, Nanoparticle-Mediated Synthesis.* ACS Nano, 2013. **7**(2): p. 1699–1708.
201. Jongh, P.E.d., D. Vanmaekelbergh, and J.J. Kelly, *Cu2O: a catalyst for the photochemical decomposition of water?* Chemical Communications, 1999: p. 1069–1070.
202. Zhang, Q., et al., *CuO nanostructures: Synthesis, characterization, growth mechanisms, fundamental properties, and applications.* Progress in Materials Science, 2014. **60**: p. 208-337.
203. Sun, S., *Recent advances in hybrid Cu2O-based heterogeneous nanostructures.* Nanoscale, 2015. **7**: p. 10850-10882.
204. Hara, M., et al., *Cu2O as a photocatalyst for overall water splitting under visible light irradiation.* Chemical Communications, 1998. **3**: p. 357-358.
205. Barreca, D., et al., *The Potential of Supported Cu2O and CuO Nanosystems in Photocatalytic H2 Production.* ChemsusChem, 2009. **2**(3): p. 230-233.
206. Huang, Q., et al., *Highly aligned Cu2O/CuO/TiO2 core/shell nanowire arrays as photocathodes for water photoelectrolysis.* Journal of Materials Chemistry A, 2013. **1**: p. 2418–2425.
207. Han, J., et al., *Cu2O/CuO photocathode with improved stability for photoelectrochemical water reduction.* RSC Advances, 2015. **5**: p. 10790-10794
208. Wang, P., Y.H. Ng, and R. Amal, *Embedment of anodized p-type Cu2O thin films with CuO nanowires for improvement in photoelectrochemical stability.* Nanoscale, 2013. **5**: p. 2952-2958.
209. Koffyberg, F.P. and F.A. Benko, *A photoelectrochemical determination of the position of the conduction and valence band edges of p-type CuO.* Journal of Applied Physics, 1982. **53**: p. 1173-1177.
210. Cudennec, Y. and A. Lecerf, *The transformation of Cu(OH)2 into CuO, revisited.* Solid State Science, 2003. **5**: p. 1471–1474.
211. Siripala, W., et al., *A Cu2O/TiO2 heterojunction thin film cathode for photoelectrocatalysis.* Solar Energy Materials & Solar Cells, 2003. **77**(3): p. 229-237.
212. Morales-Guio, C.G., et al., *Hydrogen evolution from a copper(I) oxide photocathode coated with an amorphous molybdenum sulphide catalyst.* Nature Communications, 2013. **5**(3059): p. 1-7.
213. Pihosh, Y., et al., *Photocatalytic generation of hydrogen by core-shell WO3/BiVO4 nanorods with ultimate water splitting efficiency.* Scientific Reports, 2015. **5**(11141): p. 1-10.
214. Yang, L., et al., *Semiconductor photocatalysts for water oxidation: current status and challenges.* Physical Chemistry Chemical Physics, 2014. **16**: p. 6810-6826.
215. Liu, X., F. Wang, and Q. Wang, *Nanostructure-based WO3 photoanodes for photoelectrochemical water splitting.* Physical Chemistry Chemical Physics, 2012. **14**: p. 7894–7911.
216. Cesar, I., et al., *Influence of Feature Size, Film Thickness, and Silicon Doping on the Performance of Nanostructured Hematite Photoanodes for Solar Water Splitting.* Journal of Physical Chemistry C, 2009. **113**: p. 772-782.
217. Kim, T.W. and K.-S. Choi, *Nanoporous BiVO4 Photoanodes with Dual-Layer Oxygen Evolution Catalysts for Solar Water Splitting.* Science, 2014. **343**: p. 990-994.
218. Gan, J., X. Lu, and Y. Tong, *Towards highly efficient photoanodes: boosting sunlight-driven semiconductor nanomaterials for water oxidation.* Nanoscale, 2014. **6**: p. 7142-7164.
219. Yang, J., et al., *Roles of Cocatalysts in Photocatalysis and Photoelectrocatalysis.* Accounts of Chemical Research, 2013.
220. Trasatti, S., *Work function, electronegativity, and electrochemical behaviour of metals: III. Electrolytic hydrogen evolution in acid solutions.* Journal of Electroanalytical Chemistry, 1972. **39**(1): p. 163–184.
221. Trasatti, S., *Electrocatalysis by oxides — Attempt at a unifying approach.* Journal of Electroanalytical Chemistry, 1980. **111**(1): p. 125–131.

222. Du, P. and R. Eisenberg, *Catalysts made of earth-abundant elements (Co, Ni, Fe) for water splitting: Recent progress and future challenges.* Energy & Environmental Science, 2012. **5**: p. 6012–6021.
223. Irshad, A. and N. Munichandraiah, *EQCM Investigation of Electrochemical Deposition and Stability of Co−Pi Oxygen Evolution Catalyst of Solar Energy Storage.* Journal of Physical Chemistry C, 2013. **117**: p. 8001-8008.
224. McCrory, C.C.L., et al., *Benchmarking Heterogeneous Electrocatalysts for the Oxygen Evolution Reaction.* Journal of the American Chemical Society, 2013. **135**(45): p. 16977-16987.
225. Kanan, M.W. and D.G. Nocera, *In Situ Formation of an Oxygen-Evolving Catalyst in Neutral Water Containing Phosphate and Co2+*. Science, 2008. **321**: p. 1072-1075.
226. Kanan, M.W., Y. Surendranath, and D.G. Nocera, *Cobalt–phosphate oxygen-evolving compound.* Chemical Society Review, 2009. **38**: p. 109-114.
227. Lutterman, D.A., Y. Surendranath, and D.G. Nocera, *A Self-Healing Oxygen-Evolving Catalyst.* Journal of the American Chemical Society, 2009. **131**(11): p. 3838-3839.
228. Surendranath, Y., M. Dinca, and D.G. Nocera, *Electrolyte-Dependent Electrosynthesis and Activity of Cobalt-Based Water Oxidation Catalysts.* Journal of the American Chemical Society, 2009. **131**(7): p. 2615-2620.
229. Surendranath, Y., M.W. Kanan, and D.G. Nocera, *Mechanistic Studies of the Oxygen Evolution Reaction by a Cobalt-Phosphate Catalyst at Neutral pH.* Journal of the American Chemical Society, 2010. **132**(46): p. 16501-16509.
230. Dincă, M., Y. Surendranath, and D.G. Nocera, *Nickel-borate oxygen-evolving catalyst that functions under benign conditions.* Proceedings of the National Academy of Sciences, 2010. **107**(23): p. 10337–10341.
231. Lin, F. and S.W. Boettcher, *Adaptive semiconductor/electrocatalyst junctions in water-splitting photoanodes.* Nature Materials, 2013. **13**: p. 81-86.
232. Trotochaud, L. and S.W. Boettcher, *Precise oxygen evolution catalysts: Status and opportunities.* Scripta Materialia, 2014. **74**: p. 25–32.
233. Trotochaud, L., et al., *Solution-Cast Metal Oxide Thin Film Electrocatalysts for Oxygen Evolution.* Journal of the American Chemical Society, 2012. **134**(41): p. 17253–17261.
234. Trotochaud, L., T.J. Mills, and S.W. Boettcher, *An Optocatalytic Model for Semiconductor−Catalyst Water-Splitting Photoelectrodes Based on In Situ Optical Measurements on Operational Catalysts.* Journal of Physical Chemistry Letters, 2013. **4**: p. 931-935.
235. Hernandez-Pagan, E.A., et al., *Resistance and polarization losses in aqueous buffer–membrane electrolytes for water-splitting photoelectrochemical cells.* Energy & Environmental Science, 2012. **5**: p. 7582-7589.
236. Modestino, M.A., et al., *Robust production of purified H2 in a stable, selfregulating, and continuously operating solar fuel generator.* Energy & Environmental Science, 2014. **7**(1): p. 297-301.
237. Crawford, S., E. Thimsen, and P. Biswas, *Impact of Different Electrolytes on Photocatalytic Water Splitting.* Journal of the Electrochemical Society, 2009. **156**(5): p. H346-H351.
238. Hill, J.C. and K.-S. Choi, *Effect of Electrolytes on the Selectivity and Stability of n-type WO3 Photoelectrodes for Use in Solar Water Oxidation.* Journal of Physical Chemistry C, 2013. **116**(14): p. 7612–7620.
239. Schalenbach, M., et al., *Gas Permeation through Nafion. Part 1: Measurements.* Journal of Physical Chemistry C, 2015. **119**(45): p. 25145–25155.
240. Schalenbach, M., et al., *Gas Permeation through Nafion. Part 2: Resistor Network Mode.* Journal of Physical Chemistry C, 2015. **119**(45): p. 25156-25169.
241. Chatchai, P., et al., *Efficient photocatalytic activity of water oxidation over WO3/BiVO4 composite under visible light irradiation.* Electrochimica Acta, 2009. **54**: p. 1147–1152.
242. Park, Y., K.J. McDonald, and K.-S. Choi, *Progress in bismuth vanadate photoanodes for use in solar water oxidation.* Chemical Society Review, 2013. **42**: p. 2321--2337.

243. Young, E.R., et al., *Photo-assisted water oxidation with cobalt-based catalyst formed from thin-film cobalt metal on silicon photoanodes.* Energy & Environmental Science, 2011. **4**: p. 2058-2061.
244. Hamd, W., et al., *Mesoporous a-Fe2O3 thin films synthesized via the sol–gel process for light-driven water oxidation.* Physical Chemistry Chemical Physics, 2012. **14**: p. 13224-13232.
245. Butler, M.A., R.D. Nasby, and R.K. Quinn, *Tungsten trioxide as an electrode for photoelectrolysis of water.* Solid State Communications, 1976. **19**(10): p. 1011-1014.
246. Hodes, G., D. Cahen, and J. Manassen, *Tungsten trioxide as a photoanode for a photoelectrochemical cell.* Nature, 1976. **260**: p. 312-313.
247. Tacca, A., et al., *Photoanodes Based on Nanostructured WO3 for Water Splitting.* ChemPhysChem, 2012. **13**: p. 3025 – 3034.
248. Alexander, B.D., et al., *Metal oxide photoanodes for solar hydrogen production.* Journal of Materials Chemistry, 2008. **18**: p. 2298-2303.
249. Ng, C., et al., *Influence of Annealing Temperature of WO3 in Photoelectrochemical Conversion and Energy Storage for Water Splitting.* ACS Applied Materials & Interfaces, 2013. **5**: p. 5269−5275.
250. Kim, J.K., et al., *Inverse opal tungsten trioxide films with mesoporous skeletons: synthesis and photoelectrochemical responses.* Chemical Communications, 2012. **48**.
251. Patra, A., et al., *Sol–gel electrochromic WO3 coatings on glass.* Materials Letters, 2004. **58**: p. 1059-1063.
252. Santato, C., M. Ulmann, and J. Augustynski, *Photoelectrochemical Properties of Nanostructured Tungsten Trioxide Films.* Journal of Physical Chemistry B, 2001. **105**: p. 936-940.
253. Yang, B., et al., *Tungsten Trioxide Films with Controlled Morphology and Strong Photocatalytic Activity via a Simple Sol–Gel Route.* Catalysis Letters, 2007. **118**: p. 280-284.
254. Li, W., et al., *Visible light photoelectrochemical responsiveness of self-organized nanoporous WO3 films.* Electrochimica Acta, 2010. **56**: p. 620–625.
255. Tacconi, N.R.d., et al., *Nanoporous TiO2 and WO3 Films by Anodization of Titanium and Tungsten Substrates: Influence of Process Variables on Morphology and Photoelectrochemical Response.* Journal of Physical Chemistry B, 2006. **110**: p. 25347-25355.
256. Caramori, S., et al., *Efficient Anodically Grown WO3 for Photoelectrochemical Water Splitting.* Energy Procedia, 2012. **22**: p. 127-136.
257. Cristino, V., et al., *Efficient photoelectrochemical water splitting by anodically grown WO3 electrodes.* Langmuir, 2011. **27**: p. 7276-7284.
258. Reyes-Gil, K.R., et al., *Comparison between the Quantum Yields of Compact and Porous WO3 Photoanodes.* Journal of Physical Chemistry C, 2013. **117**: p. 14947−14957.
259. Khare, C., et al., *Layered WO3/TiO2 nanostructures with enhanced photocurrent densities.* International Journal of Hydrogen Energy, 2013. **38**(36): p. 15954-15964.
260. Johansson, M.B., et al., *Electronic and optical properties of nanocrystalline WO3 thin films studied by optical spectroscopy and density functional calculations.* Journal of Physics: Condensed Matter, 2013. **25**.
261. Chandra, D., et al., *Crystallization of Tungsten Trioxide Having Small Mesopores: Highly Efficient Photoanode for Visible-Light-Driven Water Oxidation.* Angewandte Chemie, 2013. **52**: p. 1-5.
262. Santato, C., M. Ulmann, and J. Augustynski, *Enhanced Visible Light Conversion Efficiency Using Nanocrystalline WO3 Films.* Advanced Materials, 2001. **13**(7): p. 511-514.
263. Seabold, J.A. and K.-S. Choi, *Effect of a Cobalt-Based Oxygen Evolution Catalyst on the Stability and the Selectivity of Photo-Oxidation Reactions of a WO3 Photoanode.* Chemistry of Materials, 2011. **23**(5): p. 1105-1112.
264. Chou, L.-Y., et al., *Direct oxygen and hydrogen production by photo water splitting using a robust bioinspired manganese-oxo oligomer complex/tungsten oxide catalytic system.* International Journal of Hydrogen Energy, 2012. **37**: p. 8889-8896.

265. Cherevko, S., et al., *Stability of nanostructured iridium oxide electrocatalysts during oxygen volution reaction in acidic environment*. Electrochemistry Communications, 2014. **48**: p. 81-85.
266. Salje, E., *The orthorhombic phase of WO3.* Acta Crystallographica, 1977. **B33**(2): p. 574-577
267. Loopstra, B.O. and H.M. Rietveld, *Further refinement of the structure of WO3.* Acta Crystallographica, 1969. **B25**(7): p. 1420-1421
268. Dollase, W.A., *Correction of intensities for preferred orientation in powder diffractometry: application of the March model.* Journal of Applied Crystallography, 1986. **19**: p. 267-272.
269. Cantalini, C., et al., *Characterization of sol-gel prepared WO3 thin films as a gas sensor*. Journal of Vacuum Science & Technology A, 1999. **17**(4): p. 1873-1879.
270. Pankove, J.I., *Optical Processes in Semiconductors*. 1971, New York: Dover Publications.
271. González-Borrero, P.P., et al., *Optical band-gap determination of nanostructured WO3 film.* Applied Physics Letters 2010. **96**: p. 061909
272. Hong, W.Q., *Extraction of extinction coefficient of weak absorbing thin films from special absorption.* Journal of Physics D: Applied Physics, 1989. **22**(9): p. 1384-1385.
273. Lide, D.R., *CRC Handbook of Chemistry & Physics*. Internet Version ed. 2005: CRC Press.
274. Dotan, H., et al., *Probing the photoelectrochemical properties of hematite (a-Fe2O3) electrodes using hydrogen peroxide as a hole scavenger*. Energy & Environmental Science, 2011. **4**: p. 958-964
275. Butler, M.A., *Photoelectrolysis and physical properties of the semiconducting electrode WO3.* Journal of Applied Physics, 1977. **48**(5): p. 1914-1920.
276. Sanchez, C., K.D. Sieber, and G.A. Somorjai, *The photoelectrochemistry of niobium doped a-Fe2O3.* Journal of Electroanalytical Chemistry, 1988. **252**: p. 269-290.
277. Formal, F.L., et al., *Passivating surface states on water splitting hematite photoanodes with alumina overlayers.* Chemical Science, 2011. **2**: p. 737–743.
278. Santato, C., et al., *Crystallographically Oriented Mesoporous WO3 Films: Synthesis, Characterization, and Applications.* Journal of the American Chemical Society, 2001. **123**: p. 10639-10649.
279. Su, J., et al., *Vertically Aligned WO3 Nanowire Arrays Grown Directly on Transparent Conducting Oxide Coated Glass: Synthesis and Photoelectrochemical Properties.* Nano Letters, 2011. **11**: p. 203-208.
280. Rao, P.M., I.S. Cho, and X. Zheng, *Flame synthesis of WO3 nanotubes and nanowires for effcient photoelectrochemical water-splitting.* Proceedings of the Combusion Institute, 2013. **34**: p. 2187-2195.
281. Savenije, T.J., et al., *Spatially resolved photoconductive properties of profiled polycrystalline silicon thin films.* Journal of Applied Physics, 2002. **91**(9): p. 5671-5676.
282. Wang, G., et al., *Hydrogen-treated WO3 nanoflakes show enhanced photostability.* Energy & Environmental Science, 2012. **5**: p. 6180-6187.
283. Zhang, J. and Y. Nosaka, *Generation of OH radicals and oxidation mechanism in photocatalysis of WO3 and BiVO4 powders.* Journal of Photochemistry and Photobiology A: Chemistry, 2015. **303-304**: p. 53-58.
284. Zhao, Y., et al., *A High Yield Synthesis of Ligand-Free Iridium Oxide Nanoparticles with High Electrocatalytic Activity.* Journal of Physical Chemistry Letters, 2011. **2**: p. 402–406.
285. Zhao, Z., Z. Li, and Z. Zou, *Electronic structure and optical properties of monoclinic clinobisvanite BiVO4.* Physical Chemistry Chemical Physics, 2011. **13**: p. 4746–4753.
286. Walsh, A., et al., *Band Edge Electronic Structure of BiVO4: Elucidating the Role of the Bi s and V d Orbitals.* Chemistry of Materials, 2009. **21**: p. 547–551.
287. Kudo, A., et al., *Photocatalytic O2 evolution under visible light irradiation on BiVO4 in aqueous AgNO3 solution.* Catalysis Letters, 1998. **53**: p. 229-230.
288. Bierlein, J.D. and A.W. Sleight, *Ferroelasticity in BiVO4.* Solid State Communications, 1975. **16**(1): p. 69-70.

289. Roth, R.S. and J.L. Waring, *Synthesis and Stability of Bismutotantalite Stibiotantalite and Chemically Similar ABO4 Compounds.* American Minerologist, 1963. **48**: p. 1348-1356.
290. Bhattacharya, A.K., K.K. Mallick, and A. Hartridge, *Phase transition in BiVO4.* Materials Letters, 1997. **30**: p. 7-13.
291. Kudo, A., K. Omori, and H. Kato, *A Novel Aqueous Process for Preparation of Crystal Form-Controlled and Highly Crystalline BiVO4 Powder from Layered Vanadates at Room Temperature and Its Photocatalytic and Photophysical Properties.* Journal of the American Chemical Society, 1999. **121**(49): p. 11459–11467.
292. Suarez, C.M., S. Hernández, and N. Russo, *BiVO4 as photocatalyst for solar fuels production through water splitting: A short review.* Applied Catalysis A: General, 2015. **504**: p. 158-170.
293. Iwase, A. and A. Kudo, *Photoelectrochemical water splitting using visible-light-responsive BiVO4 fine particles prepared in an aqueous acetic acid solution.* Journal of Materials Chemistry, 2010. **20**: p. 7536–7542.
294. Oshikiri, M. and M. Boero, *Water Molecule Adsorption Properties on the BiVO4 (100) Surface.* Journal of Physical Chemistry B, 2006. **110**(18): p. 9188-9194.
295. Ghamri, J., et al., *Spectroscopic study of BixEu1−xVO4 and BiyGd1−yVO4 mixed oxides.* Journal of Physics and Chemistry of Solids, 1989. **50**(12): p. 1237–1244.
296. Thalluri, S.M., et al., *Elucidation of important parameters of BiVO4 responsible for photo-catalytic O2 evolution and insights about the rate of the catalytic process.* Chemical Engineering Journal, 2014. **245**: p. 124-132.
297. Abdi, F.F., et al., *The Origin of Slow Carrier Transport in BiVO4 Thin Film Photoanodes: A Time-Resolved Microwave Conductivity Study.* Journal of Physical Chemistry Letters, 2013. **4**(16): p. 2752−2757.
298. Pilli, S.K., et al., *Cobalt-phosphate (Co-Pi) catalyst modified Mo-doped BiVO4 photoelectrodes for solar water oxidation.* Energy & Environmental Science, 2011. **4**: p. 5028–5034.
299. Wang, M., et al., *Effective visible light-active boron and europium co-doped BiVO4 synthesized by sol–gel method for photodegradion of methyl orange.* Journal of Hazardous Materials, 2013. **262**: p. 447-455.
300. Li, Z., et al., *Photoelectrochemical cells for solar hydrogen production: current state of promising photoelectrodes, methods to improve their properties, and outlook.* Energy & Environmental Science, 2013. **6**: p. 347-370.
301. Liang, Y., C.S. Enache, and R. van de Krol, *Photoelectrochemical Characterization of Sprayed α-Fe2O3 Thin Films: Influence of Si Doping and SnO2 Interfacial Layer.* International Journal of Photoenergy, 2008. **2008**: p. 7.
302. Park, H.S., et al., *Factors in the Metal Doping of BiVO4 for Improved Photoelectrocatalytic Activity as Studied by Scanning Electrochemical Microscopy and First-Principles Density Functional Calculation.* Journal of Physical Chemistry C, 2011. **115**: p. 17870–17879.
303. Liu, H., N. Ryuhei, and Y. Nakato, *Promoted Photo-oxidation Reactivity of Particulate BiVO4 Photocatalyst Prepared by a Photoassisted Sol-gel Method.* Journal of the Electrochemical Society, 2005. **152**(11): p. G856-G861.
304. Dunkle, S.S., R.J. Helmich, and K.S. Suslick, *BiVO4 as a Visible-Light Photocatalyst Prepared by Ultrasonic Spray Pyrolysis.* Journal of Physical Chemistry C, 2009. **113**.
305. Cho, S.K., et al., *Metal Doping of BiVO4 by Composite Electrodeposition with Improved Photoelectrochemical Water Oxidation.* Journal of Physical Chemistry C, 2013. **117**(44): p. 23048-23056.
306. Xie, S., et al., *NiO decorated Mo:BiVO4 photoanode with enhanced visible-light photoelectrochemical activity.* International Journal of Hydrogen Energy, 2014. **39**(10): p. 4820–4827.
307. Sayama, K., et al., *Photoelectrochemical decomposition of water on nanocrystalline BiVO4 film electrodes under visible light.* Chemical Communications, 2003: p. 2908-2909

308. McDowell, M.T., et al., *Improved Stability of Polycrystalline Bismuth Vanadate Photoanodes by Use of Dual-Layer Thin TiO2/Ni Coatings.* Journal of Physical Chemistry C, 2014. **118**: p. 19618−19624.
309. Zhong, D.K., S. Choi, and D.R. Gamelin, *Near-Complete Suppression of Surface Recombination in Solar Photoelectrolysis by "Co-Pi" Catalyst-Modified W:BiVO4.* Journal of the American Chemical Society, 2011. **133**: p. 18370-18377.
310. Galembeck, A. and O.L. Alves, *BiVO4 thin film preparation by metalorganic decomposition.* Thin Solid Films, 2000. **365**(1): p. 90-93.
311. Luo, W., et al., *Solar hydrogen generation from seawater with a modified BiVO4 photoanode.* Energy & Environmetnal Science, 2011. **4**: p. 4046–4051.
312. Abdi, F.F., N. Firet, and R. van de Krol, *Efficient BiVO4 Thin Film Photoanodes Modified with Cobalt Phosphate Catalyst and W-doping.* ChemCatChem, 2013. **5**: p. 490 – 496.
313. Hong, S.J., et al., *Heterojunction BiVO4/WO3 electrodes for enhanced photoactivity of water oxidation.* Energy & Environmental Science, 2011. **4**: p. 1781-1787.
314. Saito, R., Y. Miseki, and K. Sayama, *Highly efficient photoelectrochemical water splitting using a thin film photoanode of BiVO4/SnO2/WO3 multi-composite in a carbonate electrolyte.* Chemical Communications, 2012. **48**: p. 3833-3835.
315. Lichterman, M.F., et al., *Enhanced Stability and Activity for Water Oxidation in Alkaline Media with Bismuth Vanadate Photoelectrodes Modified with a Cobalt Oxide Catalytic Layer Produced by Atomic Layer Deposition.* Journal of Physical Chemistry Letters, 2013. **4**(23): p. 4188–4191.
316. Ye, H., H.S. Park, and A.J. Bard, *Screening of Electrocatalysts for Photoelectrochemical Water Oxidation on W-Doped BiVO4 Photocatalysts by Scanning Electrochemical Microscopy.* Journal of Physical Chemistry C, 2011. **115**: p. 12464–12470.
317. Wang, J. and F.E. Osterloh, *Limiting factors for photochemical charge separation in BiVO4/Co3O4, a highly active photocatalyst for water oxidation in sunlight.* Journal of Materials Chemistry A, 2014. **2**: p. 9405–9411.
318. Long, M., W. Cai, and H. Kisch, *Visible Light Induced Photoelectrochemical Properties of n-BiVO4 and n-BiVO4/p-Co3O4.* Journal of Physical Chemistry C, 2008. **112**(2): p. 548–554.
319. Liang, Y. and J. Messinger, *Improving BiVO4 photoanodes for solar water splitting through surface passivation.* Physical Chemistry Chemical Physics, 2014. **16**: p. 12014-12020.
320. Jung, H., et al., *Effect of the Si/TiO2/BiVO4 Heterojunction on the Onset Potential of Photocurrents for Solar Water Oxidation.* ACS Applied Materials & Interfaces, 2015. **7**(10): p. 5788–5796.
321. Joya, K.S. and H.J.M. de Groot, *Artificial Leaf Goes Simpler and More Efficient for Solar Fuel Generation.* ChemSusChem, 2013.
322. Sayama, K., et al., *Photoelectrochemical Decomposition of Water into H2 and O2 on Porous BiVO4 Thin-Film Electrodes under Visible Light and Significant Effect of Ag Ion Treatment.* Journal of Physical Chemistry B, 2006. **110**(23): p. 11352-11360.
323. Tokunaga, S., H. Kato, and A. Kudo, *Selective Preparation of Monoclinic and Tetragonal BiVO4 with Scheelite Structure and Their Photocatalytic Properties.* Chemistry of Materials, 2001. **13**(12): p. 4624-4628.
324. Wang, D., et al., *Crystal Facet Dependence of Water Oxidation on BiVO4 Sheets under Visible Light Irradiation.* Chemistry A European Journal, 2011. **17**(4): p. 1275–1282.
325. Savenije, T.J., M.P. de Haas, and J.M. Warman, *The Yield and Mobility of Charge Carriers in Smooth and Nanoporous TiO2 Films.* Zeitschrift für Physikalische Chemie, 1999. **212**(Part 2): p. 201-206.
326. Su, J., et al., *Aqueous Growth of Pyramidal-Shaped BiVO4 Nanowire Arrays and Structural Characterization: Application to Photoelectrochemical Water Splitting.* Crystal Growth & Design, 2010. **10**(2): p. 856–861.
327. Enache, C.S., et al., *Photo-electrochemical properties of thin-film InVO4 photoanodes: the role of deep donor states.* Journal of Physical Chemistry C, 2009. **113**: p. 19351–19360.

328. Horowitz, G., *Capacitance-voltage measurements and flat-band potential determination on Zr-doped α-Fe2O3 single-crystal electrodes.* Journal of Electroanalytical Chemistry and Interfacial Electrochemistry, 1983. **159**(2): p. 421-436.
329. Formal, F.L., K. Sivula, and M. Gratzel, *The Transient Photocurrent and Photovoltage Behavior of a Hematite Photoanode under Working Conditions and the Influence of Surface Treatments.* Journal of Physical Chemistry C, 2012. **116**: p. 26707−26720.
330. Salvador, P. and C. Gutiérrez, *Analysis of the transient photocurrent-time behaviour of a sintered n-SrTiO3 electrode in water photoelectrolysis.* Journal of Electroanalytical Chemistry and Interfacial Electrochemistry, 1984. **160**(1-2): p. 117–130.
331. Risch, M., et al., *Nickel-oxido structure of a water-oxidizing catalyst film.* Chemical Communications, 2011. **47**: p. 11912-11914
332. Pihosh, Y., et al., *Nanostructured WO3/BiVO4 Photoanodes for Efficient Photoelectrochemical Water Splitting* Small, 2014. **10**(18): p. 3692-3699.
333. Bourgeteau, T., et al., *A H2-evolving photocathode based on direct sensitization of MoS3 with an organic photovoltaic cell.* Energy & Environmental Science, 2013. **6**: p. 2706-2713
334. Laursen, A.B., et al., *Molybdenum sulfides—efficient and viable materials for electro - and photoelectrocatalytic hydrogen evolution.* Energy & Environmental Science, 2012. **5**: p. 5577-5591.
335. Merki, D., et al., *Amorphous molybdenum sulfide films as catalysts for electrochemical hydrogen production in water.* Chemical Science, 2011. **2**: p. 1262–1267.
336. Ahmad, H., et al., *Hydrogen from photo-catalytic water splitting process: A review.* Renewable and Sustainable Energy Reviews, 2015. **43**: p. 599-610.
337. Wang, M., et al., *The intensification technologies to water electrolysis for hydrogen production – A review.* Renewable and Sustainable Energy Reviews, 2014. **29**: p. 573–588.
338. Hisatomi, T., J. Kubota, and K. Domen, *Recent advances in semiconductors for photocatalytic and photoelectrochemical water splitting.* Chemistry Society Reviews, 2014.
339. Wang, G., et al., *Hydrogen-Treated TiO2 Nanowire Arrays for Photoelectrochemical Water Splitting.* Nano Letters, 2011. **11**: p. 3026–3033.
340. Vermaas, D.A., M. Sassenburg, and W.A. Smith, *Photo-assisted water splitting with bipolar membrane induced pH gradients for practical solar fuel devices.* Journal of Materials Chemistry A, 2015. **3**: p. 19556-19562.
341. Vargas-Barbosa, N.M., et al., *Assessing the Utility of Bipolar Membranes for use inPhotoelectrochemical Water-Splitting Cells.* ChemSusChem, 2014. **7**(11): p. 3017–3020.
342. McDonald, M.B., et al., *Use of Bipolar Membranes for Maintaining Steady-State pH Gradients in Membrane-Supported, Solar-Driven Water Splitting.* ChemSusChem, 2014. **11**(7): p. 3021–3027.
343. Yang, J., et al., *A Theoretical Study on the Mechanism of Photocatalytic Oxygen Evolution on BiVO4 in Aqueous Solution.* Chemistry - A European Journal, 2012. **19**: p. 1320 – 1326.

APPENDIX

METAL OXIDE THIN FILM FABRICATION

FTO substrates were bought and precut from Solems. The Ahasi-100 substrates were used for all n-photoanode optimized samples measuring 1 x 4 cm for general samples and 2.5 x 4.5 cm for samples used in the photoelectrocatalytic cell. These substrates are 1mm glass with approximately 80 nm of FTO deposited by chemical vapor deposition, measuring 100Ω resistivity.

SOL GEL PRECURSORS

Mesoporous WO_3

Amount	Product	Supplier	Information
5.5 g	ethanol	VWR	AnalaR NORMAPUR® ACS, Reag. Ph. Eur. analytical reagent (99.9%)
1.8 g	tetrahydrofuran	VWR	AnalaR NORMAPUR® ACS, Reag. Ph. Eur. analytical reagent (99.9%)
0.1 g	Poly(isobutylene-b-ethylene oxide)	Polymer Source	P4973-IbEO or P4972-IbEO
1 g	Tungsten (VI) chloride	Sigma Aldrich	≥99.9% trace metals basis

Tungsten sol gel has a concentration of 0.42 M and pH of 1. Ethanol and THF are added together in a vial. Then the block-copolymer is added and the vial sealed and placed in an oven at 70°C for at least 45 minutes or until the polymer is dissolved. When the solution has cooled to room temperature the WCl_6 is added slowly under a fume hood to avoid the exothermic reaction and chlorine gas produced. Then, the solution is left to spin with a magnetic stirrer at least 1 hour before use. Solution color is initially orange and changes to turquoise-blue within several minutes. Solution should be used the day of synthesis.

Dense WO_3

Amount	Product	Supplier	Information
5.5 g	ethanol	VWR	AnalaR NORMAPUR® ACS, Reag. Ph. Eur. analytical reagent (99.9%)
1.8 g	tetrahydrofuran	VWR	AnalaR NORMAPUR® ACS, Reag. Ph. Eur. analytical reagent (99.9%)
1 g	Tungsten (VI) chloride	Sigma Aldrich	≥99.9% trace metals basis

Tungsten sol gel has a concentration of 0.42 M and pH of 1. Ethanol and THF are added together in a vial. Then the WCl_6 is added slowly under a fume hood to avoid the exothermic reaction and chlorine gas produced. Then the solution is left to spin at least 1 day before use. Solution color is initially orange and changes to turquoise-blue within several minutes. Solution should be used the day after synthesis and is good for about one week.

$BiVO_4$

Amount	Product	Supplier	Information
4.365 g	acetylacetone	Sigma Aldrich	Fluka analytical puriss. p.a. ≥99.5% (GC)
0.56 g	acetic acid	Merck	Suprapur 100% glacial
0.173 g	bismuth (III) nitrate pentahydrate	Sigma Aldrich	ACS reagent ≥98.0%
0.095 g	vanadyl acetylacetonate	Sigma Aldrich	99.98% trace metals basis

$BiVO_4$ sol-gel was adapted and optimized from Sayama et al.[176] $BiVO_4$ sol-gel has a concentration of 0.07 M solution and a pH of 4. Typically 0.097 g of vanadyl acetylacetonate was added due to the poor solubility of vanadium in order to keep the 1:1 stoichiometry of Bi:V. Acetic acid is added to the acetylacetone in a vial. Then, $Bi(NO_3)_3 \cdot 5H_2O$ is added to the vial followed by vanadyl acetylacetonate. (If dopant is introduced this is followed, replacing vanadium in concentration. MoO_3 was found to be the most soluble in the solvent). The solution is then closed and placed in an ultrasonic bath of at 25 – 30°C and sonicated for 15 minutes. The solution is then left overnight, unexposed to light, for use the next day. This sol-gel is generally usable for 1 – 2 weeks, but had the best performance the day after synthesis. Solutions sonicated at room temperature revealed less dense microstructures than those sonicated at slightly higher 30°C temperatures.

SnO_2

Amount	Product	Supplier	Information
5 g	ethanol	VWR	AnalaR NORMAPUR® ACS, Reag. Ph. Eur. analytical reagent (99.9%)
2 g	tetrahydrofuran	VWR	AnalaR NORMAPUR® ACS, Reag. Ph. Eur. analytical reagent (99.9%)
0.4 g	distilled water	Merck	Millipore Q-pod 18MΩ
0.345 g	tin (II) chloride	Sigma Aldrich	Reagent grade 98%

Tin sol-gel has a concentration of 0.29 M and a pH of 1. Ethanol and THF are added together in a vial followed by distilled water. Tin chloride is then added to the solution. The solution is left to stir with a magnetic stirrer for at least 1 day. Solution is best when used 2 – 3 days after synthesis. Solution can be used up to 1 month after synthesis.

DIP COATING

WO_3

WO_3 was dip coated at room temperature with < 3% relative humidity. Dip speed was 2.7 mm/s resulting in an average of 80 nm /layer. A total of 8 layers were generally dipped with annealing at 350°C for 2 – 5 minutes between layers. Final calcination was effectuated at 400°C for 30 minutes resulting in mesoporous layers of 550 – 600 nm or dense layers of 300 – 350 nm.

$BiVO_4$

$BiVO_4$ was dip coated at room temperature with < 3% relative humidity. Dip speed was 0.8 mm/s resulting in an average of 10 nm /layer. Optimized $BiVO_4$ requires an annealing step of at least 400°C between layers for 2 – 5 minutes and a final calcination treatment for 60 minutes at 450°C. Annealing at 450°C between layers instigates larger crystal size but requires more than 10 layers to successfully connect these large crystals and cover the FTO surface. Several successive annealing treatments weaken the glass substrate and will generally break the substrate; therefore annealing between layers at 400°C is more accommodating for glass substrates, but produces smaller crystal sizes.

SnO_2

SnO_2 was dip coated at room temperature with < 3% relative humidity. Dip speed was 1.62 mm/s resulting in an average of 10 nm/layer. 1 – 2 layers of SnO_2 were generally deposited to be used as a hole blocking layer between FTO and $BiVO_4$ or WO_3 and $BiVO_4$, measuring 10 – 20 nm. An annealing step between layers at 350°C for 2 – 5 minutes was used, with a final calcination treatment of 400°C for 30 minutes.

CATALYST DEPOSITION

All catalyst electrodeposition, electroflocculation, and photo-assisted electrodeposition were completed with a platinum grill counter electrode measuring 1.5 x 4 cm (6 cm^2). These were done in a laboratory made borosilicate cylindrical vial. The platinum grill was in general 1 cm away from the sample (which was typically 1 x 2 cm or 2 cm^2 on the FTO substrate due to dip coating and leaving the FTO bare for contact connection) during catalyst deposition and the sample was illuminated from the back for photo-assisted electrodepositions.

IrO_X

Iridium nanoparticles were synthesized according to previous reports [284].

Amount	Product	Supplier	Information
0.097 g	K_2IrCl_6	Sigma Aldrich	99.9% trace metal basis
100 mL	distilled water	Merck	Millipore Q-pod 18MΩ
1 mL	10% sodium hydroxide	Sigma Aldrich	ACS reagent, ≥97.0%, pellets
1 mL	3 M HNO_3	Sigma Aldrich	ACS Reagent grade 98%

Potassium hexachloroiridate (IV) was dissolved in distilled water to produce a brown liquid of pH 5 – 6. Subsequently, a 10% weight solution of NaOH was added to produce a brown/orange liquid of pH 12 – 13. This solution was placed in a 250 mL round bottom flask and heated in an oil bath at 90°C for 20 minutes. During this time the solution turned yellow then light blue, still maintaining a pH of 12 – 13. After 20 minutes the solution was quickly placed into an ice bath and 3 M HNO_3 was added until the solution had a pH of 1 (≈ 1 mL of 3 M HNO_3) resulting in a dark blue solution. The solution was then left

to spin with a magnetic stirrer in the ice bath for 80 minutes. The solution was then kept at 2 – 4°C and usable for 1 month.

These nanoparticles measuring 1 – 2 nm in diameter were confirmed by HR-TEM and UV-vis absorption of the characteristic peak of 580 nm shown below in Figure 130 (using water as a baseline) [284]:

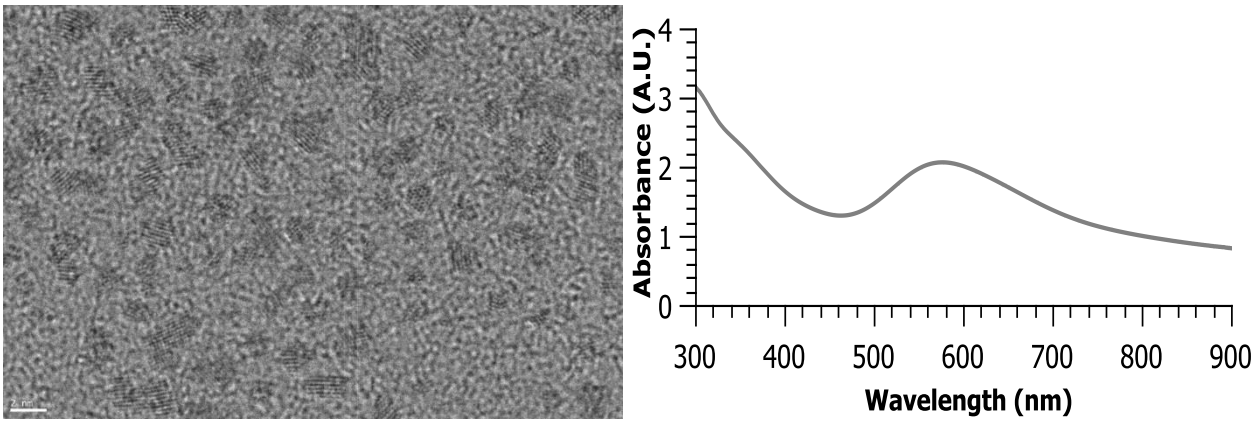

Figure 130: HR-TEM image (left) of IrO_X nanoparticles and UV-vis absorbance spectrum (right) with characteristic peak of IrO_X nanoparticles at 580 nm

The dark blue solution of nanoparticles was kept in the refrigerator for up to one month. Nanoparticles were deposited by electroflocculation. WO_3 thin films were immersed in a solution of 2 mM $IrO_X \cdot nH_2O$ (in H_2O/HNO_3 measuring pH 1). Then +1.4 V vs. Ag/AgCl KCl saturated was applied to the working electrode for 1, 5, and 10 minutes. Samples were rinsed with deionized water and dried with compressed air after deposition.

RuO_2

RuO_2 nanoparticles were synthesized by Capucine Sossoye of the Laboratoire de Chimie de la Matière Condensée de Paris (LCMCP) at the Collège de France. Depositions by electroflocculation (like with IrO_X) or wet impregnation were unsuccessful.

Co-Pi

Cobalt phosphate was deposited onto metal oxides by photo-assisted electrodeposition according to the protocol reported by Nocera et al.[226]. Photo-assisted electrodeposition was done in a solution of 0.5 mM $Co(NO_3)_2$ in 0.1 M KPi pH 6 (for WO_3) or pH 7 (for $BiVO_4$) at 0.9 V vs. Ag/AgCl (KCl sat'd) reference for 1, 5, or 10 minutes with 300mW/cm² illumination Xe lamp 280 W with 400 nm UV filter with Pt grill counter electrode (2cm² active area exposed to catalyst deposition – back illuminated). Samples were rinsed with deionized water and dried with compressed air after deposition.

FeOOH

Iron oxyhydroxide photo-assisted electrodeposition was effectuated according to Kim et al. protocol [217]. 0.1 M $FeSO_4 \cdot 7H_2O$ was dissolved into 100 mL deionized water and the solution was degassed with N_2 for 1 hour just before use.

1st step: 0.25V vs Ag/AgCl (KCl sat'd) reference electrode for 5, 10, or 30 minutes with 300mW/cm² illumination Xe lamp 280W with 400nm UV filter with Pt grill counter electrode (2cm² active area exposed to catalyst deposition – back illuminated)

2nd step: 1.2V vs. Ag/AgCl (KCl sat'd) reference electrode for 60s without illumination to potentially cover sites which were not photoactive with Pt grill counter electrode

Finally the sample was rinsed with deionized water and dried with compressed air. EDX detected a 4 – 5% atomic ratio to $BiVO_4$ for 10 minute (1st step) followed by 1 min (2nd step) depositions.

NiOOH

Nickel co-catalysts were deposited in two attempts. The first effort, by photo-assisted electrodeposition from 0.5 mM nickel nitrate in 0.1 M potassium phosphate, was effectuated deriving from Nocera et al. Co-Pi procedures 0.9 V vs. Ag/AgCl KCl saturated reference electrode while back illuminated by 300 mW/cm², followed by rinsing with deionized water and air drying [226]. Nickel was not detected by neither EDX nor XPS with this method on WO_3 and therefore abandoned.

NiOOH was attempted to deposit on $BiVO_4$ from Kim et al. but again undetectable by EDX and XPS [217]. A 0.1 M nickel sulfate hexahydrate in water was degassed with nitrogen for 1 hour before use and then photo-assisted electrodeposited onto samples

1st step: 0.11V vs Ag/AgCl (KCl sat'd) reference electrode until 22mC/cm² charge passed (730 – 935s) with 300mW/cm² illumination Xe lamp 280W with 400nm UV filter with Pt grill counter electrode (2cm² active area exposed to catalyst deposition – back illuminated)

2nd step: 1.2V vs. Ag/AgCl (KCl sat'd) reference electrode for 60s without illumination to potentially cover sites which were not photoactive with Pt grill counter electrode

Finally the samples were rinsed with deionized water and dried with compressed air.

NiB_i

Finally nickel borate was electrodeposited on $BiVO_4$ derived from Dincă et al. [230]. $Ni(NO_3)_2 \cdot H_2O$ was dissolved in 0.1 M solution of boric acid adjusted to pH 7 with 0.1 M NaOH making a solution of 1 mM

nickel. A cyclic voltammogram is shown below which corresponds to literature values reported of increasing peaks suggesting growth of the deposited material [230].

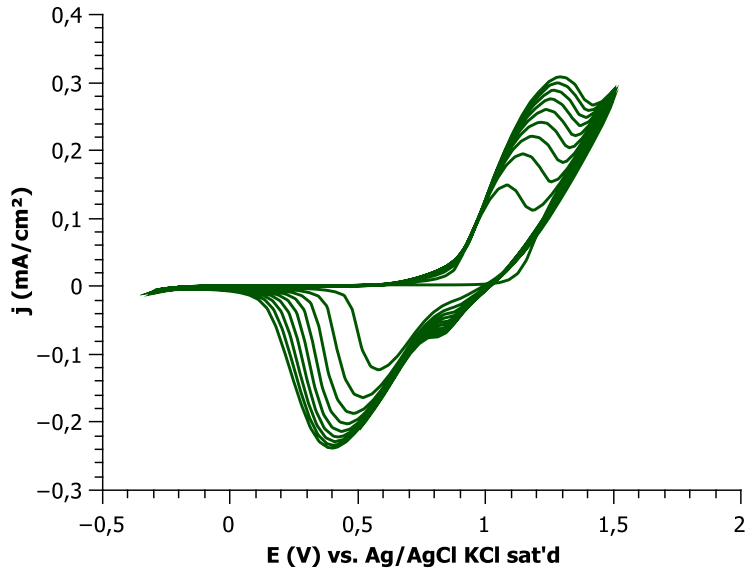

Figure 131: Cyclic voltammogram scans at 50 mV/s of nickel borate solution with FTO as working electrode and platinum grill counter electrode

NiB_i was deposited onto samples at 1.229 V vs. Ag/AgCl KCl saturated reference electrodes until 0.05 C/cm² was reached (generally about 25 minutes). This resulted in nickel like sheets seen in Figure 73.

CHARACTERIZATION

PHOTOELECTROCHEMICAL MEASUREMENTS

Sample Preparation

Samples were masked with 3M polyimide 929219A electrochemical tape. Active area was defined by hole puncher measuring 0.2 cm² to define the area illuminated and exposed to electrolyte. Contacts were placed directly onto FTO (making sure to not touch the metal oxide being characterized to create a short circuit) with copper 3M Scotch 1245 tape 6 mm in width. The adhesive was acrylic based and the tape is characterized to have an internal resistance of 0,001 Ω. The FTO was generally rinsed with ethanol before scotch adhesion.

Figure 132: Masked sample with copper tape contact

Lamp

A Newport xenon arc lamp was used throughout photoelectrochemical experiments. Newport model 6258 300 W sans ozone lamp working at 280 W was regulated to have an output of 100 – 350 mW/cm² illumination for photoelectrochemical measurements in an Arc Lamp Housing enclosure, model 67001. This was powered by a Newport power supply 69911in junction with an Oriel UV filter 51272 (400 nm) and an Oriel liquid filter 61945 (250-950 nm). For AM1.5G measurements a Newport AM1.5G filter was placed in addition to the infrared filter. All photoelectrochemical measurements were done 50 cm away from the arc lamp source and the light output was verified by a 1918-R Newport power meter 918D-UV-OD3R, UV Silicon Detector (200 – 1100 nm). All measurements were done with a xenon arc lamp possessing less than 900 hours of lamp life to ensure reliability of the spectrum. (Shown below) in Figure 133:

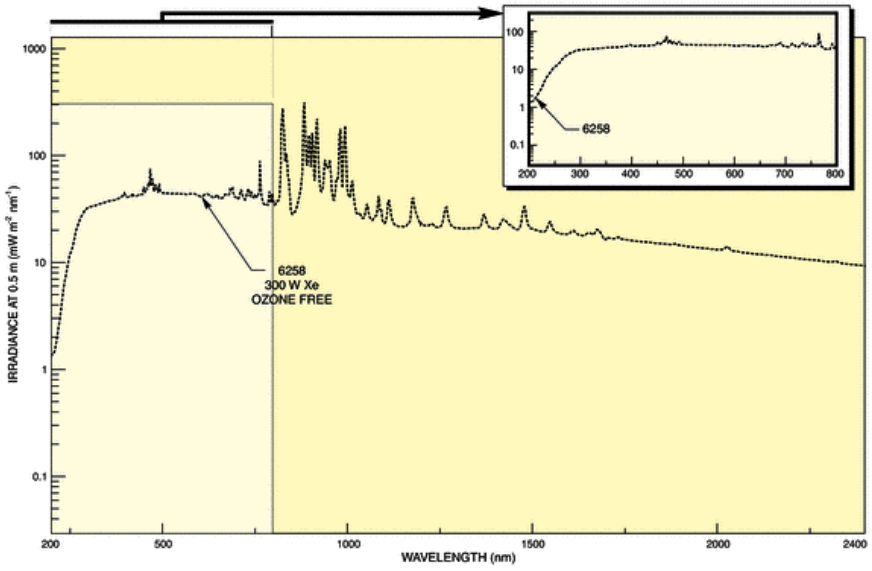

Figure 133: Newport 300W Xe arc lamp sans ozone spectrum (model 6258)

Electrodes

Linear voltage sweeps, chronoamperometry, and cyclic voltammetry were done with a platinum coil counter electrode. All 3-electrode setups were done versus an Ag/AgCl KCl saturated reference electrode. Using the Nernstian relation of 0.197 V vs. NHE and accounting for pH by a 0.059 V/pH shift to reference versus RHE. For 2-electrode cell measurements the counter electrode was the photocathode which was also connected to the reference. The photoanode was employed as the working electrode.

UV-visible cuvettes were used for simple linear voltage sweeps and electrochemical tests that did not require hermetically sealed cells for gas detection (setup shown in Figure 135). These cuvettes limit the amount of electrolyte used to small quantities and allow 340 – 900 nm light wavelengths. Considering photoanode substrates on glass, a large number of UV wavelengths do not reach the metal oxide under study, thus the polystirol cuvettes did not optically affect performance significantly. The same type of cuvettes, Carl Roth GmbH Rotilabo®-disposable cuvettes made of polystyrene (8127.1) with a volume of 4.5 mL (Passband PS: 340 – 900 nm) were used throughout all photo-electrochemical tests. The UV-vis transmittance spectrum is seen below with air as a baseline in Figure 134:

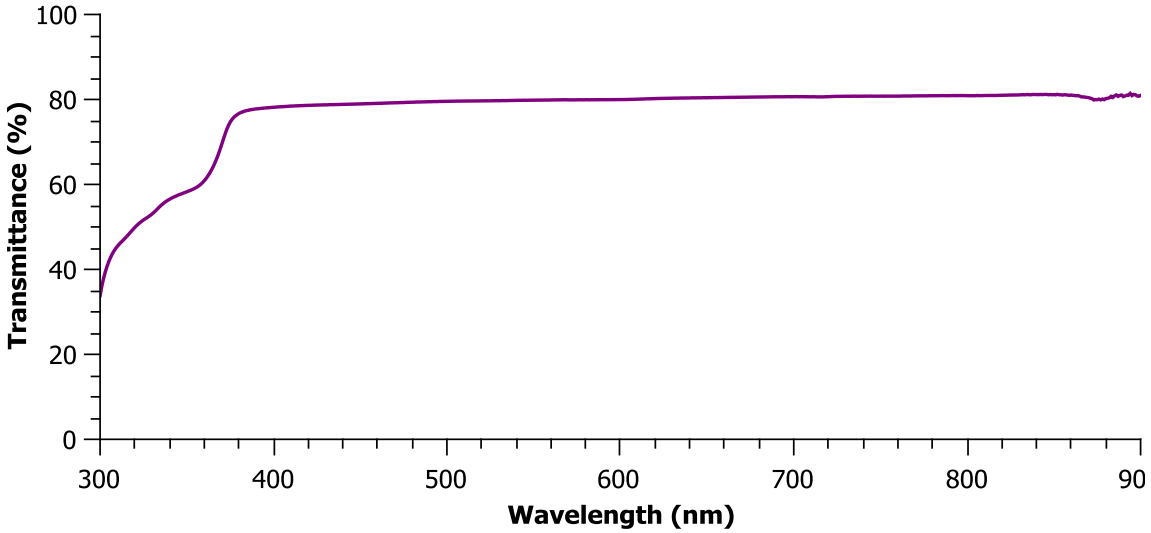

Figure 134: Light transmission of UV-vis cuvette Roth 1827

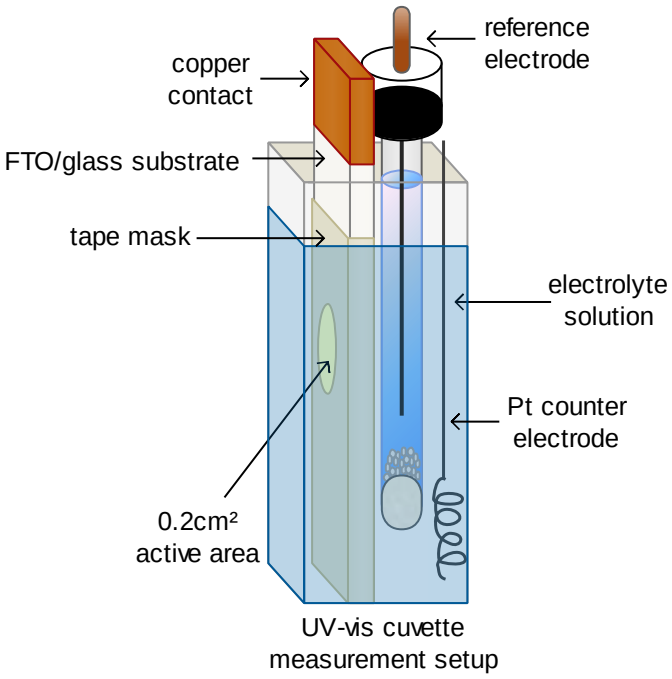

Figure 135: UV-vis 3-electrode setup for photoelectrochemical and electrochemical measurements

Solutions

Solutions for photoelectrochemical and electrochemical tests were measured to be 1 M in concentration and pH was verified with a Mettler Toledo FiveEasy™ FE20 pH meter calibrated with standards of pH 4, 7.01, and 10.01 regularly in a 2 point calibration in the pH range of interest. The pH sensor used was a radiometer analytical Ag/AgCl electrode type pHC3001-9.

K_2HPO_4, KH_2PO_4, H_2SO_4, and H_3PO_4 were mainly used as electrolyte salts and always at concentrations of 1 M with pH ranging between 0 – 7 (verified by pH meter). Salts and solutions used for these electrolytes are specified below:

Product	Supplier	Information
K_2HPO_4	Sigma Aldrich	ACS reagent, ≥98%
KH_2PO_4	Sigma Aldrich	*Trace*SELECT®, for trace analysis, ≥99.995% (metals basis)
distilled water	Merck	Millipore Q-pod 18MΩ
H_2SO_4	Sigma Aldrich	ACS reagent, 95.0-98.0%
H_3PO_4	Sigma Aldrich	85 wt. % in H_2O

With one exception, a 1 M solution of sodium phosphate (Sigma Aldrich) was used for the Faradaic test of $BiVO_4$ due to unavailability upon dislocation in another laboratory; though post-performed tests suggest similar results between sodium and potassium cations with $BiVO_4$.

Potentiostat

Several potentiostats were used during this PhD. Most notably AMETEK Solartron pstat 1 MS/s, Princeton 273A, and Bio-Logic SP300.

Linear voltage sweeps were done with a 10 mV/s step from –0.6 – 1.4 V for $BiVO_4$ and –0.2 – 1.8 V vs. reference electrode for WO_3; using a reference Ag/AgCl KCl (sat'd). Cyclic voltammetry was effectuated between these respective potentials for each material as well. Cyclic voltammetry was also used in order to determine oxidation potentials of co-catalysts in solution indicating at which potentials to deposit them onto the photoelectrodes for use.

EIS

Mott Schottky measurements were done with 10 mV amplitude at frequencies varying from 5Hz to 20kHz. These scans for n-type materials were done in the cathodic range, −0.8 V to 0 V for $BiVO_4$ and −0.4 V – 0.2 V vs. Ag/AgCl KCl saturated reference electrode for WO_3 (to avoid reduction of WO_3). Impedance measurements were done by scanning from 200 kHZ – 0.1 Hz at 10 mV amplitude for different potentials (notably 2 V vs. ref) in the cell employing FTO as working and counter electrodes and Ag/AgCl KCl saturated reference electrode.

Ultraviolet Visible Spectroscopy

Absorption and transmission

Agilent Technologies Cary Series UV-vis-NIR 5000 spectrometer was used for absorbance and transmittance measurements. Double beam measurements were taken with glass/FTO substrates as a zero/baseline and scans were completed between 300 – 900 nm with a data point at every nanometer. The optical band gap was extrapolated by equation (16) the intercept at the x-axis for when y = 0. Using m = ½ for direct semiconductors and m = 2 and for indirect semiconductors. Both WO_3 and $BiVO_4$ were considered to be indirect semiconductors.

Field Gun Emission Scanning Electron Microscopy and EDX

Imaging and microanalysis was performed on a SU-70 Hitachi FEG-SEM and a X-Max Oxford EDX detector, instruments facilitated by the IMPC (Institut des Matériaux de Paris Centre FR2482) financially supported by the C'Nano projects of the Region Ile-de-France. FEG-SEM images were collected under 10 – 15 kV tension for $BiVO_4$ and WO_3 top images and at 10 kV for cross section images due to the glass substrate charging. Working distances were typically 4.6 mm and images taken under secondary electron

signals. EDX measurements were effectuated using 3 – 10 kV depending on the element and penetration depth desired with a molybdenum or silicon standard for quantification. Measurements under 1% atomic were considered below the limit of detection and therefore considered unreliable.

High Resolution Transmission Electron Microscopy

High resolution transmission electron microscopy (HR-TEM) was effectuated using a JEOL JEM-2010 at Université de Pierre et Marie Curie at l'Institut des Matériaux de Paris Centre by Sandra Casale.

X-ray Diffraction

A Bruker AXS D8 advance copper was used for XRD measurements. Using a copper anode and kα x-ray wavelength of 1.54 Å. Crystallite size was determined by the Scherrer equation shown below, applicable to crystallite sizes less than 0.1μm nanoscale particles:

$$\tau = \frac{K\lambda}{\beta cos\theta} \tag{38}$$

Where τ is the is the mean size of the ordered crystalline size, K is a dimensionless shape factor (defined as 0.9 but can vary with crystallite shape), λ the x-ray wavelength (1.54Å), β the line broadening at half the maximum intensity (FWHM), after subtracting the instrumental line broadening in radians, and Θ the Bragg angle. Scans were effectuated from 2Θ = 20 – 80. Using 40 kV and 40 mA along with symmetric angles of phi at 90° and chi, x, y, and z at 0°. Freeware Jana and Visualization for Electronic and Structural Analysis (VESTA by JP minerals) were used for 3D crystal models. XRD aid was given by Guido

X-ray Photoelectron Spectroscopy

XPS measurements were done using an ESCA+ d'Omicron Nano Technology with an Al Kα ($h\nu$ = 1486.6 eV) X-ray source. These measurements were completed at the Unversité de Pierre et Marie Curie (Paris VI) Laboratoires de l'Institut des Matériaux de Paris Centre (IMPC, FR 2482) in association by the Centre national de la recherche scientifique (CNRS) at Laboratoire de Réactivité de Surface (LRS) by Christophe Calers.

Time Resolved Microwave Conductivity

Time resolved microwave conductivity experiments were completed at the Helmholtz Zentrum in Berlin. These measurements were completed with studied metal oxides but deposited onto quartz instead of glass/FTO. Measurements were completed under microwave frequencies with laser pulses of 350 nm (within the band gap of materials) and done by Dennis Friedrich [297].

GAS CHROMATOGRAPH

For gas quantification and detection by direct injections, 50 µL aliquots were taken from headspace by an airtight syringe from an air tight 3-electrode cell divided by glass frits containing the metal oxide under illumination in the appropriate electrolyte solution. Before measurements, the cell was purged with nitrogen gas for at least 30 minutes and a zero measurement was made to ensure no oxygen was detected by the GC. A Perkin Elmer Clarus 580 working at 32°C with a column time of 2 minutes detected O_2 by aid of a TCD working at 90°C. Unfortunately, the detection of O_2 in nitrogen carrier gas and in the GC column is quite low, suggesting under estimation and large error source. Considering oxygen is quite soluble in solution, a Clark electrode was occasionally used in parallel for complementary measurements of O_2 which remained in solution.

For continuous gas detection, an SRA S-series high sensibility micro-gas chromatograph was used for O_2 and H_2 detection. The carrier gas was high purity argon flowing at 5 mL/min by use of a Bronkhorst EL Flow® select mass flow. The carrier gas was input into the photoelectrocatalytic cell and then transferred to a guard in order to avoid solvent being injected directly to the µGC. Approximately 1.5 m of PEEK tubing (with a diameter of 0.3mm) was used to transfer this gas as well as the guard which measured 13m in diameter and 150 mm long, equaling a total volume from the cell to the µGC of 20.96 cm^3. Internal pressure of the MS-5A large volume high sensibility column is 28 PSI (1.93 bar) with an injection temperature of 50°C and TCD temperature of 90°C. The pump is activated for 20 seconds effectuating an injection during 50 ms while measuring every 60 seconds. Carrier gas for the SRA µGC requires to be high purity of at least 99, 9995% (argon), and error can derive from impurities.

CLARK ELECTRODE

Unisense Ox-N 13987 oxygen detector was calibrated by a two-point calibration in air saturated 1 M solutions of KPi and in a nitrogen purged 1 M same solution. Due to the fluctuation in temperature due to continuous illumination of samples during faradaic testing, these calibrations were effectuated at 40°C (which was measured to be the saturation temperature of the cell for injection faradaic tests, occurring 45 minutes into testing). Therefore tests with the oxygen detector in solution were calibrated and effectuated at 40°C to account for this eventual change in temperature.

PHOTOELECTROCATALYTIC CELL PLAN

The photoelectrocatalytic cell was constructed by Bernard Sartor at the CEA in Grenoble. The plan is shown next as Figure 136:

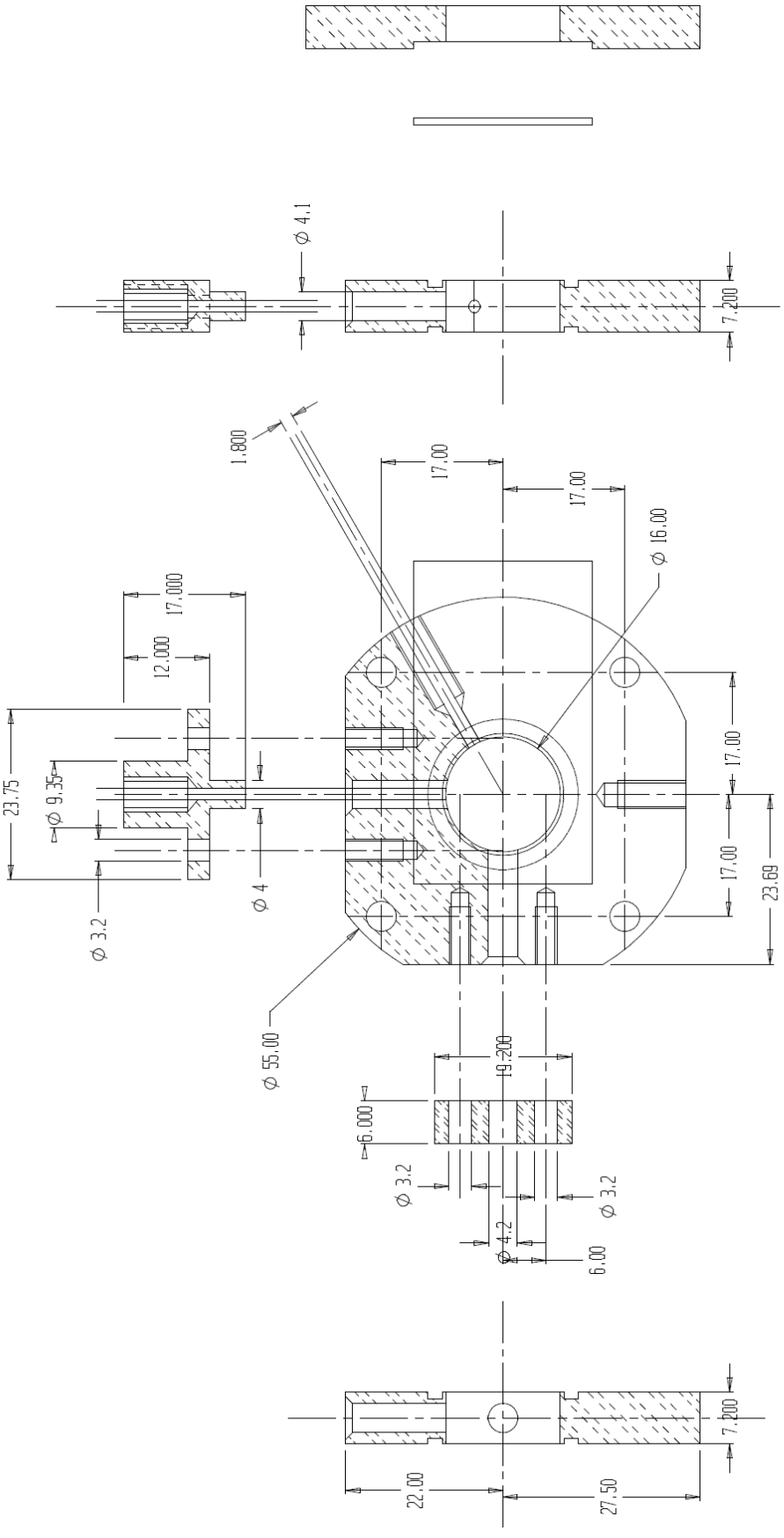
ϕ 4.1
7.200
1.800
17.00
17.00
ϕ 16.00
17.000
12.000
23.75
ϕ 9.35
ϕ 4
ϕ 3.2
17.00
17.00
23.69
ϕ 55.00
19.200
6.000
ϕ 3.2
ϕ 3.2
ϕ 4.2
6.00
7.200
22.00
27.50